11 April 2014 | $10

Science

Killing Fields

Medical mystery in Central America

AAAS

CONTENTS continued >>

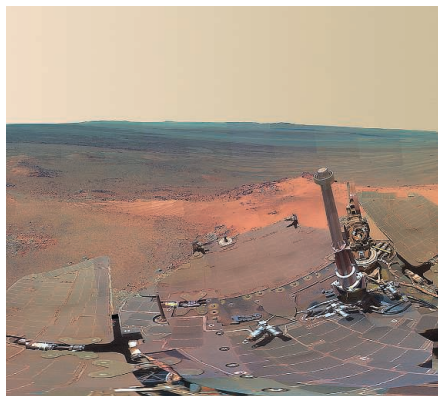

page 138

page 154

ON THE WEB THIS WEEK

>> *Science* Podcast
On this week's show: the mechanics of flies' evasive maneuvers and a roundup from our daily news site.

>> Find More Online
Check out *Science* Express, the weekly podcast, videos, daily news, our research journals, and *Science* Careers at **www.sciencemag.org.**

COVER

A sugar cane cutter near the town of El Paisnal, El Salvador, at dawn. Agricultural workers in El Salvador and many neighboring countries have been suffering from a chronic kidney disease that has no obvious cause, but many researchers believe it is linked to heat and dehydration. See page 143.
Photo: Malcolm Linton

DEPARTMENTS

RESEARCH ARTICLES

REPORTS

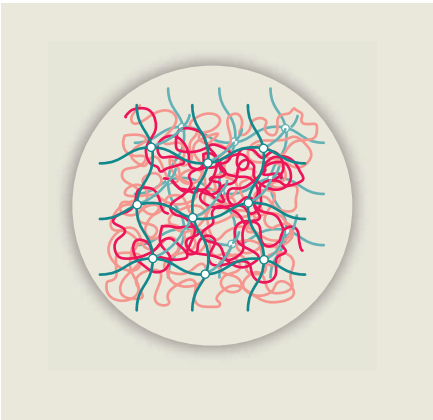

pages 161 & 186

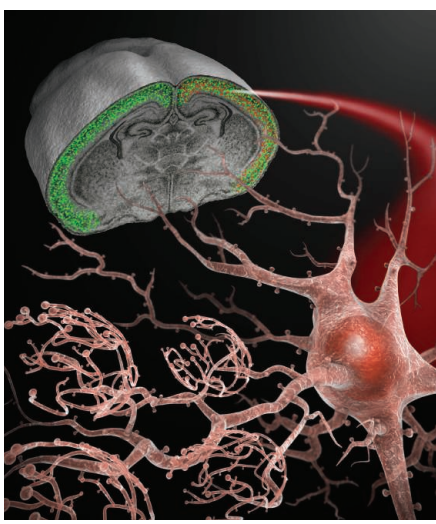

page 167

SCIENCE (ISSN 0036-8075) is published weekly on Friday, except the last week in December, by the American Association for the Advancement of Science, 1200 New York Avenue, NW, Washington, DC 20005. Periodicals Mail postage (publication No. 484460) paid at Washington, DC, and additional mailing offices. Domestic individual membership and subscription (51 issues): $153 ($74 allocated to subscription). Domestic institutional subscription (51 issues): $1282; Foreign postage extra: Mexico, Caribbean (surface mail) $55; other countries (air assist delivery) $85. First class, airmail, student, and emeritus rates on request. Canadian rates with GST available upon request, GST #1254 88122. Publications Mail Agreement Number 1069624. **Printed in the U.S.A.**

Change of address: Allow 4 weeks, giving old and new addresses and 8-digit account number. **Postmaster:** Send change of address to AAAS, P.O. Box 96178, Washington, DC 20090–6178. **Single-copy sales:** $10.00 current issue, $15.00 back issue prepaid includes surface postage; bulk rates on request. **Authorization to photocopy** material for internal or personal use under circumstances not falling within the fair use provisions of the Copyright Act is granted by AAAS to libraries and other users registered with the Copyright Clearance Center (CCC) Transactional Reporting Service, provided that $30.00 per article is paid directly to CCC, 222 Rosewood Drive, Danvers, MA 01923. The identification code for *Science* is 0036-8075. *Science* is indexed in the *Reader's Guide to Periodical Literature* and in several specialized indexes.

Tripeptide Maternal Support

In flowering plants, fertilization involves multiple gametes. The diploid zygote, which will form the embryonic plant, is surrounded by the often triploid endosperm, which provides a supportive and nourishing function. Working in *Arabidopsis*, **Costa *et al.*** (p. 168; see the Perspective by **Bayer**) identified a trio of small signaling peptides that derive from the endosperm but that regulate growth of the embryo. RNA interference was used to down-regulate expression of all three peptides. Fertilization was not affected, but seed growth was. The peptides were critical for normal development of the suspensor, which tethers and nourishes the growing embryo.

Taking Flight

Anyone who has tried to swat a fly knows that their powers of avoidance are impressive. Executing such rapid avoidance requires that the sensory recognition of an approaching threat be translated into evasive movement almost instantaneously. **Muijres *et al.*** (p. 172) used high-speed videos and winged robots to show that flies respond to approaching threats by making rapid banked turns initiated through subtle wing changes over just a few wing beats. The rapid nature of the turns suggests the existence of dedicated sensory-motor circuits that allow the flies to respond within a fraction of a second.

Exposing a Hidden State

Shining intense laser light on a material can temporarily alter its properties. The effect usually subsides after a few picoseconds, unless the system is trapped in a metastable state, in which case the transient period may last as long as microseconds. **Stojchevska *et al.*** (p. 177) observed that, following exposure to a 35-femtosecond laser pulse, the layered dichalcogenide *1T*-TaS_2 entered a stable "hidden" state not present in the equilibrium phase diagram and stayed there indefinitely. The switch to the hidden state could be reversed by heat or a train of laser pulses. Because the switch alters the sample's conducting properties, the phenomenon might also lead to practical applications.

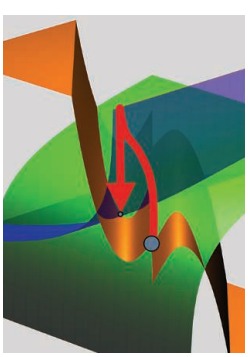

CREDITS: (TOP TO BOTTOM) V. ALTOUNIAN/*SCIENCE*; DRAGAN MIHAILOVIC

Axon Routing in the Olfactory System >>

The olfactory system of mice entails a developmental program that wires neurons expressing similar olfactory receptors into glomeruli together. Although the adult olfactory system continues to produce and incorporate new neurons, it cannot withstand severe damage (see the Perspective by **Cheetham and Belluscio**). **Ma *et al.*** (p. 194) and **Tsai and Barnea** (p. 197) examined the difference in responses between early development and adulthood. Manipulating the expression of an odorant receptor or the activity of the olfactory neurons altered olfactory neuron axonal pathfinding. The results suggest that the guidance systems used differ between early development and adulthood: Early axons find their own way, but later-in-life axons can only follow existing pathways.

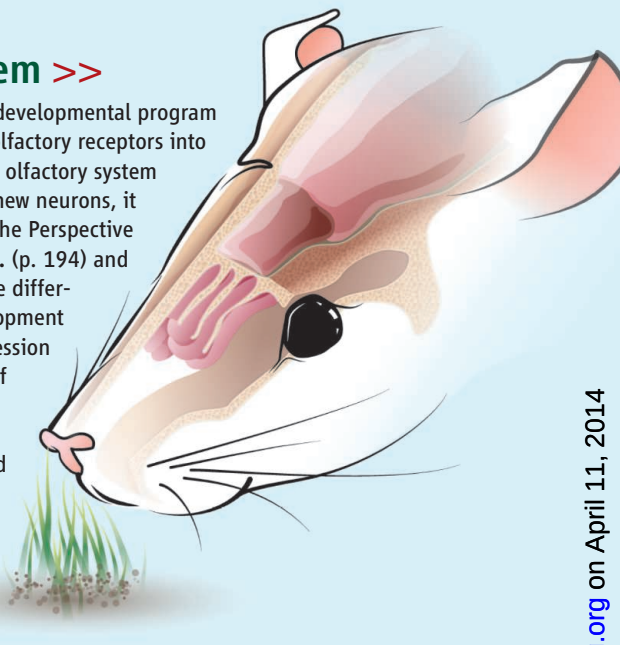

Yeasty HIPHOP

In order to identify how chemical compounds target genes and affect the physiology of the cell, tests of the perturbations that occur when treated with a range of pharmacological chemicals are required. By examining the haploinsufficiency profiling (HIP) and homozygous profiling (HOP) chemogenomic platforms, **Lee *et al.*** (p. 208) analyzed the response of yeast to thousands of different small molecules, with genetic, proteomic, and bioinformatic analyses. Over 300 compounds were identified that targeted 121 genes within 45 cellular response signature networks. These networks were used to extrapolate the likely effects of related chemicals, their impact upon genetic pathways, and to identify putative gene functions.

Shutting Down Repair to Protect

Cells repair DNA double-strand breaks (DSBs) by halting the cell cycle and activating the machinery involved in mending the breaks. However, during mitosis neither the DNA damage checkpoint nor DSB repair occur, apparently leaving the cell extremely vulnerable to DSBs. **Orthwein *et al.*** (p. 189, published online 20 March) found that the DSB response was blocked by the phosphorylation of two crucial repair factors, RNF8 and PB531, preventing their recruitment to the site of damage. Restoring DSB repair during mitosis caused end-to-end chromosome fusions, which are catastrophic for chromosome segregation and normal cell division, explaining why the repair machinery is shut down during cell division.

Toughening Up Elastomers

Elastomers are soft polymer materials widely used in industry and daily life. Inspired by recent work on double-network hydrogels, **Ducrot *et al.*** (p. 186; see the Perspective by **Gong**) designed interpenetrated network elastomers that contained isotropically prestretched chains as the first network. Double- and triple-network structures yielded elastomers with very high strength and toughness in comparison with the corresponding single networks.

Mapping Stardust

A galaxy's structure throughout time depends largely on its ability to convert the raw material of molecular clouds into stars. One of the most influential properties in determining star formation rates is the distribution of densities among individual molecular clouds, which can be described by a probability density function of volume densities. **Kainulainen *et al.*** (p. 183) devised a method to quantify these distributions from empirical dust extinction maps of nearby clouds. The threshold for star formation in these observationally based calculations was significantly lower than theoretical predictions.

Additional summaries

Interneurons Reach Far and Wide

Interneurons in the brain have been garnering increasing attention. **Southwell *et al.*** (p. 167) review the development of this unique class of neurons. The cells migrate long distances during brain development. Transplantation of interneurons derived from embryonic stem cells is yielding insight into disease processes and may have therapeutic potential. For example, Parkinson's disease, epilepsy, certain psychiatric disorders, and even some sorts of chronic pain either involve interneurons or may respond to transplanted interneurons.

All Together Now

In quantum entanglement, correlations between particles mean that the measurement of one determines the outcome of the other(s). Generally, when trying to exploit quantum entanglement, the larger the number of entangled particles, the better. However, the size of entangled systems has been limited. **Haas *et al.*** (p. 180, published online 27 March; see the Perspective by **Widera**) prepared a small ensemble of ultracold atoms into a collective entangled state. Starting from one internal quantum state, the system of cold atoms was excited with a weak microwave pulse leading to a small excitation probability. Because it is not known which atom is promoted into the excited state, the detection of one quantum of excitation projects the system into an entangled quantum state, called a W-state. A fast repeat-until-success scheme produced such W-states quasi-deterministically. Using such a technique was able to yield entangled states of more than 40 particles. The relatively large ensemble-entangled states could potentially in the future find use in quantum sensing or enhanced quantum metrology applications.

Tangling Evolutionary Trees

Evolutionary rates tend to vary among taxa and may result in phylogenetic trees that do not reflect the true relationships among taxa, depending on the sequences input into the analysis. Examining vertebrate trees, **Evans *et al.*** (p. 200) demonstrate that differences in evolutionary rates, leading to phylogenetic distortions, are correlated with the mechanisms underlying germ cell formation. Evolutionary rate is faster in cases where germ cells are established by maternal molecules ("preformed") relative to those that are induced during embryogenesis ("epigenesis") in slowly evolving and, presumably, ancestral lineages. For example, frogs evolve more rapidly than salamanders, and teleosts more rapidly than ascipenseriform fishes. Thus, epigenesis constrains the ability of gene regulatory networks to change, with the repeated and convergent evolution of preformation eliminating this constraint.

In the PINK1

Pathogenic mutations in the kinase PINK1 are causally related to Parkinson's disease (PD). One hypothesis proposes that PINK1 regulates mitophagy—the clearance of dysfunctional mitochondria. A second hypothesis suggests that PINK1 has a direct effect on mitochondrial complex I, affecting the maintenance of the electron transport chain (ETC) resulting in decreased mitochondrial membrane potential and dysfunctional mitochondria. In support of the second hypothesis, **Morais *et al.*** (p. 203, published online 20 March) observed a complex I deficit in fibroblasts and neurons derived from induced pluripotent stem cells from PINK1 patients before any mitophagy was induced. The phosphoproteome of complex I in liver and brain from mice deficient for Pink1, compared

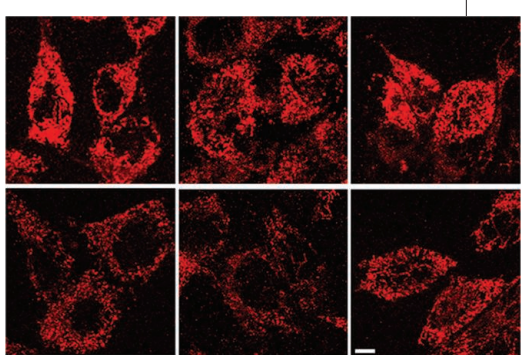

to wild-type animals, revealed that Ser^{250} in complex I subunit NdufA10 was differentially phosphorylated. Ser^{250} is critically involved in the reduction of ubiquinone by complex I, explaining why *Pink1* knockout mice, flies, and patient cell lines show decreased mitochondrial membrane potential. Synaptic defects in *pink1* null mutant *Drosophila* could be rescued using phosphomimetic NdufA10.

CREDIT: MORAIS *ET AL.*

Marcia McNutt is Editor-in-Chief of *Science*.

Li and Me

DURING A WEEK-LONG TRIP TO CHINA IN JANUARY THIS YEAR, I WAS INVITED TO MEET WITH PREMIER LI Keqiang in Beijing to discuss science. At first, I was in disbelief. After all, China is a nation of 1.3 billion people. Li, as Premier and Party Secretary of the State Council, has many pressing issues of national and international concern to attend to. In all my years as a scientist, including heading a billion-dollar U.S. research agency, this was the most significant invitation I had ever received to meet with a sitting national leader to hear his vision for science and discuss important global science matters.The fact that the Chinese Premier wanted to meet with me sent strong signals as to how China is seeing science as critical to its future well being.

The meeting would have clear ground rules. Just me, no U.S. reporters, for 30 minutes. We would discuss science and the economy, not politics. Some topics were off limits for the Premier, suggested as more appropriate for conversations between President Bai Chunli of the Chinese Academy of Sciences (CAS) and me. I arrived early for the meeting at a beautiful traditional Chinese reception hall. No x-ray machines or body scanners such as you find at the entrance to the U.S. Capitol and the White House. The Premier and me, having tea. And we talked, and talked, for 70 minutes, on topics ranging from space exploration to international cooperation to climate change and environmental protection [see related AAAS News and Notes (http://www.sciencemag.org/lookup/doi/10.1126/science.1253962) and a transcript of the meeting (http://www.sciencemag.org/cgi/content/full/science.1253962/DC1)]. At one point early in the conversation, Li's aide rushed in with an urgent note. And yet Premier Li dismissed him; whatever important matter demanded his attention elsewhere would have to wait.

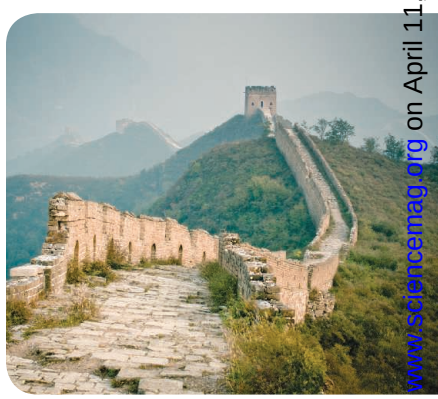

The Premier was clearly well prepared to demonstrate that China's efforts to address its environmental woes have gone beyond intent to yield results. He quoted numbers on carbon stored through returning farmland to forest since 2000 (160 million tons) and the value of China's energy-saving and environmental industries [4.5 trillion RMB yuan (approximately US$0.72 trillion) by 2015]. He stated: "We need to declare war on environmental pollution, on unclean water and dirty air."As an example of how China is moving forward aggressively on this front, Li claimed that 60 million rural water users were supplied with clean drinking water in 2013, with another 60 million scheduled to benefit in 2014. Yet there is still much to do. The day after I left Beijing, the capital experienced dangerous smog, with concentrations of 2.5-micrometer particles that were 20 times the level considered safe by the World Health Organization.

Ensuring that China has the best and brightest scientists to solve these problems is not just good policy for the Premier, but something personal. Over 30 years ago, Li was a peasant from a poor rural part of China. Thanks to his excellent performance on the college entrance examination, he was admitted to the elite Peking University, which helped launch his own illustrious career. When Li became Premier, he noted that the proportion of poor students at the elite Chinese universities was declining. Therefore, last year the Chinese government asked those universities to enroll more rural students from underdeveloped central and western areas of China and provided 50 billion RMB (approximately US$0.8 billion) in scholarships to offset the cost of their college attendance. Their representation increased by 10% over the previous year, Li noted.

Our meeting made the 7 p.m. national news and was all over the morning papers. Even cab drivers knew about the meeting and were impressed. Scientific research had attained rock-star status in China. I suspect that this was the hoped-for intent when Dr. Bai of the CAS made the request for my meeting with the Premier. If the long-term result is that China's most talented youth become researchers to find environmental solutions, then we all win.

– Marcia McNutt

10.1126/science.1251293

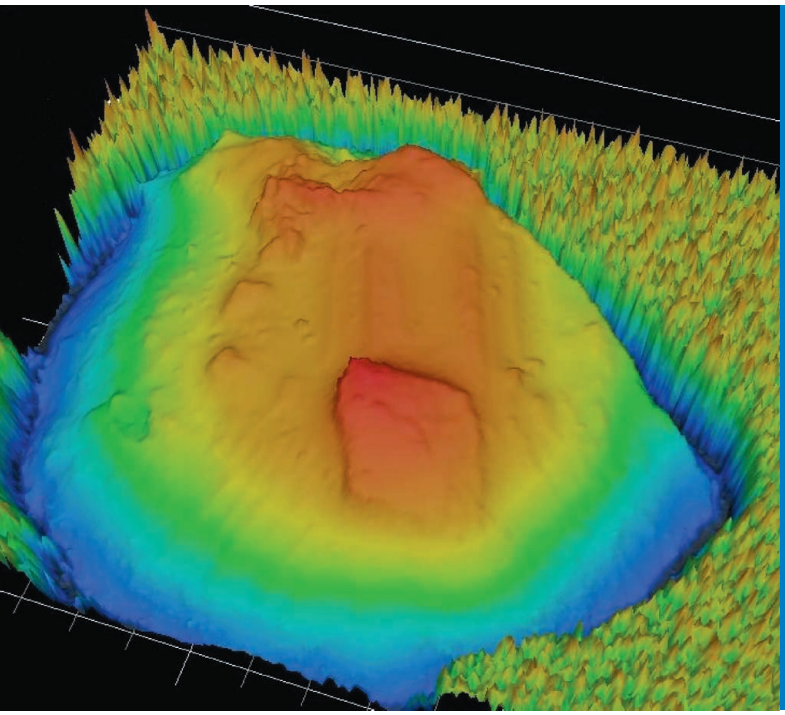

PLANETARY SCIENCE

Organic Delivery Device

Several plausible mechanisms could produce complex organic molecules on the Moon, including synthesis by energetic UV radiation or impact shocks, delivery from meteorites, and even decay of biotic matter. However, Apollo samples have shown surprisingly low levels of carbon. Thomas-Keprta *et al*. have now detected complex organics larger than methane within lunar samples from Shorty Crater. They probed glassy beads tens of micrometers in diameter for fluorescence, revealing some with thin layers of carbonaceous material that were apparently embedded while the silicate surface was still molten. Chemical characterization with micro-Raman spectroscopy indicated the presence of macromolecular matter similar to kerogen, a compound that composes the bulk of stony meteorites. The authors favor a production scenario in which these abiotic organics were delivered via micrometeorites around the time that the volcanic glass beads formed. More substantial meteoritic accretion from cometary and asteroidal fragments also is thought to have occurred on the early Earth. The specific quantity and nature of these organics remain under investigation in the context of possible precursors for life in the solar system. — MMM

Geochim. Cosmochim. Acta 10.1016/j.gca.2014.02.047 (2014).

BIOPHYSICS

Weevils: Now in 4D

Methods are ever improving for the study of anatomic structures and their associated dynamics as they occur in real time and 3D space. dos Santos Rolo *et al.* developed in vivo x-ray cinetomography for 4D analysis, which allows the visualization of optically opaque tissue in small living organisms. The method combines ultrafast x-ray computed microtomography and motion analysis procedures to examine structures in the micrometer range and with temporal resolution of a few tens of milliseconds. The method was applied to the exoskeletal hip joints of the wheat weevil *Sitophilus granarius* to reconstruct 4D kinematics. Weevil hip joints are fast-moving and display what is termed a screw-and-nut system. The imaging method was able to track the movement of the hip joint and elucidate its structural displacement from the main body by following the geometrical center of the hip and by separating angular velocities. The kinematics of the wheat weevil reveals features of its mobility and can be compared to that of different weevil species or other arthropods. The method may also be applied more widely for morphological dynamics in animals and biomaterials. — BAP

Proc. Natl. Acad. Sci. U.S.A. **111**, 10.1073/pnas.1308650111 (2014).

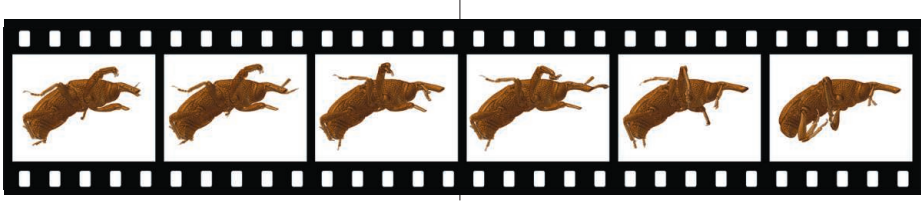

APPLIED PHYSICS

More Memory Please

The storage density of digital media has soared by many orders of magnitude over the past several decades, but still there is demand to store even more on an even smaller scale. Doing so, however, has its bounds, as engineering capabilities or fundamental physical limitations may hinder further size reduction. Phase-change memory materials provide a platform to store digital information in the form of bits, the state of the bit being distinguished by the different reflective properties of the amorphous and crystalline state. The state of the bit typically is set by optical, electrical, or thermal pulses that change the phase of the materials. Instead of shrinking the size of the bit, Wang *et al*. show that such a phase-change memory bit can access several levels. Using a series of ultrafast laser pulses to the control the amount of energy pumped into the bit, they show that a ladder (or gray scale) of stable states can be accessed. Such a multilevel approach could be useful for enhancing effective storage density without the need to shrink the device size. "What I know can be written on the back of a postage stamp" may actually turn out to be a rather showy feat of memory recall, and not a self-deprecating claim of modest knowledge as intended. — ISO

Appl. Phys. Lett. 104, 121105 (2014).

ECONOMICS

Problematic Permitting

When faced with environmental regulations and the costs they impose, companies may relocate to a less-regulated jurisdiction, taking with them jobs and contributing to "leakage" in which targets of regulation, such as carbon emissions, are not reduced, just redistributed. To retain companies, jurisdictions often include exemptions and other incentives in their regulations. Yet these incentives may be seen as taxpayer-funded "handouts" to industry, threatening political support. Thus, the balance is critical. Martin *et al.* studied the European Union (EU) Emissions Trading Scheme (ETS), which offered emissions permits for free, rather than auctioning them, to many companies deemed at risk of relocating. They interviewed managers of 761 manufacturing

Continued on page 131

Continued from page 129

firms across six EU countries, and combined this with economic performance data and official ETS carbon emissions data. They found that reductions in the risk of relocation under the ETS permit allocation rules could have been achieved with far fewer free permits. The mismatch was especially problematic in terms of reducing the risk of job loss. Although their initial analyses drew on information gleaned from interviews with companies, the authors developed permit allocation schemes that drew on more easily accessible information, such as firm-level employment and carbon emissions, that were still more effective in terms of minimizing leakage and job loss. Such optimization is critical as ETS considers revising its permitting process, and more emissions trading markets worldwide adopt similar exemption rules. — BW

Am. Econ. Rev., http://papers.ssrn.com/sol3/papers.cfm?abstract_id=2033683 (2014).

PSYCHOLOGY

A Personal Connection

Telephone companies have long used recorded voices, usually female, and many services companies have chosen to confront callers with voice-based menus of options. Personalized assistance became available by means of Siri for iPhone users, and Waytz *et al.* have now begun to explore the psychological consequences of endowing autonomous vehicles, one of the latest technological innovations to come to market, with a voice. They monitored drivers' physiological status while in a driving simulator operated either by themselves or by an

CREDIT: ANGELA PIAZZA/ZUMA PRESS/NEWSCOM

autonomous entity, referred to as Iris, that spoke to the human drivers. Not surprisingly, audio communication increased the sense of liking and of anthropomorphization; it also enhanced feelings of trust—which was measured both by self-reported ratings and by fluctuations in heart rate—under normal driving conditions. Furthermore, in the aftermath of a collision with another car, programmed so as to be unavoidable, drivers were more likely to absolve Iris of blame in comparison to a similar, nonverbal autonomous vehicle. These effects fit neatly into a framework of greater humanization as being reflective of an entity's capacities to carry out actions (agency) and to embody feelings. — GJC

J. Exp. Soc. Psychol. **52**, 113 (2014).

ENGINEERING

Bacterial Diagnosis

You've read about the enormous community of microbes that live in the guts of humans and other animals. But what if we could train some of them to perform non-invasive but reliable diagnostic procedures deep inside the body? Kotula *et al*. report experiments showing that such a strategy is not at all farfetched. Bacteria were engineered to contain a stable genetic switch that would record exposure to a chemical while the bacteria were living in the gut of a mouse. The switch was then rigged to be activated if the bacteria were exposed to a certain chemical, low concentrations of which regulated a repressor element built into the trigger mechanism for the sensor. The modified bacteria could then be fed to mice. When the bacteria were later collected from fecal samples, they accurately "remembered' whether or not the host animal had been exposed to the chemical more than a week earlier. Given these results, one can imagine similar programming of bacteria that would report the presence of diagnostically sensitive chemicals indicative of cancer, inflammation, or other conditions within the gut of the host animal. — LBR

Proc. Natl. Acad. Sci. U.S.A. **111**, 10.1073/pnas.1321321111 (2014).

VIROLOGY

A Mouse Model for MERS

Coronavirus (CoV) infections acquired from wild and domesticated animals pose a threat of causing severe and often fatal human pneumonias, as witnessed by the severe acute respiratory syndrome (SARS) CoV, originating in edible wildlife, and more recently by the Middle East respiratory syndrome (MERS) CoV, possibly from camels. The pathogenesis of MERS is poorly understood, and animal models have been restricted to macaques until now. Zhao *et al.* have developed a way of rapidly producing models by transducing mice with a non-replicating adenovirus vector carrying the human MERS virus cellular receptor dipeptidyl peptidase 4 (hDPP4). The receptor was expressed on the surface of mouse lung alveolar epithelial cells. Receptor-bearing mice were susceptible to MERS, showed pathology, and had immune responses similar to those seen in humans and thus can be used to test vaccines and antiviral drug candidates. — CA

Proc. Natl. Acad. Sci. U.S.A. **111**, 4970 (2014).

www.sciencemag.org

Science

1200 New York Avenue, NW
Washington, DC 20005
Editorial: 202-326-6550, FAX 202-289-7562
News: 202-326-6591, FAX 202-371-9227
Bateman House, 82-88 Hills Road
Cambridge, UK CB2 1LQ
+44 (0) 1223 326500, FAX +44 (0) 1223 326501

Subscription Services For change of address, missing issues, new orders and renewals, and payment questions: 866-434-AAAS (2227) or 202-326-6417, FAX 202-842-1065. Mailing addresses: AAAS, P.O. Box 96178, Washington, DC 20090-6178 or AAAS Member Services, 1200 New York Avenue, NW, Washington, DC 20005

Institutional Site Licenses please call 202-326-6755 for any questions or information

Reprints: Author Inquiries 800-635-7181
Commercial Inquiries 803-359-4578

Permissions 202-326-6765, permissions@aaas.org

Member Benefits AAAS Travels: Betchart Expeditions 800-252-4910; Apple Store www.store.apple.com/us/go/eppstore/aaas; NASA Federal, 1-888-NASA-FCU (1-888-627-2328) or www.nasafcu.com; Cold Spring Harbor Laboratory Press Publications www.cshlpress.com/affiliates/aaas.htm; Hertz 800-654-2200 CDP#343457; Seabury & Smith Life Insurance 800-424-9883; Subaru VIP Program 202-326-6417; Nationwide Insurance http://nationwide.com/aaas; Other Benefits: AAAS Member Services 202-326-6417 or http://membercentral.aaas.org/discounts.

science_editors@aaas.org	(for general editorial queries)
science_letters@aaas.org	(for queries about letters)
science_reviews@aaas.org	(for returning manuscript reviews)
science_bookrevs@aaas.org	(for book review queries)

Published by the American Association for the Advancement of Science (AAAS), *Science* serves its readers as a forum for the presentation and discussion of important issues related to the advancement of science, including the presentation of minority or conflicting points of view, rather than by publishing only material on which a consensus has been reached. Accordingly, all articles published in *Science*—including editorials, news and comment, and book reviews—are signed and reflect the individual views of the authors and not official points of view adopted by AAAS or the institutions with which the authors are affiliated.

AAAS was founded in 1848 and incorporated in 1874. Its mission is to advance science, engineering, and innovation throughout the world for the benefit of all people. The goals of the association are to: enhance communication among scientists, engineers, and the public; promote and defend the integrity of science and its use; strengthen support for the science and technology enterprise; provide a voice for science on societal issues; promote the responsible use of science in public policy; strengthen and diversify the science and technology workforce; foster education in science and technology for everyone; increase public engagement with science and technology; and advance international cooperation in science.

Information for Authors
See pages 680 and 681 of the 7 February 2014 issue or access www.sciencemag.org/about/authors

EDITOR-IN-CHIEF **Marcia McNutt**
EXECUTIVE EDITOR **Monica M. Bradford** NEWS EDITOR **Tim Appenzeller**
MANAGING EDITOR, RESEARCH JOURNALS **Katrina L. Kelner**
DEPUTY EDITORS **Barbara R. Jasny, Andrew M. Sugden, Valda J. Vinson, Jake S. Yeston**

Editorial senior editors/commentary Lisa D. Chong, Brad Wible; **senior editors** Gilbert J. Chin, Pamela J. Hines, Paula A. Kiberstis (Boston), Marc S. Lavine (Toronto), Kristen L. Mueller, Beverly A. Purnell, L. Bryan Ray, Guy Riddihough, H. Jesse Smith, Phillip D. Szuromi (Tennessee), Laura M. Zahn (San Diego); **associate editors** Melissa R. McCartney (Education Projects), Margaret M. Moerchen, Jelena Stajic, Sacha Vignieri (Oregon), Nicholas S. Wigginton (Michigan); **book review editor** Sherman J. Suter; **associate letters editor** Jennifer Sills; **editorial manager** Cara Tate; **senior copy editors** Jeffrey E. Cook, Chris Filiatreau, Cynthia Howe, Harry Jach, Lauren Kmec, Barbara P. Ordway, Trista Wagoner; **senior editorial coordinators** Carolyn Kyle, Beverly Shields; **editorial coordinators** RamatoulayeDiop, Joi S. Granger, Lisa Johnson, Anita Wynn; **publications assistants**, AneeraDobbins, Jeffrey Hearn, Dona Mathieu, Le-Toya Mayne Flood, Shannon McMahon, Scott Miller, Jerry Richardson, Brian White; **editorial assistant** Patricia M. Moore; **executive assistant** Alison Crawford; **administrative support** Maryrose Madrid

Senior web editor Sarah Crespi; **web development manager** Martyn Green **News managing editor** John Travis; **international news editor** Richard Stone; **deputy news editors** Robert Coontz, Elizabeth Culotta, David Grimm (Online), David Malakoff, Leslie Roberts; **senior correspondents** Eliot Marshall, Jeffrey Mervis, Elizabeth Pennisi **news writers** Yudhijit Bhattacharjee, Adrian Cho, Jennifer Couzin-Frankel, Carolyn Gramling, Jocelyn Kaiser, Richard A. Kerr, Robert F. Service (Pacific NW), Kelly Servick, Erik Stokstad, Emily Underwood; **web developer** Daniel Berger; **social media strategist** Meghna Sachdev; **interns** Thomas Sumner, Nadia Whitehead; **contributing correspondents** John Bohannon, Jon Cohen (San Diego, CA), Ann Gibbons, Sam Kean, Eli Kintisch, Andrew Lawler, Mitch Leslie, Charles C. Mann, Virginia Morell, Heather Pringle; **copy editors** Kara Estelle, Nora Kelly, Jennifer Levin; **administrative support** Scherraine Mack; **bureaus** San Diego, CA: 760-942-3252, FAX 760-942-4979; Pacific Northwest: 503-963-1940

Production director Wendy K. Shank; **assistant manager** Rebecca Doshi; **senior specialists** Steve Forrester, Anthony Rosen; **specialist** Jacob Hedrick **Preflight director** David M. Tompkins; **manager** Marcus Spiegler; **specialists** Jason Hillman, Tara Kelly

Art director Yael Fitzpatrick; **associate art director** Laura Creveling; **senior illustrators** Chris Bickel, Katharine Sutliff; **illustrator** Valerie Altounian; **senior art associates** Holly Bishop, Preston Huey; **art associates** Kay Engman, Garvin Grullón, Chrystal Smith; **photo editor** Leslie Blizard

***Science* International**

Europe (science@science-int.co.uk) **editorial: international managing editor** Andrew M. Sugden; **senior editor/commentary** Julia Fahrenkamp-Uppenbrink; **senior editors** Caroline Ash, Stella M. Hurtley, Ian S. Osborne, Peter Stern, Maria Cruz; **contributing editor** Helen Pickersgill; **editorial support** Rachel Roberts, Alice Whaley; **administrative support** Janet Clements, Joan Cuthbert, John Wood; **news: deputy news editor, u.k.** Daniel Clery; **contributing editor, europe** Martin Enserink; **contributing correspondents** Michael Balter (Paris), Kai Kupferschmidt (Berlin), Tania Rabesandratana (Brussels), Gretchen Vogel (Berlin)

Asia Japan Office: Asca Corporation, Tomoko Furusawa, Rustic Bldg. 7F, 77 Tenjin-cho, Shinjuku-ku, Tokyo 162-0808, Japan; +81 3 6802 4616, FAX +81 3 6802 4615, inquiry@sciencemag.jp; **contributing editor, asia** Mara Hvistendahl [China: mhvisten@aaas.org]; **contributing correspondents** Dennis Normile [Japan: dnormile@gol.com]; Christina Larson [China: christina.larson@gmail.com]; Pallava Bagla [South Asia: pallava.bagla@gmail.com]

Latin America contributing correspondent Lizzie Wade [Mexico City: lizziewade@outlook.com]

EXECUTIVE PUBLISHER **Alan I. Leshner**
PUBLISHER **Beth Rosner** CHIEF DIGITAL MEDIA OFFICER **Rob Covey**

Fulfillment Systems and Operations (membership@aaas.org); **customer service supervisor** Pat Butler; **specialists** LaToya Casteel, Michelle Ofordire, Javia Jennings, Chanta Stewart; **manager, data entry** Mickie Napoleoni; **data entry specialists** JJ Regan, Jaimee Wise, Fiona Giblin

Business Operations and Administration director Deborah Rivera-Wienhold; **business systems and financial analysis director** Randy Yi; **manager of fulfillment systems** Neal Hawkins; **systems analyst** Nicole Mehmedovich; **manager, business analysis** Eric Knott; **manager, business operations** Jessica Tierney; **business analysts** Cory Lipman, Cooper Tilton, Celeste Troxler; **financial analyst** Jeremy Clay; **rights and permissions: assistant director** Emilie David; **permissions associate** Elizabeth Sandler; **rights, contracts, and licensing associate** Lili Kiser; **marketing director** Ian King; **marketing managers** Alison Chandler, Julianne Wielga, Justin Sawyers; **marketing associates** Mary Ellen Crowley, Elizabeth Sattler; **senior marketing executive** Jennifer Reeves; **director, site licensing** Tom Ryan; **director, corporate relations** Eileen Bernadette Moran; **senior publisher relations specialist** Kiki Forsythe; **publisher relations manager** Catherine Holland; **publisher relations, eastern region** Keith Layson; **publisher relations, western region** Ryan Rexroth; **customer relations manager** Iquo Edim; **customer relations analysts** Simon Chong, Lana Guz; **associate director, marketing** Christina Schlecht; **marketing associates** Thomas Landreth; **electronic media: director** Lizabeth Harman; **assistant manager** Lisa Stanford; **production specialists** Antoinette Hodal, Nichele Johnston, Lori Murphy, Kimberly Oster; **web and new media: senior project manager** Trista Smith, **project leader** Luke Johnson **computer specialists** Walter Jones, Kai Zhang, **web developer** Chris Coleman; **program director, aaas member central** Peggy Mihelich

director, global collaboration, custom publications, advertising Bill Moran

editor, custom publishing Sean Sanders: 202-326-6430

assistant editor, custom publishing Tianna Hicklin 202-326-6463

associate director, collaboration, custom publications/china/taiwan/korea/singapore Ruolei Wu +86-1367-101-5294

Product (science_advertising@aaas.org); **east coast/e. canada** Laurie Faraday: 508-747-9395, FAX 617-507-8189; **west coast/w. canada** Lynne Stickrod: 415-931-9782, FAX 415-520-6940; **uk europe/asia** Roger Goncalves: TEL/FAX +41 43 243 1358; **japan**, Makiko Hara: +81 (0) 3 6802 4616, FAX +81 (0) 3 6802 4615; ads@sciencemag.jp; **china/taiwan** Ruolei Wu: +86 1367 1015 294 rwu@aaas.org

worldwide associate director of *Science* Careers Tracy Holmes: +44 (0) 1223 326525, FAX +44 (0) 1223 326532, tholmes@science-int.co.uk

Classified (advertise@sciencecareers.org); **u.s. sales** Tina Burks: 202-326-6577, Nancy Toema 202-326-6578; **sales administrator** Marci Gallun; **europe/row sales** Axel Gesatzki, Sarah Lelarge; **sales assistant** Kelly Grace; **japan** Yuri Kobayashi +81 (0)90-9110-1719; careerads@sciencemag.jp; **china/taiwan** Ruolei Wu: +86 1367 1015 294 rwu@aaas.org; **advertising support manager** Karen Foote: 202-326-6740; **advertising production operations manager** Deborah Tompkins; **senior production specialist/graphic designer** Amy Hardcastle; **production specialist** Yuse Lajiminmuhip; **senior traffic associate** Christine Hall; **sales coordinator** Shirley Young; **marketing manager** Allison Pritchard; **marketing associate** Aimee Aponte

AROUND THE WORLD

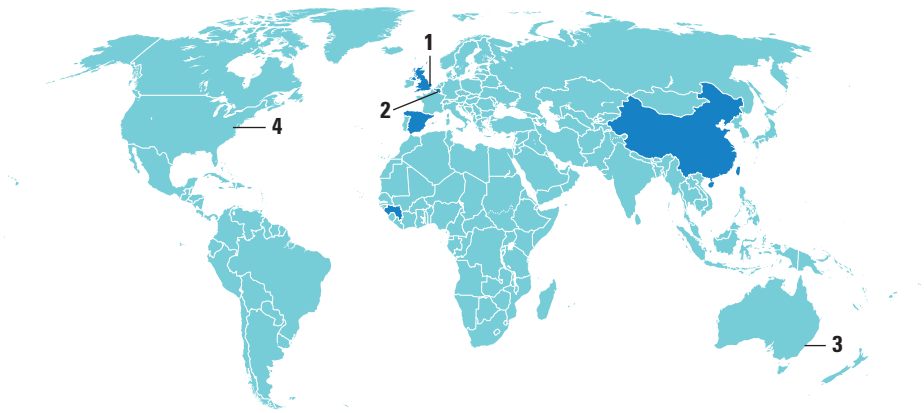

London **1**

Biomedical Hub 'MedCity' Launches

London's media-friendly mayor, Boris Johnson, unveiled an initiative this week to attract investment to the bioscience research powerhouses of London, Oxford, and Cambridge. Johnson hopes the plan—dubbed MedCity—will forge a "golden triangle," bringing in venture capital and luring pharmaceutical companies to set up shop.

At the heart of the plan are two centers due to open in 2015: the $1 billion Francis Crick Institute, slated to be the biggest biomedical research facility in Europe, and an offshoot from Imperial College London that will host a $250 million multidisciplinary research center. Other London universities also have major expansion plans.

New ground. The Crick institute will open in 2015.

Backed by $2 million from Johnson's own budget and $4.9 million from the Higher Education Funding Council for England, MedCity will coax researchers, companies, and investors to collaborate. "MedCity will span everything from research to clinical trials to manufacturing, across biotech, med tech, and health tech," said Johnson at the launch event. But MedCity may struggle to emulate its model—Boston—because of the distances between the cities. "Proximity is important," says Alan Barrell of Cambridge's Judge Business School, a MedCity adviser.

Brussels **2**

Pro-Life Groups Target E.U. Stem Cell Research

A coalition of European pro-life organizations has launched a fresh legislative attack against E.U. funding for embryonic stem cell research. The groups have organized a European citizens' initiative, a democratic novelty that gives citizens the right to propose legislation if they gather at least 1 million signatures from seven member states. The organizers of the initiative, backed by 1.7 million people in all 28 E.U. countries, were scheduled to meet with research commissioner Máire Geoghegan-Quinn and the European Parliament this week.

Under a delicate compromise, E.U. funds can be used to study embryonic stem cells, but only in countries where such research is legal, and only using embryos left over from in vitro fertilization procedures. The new initiative proposes a ban on funding for any activities in which embryos are destroyed, not just in research but also in public health and development aid. Experts say it's hard to predict what the European Commission, which must consider turning the proposal into legislation, will do; it has until 28 May to respond. **http://scim.ag/_stemcell**

Sydney, Australia **3**

Scientists Alarmed Over Dwindling Antarctic Research

Australia's peak scientific body, the Australian Academy of Science, warned last week that the country's territorial claims to Antarctica and its strategic position in the region are at risk due to a serious decline in scientific effort there. Since 1997, the number of Australian projects there has plummeted from 142 to just 62 this year, and from 1999 to 2006 the number of peer-reviewed publications on Antarctica by Australian researchers dropped from about 200 a year to less than 100. The drop in performance is a result of federal cost-cutting, which has hit both research and infrastructure such as refueling, resupplying, and restaffing three bases. The warning that Antarctic research is "chronically underinvested" comes in the academy's submission to the Australian government's 20 Year Australian Antarctic Strategic Plan.

Of the seven countries to make territorial claims to Antarctica under the 1961 Antarctic Treaty, Australia's claim of 43% is the largest and is based on its geographic proximity and history of exploration, discovery, and activity in the frozen continent. But "national claims are not sovereign claims," says Will Howard, deputy chair of the academy's National Committee for Antarctic Research. "They imply responsibility for managing the claim and the offshore territory."

Washington, D.C. **4**

NASA to Staff: No Fraternizing With Russia

After an internal memo revealing the policy change leaked, NASA officials last week announced that they were suspending the agency's collaborations with Russia in light of its incursion into Ukraine's territory. However, the announcement appears to be purely symbolic: The one key existing area of partnership—using Russia's Soyuz capsules to ferry NASA astronauts to the International Space Station (ISS)—will be insulated from the new policy. "NASA

All together. Russian, Japanese, Belgian, and U.S. astronauts on the ISS in 2009.

and Roscosmos [the Russian space agency] will … continue to work together to maintain safe and continuous operation of the International Space Station," according to a statement issued by NASA on 2 April.

CREDITS (LEFT TO RIGHT): SEAN DEMPSEY/AP; BY NASA [PUBLIC DOMAIN], VIA WIKIMEDIA COMMONS

Published by AAAS

NEWSMAKERS

Three Q's

Saudi Prince **Sultan Bin Salman Bin Abdul-aziz Al-Saud** wants to change how the kingdom's subjects think about their pre-Islamic past. The 57-year-old science enthusiast, who 3 decades ago was the youngest—and the first Muslim and Arab—astronaut to fly on NASA's space shuttle, is now president of Saudi Arabia's Commission for Tourism and Antiquities. He oversees a $1.7 billion effort to build new museums and welcome

Sultan Bin Salman Bin Abdul-aziz Al-Saud

foreign archaeologists; he also recently helped uncover an ancient hand ax (shown) at an excavation. This month, he is in the United States for the opening of the "Roads of Arabia" traveling exhibit.

Q: Why are you so excited about Arabia's prehistoric past?
S. A.-S.: I go to places and touch things. We're taking local police, governors, university staffs, and kids to excavate—then they can own it. It is quite a challenge for us, but archaeology is not separate from who we are. In the early years, people wanted to have nothing to do with historic sites. All walks of life, including religious scholars, are now visiting pre-Islamic sites.

Q: You feature human and animal images in the exhibition. Isn't this a taboo among some Muslims?
S. A.-S.: Artifacts that people thought were taboo are just objects made by other civilizations. When there was a recent find of ancient horse statues, King Abdullah went to look—we are very proud of our horses!

Q: Are foreign and domestic women welcome at excavations?
S. A.-S.: My deputy's wife is an archaeologist, and she certainly goes to sites. The women of Saudi Arabia have come a long way. And they have literally carried a lot of the history of Arabia on their backs. We just hired several of the smartest Saudi women to help with reinventing our museums.

CREDITS (TOP TO BOTTOM): EU; MATTHEW TOMKINSON/WWW.MATTHEWPHOTO.CO.UK; ALAIN DUPUIS

Bird Flu Scientist Allegedly Under Investigation

Capua

A story in Italian magazine *l'Espresso* published on 4 April claims that Italian prosecutors are investigating whether former avian influenza scientist **Ilaria Capua**, now a member of the Italian Parliament, trafficked in flu viruses and created a cartel to boost sales of a technology called DIVA, which she helped develop while head of the Istituto Zooprofilattico Sperimentale delle Venezie (IZSVe) in Legnaro.

During her leadership at IZSVe, which ended with her election to the Chamber of Deputies in 2013, Capua became known for helping quash major bird flu outbreaks and starting a global campaign to allow scientists more access to genetic information from bird flu strains (*Science,* 10 November 2006, p. 918).

The office of the Italian prosecutor could not confirm to *Science* that an investigation is taking place. Capua denies any wrongdoing and says the *l'Espresso* article is riddled with errors. "This is a pile of rubbish," says Capua, adding that she has filed a defamation suit against the magazine. She says she doesn't know whether the inquiry or the story might be politically motivated. **http://scim.ag/Capuaflu**

Experimental Lakes Lab Saved

Canada's flagship environmental research center, the Experimental Lakes Area (ELA), has been under threat of closure for 2 years after its funding was pulled by the government. But ELA has found a savior: It will leave government hands and will be managed by the International Institute for Sustainable Development (IISD), a Winnipeg-based think tank. The 1 April announcement guarantees that the 46-year-old field site in northwestern Ontario will survive, at least for another 5 years.

The ELA, which conducts experiments in a system of 58 lakes, has an impressive research record: Its scientists were the first to find evidence for acid rain, and to fully diagnose the effects of pollutants such as mercury, phosphate, and synthetic hormones on aquatic life.

IISD President Scott Vaughan says that he intends to build upon this past research, while looking to expand the scope of the facility's science to investigate the effects of micropollutants and climate change on aquatic systems. The deal will hopefully bring the ELA some "stability," says freshwater ecologist Diane Orihel. But, she adds, IISD's plan to invite back former ELA scientists might prove difficult. "Some scientists got frustrated and took other positions." http://scim.ag/ELAsaved

Published by AAAS

THEY SAID IT

"Many scientists have been severely distressed by the outcomes of the L'Aquila trial and tend to share critical information only among themselves."

—Italian geologist Gianluca Valensise, on changes in scientists' and the public's interaction 5 years after an earthquake struck L'Aquila, killing 309 people. The disaster led to a court case that found scientists guilty of manslaughter for misleadingly reassuring citizens after earlier tremors. **http://scim.ag/LAquilaanniv**

FINDINGS

As Good as Old

Even elite violinists cannot tell a Stradivarius and a top-quality modern violin apart, a double-blind study suggests. Claudia Fritz, a musical acoustician at Pierre and Marie Curie University in Paris, and colleagues assembled more than 20 new and old violins, including six Stradivariuses and two Guarneri del Gesús. In a listening test with 10 leading soloists, researchers winnowed the list to six old violins and six new ones. Wearing dark goggles, the soloists played the remaining instruments in a small room and in a 300-seat auditorium, the researchers report in the *Proceedings of the National Academy of Sciences*. Violinists generally preferred the new instruments and did no better identifying old and new instruments than they would have by guessing.

Outta sight. Soloist Ilya Kaler tests a violin.

"There is nothing magical [about old Italian violins]," says soloist and participant Olivier Charlier. However, Yi-Jia Susanne Hou, who also participated in the study, questions its fairness: "Whereas I believe that [the researchers] assembled some of the finest contemporary instruments, I am quite certain that they didn't have some of the finest old instruments." **http://scim.ag/violintest**

Random Sample

Pterosaurs Take Manhattan!

It's a bird! It's a plane! No, it's a pterosaur! These flying reptiles first appeared on Earth about 220 million years ago, just 10 million or so years after the earliest dinosaurs. They were excellent fliers, the first and the largest vertebrates to evolve that ability. (Birds and bats are the only other vertebrates that engage in true muscle-powered flight.) On 5 April, the largest ever pterosaur exhibit in the United States—"Pterosaurs: Flight in the Age of Dinosaurs"—opened at the American Museum of Natural History in New York City. Visitors have until 4 January 2015 to view the wonders on display.

Among them: Life-size models of the largest pterosaur known, *Quetzalcoatlus northropi* (below, wingspan 10 meters), and the smallest, *Nemicolopterus crypticus* (above, wingspan 25 centimeters); eight real fossil specimens, including one of long-tailed, beak-snouted *Rhamphorhynchus* with its wing membranes preserved; and "Fly Like a Pterosaur," an interactive exhibit that allows visitors to pilot bug-hunting pterosaurs over forests, seas, and volcanoes. Visitors can also try their hand at a pterosaur trading card game developed by Big Apple teenagers.

The exhibit is brimming with fun facts, including what pterosaurs ate (fish, insects, and algae), how they walked on land (on all fours, with their wings tucked up like folded umbrellas), and their evolutionary relationship to other creatures (dinosaurs are their closest relatives). Pterosaurs ruled the skies for some 150 million years until they went extinct along with the dinosaurs about 66 million years ago, but they've come back to life in the Big Apple.

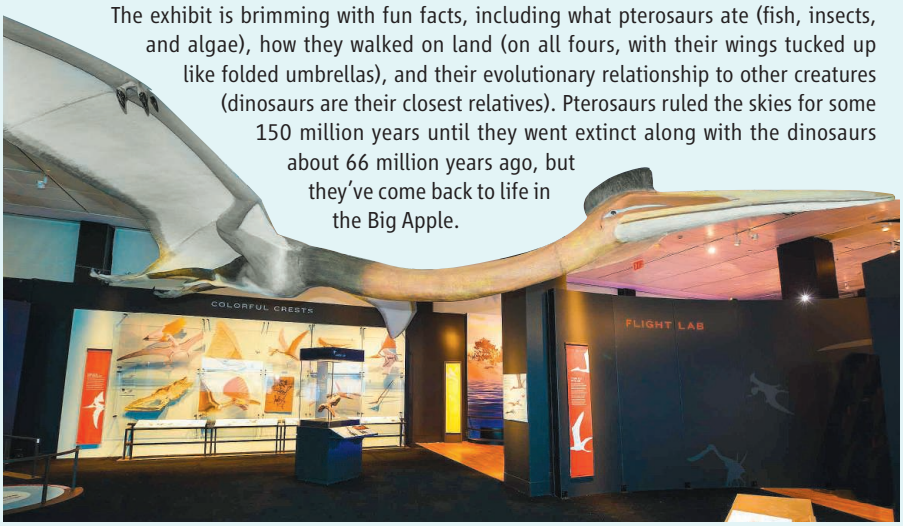

BY THE NUMBERS

$240 million Amount of new money pledged by the Bill & Melinda Gates Foundation, the World Bank, and other donors to combat 10 neglected tropical diseases in Africa by 2020.

23 Number of square meters of living space that the National Institutes of Health decided is enough for an individual chimpanzee—one-fourth the area that an advisory committee had recommended.

85,000 Number of requests for high-skilled (H-1B) visas submitted by companies and universities within a few days of the start of the new application cycle—matching the maximum number of visas the United States can issue in the next fiscal year.

CREDITS (TOP TO BOTTOM): STEFAN AVALOS; © AMNH/CRAIG CHESEK; ©AMNH/DENIS FINNIN

Published by AAAS

CONSERVATION BIOLOGY

Can Cloning Revive Spain's Extinct Mountain Goat?

The very last Pyrenean ibex, a female known as Celia, died in January 2000, its skull crushed by a fallen tree. But that will not be the end of the imposing mountain goat, if Spanish veterinarian Alberto Fernández-Arias has his way. Fernández-Arias is part of a research team that has cloned cells taken from Celia before she died and implanted them in surrogate goats. On 14 April, the researchers will perform an ultrasound to see if any of the embryos have implanted. If so, the work could lead to the world's first "de-extinction" of an animal species.

Several scientists have recently developed similar plans to bring back extinct species, including the woolly mammoth, the passenger pigeon, and a wolflike marsupial called the thylacine (*Science*, 5 April 2013, p. 19). But the Spanish researchers have two key advantages. While other groups have to rely on ancient DNA in museum specimens, they can use Celia's frozen cells. And they can use surviving, closely related species to create surrogate mothers. "It's a terrific team and I expect them to be the first to cross the line," says Michael Archer of the University of New South Wales in Sydney, Australia, who wants to bring back Australia's gastric brooding frog, famous for giving birth through its mouth. "I have my fingers crossed that it works."

Fernández-Arias has been working to save the Pyrenean ibex for decades. While a few were still alive in the wild, he studied how to capture and keep the animals and help them reproduce. And in 2003, after Celia's death marked the failure of that effort, his team made a first attempt to bring back the species by cloning. They delivered a cloned ibex by cesarean section, but the animal died within minutes from a lung defect. "All of the participants were watching this little dead body, all excited and quiet," recalls team member José Folch, who led the cloning work at the Centre of Food Technology and Research of Aragon in Zaragoza, Spain. "Someone cried." The project drew little attention at the time, and the team disbanded shortly afterward because of a lack of money and support.

Now, renewed interest in de-extinction in general and a private donation have allowed Fernández-Arias and Folch to reassemble the old team. "It has been like one of these movies where all the people who are already retired are called back for a special mission," Fernández-Arias says.

The comeback goat. The Pyrenean ibex, seen here in an illustration from 1898, went extinct in 2000.

CREDIT: JOSEPH WOLF/WIKIMEDIA COMMONS

Pyrenean ibexes, also called bucardos, were impressive creatures, much bigger than the two surviving subspecies of Spanish ibex. Perfectly adapted to their mountain habitat, they were able to brave the worst winter weather and climb the sheerest cliffs. But hunters coveted their large, curving horns, and by 1913 the bucardo was considered extinct. That same year, however, a small population was discovered in the Ordesa Valley in the central Pyrenees; the government passed a hunting ban and declared the area a national park.

But the species never recovered. When Fernández-Arias took on the project in 1989, only an estimated six to 14 bucardos were still alive. In 1996, two of the last three remaining animals died, dashing all hopes of recovery. "That was the hardest year," Fernández-Arias says. But that same year the birth of Dolly the sheep, the first cloned mammal, brought fresh hope of a renaissance even after extinction. Scientists captured Celia, took skin biopsies from her left ear and left flank, and stored them at two laboratories.

Earlier this year, the scientists thawed some of these cells and let them multiply for several days to prove that they were still alive. In late February, they injected the cells into goat oocytes whose nucleus had been removed. They then applied a short electric current to fuse the two cells and used a chemical called ionomycin to kick-start the embryo's division. (The recipe was essentially the same as the one for the 2003 attempt.)

Cloning is high-tech work, but much of Fernández-Arias's time has been spent solving other problems, for instance working out the best strategy for surrogate motherhood, using the closely related Spanish ibex as a stand-in for the Pyrenean ibex. Initially, the team tried implanting Spanish ibex embryos in domestic goats, but these were rejected until the scientists "fooled" goats by implanting one of their own embryos as well. They finally settled on a more accommodating surrogate—hybrids between a domestic goat and a Spanish ibex.

In the first week of March, after the embryos had been growing in cell culture for seven days, Folch and others implanted embryos into several hybrids. On Monday, they will perform an ultrasound to see whether the embryos are developing as hoped. A pregnancy would be "only the first step, of course," Archer says. "Nobody will start celebrating until they see what pops out

Published by AAAS

of the other end of the goat."

In fact, even if a healthy animal is born in August, huge hurdles remain before a healthy new population roams the Pyrenees. For starters, scientists will have to create a male ibex—and they have only female cells. One possibility would be to transfer a Y chromosome from a related species, says Harvard University geneticist George Church. To create the genetic diversity an animal population may need to survive, researchers could sequence bucardo specimens in museums and edit the DNA of cloned embryos to reflect the diversity found there, he says. The animals could then be "rewilded," as has been done with other captive populations, such as the condor.

Many conservationists worry that bringing back extinct species will weaken efforts to protect existing populations and drain money from conservation causes. But Church believes that de-extinction will be a big psychological boost. The birth of a twin Celia would be "mythical level news," adds biologist and conservationist Stewart Brand, the founder of a nonprofit organization that funds de-extinction work.

If the effort fails and he can raise more money, Brand says he would be delighted to fund future research on the bucardo. For now, the work has an unlikely benefactor: The cloning efforts are bankrolled by the Aragon Hunting Federation, which says it now promotes conservation and is keen to see bucardos roam the Pyrenees once again.

–KAI KUPFERSCHMIDT

PLANETARY SCIENCE

NASA to Researchers: Sell Your Mission or Be Terminated

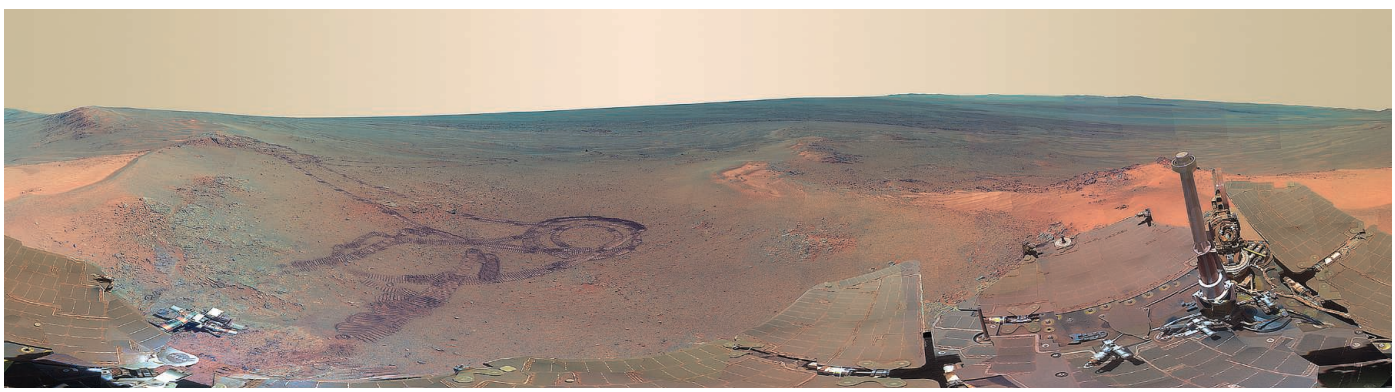

Ever more Mars? The Opportunity rover (*foreground*) has been leaving tracks in martian soil for a decade, but NASA funding troubles threaten its mission.

CREDIT: NASA

The robots that explore the solar system on humanity's behalf face multiple hazards. Rockets fail, instruments break, human error kills a spacecraft. But now, NASA's spacecraft face another mission-ending threat: the federal budget. NASA has put two long-lived but still productive planetary science missions on the budgetary chopping block, daring Congress to swing the ax. The agency is also asking researchers on other long-lived missions to explain why theirs should live on if others must die.

Both the hardy and much-loved Opportunity rover—which has been exploring the watery history of early Mars since it landed in 2004—and the 5-year-old Lunar Reconnaissance Orbiter (LRO) were left out of the president's fiscal year 2015 budget request released last month. Both missions, however, still have a chance to save their science. This week, proposals are due to NASA from the researchers running six major projects—including Opportunity and LRO—that have successfully completed their prime missions and are looking for a fresh piece of the NASA budget to operate for another 2 years (see graphic, 139).

NASA has routinely conducted such "senior reviews" in the past, but it always found a way to let still-kicking robots live on. This time is different. Funding for NASA's Planetary Science Division has been under pressure in recent years, with the Obama administration proposing a series of cuts. For the 2015 fiscal year that begins 1 October, for instance, the White House wants to trim about 5% from the division's $1.35 billion kitty, to $1.28 billion. Congress often rejects such proposals, and sometimes adds funding. That could be difficult this year, however, because lawmakers are operating under a relatively austere $1.102 trillion cap on discretionary federal spending. So NASA may have to find ways to fit both new and existing projects into a flat planetary sciences budget.

One mission new to the senior review this year already has a strong claim on funding for an extension: the Mars Curiosity rover. NASA officials are unlikely to cut off the $60 million annually it needs to keep roving. The squeeze could force the agency, for the first time, to turn off a still capable planetary mission, or even two, unless Congress comes to the rescue.

Running the gantlet

No one is saying exactly why NASA singled out Opportunity and LRO for execution, but apparently the administration decided that it couldn't afford the $35 million required to keep them alive. Congress could give them a reprieve, the White House says, by agreeing to a package of revenue-raising policy changes, known as the Opportunity, Growth, and Security Initiative, that could provide an additional $187.3 million for NASA science. That idea is unlikely to fly, however, so it appears that Opportunity and LRO team members are going to have to sell NASA on their ability to do new science well worth the scarce dollars.

That task could be formidable. After 10 years and 36 kilometers of roving, the $400 million Opportunity rover is walking wounded. It has one bum wheel and its instrument-laden arm has a frozen shoulder joint. Its two instruments for identifying minerals are useless; team members have had to make do with a less capable sensor. (In contrast, almost everything is working wonderfully on Opportunity's successor, Curiosity, which has the resources to roam Mars for another decade or two.) And

Opportunity has already done the job it was sent to do; twice over, actually. It found water-deposited minerals just a couple of meters from its landing site, although the water was so acidic and briny as to be inimical to life. But 8 years later, it did find other minerals formed by water that could have not only hosted life but also favored the origin of life.

Mission accomplished? Not according to Opportunity project scientist Matthew Golombek of NASA's Jet Propulsion Laboratory (JPL) in Pasadena, California. "What we can do is go to a new place," Golombek says. "The rover still has the basic tools a field geologist has." Despite its injuries, Opportunity should be able to rove another few kilometers to "the perfect place to look at potentially the most habitable [ancient] environment on Mars," he says. Not that it would be a brand-new place. Judging from orbital observations, Opportunity would be examining a more detailed version of the same rock record that it recently discovered.

Closer to Earth, LRO is right where it has always been, orbiting the moon 4 years after finishing its primary job: mapping out possible landing sites for U.S. astronauts. But after the Obama administration's about-face on human space exploration, moonwalkers look unlikely to be returning for many decades (*Science*, 18 February 2011, p. 841). Still, there's plenty more science to be done from lunar orbit, argues LRO project scientist John Keller of NASA's Goddard Space Flight Center in Greenbelt, Maryland.

If NASA extends LRO's mission, he says, it could continue its observations of the ongoing bombardment of the moon by chunks of asteroids. That could provide a firm number for the rate at which the moon and Earth are pelted with solar system debris. An extension would also allow LRO to keep mapping the near-surface ice deposits in shadowy lunar craters and pursuing hints of morning frost. All in all, Keller says, "we think we've got great science."

Angling for a rescue

"Great science" is a distinction all six major proposals for mission extensions will be vying for when the senior review board sits down in May to rate them. "This is a competition," says NASA Planetary Science Division Director James Green, and "we don't have endless money." All six major missions will be going head-to-head for survival without regard to their status in the White House budget request, Green adds. "If LRO or Opportunity comes out on top [of the senior review rankings], we'll fund them, we'll reprogram as needed," Green told a forum at last month's Lunar and Planetary Science Conference.

Two missions are likely to be shoo-ins for extension: the Curiosity Mars rover and the Cassini orbiter. Since arriving at Saturn in 2004, the $3.2 billion Cassini mission has produced 100 flybys of Saturn's big moon Titan, surveys of lesser moons, and long looks at the planet's spectacular rings. It has trained its dozen instruments on all manner of phenomena, much of it in constant change, from the fine detail of the rings to the icy plumes spewed from a potentially inhabited subsurface sea in the moon Enceladus (*Science*, 4 April, p. 17).

Like the Opportunity and LRO teams, the Cassini team is bidding to do new science, according to project scientist Linda Spilker of JPL. Given two more years, Cassini would repeatedly dive through a skinny gap between Saturn's innermost ring of orbiting debris and the wisps of its uppermost atmosphere. This risky maneuver would greatly improve Cassini's view of the rings, and skimming so close to the planet would allow it to gather unprecedented observations of its magnetic field and gravity, potentially revealing much of Saturn's internal structure. NASA has sent the Juno spacecraft on a billion-dollar mission to collect the same sort of data at Jupiter, suggesting Cassini's opportunity at about $66 million a year would be a bargain. "This set of orbits is so fantastic," Spilker says.

Topping "fantastic" will be a challenge for the other missions, but there are ways to get an edge. The team operating the Mars Reconnaissance Orbiter (MRO), the most powerful Mars orbiter, says it could take on tasks that are out of any other spacecraft's reach. Since 2006, MRO has been detailing a whole raft of martian phenomena, from water-altered minerals to impact craters freshly blasted into subsurface ice. With more time, MRO could delve deeper into martian geology as well as extend the impact record and others, the team says. But MRO is also the only U.S. Mars orbiter that could scout out safe and scientifically interesting landing sites for future landers and rovers like NASA's successor to Curiosity, the 2020 Mars rover. And MRO is by far the most capable available orbiter for relaying data from rovers back to Earth. (NASA says it will consider such essential relay services in addition to the senior review's science rankings in its decision about which missions to extend.)

Mars Odyssey, another orbiter, doesn't have anything like MRO's capabilities. It was never as powerfully equipped, and one of its three instrument suites no longer works. A second has finished its primary goal of mapping subsurface water ice. But Odyssey can still do new science despite 12 years in orbit, its team argues. It will be shifting its orbit in order to catch frosts and ice clouds before the morning sun destroys them, for instance. And despite a relatively slow data transmission rate, Odyssey could also continue its role as a less capable rover relay and MRO relay backup.

Team members won't know whether their arguments are persuasive until 14 June, when the NASA review panel is scheduled to release its rankings. The list should help determine the fates of the six missions, but the agency will not get the final word. As NASA's Green says, the administration proposes and "Congress disposes."

–RICHARD A. KERR

The Competitors for Mission Extension

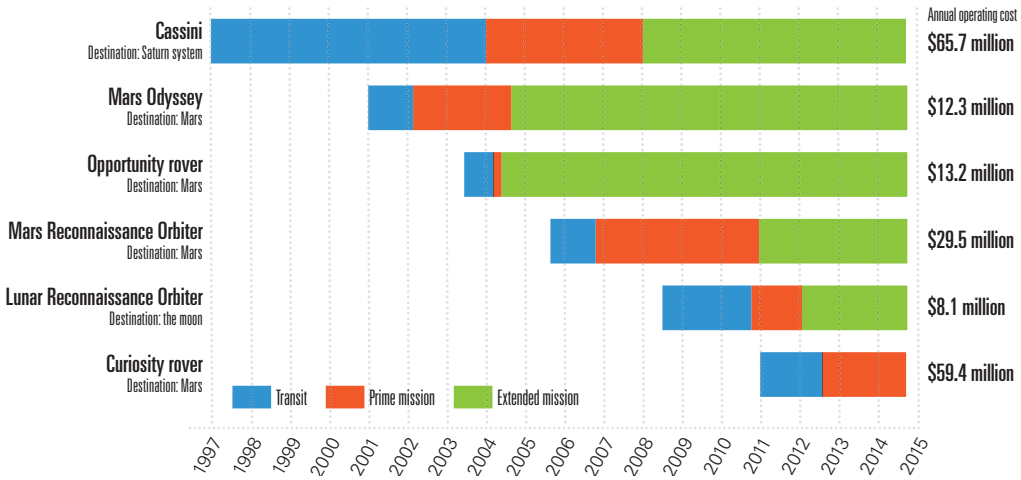

DATA SOURCE: NASA

INFECTIOUS DISEASE

Are Bats Spreading Ebola Across Sub-Saharan Africa?

The first cases went unrecognized. Ebola had never been seen in Guinea before, so when people became ill with fever, muscle pain, vomiting, and diarrhea, health workers initially assumed Lassa fever or yellow fever—both endemic in the region—were to blame. No one put the pieces together until late March. By then, the virus had been spreading for months. Now, health workers are struggling to contain the outbreak, which has already killed more than 100 and has affected at least two neighboring countries. At the same time, scientists are combing the forests, and the genome of the virus itself, looking for clues to how this strain—well known in Central Africa—ended up so far west, and whether its spread suggests people in forested areas all across sub-Saharan Africa are at risk.

Ebola is not a complete stranger to West Africa. In the mid-1990s, two outbreaks hit chimpanzees in Taï National Park in the Ivory Coast, and one researcher studying the animals was infected. (She survived.) "We expected to find the Taï strain," says Sylvain Baize, a virologist at the Institut Pasteur in Lyon, France, who with his colleagues sequenced some of the first samples of the virus from Guinea. To their surprise, it turned out to be Ebola Zaire, the deadliest of the five known Ebola species.

"We have no idea how it's moved from Central Africa to Guinea," says primatologist Christophe Boesch of the Max Planck Institute for Evolutionary Anthropology in Leipzig, Germany. A leading suspect is fruit bats. In Central African rainforests, several species have shown evidence of infection with Ebola without getting sick. And at least one of the species, the little collared fruit bat, *Myonycteris torquata*, has a range that stretches as far west as Guinea. "We've always been very suspicious of bats," says William Karesh of EcoHealth Alliance in New York City, who studies the interactions among humans, animals, and infectious diseases.

"We need to see if [Ebola Zaire] is circulating in bats in the Guinean forest," Baize says. If so, he says, then bats throughout the forests of West Africa are likely harboring the virus, which would put about 150 million more people than previously thought at risk of the disease. The threat isn't particularly high, as outbreaks are rare. But people across the region should be warned about potential dangers of eating bats and other bush meat, and health workers would need to be trained to spot Ebola symptoms so outbreaks could be stopped more quickly.

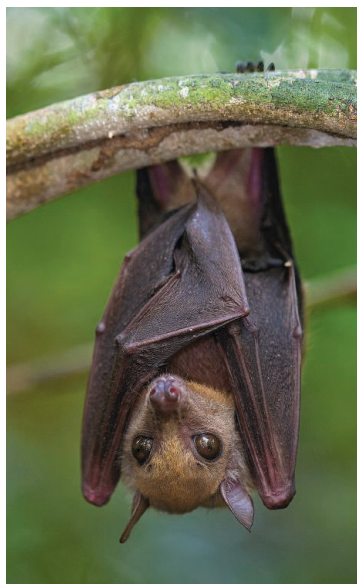

Leading suspect. Researchers have found evidence of Ebola infections in the little collared fruit bat, *Myonycteris torquata*, but the bats don't seem to get sick from the virus.

On 1 April, a team assembled by Boesch and Fabian Leendertz, a wildlife epidemiologist at the Robert Koch Institute in Berlin, began surveying six sites in southern Guinea. Leendertz, with three more German veterinarians and eight Guinean biosurvey experts from the nonprofit Wild Chimpanzee Foundation, will capture and test bats for Ebola while at the same time looking for recent dips in the populations of chimpanzees, monkeys, forest antelopes, or other animals—a sign that the disease could be circulating in those species.

The researchers will also use a relatively new technique for monitoring forested areas: collecting blow flies, which feed on carrion, and analyzing the DNA that persists from their recent meals. If monkey flesh, for example, is common in the blow flies' diets, then monkeys might have been hit by Ebola.

Even with a dozen researchers combing the forest for a month, Leendertz says, the odds are long of finding solid answers. "Our biggest challenge will be to find the right spot," he says, especially because it isn't clear where the first human cases originated. "We will have to be lucky."

Although bats may have carried the virus west from Central Africa, they may not be infecting humans directly. No clear case of bat-to-human transmission of Ebola has ever been proven, Karesh notes, and intermediate species may transmit the virus from bats to humans. Other human outbreaks have been associated with outbreaks in great apes, monkeys, and duikers, a kind of forest antelope. It is also possible that the virus has been in the region for decades but never sparked a noticeable outbreak.

Another clue to the virus's origin will come when its full genome is available. By determining how closely it is related to the viruses found in other outbreaks, Baize and others will try to estimate whether the Guinean outbreak is part of a relatively recent wave of Ebola Zaire moving across the continent or whether it has more likely been circulating silently in West Africa for years.

Meanwhile, health workers can only give supportive care to patients and try to stop the spread to new victims. Researchers are close to a vaccine and treatments that could be used in an outbreak, says virologist Heinz Feldmann of the National Institute of Allergy and Infectious Diseases' Rocky Mountain Laboratories in Hamilton, Montana. But the difficulties of conducting clinical trials or introducing experimental techniques in an emergency setting are daunting. An outbreak-ready vaccine or treatment "is achievable" in as little as 2 years, he says. "But I'm almost afraid that the next time an outbreak happens, we're going to say the same thing."

–GRETCHEN VOGEL

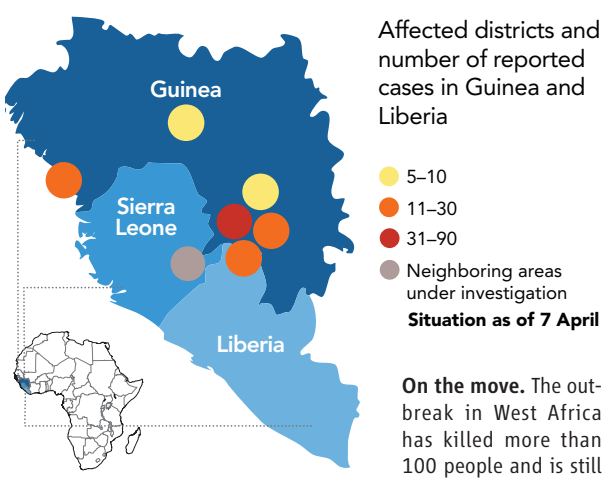

On the move. The outbreak in West Africa has killed more than 100 people and is still spreading.

Published by AAAS

Shock waves. The 2012 earthquakes in Emilia-Romagna killed 27 people and caused major damage.

CREDIT: (TOP) ASSOCIATED PRESS

SEISMOLOGY

Human Activity May Have Triggered Fatal Italian Earthquakes, Panel Says

ROME—A pair of deadly earthquakes that struck the north of Italy in 2012 could have been triggered by the extraction of petroleum at a local oil field, according to an international panel of geoscientists.

The group's long-awaited and as-yet-unpublished report, commissioned in the wake of the disaster that killed 27 and injured hundreds in the Emilia-Romagna region, could have important political and economic ramifications, some scientists say. While previous studies in other countries have linked earthquakes to gas and oil exploration, human casualties have been very rare. Fear of humanmade seismicity has already triggered fierce opposition against new oil and gas drilling efforts in Italy, and Vasco Errani, the president of the Emilia-Romagna region, announced in May last year that all new requests for hydrocarbon exploration in the quake area would be put on hold until the commission delivered its report.

Sources with close knowledge of the study say it was presented to the Emilia-Romagna regional government at least a month ago, but that politicians at both the regional and national level are nervous about its effects and are delaying its release. Although phrased cautiously, the panel's conclusions could lead the presidents of Italy's regions to turn down new requests for fossil-fuel exploration; existing production could also be hit.

The panel, known as ICHESE, was asked in late 2012 to review possible links between hydrocarbon production and the earthquakes, a magnitude-5.9 event on 20 May 2012, and a magnitude-5.8 event 9 days later. ICHESE consists of two Italian and three foreign geoscientists—including the chair, Peter Styles of Keele University in the United Kingdom—as well as Franco Terlizzese, an engineer at Italy's Ministry of Economic Development.

In its report, dated February 2014, ICHESE refutes one alleged factor: the development of a 3.7-billion-m^3 natural gas deposit in an aquifer above an active geological fault near the village of Rivara in the Po Valley, close to the two epicenters. Drilling for the facility had yet to begin when the quakes struck. But the panel does finger another site: the Cavone oil field, owned and operated by Gas Plus. *Science* has seen the conclusions of the report, which says it "cannot be excluded" that activities there initiated the 20 May quake, whose epicenter lies about 20 km away.

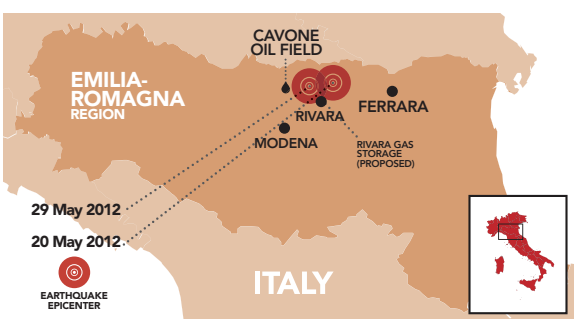

Changes in stress and pressure within Earth's crust resulting from both the removal of oil and the injection of fluids to enhance oil flow would almost certainly not have been sufficient on their own to have induced a major earthquake, the experts explain. But it is possible that the fault involved in the 20 May tremor was close to the breaking point, and that the human-induced changes in the crust, although extremely small, were enough to "trigger" the earthquake. That quake could in turn have triggered the 29 May event by further altering crustal stress.

The group reached this conclusion on the basis of a correlation between increased output from the Cavone field beginning in April 2011 and rising seismicity in the area before 20 May 2012. They say this link should now be backed up by a physical model incorporating "the fluid dynamics in the reservoir and in the surrounding rocks."

Styles did not respond to questions about the report, and a spokesperson for Gas Plus says the company cannot comment on the findings. But an earth scientist who asked not to be named argues that several factors rule out a connection between crude oil production at Cavone and the 20 May earthquake: an absence of small quakes induced directly by the oil production, the significant distance between oil field and epicenter, and the plant's modest output of about 500 barrels a day.

Geoffrey Abers of Columbia University cautions that these factors wouldn't necessarily rule out a link. Three tremors with magnitudes between 4.5 and 5 in Denver in 1967 have been attributed to chemicals being pumped down a deep well, he notes, even though injection had stopped more than a year earlier and taken place up to 10 kilometers from the quakes' epicenters. And three quakes with magnitudes 5 and above that occurred in Oklahoma in November 2011 were probably a result of wastewater being pumped into a depleted oil well, even though the volumes involved were quite small. "We think that in Oklahoma the injected water was jacking up the pressure in just the right place," Abers says, "and that caused a cascading sequence of earthquakes."

Some Italian geologists worry the political noise that the report could generate will discourage rational and open discussion about the seismic risks of oil and gas development. Similar fears were aired after the L'Aquila earthquake, which killed more than 300 people 5 years ago this week. In its aftermath, seven experts were each sentenced to 6 years in prison for downplaying seismic risk ahead of the deadly event, a sentence that some, though by no means all, scientists believed betrayed ignorance by the public and the judiciary about the uncertainties inherent in science. An appeal in the L'Aquila case is pending.

–EDWIN CARTLIDGE

Edwin Cartlidge is a science writer in Rome.

Published by AAAS

NEGLECTED TROPICAL DISEASES

Oral Antibiotic Raises Hopes of Eradicating Yaws

"Where the road ends, yaws begins," experts like to say of the disfiguring disease, which afflicts hundreds of thousands of people in remote corners of the tropics. Now, they hope, yaws could be facing the end of its own road.

At a meeting in the World Health Organization's (WHO's) Geneva headquarters last month, researchers reported preliminary results from four pilot projects suggesting that the disease might be vanquished by simply giving all vulnerable populations a single dose of an oral antibiotic, repeated if necessary. The findings give a boost to a plan devised 2 years ago by 17 tropical disease specialists who met in Morges, Switzerland. Their goal: to eradicate yaws by 2020.

The obstacles are daunting, however, not the least of which is sustaining financial and political commitment for a disease that affects relatively few people. Despite many attempts, only one human pathogen has ever been eradicated, smallpox in 1979. The ongoing efforts to vanquish polio and guinea worm are both far over budget and years past deadline. And yaws eradication was tried, and failed, before.

Still, with a new tool in hand, would-be eradicationists are upbeat. "For sure, yaws is not in the same epidemiological ballpark as killer diseases like AIDS, malaria, pneumonia, and so on, but it causes immense suffering in thousands of people, especially children," says Kingsley Asiedu, who is spearheading yaws eradication activities in WHO's neglected tropical disease department. "We can put an end to this suffering."

Although rarely fatal, yaws causes weeping skin ulcers, usually on the face, back, buttocks, and legs. The agent, a close cousin to the syphilis bacterium, causes an estimated 100,000 new cases each year, 75% of them in children. Most resolve with no lasting damage. But in about 10%, the infection causes disfiguring erosion of tissue, cartilage, and bone.

The previous yaws eradication campaign was launched in 1952, when estimated cases totaled 50 million worldwide. Health workers fanned out over 46 countries, treating people with a long-acting antibiotic, benzathine penicillin, which required painful injections and skilled health workers to deliver them. Twelve years later, prevalence had plunged 95%. But governments and funding agencies lost interest, and in the 1970s the disease began climbing back.

Since then, international agencies and donors have launched concerted efforts to reduce the burden of neglected tropical diseases. And right before the 2012 Morges meeting came evidence that, for yaws, a different drug could simplify the task. In a study in Papua New Guinea, Oriol Mitjà of the Barcelona Institute for Global Health and the University of Barcelona in Spain showed that a single oral dose of azithromycin, an inexpensive antibiotic made by Pfizer, was as effective as benzathine in curing yaws.

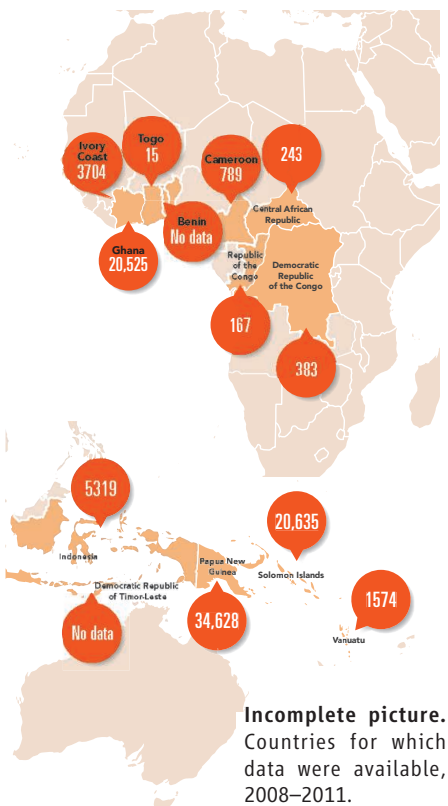

Incomplete picture. Countries for which data were available, 2008–2011.

While the earlier strategy targeted just those people who were visibly infected, the Morges plan calls for blanket coverage of at least 90% of the population in yaws-affected areas. This is key, Mitjà says, as researchers have learned that for every one person visibly infected, six others have latent infections and no symptoms. Repeated mass treatments will catch people not treated the first time round.

After the 2012 meeting, WHO funded pilot studies in four countries with yaws—Republic of the Congo, Ghana, Papua New Guinea, and Vanuatu. Mass azithromycin treatment was doable, the researchers reported last month. In each country, 95% of the population in selected yaws-affected areas—90,000 people in total—received the drug. The pills were easy to give to children, who used to run from the sight of a benzathine-filled syringe.

So far, only the Papua New Guinea pilot study has effectiveness data. "Six months after the first treatment, we saw a 10-fold drop, from 926 to 94 cases," says Mitjà, who led this study. "If the other pilot studies show similar results, there will be little doubt about the feasibility of the new eradication strategy."

But several tropical disease experts are cautious. For one, the geographic scope of the disease is unknown. "Inadequate surveillance is the most serious pitfall that could jeopardize the whole campaign," warns Donald Hopkins of the Carter Center, who chairs the International Task Force for Disease Eradication and has led the guinea worm eradication effort since 1986. Many countries where yaws is endemic do not track cases.

What's more, success will depend on reaching mobile populations in remote, sometimes dangerous, places. "The Pygmies are nomadic and move continually," says Matthew Coldiron, who headed a recent azithromycin campaign during the pilot study in the Republic of the Congo. "After a first round of treatment in a community, 6 months later we found that over a quarter of community members had arrived since the previous treatment, and many were infected." Drug resistance is another potential problem. And if the disease has an animal reservoir, which is not known, the entire plan could be severely hampered and possibly doomed, as infected animals could reinfect people already treated.

Funding will make or break the project, which is estimated to cost anywhere from $100 million to $1 billion. Negotiations are already under way with Pfizer about donating still unknown quantities of the drug. And to pull it off, at least 85 countries would have to commit to conducting intense surveillance for years.

Eradication of yaws is worthwhile and not impossible, Hopkins says. But, he adds, "It will be tougher, take longer, and cost more than originally planned."

–JOHN MAURICE

John Maurice is a science writer and editor in France.

DATA SOURCE: WORLD HEALTH ORGANIZATION

Published by AAAS

Beat the heat. Cane cutters in El Paisnal, El Salvador, start work at the break of dawn to take advantage of the cooler morning hours.

CREDIT: MALCOLM LINTON

Mesoamerica's Mystery Killer

Scientists have come up with a gallery of rogues to explain an epidemic of kidney disease in Central America. But the culprit has stayed one step ahead

SAN SALVADOR AND USULUTÁN DEPARTMENTS, EL SALVADOR—A half-hour before sunrise, Emmanuel Jarquin pulls his four-wheel-drive pickup off the road near the rural town of El Paisnal and rumbles onto a sugar cane field. Jarquin, a physician, parks and steps into the sweet and smoky air, the cane having been charred the day before to burn off leaves and thorns. He walks toward the headlamps of several machete-wielding men who will start cutting at first light.

"What are you bringing us?" one of the men cries in the darkness.

"I'm bringing you health," Jarquin replies.

Jarquin collaborates on a project studying a mysterious affliction of Central American agricultural workers known as chronic kidney disease of unknown etiology (CKDu). First reported in 2002, CKDu has no known links to diabetes or hypertension, the main causes of progressive renal damage worldwide. Much about CKDu is clouded by sketchy health statistics and the difficulty of distinguishing it from other kidney disease. But it appears to be spreading in the hot lowlands of Central America's Pacific Coast—and concerns are rising. In October, the Pan American Health Organization (PAHO) declared CKDu a "serious public health problem," with case reports streaming in from southern Mexico, Guatemala, Honduras, Nicaragua, Costa Rica, and Panama. In El Salvador alone, PAHO's latest figures say chronic kidney disease of all causes kills at least 2500 people in the country each year, and it's the main reason adults die in Salvadoran hospitals.

The disease follows a peculiar pattern. It's about three times more common in men than in women. Cane cutters have been especially hard hit, but it's killing other agricultural workers as well. Whereas traditional CKD is mainly a disease of the elderly, CKDu disproportionately strikes young adults, especially those who toil long hours in the heat. But like its more common cousin, CKDu inexorably destroys the kidneys until they can no longer filter waste from the blood, forcing victims to receive dialysis or a kidney transplant to survive. For many poor agricultural workers in this region, such costly treatments are out of reach.

As public health officials struggle to cope with what many are calling an epidemic, the origins and cause of CKDu remain a stubborn riddle. Possible culprits include dehydration and heat stress, pathogens, agrochemicals, heavy metals, a biochemical disorder, nonsteroidal anti-inflammatory drugs, antibiotics, low birth weight, and genetic susceptibility. Just as with a similar

Published by AAAS

illness in the Balkans that baffled scientists for decades (see p. 146), hard data are scarce and strong opinions are abundant. It's also difficult to disentangle the science from politics. In Nicaragua, former sugar cane workers with the disease and their families have staged demonstrations demanding compensation, igniting violent showdowns with police that included a fatal shooting of a protester in January.

But with increasing attention from researchers, community advocates, the sugar cane industry, and officials in affected countries and abroad, the research landscape is shifting markedly, with a slew of new studies under way or in the works. "The international global health community needs to take this very seriously," says Peter Hotez, a pediatrician at Baylor College of Medicine in Houston, Texas, who specializes in neglected tropical diseases and edits the Public Library of Science journal by that name. "What we're seeing is not business as usual. This is a serious outbreak and we need all hands on deck."

Early detection. Ramón García Trabanino, who now runs a dialysis center in San Salvador, reported a rise of a baffling chronic kidney disease in 2002.

A hot lead

Osmin Sorto, 49, lives in Tierra Blanca de Jiquilisco, an agricultural community near the coast in a region of El Salvador called Bajo Lempa, and says he has watched more than 100 people die of CKD. He could easily have been one of them.

At 15, Sorto started harvesting cotton and planting flags for crop-dusters, but at 22 he landed a plum government job, complete with health care. His kidney problem came to light in 1998, after a doctor's visit for an inflamed toe. Tests revealed gout due to high uric acid levels, and his doctors started closely monitoring his kidney function. He did not have diabetes or hypertension, but by 2005, he had developed end-stage renal disease. Sorto, a classic case of CKDu, was offered a kidney from his sister, and he had the rare insurance plan in El Salvador that would cover the cost of the transplant. Still, he initially was reluctant to accept his sister's kidney. "I didn't want to expose her to any risks," Sorto says. Finally, faced with an imminent death, he acceded, and both are doing fine today.

Few CKDu patients are so lucky. Hospital Nacional Rosales, in El Salvador's capital, San Salvador, is a palatial complex built of Belgian iron in the 1890s. The 525-bed landmark—El Salvador's largest public hospital—is always full. When nephrologist Zulma Cruz started working there 13 years ago, her ward had 18 beds for peritoneal dialysis, which drains kidney toxins from the abdomen, and 16 hemodialysis machines that do the more sophisticated cleansing of toxins from the blood. Today, the hospital has 85 beds filled with patients on peritoneal dialysis and 90 more coming each day to take turns on 30 hemodialysis machines. Each month, up to 70 new patients with end-stage renal disease show up seeking dialysis; the hospital can offer the life-extending treatment to only a few dozen each month. The others must seek out private care, or, more commonly, return home to die.

A young doctor in training at the hospital, Ramón García Trabanino, first brought CKDu to light. "The whole hospital was flooded by renal patients," remembers García Trabanino, who began working at the hospital in the late 1990s. "I thought, 'Why are all these people here with kidney disease? It's not normal.' " An adviser suggested he do a study.

Over 5 months, García Trabanino interviewed 202 new patients with end-stage renal disease. Medical records and personal histories uncovered an obvious cause for CKD in only one-third of the patients, equally split between men and women. Of the rest, 87% were men and the majority worked in agriculture and lived in coastal areas, he and his co-authors reported in September 2002. Their report in the *Pan American Journal of Public Health* speculated that patients who had CKD with *características peculiares* might have developed the disease after exposure to herbicides and insecticides.

Health officials took little interest in this greenhorn's findings. "I spoke with PAHO and I remember them laughing at me," García Trabanino says. "They thought I was crazy." The Ministry of Health in El Salvador took no action, but it did give him an award for his study. "The judges must have been drunk that night," he says.

García Trabanino, who now runs a private dialysis clinic, understands why this landmark report received little traction. "It was very weak," he says. "If I could travel back in time, I'd erase half of what I wrote and do more testing. But that's what we could do back then."

A newspaper article about the award caught the attention of Julio Miranda, a leader of a social fund for health emergencies in Tierra Blanca de Jiquilisco. Miranda's team contacted García Trabanino and explained that they had seen an extraordinary rise in deaths from kidney failure since the mid-1990s. "Many people thought it was pesticides," Miranda says. They agreed to

CREDIT: MALCOLM LINTON

Published by AAAS

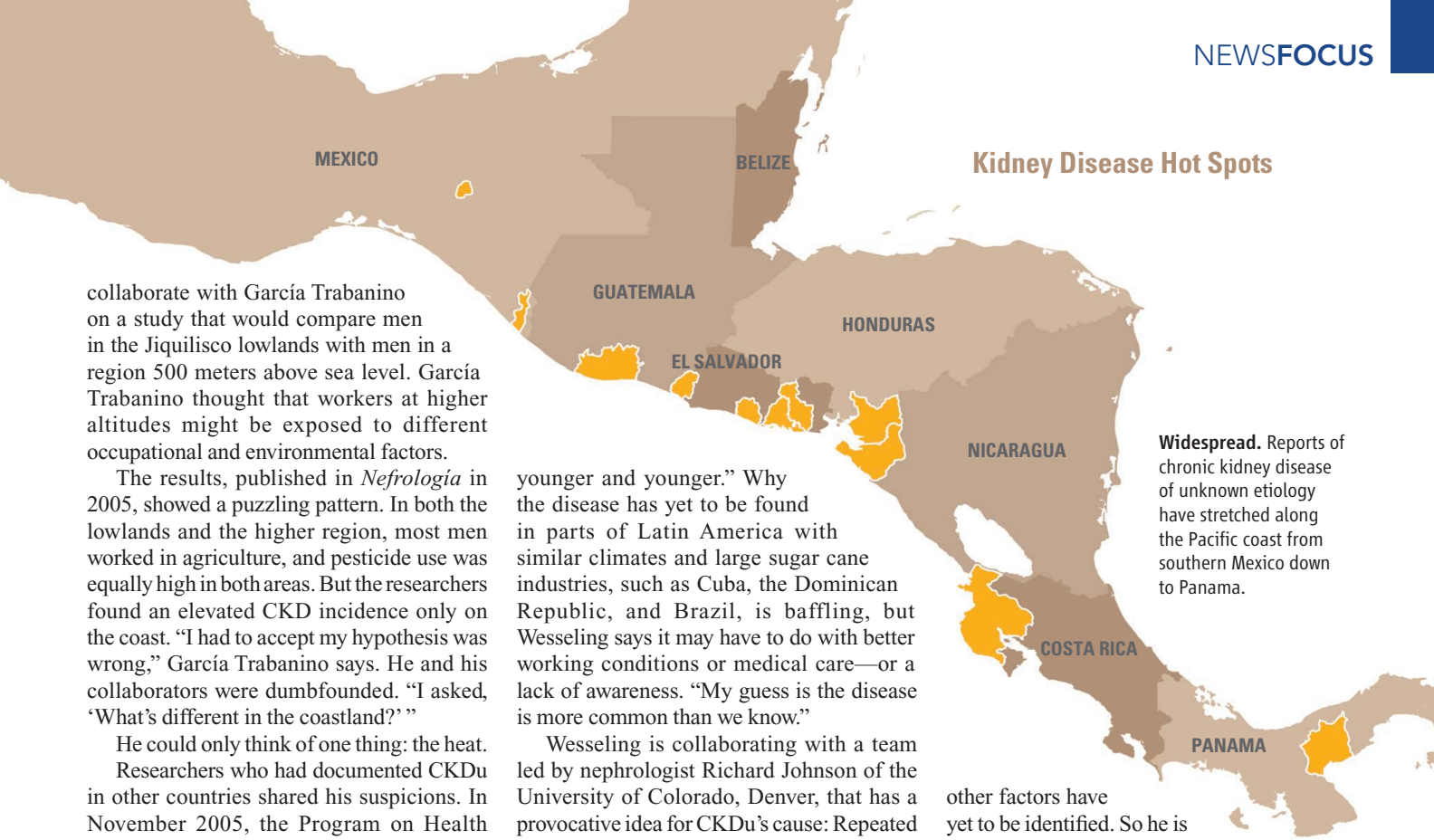

Widespread. Reports of chronic kidney disease of unknown etiology have stretched along the Pacific coast from southern Mexico down to Panama.

CREDIT: ADAPTED FROM D. BROOKS AND O. RAMÍREZ-RUBIO, *MESOAMERICAN NEPHROPATHY*; SALTRA 2013

collaborate with García Trabanino on a study that would compare men in the Jiquilisco lowlands with men in a region 500 meters above sea level. García Trabanino thought that workers at higher altitudes might be exposed to different occupational and environmental factors.

The results, published in *Nefrología* in 2005, showed a puzzling pattern. In both the lowlands and the higher region, most men worked in agriculture, and pesticide use was equally high in both areas. But the researchers found an elevated CKD incidence only on the coast. "I had to accept my hypothesis was wrong," García Trabanino says. He and his collaborators were dumbfounded. "I asked, 'What's different in the coastland?' "

He could only think of one thing: the heat.

Researchers who had documented CKDu in other countries shared his suspicions. In November 2005, the Program on Health and Work in Central America, or SALTRA, gathered García Trabanino and 17 other researchers from six countries for a workshop in León, Nicaragua. The meeting sparked studies in Nicaragua and El Salvador that would survey nearly 2000 people living at different altitudes and working in various occupations.

The studies measured two indicators of kidney damage: creatinine levels and glomerular filtration rate, or GFR. (As the kidney's filtration system breaks down, creatinine levels rise.) Both studies found elevated creatinine levels and suppressed GFRs only in the lowlands. SALTRA founder Catharina Wesseling, an epidemiologist at the Central American Institute for Studies on Toxic Substances at the National University in Heredia, Costa Rica, worked on both studies and says they deliver a clear message. "We think the evidence of heat stress and chronic dehydration is very strong," says Wesseling, who refers to the disease as Mesoamerican nephropathy. She and her collaborators hypothesize that strenuous work in hot climates repeatedly depletes bodily fluids, overtaxing kidney cells. She notes, however, that "it's still very unclear how the disease starts and who will be affected."

One population does seem to be especially vulnerable, Wesseling says. "Those who are dying are sugar cane workers and they are really dying every day and they are dying younger and younger." Why the disease has yet to be found in parts of Latin America with similar climates and large sugar cane industries, such as Cuba, the Dominican Republic, and Brazil, is baffling, but Wesseling says it may have to do with better working conditions or medical care—or a lack of awareness. "My guess is the disease is more common than we know."

Wesseling is collaborating with a team led by nephrologist Richard Johnson of the University of Colorado, Denver, that has a provocative idea for CKDu's cause: Repeated dehydration disrupts a biochemical pathway, leading to excess conversion of glucose to fructose. The enzyme fructokinase, which metabolizes the fructose, then creates high levels of kidney-damaging uric acid, oxidants, and immune system messengers that cause inflammation.

Johnson and co-workers tested their hypothesis by subjecting mice to hours of high heat at a stretch while restricting water intake in one group but not in another. They repeated the experiment in mice that could not metabolize fructose because their fructokinase gene had been intentionally crippled. As they reported online in December in *Kidney International*, kidney damage occurred only in normal mice on restricted water, providing compelling support for what some now call the "heat-plus" hypothesis.

> "We think the evidence of heat stress and chronic dehydration is very strong. [But] it's still very unclear how the disease starts."
>
> —CATHARINA WESSELING, EPIDEMIOLOGIST

Johnson wonders whether people who develop the disease might become dehydrated and then, to quench their thirst, drink sodas that are high in fructose, compounding the problem. "Rehydrating with soft drinks," he suggests, "may toast the kidneys."

García Trabanino says the fructokinase hypothesis is "the closest thing to reality we have right now." But he still suspects that other factors have yet to be identified. So he is launching a new study with Jarquin, the four-wheel-drive doctor, to examine more carefully the differences between people who live in the coast and at higher altitudes. García Trabanino chose to work with Jarquin because he is one of the few doctors who specialize in treating agricultural workers: In addition to conducting occupational health evaluations and training for agricultural companies, he runs a private practice in his boyhood town of El Paisnal, which means he has unusually close ties to the sugar cane–cutting community. The two physicians have unusually close ties to each other, too: García Trabanino's father, also a nephrologist, treated Jarquin's father, himself a victim of traditional chronic kidney disease.

A dissenting voice

Next to a cornfield in Bajo Lempa's Jiquilisco municipality, the epicenter of CKDu in El Salvador, is a small unmarked cemetery with 2 dozen aboveground tombs. Most are recent, adorned with wreaths and fresh flowers. CKD took the lives of one woman and nine men in this graveyard, says local doctor Lilian Núñez. One was her uncle. "This man was diagnosed 3 days before he died," she says.

Published by AAAS

At her side in the cemetery is Carlos Orantes, a nephrologist at the National Institute of Health in San Salvador—and a skeptic of the heat-plus hypothesis. "We are not obsessed with pesticides, but we do believe they're at the center of the cause of the disease," Orantes says. His team's 2009 CKD study in Bajo Lempa confirmed many aspects of the disease's demographics. But it left Orantes convinced that pesticides deserve a closer look.

Orantes thinks the coastal regions may have more CKDu because the heat increases susceptibility to nephrotoxic effects of the pesticides, the true cause. He also contends that pesticides may interact with heavy metals such as arsenic to poison the kidneys. He points to research from Sri Lanka suggesting that glyphosate in pesticides chelates arsenic, boosting its level in the water and its potential to damage the kidneys' delicate filtering machinery. And his team has preliminary evidence that arsenic levels are higher in fields surrounding the cemetery than in the nearby village.

Wesseling, who has built her career around studying the impact of toxic substances, says his arguments have no merit. She says neither pesticides nor arsenic can explain the geography of the disease. Arsenic, she says, is prevalent in soil and lakes across El Salvador, not just where CKDu is common. "It doesn't convince me at all," she says. "He's only looked at one specific place."

Cruz of Hospital Nacional Rosales agrees. "We need other hypotheses," she says. To that end, she and her co-workers teamed up with researchers from the Karolinska Institute in Stockholm to study kidney biopsies from CKDu patients. In a November report published in the *American Journal of Kidney Diseases*, they described how the disease inflicted consistent, distinct damage on the kidneys in the eight subjects, a finding that many researchers hope may provide a tangible new lead.

Political maelstrom

The scientific uncertainty has not deterred finger-pointing. Many agricultural workers with CKDu are convinced that pesticides are the cause and are demanding compensation from government funds set aside for health emergencies. Sandra Peraza, a chemist at the University of El Salvador in San Salvador and part of SALTRA, attended a community meeting in Bajo Lempa a few years ago where she was supposed to present data. "They were screaming about pesticides," she recalls. "I thought if I say right now that pesticides are not the answer, they'll kill me. The meeting finished without my having a chance to speak and I said, 'Thank God.' "

The biggest CKDu study to date has only fed the rancor. In the center of this maelstrom is epidemiologist Daniel Brooks, who became aware of CKDu a decade ago because his wife worked on a sister-city project connecting Brookline, Massachusetts, and Quezalguaque, Nicaragua. "She said they have this problem of this chronic

A Balkan Riddle's Serendipitous Solution

For researchers puzzling over a mysterious kidney disease in Central America dubbed CKDu (see p. 143), a tale from the Balkans offers inspiration and some cautions. In the late 1950s, reports started coming out of southeastern Europe about a kidney disease afflicting rural communities near tributaries of the Danube River. Balkan endemic nephropathy, a 1966 article in *The Lancet* declared, was "clearly a big public-health problem" whose cause "is utterly obscure and has excited much speculation." Solving the mystery took half a century—and led down multiple blind alleys.

Like CKDu, the Balkan disease had a geographic peculiarity: It was seen only in mountain valleys and lower elevations. Suspected causes were legion, including heavy metal poisoning, infectious disease, genetic predisposition, and allergies. The most intense attention fell on a common food contaminant, a mycotoxin called ochratoxin A, which often grows in stored grains and is known to damage kidneys.

In 1969, a report in a Serbian journal added another suspect: seeds from a weed that grew in fields next to cultivated wheat commonly used to bake homemade bread. And in the early 1990s, a spate of kidney failures in Belgium provided a break in the case. A number of women taking Chinese herbs in a "slimming regimen" began to suffer a kidney pathology that mirrored that seen in Balkan endemic nephropathy. Like victims of the Balkan disease, the women also had a greatly elevated risk for a urinary tract cancer. "Chinese-herb nephropathy" soon turned up in several countries and was traced to ingestion of a cousin of the weed suspected in the Balkans. Both plants contain aristolochic acid, a known nephrotoxin and carcinogen.

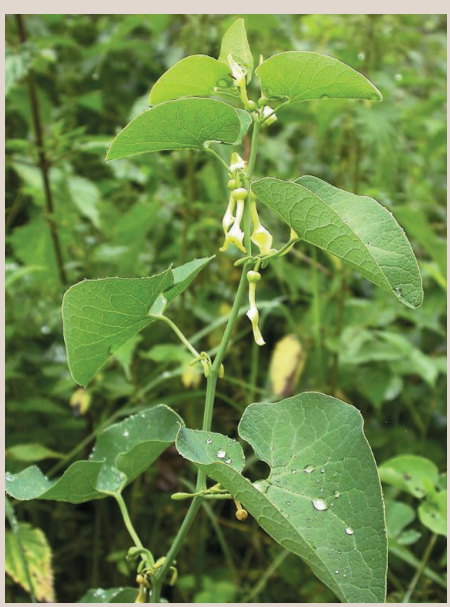

Proven guilty. *Aristolochia clematitis* has been fingered as a cause of chronic kidney disease.

CREDIT: OLIVIER PICHARD/WIKIMEDIA COMMONS

In 2005, pharmacologist Arthur Grollman of Stony Brook University in New York—who has long urged the U.S. Congress to regulate herbal medicine—sent a graduate student to Croatia to investigate. The student confirmed that the weed containing aristolochic acid still grew in wheat fields there. Grollman discovered that Croatian veterinarians in the 1950s extensively studied kidney failure in horses that had eaten the weed. His team also found molecular clues: Autopsied kidneys from victims of Chinese herbal and Balkan endemic nephropathy contained DNA–aristolochic acid complexes, and a mutation in tumors from the Balkan patients matched one seen in animal experiments with aristolochic acid.

In the face of dogged skepticism, particularly from the ochratoxin A crowd, Grollman's team developed what many see as an ironclad case that aristolochic acid causes Balkan endemic nephropathy. The coup de grâce came with a cover report in the March 2012 issue of *Kidney International*, in which a leading nephrologist wrote that "aristolochic acid nephropathy" should become the name for both the Balkan and Chinese herb maladies.

The long saga of the Balkan disease offers several lessons for CKDu researchers, Grollman says. Search for answers broadly at first, he says, and use the sophisticated tools of molecular biology to sift possibilities. And expect academic rivalries to slow progress. "The psychology is the same everywhere," Grollman says. "If you're in Croatia and they put you in the national academy for all the work you've done on ochratoxin A, you're not happy when someone comes along and says that has nothing to do it." **–J. C.**

Published by AAAS

kidney disease and maybe they need an epidemiologist," says Brooks, who works at Boston University and had long studied smoking cessation and sunburn protection.

At first, Brooks tried to help from afar. Then in 2008, a community group in Nicaragua filed a complaint with the World Bank Group's International Finance Corporation (IFC) that ultimately would catapult him to the front of the CKDu research field—and make him a lightning rod for criticism. IFC had approved a $55 million loan to Nicaragua Sugar Estates Limited (NSEL), in part so it could start producing ethanol. The complaint alleged that the company's environmental and health practices did not meet IFC loan terms. One allegation deserved special attention, an IFC ombudsman concluded: that working conditions were linked to widespread CKD.

As part of a mediation process, the company and a community group representing afflicted families hired Brooks's team—one of nine applicants—to investigate CKDu's cause. The group received $800,000 from the sugar company and another $250,000 from the IFC ombudsman's office for its studies. The researchers assessed everything from industrial hygiene to water quality, pesticide exposure, and biomarkers of kidney damage, comparing people who worked in sugar cane fields with those in factories or other hot settings like underground mines, construction, and shipping ports.

Bitter feud. Former cane cutters in Managua in March 2013 protested against sugar cane companies they believe are responsible for CKDu.

CREDIT: ESTEBAN FELIX/AP PHOTO

The 2012 report from "the Boston group" had a decidedly equivocal bottom line. "Following an evaluation of all available data, our overall conclusion was that the causes of CKD in the Western Zone of Nicaragua were unknown and that the relationship between the disease and [the company's] work practices was also unknown," Brooks and his colleagues wrote.

Wesseling and others were taken aback. "They went wrong," she says. "There's a clear link." She also objects to how the sugar cane industry in Nicaragua has used the Boston group's study to rebut criticism that it works people too many hours without enough shade, water, and rest. (El Salvador's sugar cane industry is dominated by worker-run collectives, which insulates it from such criticism.)

Jason Glaser of the nonprofit La Isla Foundation, which does public health policy and human rights work related to CKDu, contends that IFC and NSEL influenced the results. "Both have a clear interest in the disease not being related to sugar cane work," Glaser says. "To say there is no relationship at this point is willful ignorance." (In February, the Dutch Postcode Lottery awarded La Isla $4 million, more than half of which Glaser says it will invest in CKDu research.)

Brooks, who estimates the disease has prematurely killed 20,000 people, strongly rejects the assertion that industry funding influenced his group's findings. "We have the right to publish what we find, and the industry doesn't get to make a determination whether we publish it," he says. In fact, Brooks says he finds the heat-plus hypothesis the most compelling explanation of CKDu. "The nightmare from a scientific standpoint," he says, "is that there are a bunch of different things going on. It's hard to disentangle."

But he's giving it another go. In collaboration with the U.S. Centers for Disease Control and Prevention (CDC), Brooks and his team are launching three new studies. One will assess how working conditions vary by occupation and geography in Nicaragua and El Salvador. A second will probe for genetic susceptibilities. Finally, his team will investigate whether kidney damage begins to occur before people enter the workforce. The nonprofit CDC Foundation will fund the project with industry money: $1.05 million from the Sugar Producers of the Central American Isthmus and $675,000 from Nicaragua's National Committee of Sugar Producers.

Conducting research in a highly charged social and political atmosphere "makes the work a lot more challenging," says Reina Turcios-Ruiz, an epidemiologist based at CDC's Central American Regional Office in Guatemala City. "But it's an opportunity for us at CDC to demonstrate our integrity for the scientific process and to make available the highest levels of evidence," she says, "so decisions on scientific policy are based on evidence and not on myth or rumors."

Flush with cash to launch more sophisticated studies, researchers may have their best chance yet to understand the baffling disease. On top of the satisfaction of solving a complex scientific mystery and removing the "u" from CKDu, their work raises hopes for interventions that can prevent the damage. And that, in turn, may help Emmanuel Jarquin live up to his promise of "delivering health" each time he visits the sugar cane fields.

–JON COHEN

Published by AAAS

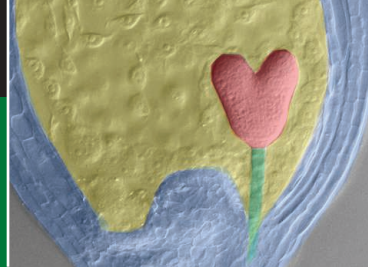

LETTERS

edited by Jennifer Sills

Immunotherapy: It Takes a Village

WE IN THE CANCER IMMUNOLOGY AND IMMUNOTHERAPY COMMUNITY ARE THRILLED THAT *Science* named "Cancer immunotherapy" as 2013's Breakthrough of the Year (J. Couzin-Frankel, 20 December 2013, p. 1432). The rapid succession of clinical successes by blocking antibodies to two immune checkpoints, CTLA-4 and PD-1, and by chimeric antigen-receptor-transduced T cells, shows the power of basic immunology when translated to therapy. As such, I write to acknowledge some of the key scientists whose basic discoveries paved the way for the clinical successes outlined in the Breakthrough issue.

CTLA-4 was originally cloned by Pierre Goldstein (*1*). Peter Linsley later demonstrated that its ligands were B7.1 and B7.2, in fact the same as for the T cell costimulatory receptor CD28 (*2*, *3*). On the basis of in vitro studies, Jeffrey Bluestone first suggested that, in contrast to CD28, CTLA-4 was an inhibitory receptor (*4*). A year later, concurrent with similar in vitro findings from Jim Allison (*5*), Arlene Sharpe and Tak Mak independently proved CTLA-4's inhibitory function in genetic knockout mice (*6*, *7*). These discoveries paved the way for Allison's seminal work demonstrating in murine tumor models that CTLA-4 blockade induced antitumor responses, supporting its subsequent clinical development.

An independent sequence of discoveries paved the way for the clinical development of PD-1/PD-L1 pathway blockers. Almost 10 years after the cloning of PD-1 by Tasuku Honjo (*8*), Gordon Freeman demonstrated that its major ligand was another B7 family member (*9*) that had been identified a year earlier by Lieping Chen (*10*). This ligand-receptor pair was also an immune "checkpoint" but biologically very different from CTLA-4. Chen went on to show that many human tumors upregulate PD-L1 (*11*), commonly as an adaptive response to γ-interferon produced by antitumor T cells (*12*). He also showed that expression of PD-L1 in cancer cells conferred immune resistance that could be abrogated by antibodies that blocked the PD-L1/PD-1 interaction, leading to tumor regression in mouse models (*11*).

The origin of chimeric antigen receptors dates back to work by Zelig Eshhar (*13*), who first demonstrated that transduction of T cells with chimeric genes encoding single-chain antibodies linked to a transmembrane region and an intracellular domain. The intracellular domain, encoding the signaling adaptor for the T cell receptor, was discovered by Larry Samelson and Richard Klausner (*14*). It could redirect T cell killing to cells expressing the antibody's cognate antigen.

Eventually, millions of cancer patients will benefit from these immunotherapies and will hopefully be reminded by their physicians that they are the fruits of decades of basic immunology research, which must continue to be supported.

DREW PARDOLL

Abeloff Professorship in Oncology, Cancer Immunology and Hematopoiesis Program, Sidney Kimmel Comprehensive Cancer Center, Johns Hopkins University, School of Medicine, Baltimore, MD 21287, USA. E-mail: dpardol1@jhmi.edu

References

1. J. F. Brunet *et al.*, *Nature* **328**, 267 (1987).
2. P. S. Linsley *et al.*, *J. Exp. Med.* **173**, 721 (1991).
3. P. S. Linsley *et al.*, *J. Exp. Med.* **174**, 561 (1991).
4. T. L. Walunas *et al.*, *Immunity* **1**, 405 (1994).
5. M. F. Krummel, J. P. Allison, *J. Exp. Med.* **182**, 459 (1995).
6. E. A. Tivol *et al.*, *Immunity* **3**, 541 (1995).
7. P. Waterhouse *et al.*, *Science* **270**, 985 (1995).
8. Y. Ishida *et al.*, *EMBO J.* **11**, 3887 (1992).
9. G. J. Freeman *et al.*, *J. Exp. Med.* **192**, 1027 (2000).
10. H. Dong *et al.*, *Nat. Med.* **5**, 1365 (1999).
11. H. Dong *et al.*, *Nat. Med.* **8**, 793 (2002).
12. J. M. Taube *et al.*, *Sci. Transl. Med.* **4**, 127ra37 (2012).
13. Z. Eshhar, T. Waks, G. Gross, D. G. Schindler, *Proc. Natl. Acad. Sci. U.S.A.* **90**, 720 (1993).
14. L. E. Samelson *et al.*, *Cell* **43**, 223 (1985).

theBUZZ

Women in Engineering

M. Klawe's Book Review about *Girls Coming to Tech!* by Amy Sue Bix (14 March, p. 1201) recounts the challenges faced by women who pursued engineering before the 1970s. The topic elicited personal accounts, including one by the woman shown in the Review's photo. See the comments below and at www.sciencemag.org/content/343/6176/1201.full.

I was delighted to see myself pictured in your article, at 17 and with a slide rule. My years at MIT were full of memorable ups and downs. Though our numbers were small, there were more women who loved math and science than I had ever known before. I met many of my closest friends and colleagues during those years. I am now in my 43rd year as a professor at Northeastern University, where I was one of the founders of the College of Computer and Information Science.

—Harriet Fell

While reading the text, some memories came to me. In 1990, during an interview for work experience, a director of an international company told me "your CV is very good technically speaking, but you have a problem: You are a woman." However, today I am very happy with my engineering work.

—Vania Salvini

CREDIT: AAAS

Published by AAAS

A New Threat to European Vultures

A DECADE AGO, DICLOFENAC WAS FOUND TO be responsible for the collapse of the Indian vulture populations (*1*). Banning its use and that of related anti-inflammatory nonsteroidal drugs allowed the beginning of a population recovery (*2*). However, Europe may now face a similar threat, as the Spanish government in 2013 licensed the use of both dolofenac and diclovet, veterinary drugs that contain 50 mg/ml of diclofenac, mainly for pig and cattle farming.

Since 2000, the bovine spongiform encephalopathy (BSE) crisis has put European vultures at risk. With the recent implementation of the European Regulations (*3*) and the Royal Decree 1632/2011 (*4*), which provide Spain with a legal framework for increasing food availability for carrion-eating birds, it appeared that the vultures were finally getting a reprieve. Until the regulations were approved, carcasses had to be taken to vulture feeding sites or destroyed. Now animals that die in grazing fields can be left for vultures as well, after being checked for disease. Although we are optimistic about the effects of these regulations, the benefits would be limited by the use of diclofenac.

ALVARO CAMIÑA,[1]* J. R. GARRIDO,[2] J. MARTIN,[2] C. H. LOPEZ-HERNÁNDEZ,[1] R. ALFARO[2]

[1]ACRENASL Environmental Consultants, 28220, Majadahonda, Spain. [2]JMM Wildlife Monitoring and Management Consultants, Villanueva del Ariscal, 41808, Seville, Spain.

*Corresponding author. E-mail: acamia@acrenasl.eu

References and Notes

1. R. T. Watson *et al.*, *Nature* **427**, 630 (2004).
2. R. Cuthbert *et al.*, *PLOS ONE* **6**, e19069 (2011).
3. Regulation CE 142/2011 of 25 February 2011 implementing Regulation (EC) No. 1069/2009 of the European Parliament and of the Council laying down health rules as regards animal by-products and derived products not intended for human consumption and implementing Council Directive 97/78/EC as regards certain samples and items exempt from veterinary checks at the border under that Directive (http://eur-lex.europa.eu/LexUriServ/LexUriServ.do?uri=OJ:L:2011:054:0001:0254:EN:PDF).
4. Royal Decree 1632/2011 of 14 November, regulating the feeding of certain wildlife species with animal by-products not intended for human consumption (www.boe.es/aeboe/consultas/bases_datos/doc.php?id=BOE-A-2011-18536)[in Spanish].

India Puts Informed Consent on Camera

IN ITS LATEST INITIATIVE TO STRENGTHEN THE regulation of clinical trials, the Indian government is now requiring clinical trial investigators to document the informed consent process through audiovisual recording (*1*). The government took this step in response to a Supreme Court order requiring clinical trials in India to incorporate audiovisual as well as written informed consent as a prerequisite to enrollment of potential study participants. The Central Drugs Standard Control Organization has issued a draft guideline describing these procedures (*2*).

The informed consent process in developing countries is largely focused on complex written documentation consisting primarily of the literal translation of consent forms designed for other countries (*3*). Rather than truly informing the trial participants, the primary purpose seems to be providing legal protection to the investigators. Audiovisual documentation of oral consent has been shown to be a valid instrument for populations with limited understanding of trial

CREDIT: JULIUS RÜCKERT/WIKIMEDIA COMMONS

elements (*4*). For those who are illiterate or otherwise unfamiliar with the process, it is difficult to establish voluntary participation based on standard written consent procedures (*4*). Audiovisual recording can also serve as an oversight mechanism for the ethics committees and drug regulators.

In response to the new requirements, concerns have been raised about the lack of clarity regarding operational issues, scope of guidance, maintenance of confidentiality, escalated trial costs, and sociocultural barriers to effective implementation in India (*5*). Although these initial concerns seem to be valid, further clarification is expected to address the uncertainties facing the clinical researchers and sponsors.

The present legislation is intended to improve the quality, reliability, and transparency of informed consent process; enhance investigator accountability; and restore public trust in clinical trials. However, as is true for any alternative strategy, audiovisual recording of trial consent needs to be examined and monitored, and its effectiveness in addressing one of the fundamental requirements of ethical research needs to be assessed.

ASHISH KUMAR KAKKAR

Department of Pharmacology, All India Institute of Medical Sciences, Saket Nagar, Bhopal, Madhya Pradesh 462024, India. E-mail: drashishkakkar@gmail.com

References

1. Central Drugs Standard Control Organization (CDSCO), Audio-Video Recording of Informed Consent Process of All New Subjects in Clinical Trials: Administrative Orders (www.cdsco.nic.in/writereaddata/Office%20Order%20dated%2019.11.2013.pdf).
2. Central Drugs Standard Control Organization (CDSCO), Draft Guidelines on Audio-Visual Recording of Informed Consent Process in Clinical Trial (www.cdsco.nic.in/writereaddata/Guidance_for_AV%20Recording_09.January.14.pdf).
3. Z. A. Bhutta, *Bull. World Health Org*. **82**, 771 (2004).
4. O. Benitez, D. Devaux, J. Dausset, *Lancet* **359**, 1406 (2002).
5. Indian Society for Clinical Research (ISCR), ISCR Media Statement on Audio-Visual Recording of Informed Consent (www.iscr.org/NewsletterRev_Doc/123963260_ISCR%20Statement%20on%20Audio-Visual%20Recording%20of%20Informed%20Consent-22%20Nov%202013.pdf).

CORRECTIONS AND CLARIFICATIONS

This Week in Science: "Immune variation" (7 March, p. 1055). M. N. Lee *et al*. analyzed expression of genes from 534 healthy subjects, rather than 30. The HTML and PDF versions online have been corrected.

News of the Week: "Threat of H10N8 surfaces" (7 February, p. 583). The H10N8 flu virus has been identified in China, but not in Taiwan.

Reports: "Stress in puberty unmasks latent neuropathological consequences of prenatal immune activation in mice" by S. Giovanoli *et al*. (1 March 2013, p. 1095). Joram Feldon was awarded grants from the Swiss National Science Foundation (SNSF) and ETH Zurich, as well as a National Alliance for Research on Schizophrenia and Depression Distinguished Investigator grant. The HTML and PDF versions online have been corrected.

Reports: "Writing about testing worries boosts exam performance in the classroom" by G. Ramirez and S. L. Beilock (14 January 2011, p. 211). The authors discovered minor mistakes in the formula used to calculate response time and in the formula used to calculate high demand problem accuracy and response time for a single subject in the unrelated writing condition. Correcting these mistakes did not in any way change the significance or interpretation of the results; however, the relevant statistics in the main text and the supplementary materials and the relevant supplementary tables have been corrected.

Letters to the Editor

Letters (~300 words) discuss material published in *Science* in the past 3 months or matters of general interest. Letters are not acknowledged upon receipt. Whether published in full or in part, Letters are subject to editing for clarity and space. Letters submitted, published, or posted elsewhere, in print or online, will be disqualified. To submit a Letter, go to www.submit2science.org.

BIOGEOGRAPHY

Unlikely Yet Pivotal Long Dispersals

Ran Nathan[1] and Oz Nathan[2]

Long-distance dispersal can enable a species to colonize new areas far from its range, with potentially drastic consequences for ecology, evolution, and biogeography. In *The Monkey's Voyage*, Alan de Queiroz argues that long-distance dispersals are necessary to explaining the evolutionary histories of many animals and plants across the world. Although Charles Darwin (*1*) and Alfred Russel Wallace (*2*) came to the same conclusion over a century ago, the dispersalist view has long been strongly resisted. In particular, the acceptance of plate tectonics in the 1960s expedited an alternative view, known as vicariance biogeography, which soon gained forceful support.

This alternative uses vicariance (splitting) events, such as those driven by the rupture and motion of continental plates, to explain the geographical distribution of species. Vicariance processes have fragmented formerly continuous distributions of taxonomic groups, and the subsequent processes of dispersal, speciation, and extinction took place within each fragment (without links through long-distance dispersals among them). Supporters of the vicariance paradigm hold that dispersals over great distances are so unlikely that they never actually happen and therefore condemned dispersal biogeography as "a science of the improbable, the rare, the mysterious and the miraculous" (*3*). However, over the past two decades new discoveries and novel tools (especially molecular phylogenetic methods) have brought the dispersal-vicariance debate toward resolution. The evidence, argues de Queiroz (an evolutionary biologist at the University of Nevada, Reno), rebuts vicariance explanations and resurrects Darwin and Wallace. He thus proposes that long-distance dispersal explanations should be described with a fifth adjective: the necessary.

De Queiroz's centerpiece example is the seemingly miraculous transoceanic dispersal of monkeys. Two major taxonomic groups of monkeys—catarrhine (downward-pointing nose) monkeys of the Old World and platyrrhine (flat nose) monkeys of the New World—are closely related sister groups, which means that their disjunct distribution offers a powerful test for the dispersal-vicariance debate. Estimates from relaxed molecular clocks indicate that the platyrrhine-catarrhine split occurred about 41 million years ago (the mean of 31 million to 51 million years). That is much later than the separation of the African and South American plates as part of the breakup of Gondwana, estimated as about 110 million years ago. Thus, de Queiroz argues that monkeys must have made a highly improbable journey of at least 1450 km across the Atlantic Ocean. The immigrants eventually gave rise to the 124 extant species of monkey in the New World. Caviomorph and simodontine rodents also diversified from transoceanic-dispersed ancestors. Together, the three clades comprise 673 extant species—73% of South America's nonflying, nonaquatic mammal species—many of which play key roles in shaping the continent's ecosystems and filling its biodiversity hotspots.

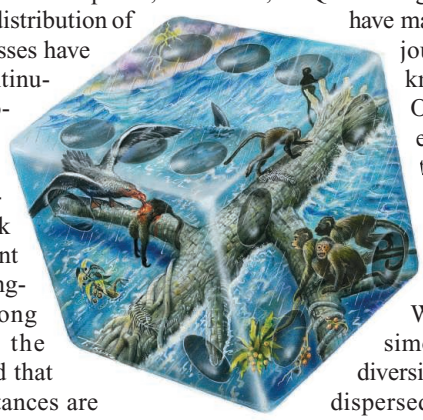

Beating the odds.

CREDIT: TUVIA KURTZ

Essayist Nassim Taleb refers to rare and unpredictable random events that have a huge impact as black swans (*4*). Most discussions of black swans focus on key anthropocentric examples, such as the rise of the Internet and 9/11, but his theory can also be applied to various geophysical and biological phenomena, including extreme weather, earthquakes, wildfires, epidemics, and tumor dissemination. Such rare events are not well captured by the typical Gaussian (bell-shaped) distribution, but by fat-tailed distributions with large deviations from the mean, characterized for those systems and also for movements of organisms (*5*, *6*). De Queiroz argues that the few Eocene monkeys that completed their improbable trans-Atlantic journey merit the moniker of black swans due to the extreme rarity of their long-distance dispersal and its massive impact.

Taking readers on a tour through time and space, de Queiroz covers the key players, ideas, discoveries, and methodological advances that have occurred since Darwin and Wallace and have collectively led to a recent paradigm shift in historical biogeography. He provides fascinating examples of plants and animals from a variety of geographic locations, mostly oceanic islands. Lucidly and captivatingly written, his narrative merges snapshots from his personal perspective with detailed descriptions of key players from the past two centuries, their characters, and lives—as if the author knew them personally. Although some readers may deem it too slow or too one-sided, we found *The Monkey's Voyage* a joy to read and a great example of how a potentially dry scientific debate can be presented to attract a broad readership.

The Monkey's Voyage
How Improbable Journeys Shaped the History of Life
by Alan de Queiroz
Basic Books, New York, 2014. 368 pp. $27.99, C$31. ISBN 9780465020515.

The arguments for and against the prevalence of transoceanic long-distance dispersal in shaping the world's biota are essentially a game of very low probabilities and innumerable trials. Darwin immersed seeds in salty seawater and ran various other experiments to explore how low (some elements of) these probabilities are, and vicariance biogeographers have dismissed dispersal explanations as ridiculously improbable. Although de Queiroz strongly emphasizes and thoroughly discusses this point, *The Monkey's Voyage* lacks a basic quantitative treatment of the link between very low probabilities and big numbers. It provides only a short—but admittedly brilliant—glimpse into this core issue through a wonderful hypothetical present-day discussion among prominent biogeographers. In it, the vertebrate paleontologist George Gaylord Simpson "pulls out a pen and jots down some calculations to show that an event with a minuscule probability of occurring in any given year, such as monkeys rafting across 1800-plus miles of ocean, might yet be reasonably likely given a long enough period of time."

The probability of dispersal strongly decays as the distance from the source increases. A probability density function (commonly called the dispersal kernel) can be used to estimate the probability of a successful dispersal event after a given number of years. The calculations require estimates for the (typically fat-tailed) dispersal kernel parameters, the (huge) number of dispersers,

[1]Movement Ecology Laboratory, Department of Ecology, Evolution and Behavior, Alexander Silberman Institute of Life Sciences, The Hebrew University of Jerusalem, Jerusalem, Israel. E-mail: ran.nathan@mail.huji.ac.il. [2]Capital Factory, 701 Brazos Street, Austin, TX 78701, USA.

Published by AAAS

and their (very low) probability of surviving the journey and establishing themselves far from the home site (*7*). Further refinements of dispersal kernels could incorporate trade winds (*8*) and other underlying mechanisms (*9*). Such a mechanistic modeling approach (*9*) is especially promising for rafting, the primary mechanism of transoceanic dispersal highlighted in *The Monkey's Voyage*—for which uncertainty can be reduced by incorporating information on the properties of the rafts as well as on the passengers, wind drifts, and oceanic currents (*10*). Furthermore, there exists a wide spectrum of dispersal-vicariance scenarios. Historical biogeography should go beyond assigning cases to these two extreme alternatives and should instead quantify their relative importance. The scope of investigation should also be expanded beyond the hallmark examples of terrestrial species moving across oceans, because long-distance movements of marine and aerial species, as well as those of terrestrial species over land, have also greatly contributed to shaping the geographical distribution of the world's biota.

Considering the probability of an explanation is essentially the common practice of nearly all aspects of our life. Yet, it is not only the histories of life and human societies that have largely been shaped by unlikely black swan events. Each of our lives is a product of an idiosyncratic chain of events, which can be considered highly improbable yet an evident reality. The central arguments of *The Monkey's Voyage* appear to be increasingly well recognized nowadays in such diverse fields as statistics, economics, engineering, computer sciences, earth sciences, chemistry, physics, and biology. It is time to proceed beyond broad awareness of the general concepts to develop quantitative frameworks to better understand the unexpected—and to cope with the high impact of rare and unpredictable "monkey's voyage" events.

References

1. C. Darwin, *The Origin of Species by Means of Natural Selection* (John Murray, London, 1859).
2. A. R. Wallace, *Island Life* (Macmillan, London, 1880).
3. G. Nelson, *J. Hist. Biol.* **11**, 269 (1978).
4. N. N. Taleb, *The Black Swan: The Impact of the Highly Improbable* (Random House, New York, 2010).
5. J. Klafter, I. M. Sokolov, *First Steps in Random Walks: From Tools to Applications* (Oxford Univ. Press, Oxford, 2011).
6. V. Mendéz *et al.*, *Stochastic Foundations in Movement Ecology: Anomalous Diffusion, Front Propagation and Random Searches* (Springer, Heidelberg, 2014).
7. R. Nathan, *Science* **313**, 786 (2006).
8. J. Muñoz *et al.*, *Science* **304**, 1144 (2004).
9. R. Nathan *et al.*, *Trends Ecol. Evol.* **23**, 638 (2008).
10. M. Thiel, L. Gutow, *Oceanogr. Mar. Biol.* **42**, 181 (2005).

10.1126/science.1250904

EXHIBITION

"Nature and Art Beneath One Roof"

Natural Histories
A Project

by Miguel Ángel Blanco
Museo Nacional del Prado, Madrid. Through 27 April 2014. https://www.museodelprado.es/en/exhibitions/exhibitions/at-the-museum/historias-naturales

Charles III of Spain (1716–1788) was at heart a scientist. As an Enlightenment despot, he conceived the museum of the Prado in Madrid as a place where arts and sciences would be united. Unfortunately, his death and the Peninsular War (1808–1814) intervened, and his original notion of a royal natural history cabinet was eclipsed by the magnificence of Spanish and Netherlandish paintings. Perhaps it's arrogant to try to resurrect the notion of the Prado as a cabinet of curiosities, but contemporary Spanish artist Miguel Ángel Blanco has had the temerity to insert a selection of installations of natural objects in direct response to the great paintings.

Blanco has emplaced his 22 "interventions" with delicacy, because after all most visitors come to puzzle over Velázquez's *Las Meninas* and do not want to be distracted by an albino sparrow. Or they would prefer to sorrow with Juan de Flandes' *Crucifixion* rather than inspect the gems at the foot of the cross. Nor would they want to be long deflected from Goya's stunning *Witches' Sabbath* to admire the anatomy of the hags' familiars (bat skeleton, cobra, toads, salamander, and moose hoof) displayed, many in jars of formalin, below. Although the stuffed Veragua bull staring at its feminine counterpart in Peter Paul Rubens' *Rape of Europa* certainly has presence and the wolf-whistle calls of birds of paradise giving voice to Frans Snyders' *Concert of Birds* do echo down the long gallery, maybe the intrusions are too polite. And I am not sure Blanco's approach entirely works—in part, because his pieces are so dwarfed by the splendor of the Prado's permanent collection. Nevertheless, his project succeeds in prompting visitors to look again and to notice how very often natural objects were used as props and symbols in great paintings by grand masters.

– Caroline Ash

10.1126/science.1253427

CREDIT: PEDRO ALBORNOZ/MUSEO NACIONAL DEL PRADO

Miguel Ángel Blanco's *The Veragua Bull*. Rubens' *The Rape of Europa* (1628–29) and *Bos taurus*.

EDUCATION TECHNOLOGY

Computer-Guided Inquiry to Improve Science Learning

Automated guidance on essays and drawings can improve learning in precollege and college courses.

Marcia C. Linn[1]*, Libby Gerard[1], Kihyun Ryoo[2], Kevin McElhaney[3], Ou Lydia Liu[4], Anna N. Rafferty[5]

Engaging students in inquiry practices is known to motivate them to persist in science, technology, engineering, and mathematics (STEM) fields and to create lifelong learners (*1*, *2*). In inquiry, students initiate investigations, gather data, critique evidence, and make sophisticated drawings or write coherent essays to explain complex phenomena. Yet, most instruction relies on lectures that transmit information and multiple-choice tests that determine which details students recall. Massive Open Online Courses (MOOCs) mostly offer more of the same. But new cyber-learning tools may change all this, by taking advantage of new algorithms to automatically score student essays and drawings and offer personalized guidance.

Empowering Learners, Aiding Instructors

Inquiring students make predictions, gather new ideas (from investigations, visualizations, or observations); use evidence to distinguish among their predictions and ideas; and create a coherent explanation (*1*, *3*, *4*). When they write explanations, students learn more than when they select among multiple-choice answers or read explanations (*5*). Experimenting with visualizations and making drawings to illustrate ideas can develop students' spatial-reasoning skills (*6*). And, when students analyze resources to develop an explanation, they appreciate the beauty and complexity of new fields (*7*).

Analyzing students' essays or drawings and using the results to guide them can improve outcomes (*8*), but this requires more human capital than precollege and college instructors have. Precollege instructors often have five or six classes of 30 to 40 students, and college instructors may have hundreds or thousands of students in required courses or MOOCs.

However, advances in computer technologies may help offset limits in instructor time and effort. Immediate, personalized, computer-generated guidance can motivate students to deepen their understanding of complex materials. Instructors can review the automated scores to identify students who continue to flounder. Because these systems can assign guidance to every student, even students who are reluctant to ask for help can progress.

[1]Graduate School of Education, University of California Berkeley, Berkeley, CA 94720, USA. [2]School of Education, University of North Carolina, Chapel Hill, Chapel Hill, NC 27599, USA. [3]SRI International, Menlo Park, CA 94025, USA. [4]Educational Testing Service, Princeton, NJ, 08541, USA. [5]Computer Science Division, University of California Berkeley, Berkeley, CA 94720, USA. *Corresponding author. mclinn@berkeley.edu

Automated guidance was as effective as guidance provided by an expert teacher.

To make sure that inquiry activities lead to new insights and not to erroneous or superficial conjectures, experienced teachers monitor student progress and regularly add hints to keep students on the right track (*3*, *4*, *9*) (see the first figure). To figure out what hints will help students explore a complex problem, researchers and teachers (often collaboratively in professional development programs) analyze large numbers of student essays or drawings and try out alternative approaches (*3*). Online learning environments like the Web-based Inquiry Science Environment (WISE) streamline this process by recording student ideas and supporting experiments for which researchers can randomly assign diverse forms of guidance.

These experiments show that guidance encouraging students to distinguish among their predictions and new evidence helps students to better integrate their ideas about the topic (*9*). Once the links between student responses and effective guidance are established, environments like WISE can score student essays or drawings and automatically assign guidance designed to help students develop coherent explanations.

Guiding Writers, Drawers, and Teachers

Advances in natural language processing now enable computer-based learning environments to use scored answers to create systems for scoring future responses. For instance, the Educational Testing Service's (ETS) "c-rater" tool used human-rated responses to develop

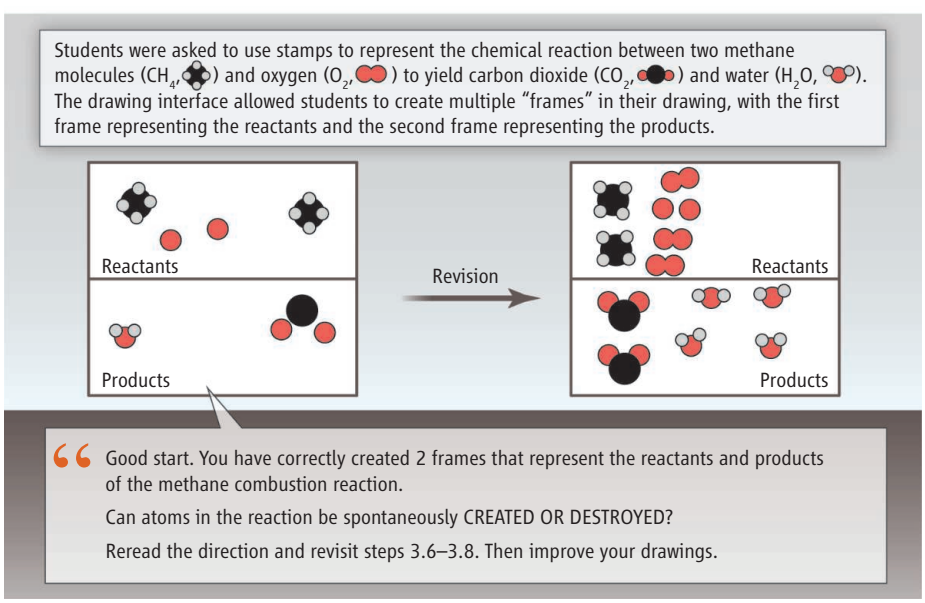

Computerized hints to improve understanding. Student response to the chemical reactions item that WISE can automatically score. Automated guidance was as effective as guidance provided by an expert teacher. [Adapted figure, based on WISE]

Published by AAAS

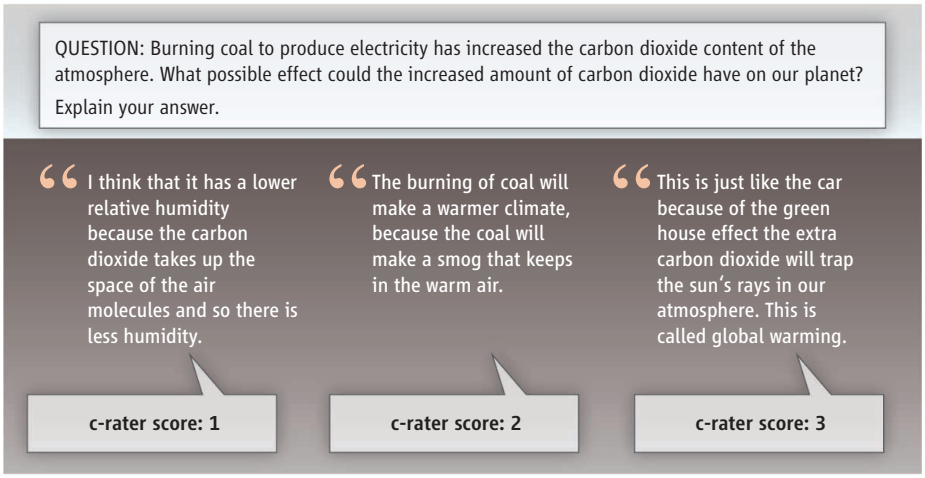

Computer evaluation of written answers. Student response to the coal item that c-rater can automatically score. Guidance that encourages students to look at relevant evidence and revise their ideas can be associated with these scores. [Figure based on c-rater]

an automated scoring system for an activity aimed at figuring out how burning coal to produce electricity affects the environment (*10*) (see the second figure). The c-rater system successfully scored new responses [inter-rater agreement reflected by κ coefficient = 0.87 (*10*)]. WISE can use these scores to assign personalized guidance while students are learning. Similarly, Writing-Pal (*11*) analyzes writing quality and recommends strategies for strengthening the essay (e.g., "think about the quality of your evidence") rather than identifying distinct errors. Students using Writing-Pal substantially improved their essays by elaborating content, improving paragraph structure, and using more precise vocabulary (*11*).

AutoTutor prompts students to explain their reasoning about how to solve a physics problem through a written dialogue with a computer avatar. The computer analyzes students' explanations for misconceptions and asks questions designed to elicit better explanations. This guidance was more effective than studying a well-written text on conceptual physics for improving physics problem-solving (*12*). Although automated scoring algorithms for written responses must be tailored to individual questions, this process can be as simple as providing the system with about 500 to 1000 existing human-scored responses and desired guidance messages.

Computers can analyze human-scored drawings to create systems that can then score subsequent drawings and provide feedback automatically (*13*) (see the first figure) (Fig. 2). For instance, in a classroom study, automated guidance was highly accurate and as effective as teacher-provided guidance for stimulating understanding of chemical reactions (*13*). Similarly, ASSISTments researchers found that proficient students could take advantage of receiving annotated solutions to math problems, designed by an expert instructor but chosen and offered by a computer, to improve their performance on future problems. Less-proficient students benefitted from automated guidance that emulated an expert teacher by asking questions but not giving answers (*14*). In addition, when using Betty's Brain, students constructed more accurate concept maps (diagrams showing relations between concepts) when they received conceptual guidance than when they received explicit directions (*15*). These studies support the value of guidance that encourages students to reconsider their ideas rather than telling them the right answer.

Teachers report spending up to 10 min to compose detailed guidance for each work group doing an inquiry activity and at least 2 min per work group assigning premade comments (*13*). When guidance is automated, teachers can instead concentrate on students the computer identifies as not making progress. Teachers can also review automated scores to gauge overall class progress or to design activities that address specific conceptual difficulties. Instructors can use student responses immediately to adjust their instruction and annually to revise courses for the next group of students.

The Need for Design and New Research

Inquiry activities in which students grapple with open-ended questions and come up with novel solutions are now feasible in large classes and MOOCs by taking advantage of automated scoring and guidance. Of course, instructors still need to design the inquiry activities, scoring rubrics, and guidance. The computer only assigns the guidance.

These technologies open up exciting opportunities. Writing explanations for complex phenomena can help students develop greater understanding in STEM and language arts. As advances increase the precision of scoring technologies, assessments featuring written work and drawings can replace detail-oriented multiple-choice questions. Adding drawing activities can help students who lack proficiency in reading and writing to explain their ideas. These technologies also raise crucial research questions including how best to design guidance and whether automated guidance works for all students. Research can help determine ways to speed up the process of creating new inquiry activities and associated automated guidance.

These findings illustrate the need for open-source learning environments that support inquiry and can be widely used in typical courses. For example, automated guidance could improve performance and sustain participation in MOOCs. Adding inquiry features and guidance to support learners' investigations should be a high priority for designers of learning environments.

References and Notes

1. National Research Council, *Taking Science to School*, R. A. Duschl, H. A. Schweingruber, A. W. Shouse, Eds. (National Academies Press, Washington, DC, 2007).
2. Next Generation Science Standards (Achieve, Inc., Washington, DC, 2013); www.nextgenscience.org/.
3. M. C. Linn, B.-S. Eylon, *Science Learning and Instruction* (Lawrence Erlbaum, Mahwah, NJ, 2011).
4. J. Osborne, *Science* **328**, 463–466 (2010).
5. K. Ryoo, M. C. Linn, *J. Res. Sci. Teach.* **51**, 147–174 (2014).
6. D. H. Uttal, D. I. Miller, N. S. Newcombe, *Curr. Dir. Psychol. Sci.* **22**, 367–373 (2013).
7. S. Wineburg, M. Smith, J. Breakstone, *Soc. Educ.* **76** (*6*), 288–291 (2012).
8. K. VanLehn, *Ed. Psychol. (Bern)* **46**, 197–221 (2011).
9. S. Sisk-Hilton, *Teaching and Learning In Public: Professional Development Through Shared Inquiry* (Teachers College Press, New York, 2009).
10. O. L. Liu, *et al.*, *Educ. Measure. Issues Pract.* 10.1111/emip.12028 (2014).
11. R. D. Roscoe, D. S. McNamara, *J. Ed. Psychol.* 10.1037/a0032340 (2013).
12. A. C. Graesser, *et al.*, *Behav. Res. Methods Instrum. Comput.* **36**, 180–192 (2004).
13. A. N. Rafferty, L. F. Gerard, K. McElhaney, M. C. Linn, in *Proceedings of the Workshops at the 16th International Conference on Artificial Intelligence in Education*, vol. 8, E. Walker, C.-K. Looi, Eds., Memphis, TN, 13 Jul 2013 (AIED, 2013), pp. 612–619.
14. L. M. Razzaq, N. T. Heffernan, in *Proceedings of the 2009 Artificial Intelligence in Education Conference*, V. Dimitrova, R. Mizoguchi, B. du Boulay, A. C. Graesser, Eds., Brighton, UK, 6 to 10 July 2009 (IOS Press, Amsterdam, 2009), pp. 457–464.
15. J. R. Segedy, J. S. Kinnebrew, G. Biswas, *Educ. Technol. Res. Dev.* **61**, 71–89 (2013).

Acknowledgments: This material is based on work supported by the NSF under grant no. DRL-1119670. Any opinions, findings, and conclusions or recommendations expressed in this material are those of the author and do not necessarily reflect the views of the NSF.

10.1126/science.1245980

NEUROSCIENCE

An Olfactory Critical Period

A critical period of plasticity allows neuronal circuitry of the mammalian olfactory system to develop.

Claire E. Cheetham and Leonardo Belluscio

During development of the mammalian nervous system, initially imprecise neuronal connections are refined to generate mature, accurately wired circuits that support perception, cognition, and behavior. This developmental refinement typically depends on neuronal activity; hence, most sensory systems exhibit "critical periods" of heightened sensitivity to sensory experience. By contrast, the olfactory system retains high levels of plasticity throughout life, and there is mixed evidence as to the existence of critical periods. On pages 197 and 194 of this issue, Tsai and Barnea (*1*) and Ma *et al*. (*2*), respectively, support the existence of an unconventional, experience-independent, critical period for the mammalian olfactory system.

Mammals detect odors when the molecular constituents of an odor bind to odorant receptors expressed by olfactory sensory neurons (OSNs) in the nasal epithelium. The axons of these OSNs project directly to the olfactory bulb, where they form spherical structures called glomeruli (see the figure). Each OSN expresses just one type of olfactory receptor, and the axons of OSNs that express the same receptor project to the same glomerulus (convergence), producing a highly organized glomerular map. In the mouse, this map forms and refines during late embryonic and early postnatal life; the timing of maturation of individual glomeruli depends in part on odorant receptor identity. Because OSNs undergo continuous, lifelong turnover, maintaining the organization of the glomerular map poses a particular challenge.

Tsai and Barnea and Ma *et al*. both used a genetic approach in mice to induce the expression of different proteins in OSNs that disrupted the glomerular map. As a result, OSN axons expressing a particular odorant receptor innervated multiple glomeruli rather than just one specific glomerulus into adulthood. Tsai and Barnea investigated the time window during which establishment of the map could be disrupted by allowing it to develop normally through embryogenesis and then switching on expression of the transgene (encoding the disruptive protein) postnatally. They found that transgene expression rarely disrupted glomerular convergence even when expression was switched on at or shortly after birth, and never disrupted it when expression began after the first postnatal week. This implies that if a normal map forms initially, it can be reestablished even after the first postnatal week following ablation of the vast majority of OSNs (regenerating OSN axons can still converge on the appropriate glomeruli). Hence, glomerular map organization becomes immutable in early postnatal life, although the timing of development of individual glomeruli (*3*) may influence precisely when this occurs.

Ma *et al*. took a complementary approach by disrupting initial map formation and assessing the ability of the map to recover when transgene expression was then switched off. Glomerular maps could recover to a completely normal state when transgene expression ended at or shortly after birth. However, when expression continued beyond postnatal day 5, the map persisted in its disrupted state even several weeks later. Notably, similar developmental profiles were seen for three different methods of map disruption, and for OSN axons expressing three different odorant receptors, suggesting a uniform early postnatal time period beyond which glomerular maps cannot recover. Tsai and Barnea also found that disrupted maps could not recover in adult mice; even when OSNs were chemically ablated at the same time that transgene expression was switched off, the regenerating OSN axons still formed a disrupted map. Together, the studies of Tsai and Barnea and Ma *et al*. illustrate an abrupt developmental decline in glomerular map plasticity in early postnatal life. This provides an attractive model by which glomerular stability can be maintained in the face of the constant plasticity that results both from OSN turnover and the ongoing influx of newborn interneurons into the olfactory bulb. However, this perinatal period of heightened plasticity, unlike classical critical periods, does not depend on sensory input.

What factors, then, are required for accurate glomerular map formation? It may be that neuronal activity per se, rather than sensory input, is essential. Indeed, the main manipulation used by Ma *et al*. to disrupt map formation was suppression of OSN activity. However, studies using different forms of activity

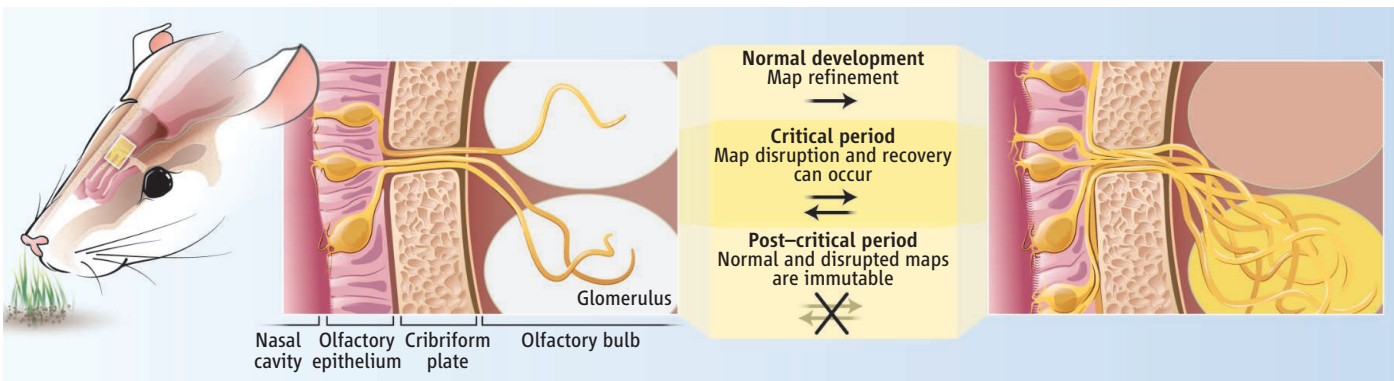

The glomerular map. The olfactory system of the mouse requires neurons expressing the same odorant receptor to converge on the same structure (glomerulus) in the olfactory bulb. This convergence can be disrupted and then recover during a critical period, but map organization is immutable after critical period closure.

CREDIT: V. ALTOUNIAN/*SCIENCE*

Developmental Neural Plasticity Section, National Institute of Neurological Disorders and Stroke, National Institutes of Health, 35 Convent Drive, Bethesda, MD 20892, USA. E-mail: belluscl@ninds.nih.gov

Published by AAAS

manipulations have provided mixed results (*4*, *5*), leaving the role of neuronal activity still unclear. Odorant receptor expression is another likely candidate, as both Tsai and Barnea and Ma *et al*. show that widespread expression of a transgene that encodes an odorant receptor disrupts convergence of other axons that express the same receptor. By comparison, if widespread receptor expression begins in immature OSNs, then greater map alterations are observed and convergence is also disrupted in axons that express a different odorant receptor (*6*). This suggests that the scale of disruption may also affect map regeneration. In support of this, the P2 glomerulus could form de novo even after the first postnatal week following ablation of OSNs expressing the P2 receptor (*7*). However, as Ma *et al*. show, the P2 glomerulus could not recover after postnatal day 3 following more widespread disruption.

Recovery capacity may also vary between odorant receptors. Following map disruption by broadly expressing the amyloid precursor protein (APP) in OSNs, P2 glomeruli failed to recover after the APP-encoding transgene was switched off whereas M71 glomeruli could form again (*8*), further suggesting that the method of disruption may play a role. Another factor to consider is time and the concomitant OSN turnover. It remains possible that some recovery can occur after the perinatal critical period, but is much slower.

Many factors are likely to interact during glomerular map formation and maintenance, highlighting the need for further investigation. Nevertheless, the studies by Tsai and Barnea and Ma *et al*. suggest that regeneration differs fundamentally from initial olfactory circuit formation, relying on some form of positional cue that arose during prior map formation. This has important implications when considering the regeneration potential of the adult brain.

References

1. L. Tsai, G. Barnea, *Science* **344**, 197 (2014).
2. L. Ma *et al.*, *Science* **344**, 194 (2014).
3. S. M. Potter *et al*., *J. Neurosci.* **21**, 9713 (2001).
4. C. Zheng *et al*., *Neuron* **26**, 81 (2000).
5. D. M. Lin *et al*., *Neuron* **26**, 69 (2000).
6. M. Q. Nguyen *et al*., *J. Neurosci.* **30**, 9271 (2010).
7. J. A. Gogos *et al*., *Cell* **103**, 609 (2000).
8. N. Cheng *et al*., *J. Neurosci.* **33**, 12208 (2013).

10.1126/science.1253136

BOTANY

Patterning Cues from the Altruistic Sibling

The endosperm acts as a signaling hub to orchestrate developmental processes in the *Arabidopsis* seed.

Martin Bayer

Double fertilization is a key feature of flowering plants. One sperm cell from the pollen grain fertilizes the egg cell to form the embryo while the other sperm fuses with a second female gamete, called the central cell. The second fertilization event gives rise to the endosperm, long thought to be mainly a nourishing tissue supporting the developing embryo or the germinating seedling (*1*). In this issue, Costa and co-workers report on page 168 that in *Arabidopsis thaliana* the endosperm also provides crucial signals for the apical-basal patterning process of the embryo (*2*).

In *Arabidopsis*, the fertilized egg cell or zygote elongates and divides asymmetrically to give rise to a smaller apical cell and a larger basal cell. While the smaller cell develops into the embryo proper, providing most of the later seedling, the larger basal cell forms a filamentous structure called the suspensor (*3*). The suspensor positions the embryo within the seed and serves as a conduit for nutrients and hormones (*4*).

Generally, three developmental pathways have so far been implicated in the apical-basal patterning of the early *Arabidopsis* embryo: (i) a mitogen-activated protein kinase (MAPK) pathway including the MAPK kinase kinase (MAPKKK) YODA (YDA), which promotes suspensor identity; (ii) a transcriptional network of WUSCHEL-RELATED HOMEOBOX (WOX) transcription factors, which is important for both apical and basal cell identity; and (iii) auxin signaling, which confers apical cell identity after the first zygotic cell division and is later involved in embryonic root formation (*3*). Because these three pathways in principle act in the embryo, it might not be surprising that little attention has been paid to the role of the endosperm in this process.

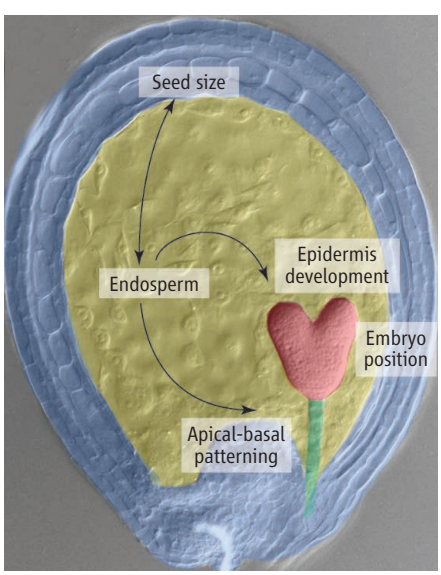

Endosperm as coordinator of seed development. Embryo proper (red), suspensor (green), endosperm (yellow), and maternal seed coat (blue) are false-colored for illustration.

Costa *et al*. now report that the endosperm has a profound influence on the patterning process of the embryo. They describe a small group of cysteine-rich peptides, termed EMBRYO SURROUNDING FACTOR 1 (ESF1). *ESF1.1* to *ESF1.3* are reported to be exclusively expressed in the central cell and the endosperm and to promote suspensor formation in the adjoining embryo in a non–cell-autonomous fashion. Genetic data tentatively place the ESF1 peptides upstream of the MAPKKK YDA, making these prime candidate ligands of a yet unknown receptor complex that positively regulates YDA activity. In addition, the authors report changes in auxin response as well as in the expression pattern of WOX genes in the embryo upon down-regulation of *ESF1* expression in the endosperm. These changes in apical-basal patterning in the embryo could be the result of altered YDA signaling, or they may reflect additional YDA-independent functions of the ESF1 peptides. Under certain in vitro conditions, microspore-derived embryos can reproduce the early division pattern of zygotic embryos in culture without surrounding endosperm (*5*). It will

Department of Cell Biology, Max Planck Institute for Developmental Biology, 72076 Tübingen, Germany. E-mail: martin.bayer@tuebingen.mpg.de

therefore be interesting to see in future studies how the ESF1 peptides contribute mechanistically to the apical-basal patterning process and whether temporal or spatial information is transduced by these signals.

Cell-to-cell signaling is a universal mechanism in plant development, and signals from the endosperm have been implicated in several developmental processes in the seed (*6*–*8*). Although the precise genetic program is not yet clear, there is increasing evidence that the endosperm is involved in epidermis specification during embryogenesis (*7*). Loss of a subtilisin-like protease in the endosperm or loss of candidate receptor kinases in the embryo lead to epidermal defects, strongly suggesting an involvement of endosperm-derived peptide signals in controlling epidermal cell identity.

Angiosperm seeds consist principally of three distinct compartments: the embryo, the endosperm, and the maternal seed coat. In recent years, it has become clear that the growth of these structures is coordinated and that the endosperm has a profound impact on seed size (*9*). The discovery of the ESF1 peptides demonstrates that the endosperm also influences suspensor proliferation. By regulating suspensor length, ESF1 signaling might ensure an optimal position of the embryo within the surrounding endosperm, which seems to be crucial for fast developmental progression of the embryo (*10*).

Signals from the endosperm regulate the coordinated growth of the seed and influence the development and patterning of the embryo and the suspensor. In this emerging picture, the endosperm seems to play a central role as a signaling hub to orchestrate various growth processes in the seed. Cysteine-rich peptides are a large class of potential receptor ligands that have an important function in diverse developmental processes (*8*). Given the temporal expression changes of many genes coding for such peptides during seed development (*2*), a broader role for these ligands in coordinating growth processes in the seed appears to be likely.

References

1. P. Maheshwari, *An Introduction to the Embryology of Angiosperms* (McGraw-Hill, New York, 1950).
2. L. M. Costa *et al.*, *Science* **344**, 168 (2014).
3. S. Lau *et al.*, *Annu. Rev. Plant Biol.* **63**, 483 (2012).
4. T. Kawashima, R. B. Goldberg, *Trends Plant Sci.* **15**, 23 (2010).
5. E. D. Supena *et al.*, *J. Exp. Bot.* **59**, 803 (2008).
6. I. De Smet *et al.*, *Nat. Cell Biol.* **11**, 1166 (2009).
7. M. Javelle *et al.*, *New Phytol.* **189**, 17 (2011).
8. E. Marshall *et al.*, *J. Exp. Bot.* **62**, 1677 (2011).
9. J. Li, F. Berger, *New Phytol.* **195**, 290 (2012).
10. Y. Babu *et al.*, *Plant Physiol.* **162**, 1448 (2013).

10.1126/science.1252985

ASTRONOMY

Pulsar Beams—Big and Bright

Recent studies of gamma-ray beams emitted from rotating neutron stars are providing a better understanding of the mechanism underlying pulsars.

Roger W. Romani

The standard picture of a pulsar, or rotation-powered neutron star, has narrow beams of radiation lancing out of the magnetic poles and sweeping across the sky as the star spins. For nearly 50 years, astronomers have been observing radio flashes from these objects and, on the whole, this lighthouse model does a good job of explaining pulsar phenomenology. However, we have not fully deciphered the pulsar mechanism—although we understand how pulsars pulse, we still seek to understand how they shine.

When gamma-ray pulses were seen from the Crab and Vela pulsars in 1974 and 1975, it was thought that this would advance our understanding. Unlike the energetically small radio beacons, the gamma rays represent several percent of the pulsars' mechanical energy loss and thus provide a more robust probe of particle acceleration within the pulsar.

It was, and is, widely believed that the coherent radio emission arises from instabilities in a dense plasma of electron-positron pairs in auroral zones just above the magnetic poles. The high-energy processes generating these pairs must inevitably produce gamma rays as well, and so it was natural to identify the observed gamma-ray pulsations with this polar cap zone. One complication was that, while for the Crab the gamma-ray beams followed the radio emission, for Vela the pulse structure was quite different, with a double pulse well offset from the single radio beacon. Of course, models were proposed to interpret these data, but two contradicting examples left the situation unclear.

The launch of the Energetic Gamma Ray Experiment Telescope (EGRET) on NASA's Compton Gamma Ray Observatory in 1991 allowed detection of a half-dozen additional pulsars, with a variety of gamma-ray pulse shapes. None followed the radio emission patterns. Even more important, aided by an x-ray observation (*1*), EGRET was able to find pulsations from a long-known mysterious gamma-ray source, Geminga. Here was a spin-powered neutron star, with a typical double gamma ray pulse, but no radio emission visible at all. These data led us (*2*) to argue that the gamma rays are produced in a zone well separated from the radio-emitting polar cap. The best model had wide fans of gamma-ray emission arising near the so-called light cylinder radius, where particles attempting

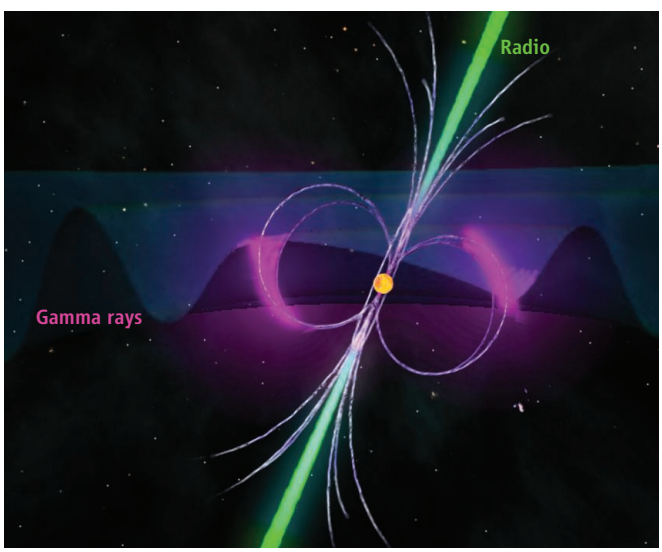

Beaming broad and bright. The neutron star is surrounded by dipolar magnetic field lines, which extend to the light-cylinder radius. The narrow radio beams (green) arise near the surface and propagate along the magnetic axes. Gamma rays are generated high in the magnetosphere (magenta) and are directed in broad beams toward the spin equator. This gamma-ray emission may extend even beyond the light cylinder into the magnetic wind, whose separatrix layer is indicated by the waving blue surface, extending away from the pulsar.

CREDIT: CRUZ DEWILDE, AVANT GRAVITY/ROGER W. ROMANI, STANFORD

Department of Physics and Kavli Institute for Particle Astrophysics and Cosmology, Stanford University, 382 Via Pueblo Mall, Stanford, CA 94305–4060, USA. E-mail: rwr@astro.stanford.edu

to corotate with the spinning pulsar would be forced to travel at relativistic speeds.

Beyond the light cylinder, the magnetosphere opens up to a transition zone through which the relativistic particles and magnetic fields flow in an energetic pulsar wind. This picture implies that the gamma-ray beams should be big, sweeping a different, and substantially larger, region of the sky than the radio beacons, and should be bright, carrying a substantial fraction of the pulsar's spin-down power.

The Large Area Telescope (LAT) on NASA's Fermi Gamma-Ray Space Observatory has now taken the crucial next step, detecting nearly 150 spin-powered pulsars, including large numbers of Geminga-like pulsars visible only via their gamma-ray beams (*3*, *4*). Even after 5 years, gamma-ray pulsar discoveries continue, with increasing numbers of millisecond period recycled pulsars, for which the magnetospheres extend only a few times the neutron star radius (*5*). The consensus view now is that gamma-ray emission is a high-altitude phenomenon and that the wide gamma-ray beams located toward the spin equator (*6*) are generally well separated from the radio axis (see the figure). The gamma-ray power of these outer magnetosphere beams appears to require as much as a third of the spin-down energy budget. This suggests that the gamma-ray–producing particle accelerator imposes large torques at the light cylinder and that its energization accounts for much of the spin-down luminosity. Detailed numerical models incorporating such torques and the currents that generate them are being pursued (*7*, *8*). In these models, the accelerator/emission zone can in fact extend somewhat beyond the light cylinder radius, into the wind zone.

The host of Fermi pulsar discoveries can be attributed to these big, bright gamma-ray beams, and the detailed study of the Fermi pulse shapes and phase-resolved spectral variations provides new hope for reverse-engineering the pulsar machine to reveal the electrodynamics of these extreme particle accelerators. What of the energetically unimportant, but extremely useful, radio-pulse sideshow? Here, too, gamma-ray studies can help. Production of the radio pair plasma should be accompanied by gamma-ray photons. Efforts are under way to improve the LAT sensitivity, especially at low energy (*9*). This enhancement would allow us to search for small, gamma-ray faint pair production regions from the near-surface polar cap zone. The hope is that the radio-producing cap accelerators can then join their big, bright outer magnetosphere cousins in the gamma-ray sky.

References

1. J. P. Halpern, S. S. Holt, *Nature* **357**, 222 (1992).
2. R. W. Romani, I. A. Yadigaroglu, *Astrophys. J.* **438**, 314 (1995).
3. A. A. Abdo *et al*., *Science* **325**, 840 (2009).
4. A. A. Abdo *et al*., *Astrophys. J. Suppl. Ser.* **208**, 17 (2013).
5. P. A. Caraveo, http://xxx.lanl.gov/abs/1312.2913 (2013).
6. K. P. Watters, R. W. Romani, *Astrophys. J.* **727**, 123 (2011).
7. X.-N. Bai, A. Spitkovsky, *Astrophys. J.* **715**, 1282 (2010).
8. C. Kalapotharakos *et al*., http://xxx.lanl.gov/abs/1310.3545 (2013).
9. W. Atwood *et al*., http://xxx.lanl.gov/abs/1303.3514 (2013).

10.1126/science.1251943

PHYSICS

The Advantages of Extra Entanglement

An ensemble of 40 ultracold atoms forms an entangled state when just one of the atoms is excited.

Artur Widera

The development of quantum physics has led to a revolution in modern technology and lies at the heart of applications in communication, computation, medicine, and navigation. Fragile quantum correlations, known from Einstein's infamous wording as "spooky action at a distance," point to novel ways to compute even faster or communicate more securely. Although the original two-particle entangled states following the seminal paper by Einstein, Podolsky, and Rosen (*1*) are well understood and can be routinely prepared in experiments, many-particle entangled states are in general hard to describe theoretically or to produce experimentally. The increasing fragility of quantum states with increasing numbers of atoms makes macroscopic entanglement rare. On page 180 of this issue, Haas *et al*. (*2*) have demonstrated the creation of a robust entangled state of more than 40 ultracold atoms within a single operation. Their method relies on a simultaneous, coherent interaction with the light field of a high-finesse optical cavity to reveal the presence of only a single atom with a different internal state.

Approaches to engineering large-scale entangled quantum states in atomic systems typically fall into two different categories. A bottom-up approach uses single, highly controllable particles, such as cold trapped ions. Quantum states can be assembled atom by atom, and entanglement of a steadily increasing number of ions has been achieved (*3*) up to a number of 14 (*4*). Current efforts aim to increase the number of entangled particles while maintaining exceptionally good control over the individual ion. In a top-down approach, quantum many-body systems such as Bose-Einstein condensates form the starting point. Here, thousands of atoms share the same quantum state. Specifically engineered interactions can drive a time evolution to entangled states of large numbers of particles (*5*–*7*), but examples of control over individual particles have been scarce.

Haas *et al*. have chosen a combination of both approaches to realize many-particle entanglement that is in principle scalable to larger numbers of particles. The atomic system is in a many-body state and there is hardly any control over individual atoms, but they have exceptionally good detection capability of atomic excitations in their cavity. Even a single quantum of excitation, corresponding to a single excited atom, can be detected.

In this system, quantum entanglement comes naturally into play. For N indistinguishable particles all sharing the same quantum state, a single excitation—adding one quantum of energy resonant to an atomic transition—would lead to an apparent ambiguity: The excitation is quantized and cannot be distributed in smaller parts over all particles of the system, but all particles are indistinguishable, and there is no reason why one in particular should be excited. The quantum system's solution is entanglement, a coherent superposition state $|\psi\rangle$ of all possible combinations that place one quantized excitation in the excited state

$$|\psi\rangle=\frac{1}{\sqrt{N}}\left(|100\ldots00\rangle+|010\ldots00\rangle+\ldots+|000\ldots01\rangle\right)$$

Physics Department and Research Center OPTIMAS, Kaiserslautern University, Erwin-Schrödinger-Str., 67663 Kaiserslautern, Germany. E-mail: widera@physik.uni-kl.de

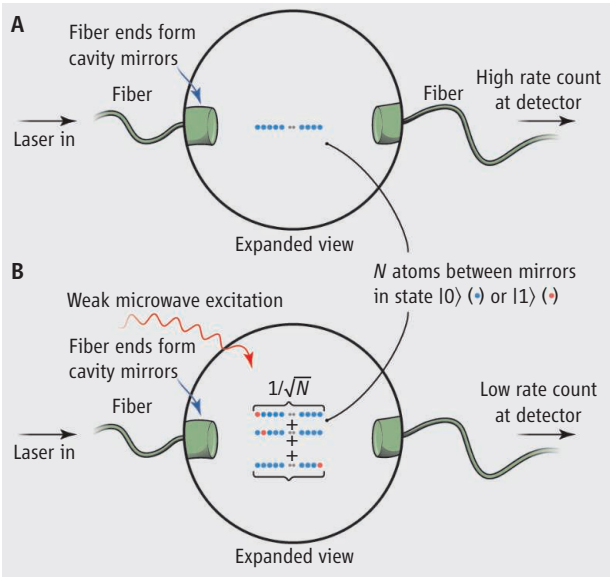

How darkness sheds light on entanglement. (**A**) An ensemble of N atoms in their internal ground state (blue) is transparent to a light field resonant with the cavity formed by the ends of two fibers (green). As a result, the photon count rate detected through one of the fibers is "high." (**B**) Upon irradiation with a weak microwave field, exciting atoms to another hyperfine state (red), a single excitation in the ensemble renders the resonator opaque. The corresponding photon count rate is "low" and indicates an entangled atomic state in the resonator.

where $|0\rangle$ denotes a particle in the ground state and $|1\rangle$ denotes the excited particle. This state, called the W state in quantum information processing and the Dicke state in quantum optics, is rather robust against decoherence relative to other entangled states, such as Schrödinger's-cat states or Greenberger-Horne-Zeilinger (GHZ) states, the many-particle generalization of Einstein-Podolsky-Rosen pairs.

Preparation of indistinguishable particles in a Bose-Einstein condensate is routinely performed in laboratories worldwide, and excitations of the atoms' hyperfine states can be achieved with microwave fields. The key question, then, is "When has a single excitation entered the system?" Haas *et al*. tackled this problem using a high-finesse optical cavity formed by two opposing mirrors at the ends of optical fibers. Photons typically bounce between these mirrors more than 10,000 times. Precisely tuning the resonator length to the wavelength of a weak impinging laser beam leads to light transmission with a small line width. Such a resonator is extremely amenable to even the slightest change of refractive index of its contents. In fact, a single atom in an excited state changes the effective optical path length for the light field sufficiently to render the resonator opaque, while atoms in other internal states are transparent for the light field. Thus, even for many atoms in one internal state, the laser beam is fully transmitted, but if an external microwave field injects just a single excitation, the transmission vanishes, heralding the presence of the entangled W state (see the figure).

Full information about a quantum state—even about a single quantum system—is in general not available from a single measurement. Rather, a whole series of measurements must be performed to extract the so-called density matrix that contains all state populations as well as coherence and correlation properties of the quantum state. For an increasing number of atoms, this task becomes harder because the number of values to be determined scales as $2^N \times 2^N$, which becomes a large number even for small numbers of particles (*8*). Instead, Haas *et al*. considered only a relevant subpart of the full density matrix spanned by symmetric Dicke-type states with varying numbers of excitations shared. By first manipulating the prepared quantum state via microwave fields and subsequently checking for the presence of excitations, they determined the overlap of the state prepared with one of the Dicke states.

Research into larger and other entangled states not only drives the development of emerging quantum applications; it elucidates the fundamental question, "Why does quantum physics explain perfectly everything we know about the microscopic world but is never observed in our everyday macroscopic life?" Only with experiments creating and analyzing larger and larger entangled states will we be able to track, and perhaps steer, the quantum-to-classical transition.

References

1. A. Einstein, B. Podolsky, N. Rosen, *Phys. Rev.* **47**, 777 (1935).
2. F. Haas *et al*., *Science* **343**, 180 (2014); 10.1126/science.1248905.
3. R. Blatt, D. Wineland, *Nature* **453**, 1008 (2008).
4. T. Monz *et al*., *Phys. Rev. Lett.* **106**, 130506 (2011).
5. O. Mandel *et al*., *Nature* **425**, 937 (2003).
6. J. Estève, C. Gross, A. Weller, S. Giovanazzi, M. K. Oberthaler, *Nature* **455**, 1216 (2008).
7. M. F. Riedel *et al*., *Nature* **464**, 1170 (2010).
8. H. Häffner *et al*., *Nature* **438**, 643 (2005).

10.1126/science.1251472

MATERIALS SCIENCE

Materials both Tough and Soft

Jian Ping Gong

Tough elastomers are created by adapting an approach previously used for hydrogels.

Hydrogels and elastomers are soft materials that have similar network structures but very different affinities to water. Consisting mostly of water, hydrogels resemble biological soft tissues and have great potential for use in biomedical applications; they tend to be very brittle, like fragile jellies. Elastomers are formed of nonhydrated polymer networks and are widely used as load-dispersing and shock-absorbing materials. They are stretchable but break easily along a notch. On page 186 of this issue, Ducrot *et al*. (*1*) show that the toughness of elastomers can be improved substantially by combining two different network materials, an approach previously applied to hydrogels.

Double-network hydrogels contain 80 to 90 weight percent (wt %) of water, yet are both hard and strong, with mechanical properties comparable to that of rubbers and cartilages (*2*, *3*). The gels consist of two interpenetrating polymer networks with contrasting mechanical properties. The first network is highly stretched and densely cross-linked, making it stiff and brittle. The second network is flexible and sparsely cross-linked, making it soft and stretchable.

The toughness of a material is its ability to absorb mechanical energy and deform without fracturing. One definition of material toughness is the fracture energy, which is the energy per unit area required to make

Faculty of Advanced Life Science, Hokkaido University, Sapporo, 060-0810, Japan. E-mail: gong@mail.sci.hokudai.ac.jp

a notched crack propagate. Double-network gels are tough because the internal fracture of the brittle network dissipates substantial amounts of energy under large deformation, while the elasticity of the second network allows it to return to its original configuration after deformation. The fracture energy of the double network is therefore much larger than those of either of the corresponding single networks. Thus, by sacrificing the rupture of the covalent bonds of the brittle first network, the material gains toughness. The covalent bonds serve as "sacrificial bonds," a term initially used to describe how bones fracture (*4*).

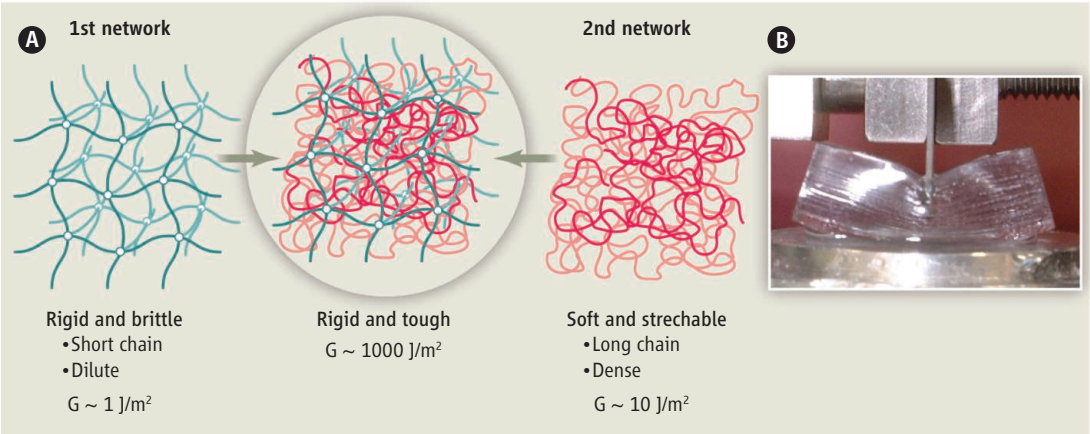

Tougher than its parts. (**A**) By combining different network materials, tough double-network materials can be created. (**B**) Photo of a tough double-network hydrogel containing 90 wt % of water (*2*). The value of the fracture energy G is an indicator of material toughness. Ducrot *et al*. now successfully apply this concept to elastomers.

In principle, the double-network principle can be used to toughen other network materials, as long as the interpenetrating network structure is formed. However, applying this concept to the nonhydrated elastomers is not trivial. The first challenge is to form an interpenetrating double-network structure in which the two networks have contrasting mechanical properties. In the case of hydrogels, this structure is synthesized in a two-step process, using a polyelectrolyte as the first network and a neutral polymer as the second network. A polyelectrolyte hydrogel swells much more than a neutral hydrogel, causing the chains to be highly stretched and stiff as well as highly dilute. In the case of elastomers, no polyelectrolyte can be used, making it difficult to form the interpenetrating network structure. Another difficulty is that elastomers do not contain solvent. Without solvent, two different polymers usually do not mix but instead separate into different phases. To synthesize double network elastomers, one must prevent the phase separation of the two polymers.

Ducrot *et al*. now show how the double-network concept can be used to improve the toughness of elastomers. To obtain a highly stretched and dilute first network, they swell the first network elastomer using monomers of the second network elastomer. They then polymerize the monomers to complete the double-network structure. In a further step, the double-network elastomers can be swelled in a third monomer, causing the first network elastomer to be stretched even further; polymerization of the third monomer leads to a triple network elastomer.

This sequential polymerization method prevents phase separation of the different polymers because the second or third network is formed from their monomer precursors in the presence of the first network. The stretched bonds of the first network are the sacrificial bonds that impart toughness to the elastomers. The authors have also developed a method to observe the fracture of the sacrificial bonds in situ by using chemoluminescent cross-linking molecules, which emit light as they break. This work should stimulate researchers to develop new classes of tough hydrogels and elastomers and investigate how they fracture.

Tough materials can dissipate substantial amounts of mechanical energy without fracturing. Compared with other tough materials in which noncovalent bonds dissipate energy, the covalent sacrificial bonds of brittle networks have the advantages of high bond energy and weak dependence of the stiffness and toughness on temperature and the rate of deformation. The disadvantage is that once the brittle network is broken, the covalent bonds cannot be reformed. The gel therefore softens permanently after large deformation. In a recent study, the covalent bonds have been replaced with ionic bonds to allow the fractured bond to be reformed in double-network hydrogels (*5*). Studies along these lines have successfully produced tough hydrogels that recover after internal rupture.

The double-network concept naturally suggests a general strategy for designing tough soft materials: incorporation of a mechanically fragile structure to toughen the material as a whole. This strategy is not limited to double- or multiple-network systems but also applies to single-network systems, as long as they have sacrificial bonds to dissipate energy and can retain the original configurations of the material after large deformation. For example, Henderson *et al*. have used block copolymers (*6*) and Sun *et al*. polyampholytes carrying opposite charges randomly distributed on the polymer chains (*7*) to create single-network hydrogels with dual cross-linking structures. The strong bonds in these gels impart elasticity, whereas the weak bonds rupture during deformation, dissipating energy. The mechanical behavior of these dually cross-linked gels thus resembles that of double-network gels. The dual cross-linking strategy may also be applied to elastomers in the future.

Another goal is to develop tough soft materials with anisotropic mechanical performance, similar to skin, cartilage, muscle, and tendons. For example, self-assembled molecules such as lipids, rodlike macromolecules, or block copolymers may be used to build anisotropic energy-dissipation structures. This possibility is demonstrated by an anisotropic hydrogel consisting of layered lipid membranes entrapped in the matrix of a neutral network (*8*). Several different mechanisms for dissipating energy and maintaining elasticity play a role in the design of tough soft materials. In a recent review, Zhao provides a guide to how these different mechanisms can be used in the design of next-generation tough hydrogels (*9*). These strategies are also applicable to elastomers, with Ducrot *et al*.'s study pointing the way to many exciting materials.

References

1. E. Ducrot *et al.*, *Science* **344**, 186 (2014).
2. J. P. Gong *et al*., *Adv. Mater.* **15**, 1155 (2003).
3. J. P. Gong, *Soft Matter* **6**, 2583 (2010).
4. J. B. Thompson *et al*., *Nature* **414**, 773 (2001).
5. J. Y. Sun *et al*., *Nature* **489**, 133 (2012).
6. K. J. Henderson *et al*., *Macromolecules* **43**, 6193 (2010).
7. T. L. Sun *et al*., *Nat. Mater.* **12**, 932 (2013).
8. M. A. Haque *et al*., *Macromolecules* **44**, 8916 (2011).
9. X. H. Zhao, *Soft Matter* **10**, 672 (2014).

10.1126/science.1252389

INTERNATIONAL

Premier Li Keqiang and Dr. Marcia McNutt Meet for a Discussion on Science

Broadly speaking. Premier Li Keqiang and Dr. Marcia McNutt discussed a range of science-related topics, including space exploration, China's scientific cooperation with other developing countries, climate change, education, and environmental protection.

During a visit to the People's Republic of China, *Science* Editor-in-Chief Marcia McNutt had the opportunity to meet with Premier Li Keqiang in Beijing on 13 January 2014. [See the related editorial by Marcia McNutt (www.sciencemag.org/lookup/doi/10.1126/science.1251293). The full transcript is available online (www.sciencemag.org/cgi/content/full/science.1253962/DC1).]

Much of the conversation centered around China's challenge of sustainably developing resources for economic growth while preserving the natural environment and curbing greenhouse gas emissions. There is no precedent for tackling these problems while supporting a population as large as China's 1.3 billion. Furthermore, China has been on an accelerated path to modernization, playing "catch up" since the Cultural Revolution in the late 1960s. Li explained that China has been heavily investing in environmental science and clean energy technologies as part of its strategy to propel the nation into the 21st century.

As further evidence of China's commitment to address environmental problems, Li pointed to efforts under way to tame air and water pollution in China. As more Chinese citizens attain middle-class economic status and find their basic life needs met, they are paying more attention to quality of life. Although past Chinese leaders declared a war on poverty, and that war continues, the current leadership has now also declared a war on pollution.

As a first step, Li explained that China is using science to address the human contribution to smog in major cities, moving beyond monitoring to take action to treat it. He noted that China has raised fuel standards to cut vehicle exhaust, developed clean technologies for coal use, taken steps to prevent the spread of dust from construction sites, carried out afforestation in arid landscapes, and returned unproductive cultivated land to forests. He said his nation is developing the world's largest wind power capacity, expanding solar energy, and investing in carbon capture and storage technologies and new battery technologies for electric cars that require less palladium, platinum, and other limited resources. China is more than doubling the number of nuclear power plants while setting aggressive targets to lower overall energy consumption. Li believes that developing renewable energy and conserving energy and resources can together contribute to GDP growth while preserving the environment. With all the current policies in place, China's energy-saving and environmental industries will have a market value of 4.5 trillion RMB yuan by 2015 (approximately US$720 billion at current exchange rates) and will soon approach US$1 trillion. This is why, he said, many companies and research institutions developing nuclear power, carbon capture, and clean energy have turned their attention to China.

Clean water in China is also a major concern. Contaminated water takes a heavy toll on human health. In rural areas, 100 million to 110 million people still do not have access to safe drinking water. Last year, with the support of central and local budgets and funds raised by individuals, Li said that China began providing clean water to over 60 million people. The plan is to extend that initiative to another 60 million people this year, and the remaining 50 million next year. By then, the drinking water problem will be basically solved. However, highly polluted water still accounts for more than 10% of China's total water resources; a plan is required to resolve this issue.

The following are excerpts from the conversation.

Published by AAAS

On China's space program, its goals, and the balance between manned and robotic missions

Li Keqiang: "China's manned space and lunar probe missions have a twofold purpose: First, to explore the origin of the universe and mystery of human life; and second, to make peaceful use of outer space. … peaceful use of outer space is conducive to China's development. China's manned space program has proceeded to the stage of building a space station, and will move forward step by step. … As human life is precious, we will start with robotic exploration before gradually expanding manned space exploration. Space is all too mysterious. We need to take risks, but not at the cost of human life when conditions are not yet right."

On international science cooperation

LK: "China … needs to fulfill the responsibility required of a big developing country and do what it can to help other developing countries. At the same time, it also needs to draw experience from them. This is a process of mutual assistance and mutual learning. … There are three priorities of cooperation: First, development, such as agricultural productivity and poverty alleviation; second, improvement of livelihood, such as disaster prevention and reduction to mitigate losses caused by natural disasters; third, nature and the environment, such as development of clean energy. … there are bright people even in a poor country. … Science research needs brilliant ideas, and this requires input from all sources."

On climate change

LK: "Climate change is a common challenge of mankind. …There is still controversy about whether the main cause of climate change is human activity or the changing dynamics of nature. Nevertheless there is no denying that human activities do impact climate change. To realize modernization, developing countries must overcome the challenges of the environment and resources facing the whole of mankind. These challenges are related to climate change and are pressing tasks for us. China is committed to achieving modernization, but there is no past precedent for us to follow in human history on how to achieve modernization in an energy-conserving and environment-friendly way. … Moreover, coal still accounts for about 66% of China's energy mix, and its emissions have a direct impact on climate change. Hence, we are determined to conserve energy, and this is a top priority. … China's energy consumption per unit of GDP in 2013 was 3.7% lower than the previous year. … we are vigorously developing clean energy. For example, China's installed hydropower capacity is 278 million kilowatts, and a total of 70 million kilowatts of wind power has been connected to the grid, larger than any other country in the world."

> "China … needs to fulfill the responsibility required of a big developing country and do what it can to help other developing countries. At the same time, it also needs to draw experience from them."
>
> —Li Keqiang

On building elite institutions versus promoting equal access

LK: "We will continue to build some world-class universities and attract top-notch professionals. We place greater emphasis on educational fairness. For example, the share of poor students in key Chinese universities was declining. This is unfair for children in China's underdeveloped and poor areas. It also makes all-round and high-end scientific progress unsustainable. Last year, the Chinese government took strong measures to ask key universities to enroll more rural students from the underdeveloped central and western regions, especially poor areas. … In 2013, the share of rural students in key universities increased by 10% over the previous year. … Our government has provided 50 billion RMB yuan in scholarships or student loans to finance the higher education of children from poor regions and families."

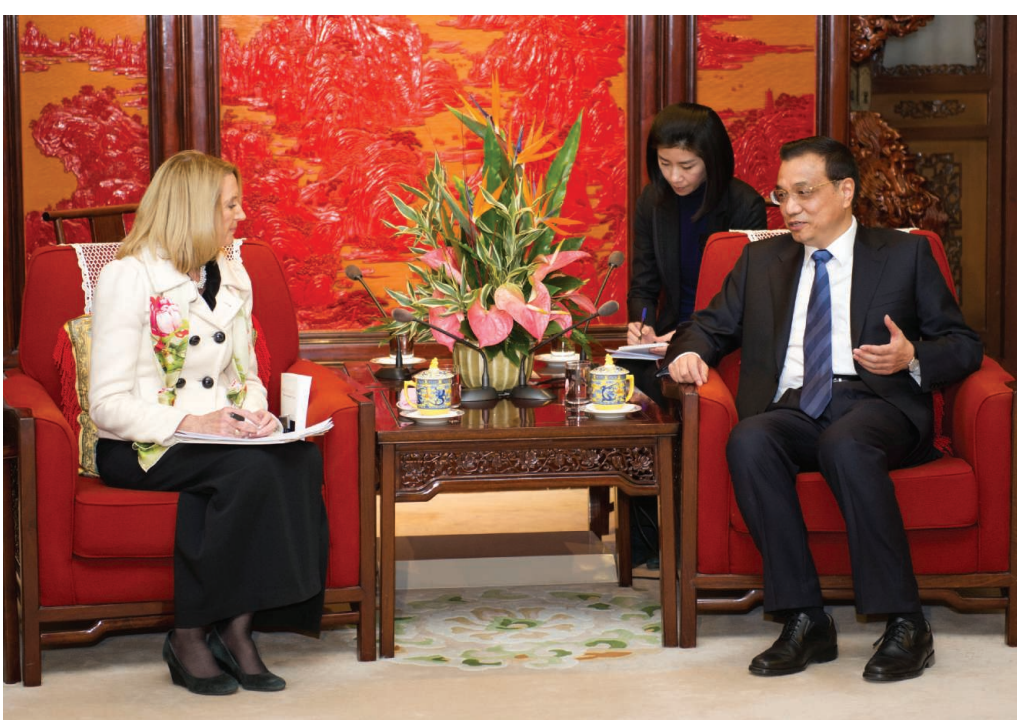

CREDIT: CHINESE ACADEMY OF SCIENCES

China's challenges. Premier Li described one of China's major challenges as sustainably developing resources for economic growth while preserving the natural environment and curbing greenhouse gas emissions.

Published by AAAS

READ THE FULL ARTICLE ONLINE
http://dx.doi.org/10.1126/science.1240622

The brain's interneurons may have unexpected uses for understanding and treating nervous system disorders.

Interneurons from Embryonic Development to Cell-Based Therapy

Derek G. Southwell, Cory R. Nicholas, Allan I. Basbaum, Michael P. Stryker, Arnold R. Kriegstein, John L. Rubenstein, Arturo Alvarez-Buylla*

Background: Alterations in neural excitation and inhibition cause a number of neurologic and psychiatric disorders. In the cerebral cortex, excitation and inhibition are mediated by two cell types born in distinct areas of the embryo: excitatory projection neurons, which are generated in the developing cortex, and inhibitory interneurons, which are produced outside the cortex in the ventral forebrain. After migrating from their origins across the developing brain, young interneurons reach the cortex and differentiate into various inhibitory neuronal cell types. Roughly two-thirds of these young cells survive in the cortex to form the local inhibitory circuits that shape excitatory neuron activity. The embryologic programs that guide interneuron migration, survival, and circuit integration are also executed by these young neurons after their transplantation into the juvenile and adult nervous systems. These processes, realized in the developmentally and topographically distinct environment of the recipient, offer a unique opportunity for studying neurodevelopment and therapeutically modifying neural circuits.

Advances: In both neonatal and adult rodents, transplanted embryonic interneurons have been shown to migrate and survive in diverse neural structures, including the cerebral cortex and the spinal cord. Transplanted interneurons form elaborate processes in host tissues, receive synaptic inputs, and make inhibitory connections with host neurons, similar to what they do in their normal setting. Functionally, transplantation has been used to modify inhibitory signaling in the host brain and to induce reorganization of the cortex by creating new windows of neural circuit plasticity. Transplanted interneurons have been shown to modify disease phenotypes in several rodent models of neurologic and psychiatric disorders, including epilepsy, chronic pain, Parkinson's disease, schizophrenia, and anxiety. Interneuron transplantation has also been used to explore how cell-intrinsic and environmental factors interact to govern cellular fate and circuit formation. To generate interneurons for possible clinical applications, researchers are developing in vitro culture systems for the derivation of interneurons from embryonic stem cells and induced pluripotent stem cells. These efforts have produced new interneurons that, like their endogenous counterparts, disperse and integrate in the recipient brain after transplantation.

Outlook: Cortical interneurons are a heterogeneous population, and little is known about how distinct subtypes of interneurons function in neural circuits. Thus far, transplantation studies have used donor pools containing large mixtures of interneurons. As the mechanisms underlying interneuron diversity become better understood, donor populations may be selected or produced to include only specific subtypes of cells. This will allow researchers to study the functional roles of different interneuron types and may permit the use of specific donor populations for different pathologies. It is unknown how transplanted interneurons modify disease phenotypes. While transplanted interneurons likely exert therapeutic effects by increasing neural inhibition, other mechanisms are also possible. By transplanting mutant cells, or cells engineered to respond to optogenetic or chemical stimulation, these mechanisms may be elucidated. Eventual clinical applications will require more subtle and detailed studies of the behavioral effects of interneuron transplantation.

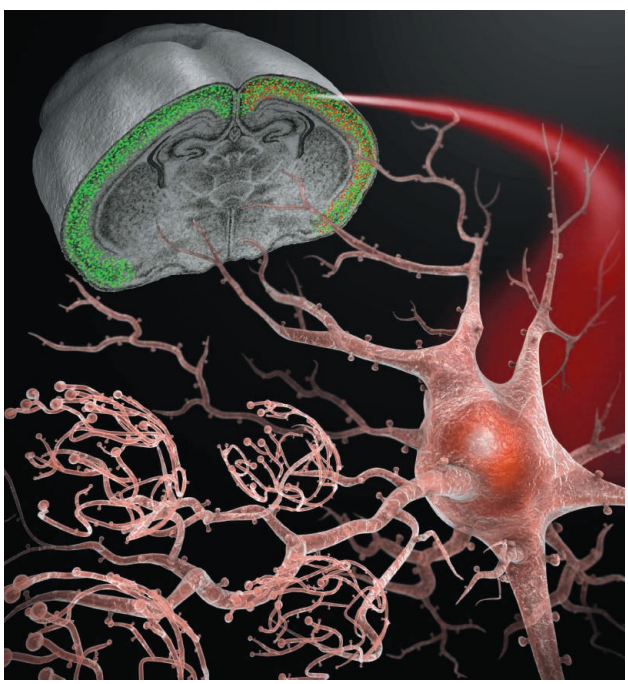

Transplanted interneurons for the study of neural development and the treatment of nervous system disorders. Precursors of inhibitory interneurons transplanted from the medial ganglionic eminence of the ventral embryonic forebrain into the juvenile or adult rodent cortex migrate from the graft site and become dispersed throughout the recipient tissue (shown as small red dots in the transplanted hemisphere in a cross section of the rodent brain, upper left). In the recipient, transplanted interneurons follow cell-intrinsic programs that normally regulate their survival and differentiation in the embryo. Interneurons in the host brain (small green dots) do not die as a result of the additional neurons; rather, transplantation increases the total interneuron population. Transplanted interneurons develop axonal and dendritic arbors (red cell magnified in foreground), synaptically integrate into neural circuits, and modify inhibitory signaling. Interneuron transplantation provides a method for studying neural circuit assembly and function and is a potential cell-based therapy for conditions such as epilepsy, Parkinson's disease, schizophrenia, anxiety, and chronic pain.

The list of author affiliations is available in the full article online.
*Corresponding author. E-mail: abuylla@stemcell.ucsf.edu
Cite this article as D. G. Southwell *et al.*, *Science* **344**, 1240622 (2014). DOI: 10.1126/science.1240622

Interneurons from Embryonic Development to Cell-Based Therapy

Derek G. Southwell,[1] Cory R. Nicholas,[2,3] Allan I. Basbaum,[4] Michael P. Stryker,[5] Arnold R. Kriegstein,[2,3] John L. Rubenstein,[2,6] Arturo Alvarez-Buylla[1,2]*

Many neurologic and psychiatric disorders are marked by imbalances between neural excitation and inhibition. In the cerebral cortex, inhibition is mediated largely by GABAergic (γ-aminobutyric acid–secreting) interneurons, a cell type that originates in the embryonic ventral telencephalon and populates the cortex through long-distance tangential migration. Remarkably, when transplanted from embryos or in vitro culture preparations, immature interneurons disperse and integrate into host brain circuits, both in the cerebral cortex and in other regions of the central nervous system. These features make interneuron transplantation a powerful tool for the study of neurodevelopmental processes such as cell specification, cell death, and cortical plasticity. Moreover, interneuron transplantation provides a novel strategy for modifying neural circuits in rodent models of epilepsy, Parkinson's disease, mood disorders, and chronic pain.

New neurons are naturally added to the adult brains of many species, including humans (*1*–*8*). Adult mammalian neurogenesis, however, is largely restricted to the hippocampus and olfactory bulb, where it contributes to local neural circuit plasticity, not repair. Identification of transplantable cells that migrate and integrate into neural circuits in a manner similar to these adult-born neurons could be useful in nervous system therapy. Indeed, neuronal transplantation has a long history, but for the vast majority of cell types, the postnatal central nervous system has proven inhospitable to migration and neural circuit integration (*9*–*11*). Immature inhibitory interneurons from the embryonic ventral telencephalon, however, show a unique capacity to disperse and integrate into neural circuits of the postnatal central nervous system. In large part, this ability reflects their ontogeny: During brain development, ventral telencephalon-derived interneurons must migrate long distances, differentiate and survive in environments distinct from their origin, and functionally integrate into extant circuits composed of other cell types—all challenges faced by cells transplanted into the nervous system. Here, we summarize the development of telencephalic interneurons—in particular, inhibitory interneurons of the cerebral cortex—and describe their behavior after transplantation into the postnatal central nervous system. In addition, we discuss the potential of interneuron transplantation as a cell-based therapy for numerous conditions, including epilepsy, Parkinson's disease, psychiatric disorders, and chronic pain. Finally, we summarize efforts to derive forebrain interneuron precursors in vitro from pluripotent stem cells.

A Developmental Fate Realized in a Distant Time and Place

During embryonic development, molecularly, morphologically, and physiologically distinct subpopulations of interneurons originate in progenitor domains of the ventral telencephalon, including the medial and caudal ganglionic eminences (*12*–*19*). From these origins, immature interneurons undergo a remarkable process of long-distance migration to many structures of the developing telencephalon, including the cerebral cortex, where they form neural circuits with locally produced excitatory neurons (*19*–*22*). In contrast to cortical excitatory neurons, which form connections onto distant cells within and outside of the cortex, cortical interneurons form inhibitory GABAergic (γ-aminobutyric acid–secreting) connections onto local neurons and establish gap junction–mediated electrical networks with other interneurons (*23*). Because of this ontogeny, ventral telencephalic interneuron precursors are endowed with developmental programs that may confer an uncommon capacity to engraft into the nervous system after transplantation.

Initial studies of neural transplantation were marked by the limited dispersion of transplanted cells throughout host tissues (*24*–*28*). In contrast to cells from the embryonic neocortex, hypothalamus, thalamus, superior colliculus, rhombic lip, and spinal cord, which display minimal capacity to migrate when placed into in vitro explants, cells from the embryonic lateral ganglionic eminence [LGE; the major source of olfactory bulb interneurons (*19*)] and the medial ganglionic eminence (MGE) migrate substantial distances (*29*). Of these two populations, immature interneurons from the MGE exhibit greater migratory potential in vitro, with dispersal distances approximately two to three times those of LGE cells. When injected into the postnatal brain, MGE cells also exhibit substantial migratory capacity. Whereas embryonic cells from the LGE and dorsal forebrain remain mostly clustered at injection sites, MGE-derived interneurons disperse widely throughout developmentally distinct regions of the adult and neonatal central nervous systems, including the striatum (*29*, *30*), hippocampus (*31*, *32*), neocortex (*29*, *33*), amygdala (*32*), thalamus (*29*), and spinal cord (*34*). Transplanted MGE interneurons migrate distances up to 2.5 mm in the adult rodent brain (*30*, *32*) and 5 mm in the neonate (*33*).

Although the differentiation of cortical interneurons extends well into postnatal life (*13*, *35*, *36*), the fates of interneuron precursors are largely determined prior to their migrations out of the embryonic ganglionic eminences (*37*, *38*). As such, when immature interneurons are heterochronically transplanted from the embryonic MGE into the postnatal cortex, they produce the complement of interneuron subtypes normally produced by the MGE, as indicated by their expression of diverse interneuron morphologies, molecular markers, and electrophysiological phenotypes (*32*, *33*, *39*, *40*). Microdissection experiments have shown that when cells from distinct subregions of the MGE are transplanted (for example, dorsal versus ventral MGE), the resultant populations vary in their compositions of neurochemically defined interneuron subtypes (*38*, *41*). Although this strategy does not yield entirely distinct populations (for example, parvalbumin-expressing interneurons are present in both dorsal and ventral MGE transplants), it allows for the selection of populations biased toward particular types of interneurons. It remains unclear, in turn, whether various types of neurochemically defined cells target different structures and serve distinct functions after transplantation (*42*), yet this finding hints that distinct transplant populations could be selected for different disease pathologies.

Just as MGE interneurons migrate when transplanted outside the cortex, they are also able to differentiate into mature inhibitory interneurons in foreign regions of the central nervous system. For example, when heterotopically transplanted into the spinal cord, immature interneurons from the ventral telencephalon survive and eventually express some of the molecular, morphologic, and physiologic properties of cortical interneurons (*34*). Thus, interneuron transplantation is a method for adding specific and, depending on the target, foreign elements to neural circuits (Fig. 1, A to C). Together, these transplantation studies highlight the notion that the behaviors and phenotypes of cortical interneurons are largely determined by intrinsic developmental programs established during the early stages of their development in the embryo.

In the host brain, transplanted MGE-derived interneurons display electrophysiologic activity patterns typical of the various subtypes of

[1]Department of Neurological Surgery, University of California, San Francisco, CA 94143, USA. [2]Eli and Edythe Broad Center of Regeneration Medicine and Stem Cell Research, University of California, San Francisco, CA 94143, USA. [3]Department of Neurology, University of California, San Francisco, CA 94143, USA. [4]Department of Anatomy, University of California, San Francisco, CA 94158, USA. [5]Center for Integrative Neuroscience and Department of Physiology, University of California, San Francisco, CA 94143, USA. [6]Department of Psychiatry, University of California, San Francisco, CA 94143, USA.

*Corresponding author. E-mail: abuylla@stemcell.ucsf.edu

physiologically defined interneurons (*32*, *33*). Transplanted interneurons also exhibit spontaneous and evoked synaptic currents, indicating that they receive functional synaptic inputs from neurons of the host brain (*30*, *33*, *40*) (Fig. 1D). Transplantation increases the frequency of inhibitory events in projection neurons (*34*, *40*, *42*) (Fig. 1E), but curiously, these effects are largely insensitive to the number of cells transplanted; in the cerebral cortex, transplant-mediated inhibition reaches a plateau with transplant sizes just 5 to 10% of that which the cortex can support (*40*). Simultaneous electrode recordings of transplanted interneurons and host projection neurons have shown that transplanted interneurons make functional inhibitory synaptic connections onto host neurons (*43*), consistent with the possibility that transplanted interneurons modify inhibitory circuits in the host cortex by forming new inhibitory synapses. Electron microscopy also has revealed synaptic contacts between transplanted interneurons and neurons of the host cortex (*39*, *40*), whereas transsynaptic tracer experiments have demonstrated the synaptic connectivity of interneurons transplanted into the spinal cord (*34*).

Transplanted cortical interneurons have a capacity to integrate synaptically into host brain circuits, where they appear to primarily target host excitatory neurons (*39*). It is unknown, however, whether transplanted interneurons form inhibitory synapses onto one another, nor whether they form gap junction–mediated electrical networks. Nonetheless, these studies have provided a strong rationale for the use of interneuron transplantation to study and experimentally modify inhibition in the host nervous system.

Interneuron Transplantation as a Window into Brain Development and Function

Interneuron transplantation permits the introduction of immature cells into foreign and developmentally distinct environments, allowing researchers to study how cell-autonomous and environmental factors determine the fates of developing neurons. For example, transplantation of MGE interneurons from mutant donors into wild-type hosts has illustrated the cell-autonomous role of the Dlx1 transcription factor in controlling the branching and survival of specific subsets of cortical interneurons. Interneuron transplantation has also proven useful for studying genes that, when mutated in all tissues, cause perinatal lethality. For example, the transplantation of *Nkx2.1* (*44*) and *TrkB* mutant interneurons (*40*) has allowed an examination of the roles of these genes in interneuron fate determination and migration, respectively, neither of which could be assessed directly in mutant animals because the animals die early in postnatal life (*45*, *46*).

Just as transplantation of mutant MGE interneurons has revealed some of the cell-autonomous determinants of interneuron development, transplantation has elucidated non–cell-autonomous determinants as well. For example, exposing wild-type MGE cells to sonic hedgehog prior to transplantation

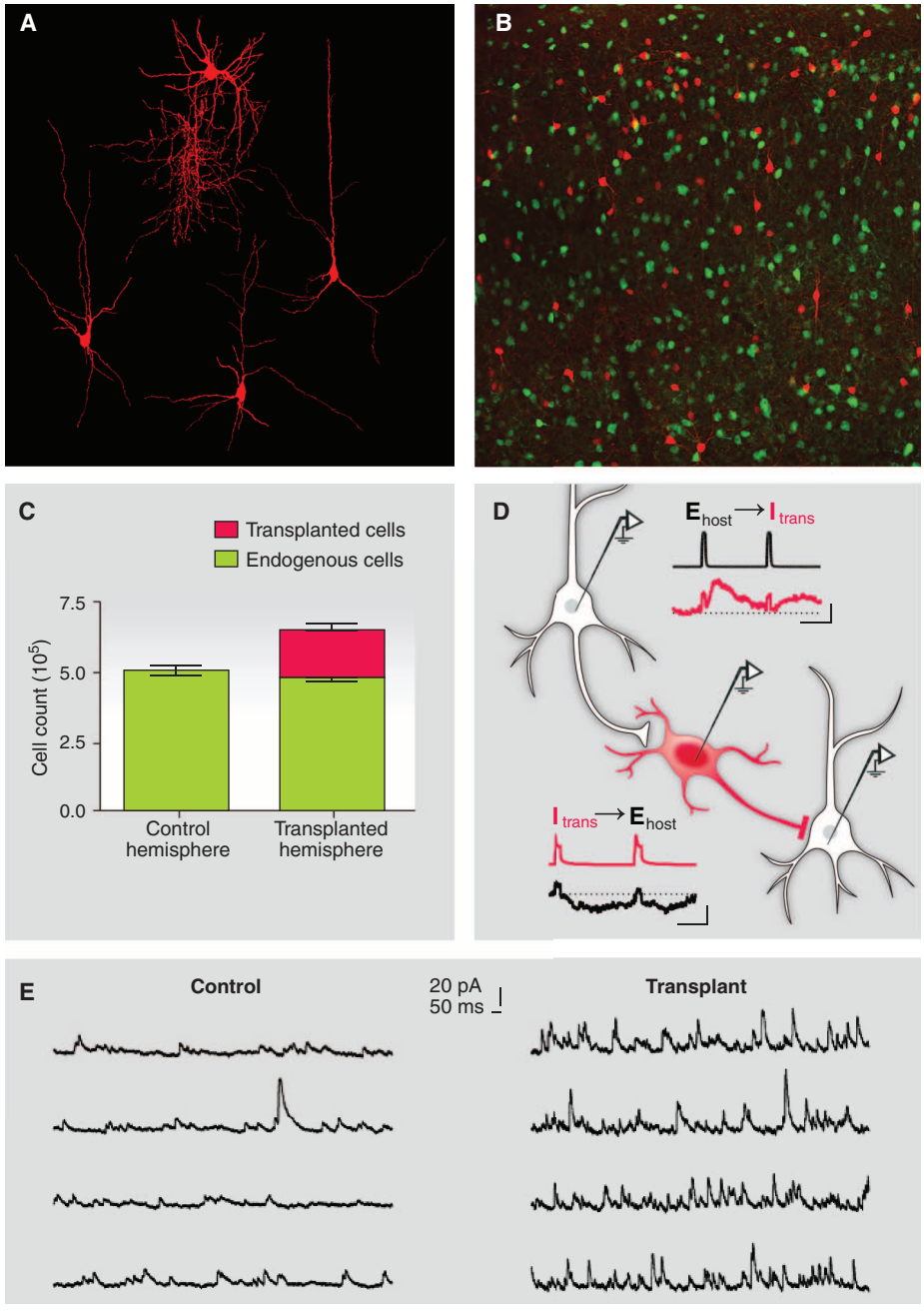

Fig. 1. Interneuron transplantation augments interneuron population size and increases inhibition in the host nervous system. (**A**) Section from the mouse cerebral cortex depicting transplanted interneurons, labeled by a red fluorescent protein. Transplanted immature interneurons disperse, survive, and develop extensive arborizations throughout the parenchyma of the host neocortex. Image width, ~400 μm. (**B**) Section from the mouse cerebral cortex depicting host interneurons (labeled by green fluorescent protein) and interneurons transplanted from the embryonic ventral telencephalon (red). Image width, ~800 μm. (**C**) Immature interneurons (red) disperse, survive, and integrate into the postnatal nervous system, where they increase the host cortical interneuron population (green) by up to 35% (*40*). (**D**) Transplanted interneurons receive excitatory synapses from host pyramidal neurons and make inhibitory synapses onto host pyramidal neurons. Simultaneous electrode recordings from a transplanted inhibitory neuron (red) and host pyramidal neurons (white). Stimulation of a host pyramidal neuron elicits excitatory postsynaptic potentials in the transplanted interneuron (red). Depolarization of the transplanted interneuron evokes inhibitory postsynaptic potentials in a postsynaptic host pyramidal neuron. Scale bars, 25 ms and 90 mV (presynaptic), 25 ms and 0.125 mV (postsynaptic). (**E**) Interneuron transplantation increases the frequency of inhibitory signaling events in host pyramidal neurons. Representative traces of inhibitory postsynaptic currents were recorded from host pyramidal neurons in vitro (left, control; right, transplant recipient). [(B) and (C) from (*40*), (D) from (*43*), (E) from (*33*)]

biases them to form somatostatin-expressing rather than parvalbumin-expressing populations (*38*, *47*). Conversely, transplantation of wild-type interneurons into mutant host backgrounds may also be a valuable approach for examining how non–cell-autonomous factors contribute to neurodegeneration (*48*).

Interneuron transplantation has also been used to study developmental cell death, where it has challenged a long-standing hypothesis of neurodevelopment (*40*). Throughout nervous system development, programmed cell death eliminates large fractions of developing neurons shortly after the formation of synaptic contacts (*49*, *50*). According to the neurotrophin hypothesis (*49*–*52*), the engraftment of transplanted interneurons should be limited by competition for survival signals derived from the host: Transplanted cells that establish sufficient connectivity receive target-derived survival signals, while those that do not receive such signals die. By contrast, transplantation studies indicate that cortical interneuron survival is determined independently of signals produced by other cell types (*40*). Transplanted interneurons undergo developmental cell death in the host cortex, but they die asynchronously from interneurons of the host at a time consistent with their own intrinsic developmental program (Fig. 2). Over transplant sizes that vary by a factor of 200, the extent of transplant cell death remains constant and is similar to the extent of native interneuron cell death during normal development. Additionally, transplanted interneurons that lack TrkB, the principal neurotrophin receptor in the central nervous system (*53*), do not demonstrate reduced survival relative to wild-type transplanted interneurons. Together, these findings suggest instead that intrinsic developmental programs regulate interneuron cell death. These programs are not governed by cellular competition for survival signals produced by other cell types, although they may involve competition for survival signals produced by other interneurons. This pattern of intrinsically determined cell death may explain why transplanted MGE interneurons can survive and augment neuronal populations both inside and outside of the cerebral cortex.

The study of transplant-induced cortical plasticity further illustrates how interneuron-intrinsic developmental programs shape cortical development and regulate the engraftment of transplanted cells (*40*) (Fig. 2). During a critical period that occurs in late postnatal life, rodent ocular dominance plasticity is transiently heightened, presumably because of the maturation of cortical inhibition in the visual cortex (*54*). Manipulations of GABAergic inhibitory signaling alter ocular dominance plasticity (*35*, *55*–*57*), suggesting that transplanted interneurons could affect plasticity of visual cortex through their known effects on inhibition (*33*). In mice, ocular dominance plasticity reaches a maximum in the fourth postnatal week, when cortical interneurons are approximately 5 weeks old, and then declines sharply thereafter (*58*). Transplantation of MGE interneurons into the visual cortex induces ocular dominance plasticity well after the normal critical period (*43*). This plasticity is only observed approximately 5 weeks after transplantation, when the transplanted interneurons are of a cellular age equivalent to that of native interneurons at the peak of the critical period. These findings suggest that the critical period is in part governed by the execution of an interneuron-intrinsic developmental program and that transplanted interneurons induce new plasticity by retaining and executing this program when transplanted into the postnatal cortex. The mechanism of transplant-induced plasticity is unknown, but it is unlikely to result merely from increased inhibition, as the pharmacologic enhancement of inhibition does not induce plasticity after the critical period (*56*). Transplanted interneurons make synapses that are three times as numerous yet approximately one-third as strong as those made by native interneurons, which may destabilize the cortical network and elicit functional reorganization (*43*). Alternatively, or in addition, transplanted interneurons may secrete molecules that alter the extracellular matrix, allowing native neurons to form new synapses (*54*, *59*).

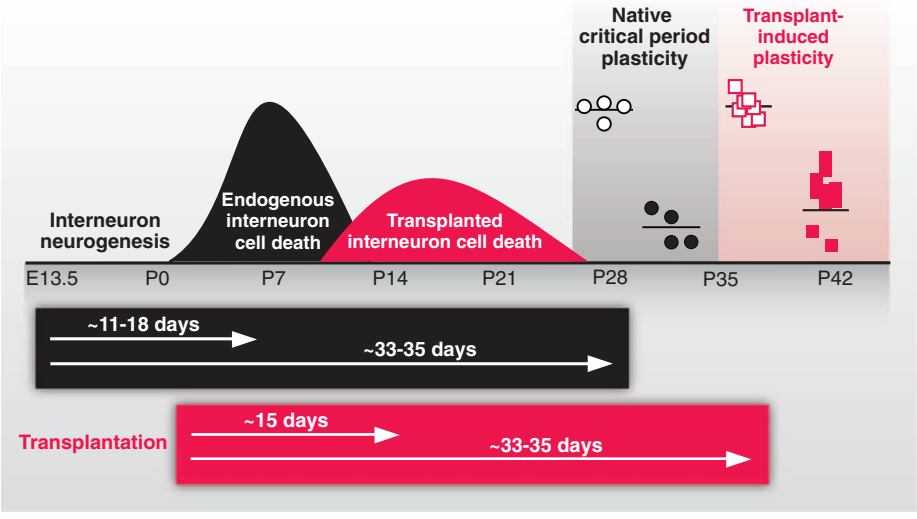

Fig. 2. Transplanted embryonic interneurons retain and execute intrinsic developmental programs when grafted into the postnatal brain. During mouse cortical development, inhibitory neurons undergo a pattern of cell death that peaks around postnatal days 7 to 11, when they reach an intrinsic cellular age of approximately 11 to 18 days (black curve). Later, around postnatal day 28, when surviving inhibitory neurons are approximately 33 to 35 days of age, a critical period for ocular dominance plasticity occurs in the visual cortex (black circles). When newborn inhibitory neurons are transplanted from the embryo into the postnatal brain (red), they undergo a similar pattern of cell death, which reaches a maximum when the transplanted cells are likewise approximately 15 days old (*40*). Moreover, when transplanted interneurons reach a cellular age of approximately 33 to 35 days, they induce ocular dominance plasticity in the host visual cortex (*43*). These findings suggest that interneuron development is governed by developmental programs that are established in the embryo, and that when transplanted, embryonic interneurons retain and carry out these developmental programs in the postnatal host nervous system.

The Clinical Potential of Interneuron Transplantation

A number of neurologic and psychiatric disorders are thought to result, at least in part, from the dysfunction of cortical interneurons. These conditions, recently termed "interneuronopathies" (*60*), include epilepsy, autism, schizophrenia, and possibly Alzheimer's disease (*61*–*66*). Other conditions, such as Parkinson's disease, Huntington's disease, spasticity, and chronic pain, result from imbalances in neural excitation and inhibition secondary to the dysfunction of other neuronal populations. Interneuron precursor transplantation has thus been explored as a strategy for restoring inhibition to neural circuits affected in these conditions (Fig. 3). Moreover, because some of them manifest in the adult, yet could arise from developmental abnormalities that endow neural circuits with a "presymptomatic signature" (*67*), interneuron transplantation has also been studied as a means of preventing the manifestation of clinical symptomatology in disease models. Through its effects on host brain plasticity, interneuron transplantation may also be a strategy for augmenting functional recovery after neurologic injury. Finally, through their ability to disperse and intercalate throughout neural tissue, transplanted interneurons may serve as vectors for the delivery of therapeutic agents.

Epilepsy is a heterogeneous disorder of both developmental and traumatic etiologies. Together, epilepsies are marked by the hyperexcitability of neuronal networks, which, in many cases, reflects the dysfunction of inhibitory circuits (*66*). It follows that interneuron transplantation, through its ability to augment local GABA-mediated synaptic inhibition, may be a means for modifying epileptogenic circuits and limiting the spread of

seizure activity across neural networks. In fact, a number of animal studies have provided evidence that transplanted interneurons improve disease phenotypes in both developmental and acquired forms of epilepsy.

Interneuron transplantation was first shown to suppress spontaneous seizures in a mouse potassium channel mutant (*Kv1.1*) that simulates a neuronal ion channelopathy associated with severe tonic-clonic seizures in humans (*39*). MGE interneuron transplants were made into the neocortex at neonatal stages, before the manifestation of seizures. Thirty days after transplantation, seizure monitoring by videoelectroencephalography demonstrated a 90% reduction in seizure number during the monitoring period. Although the potassium channelopathy was present across all cell populations of the brain, seizure suppression was achieved through interneuron transplants largely restricted to the cerebral cortex. These experiments suggest that neonatal interneuron transplantation could have a prophylactic effect in a congenital seizure disorder, but they did not address whether transplantation can suppress seizures when performed after epilepsy has emerged.

Other studies provide evidence that interneuron transplantation to neonates and adults can suppress seizures initiated by acute epileptogenic stimulation of the adult brain. Two months after transplantation of MGE interneurons to the neonatal mouse cortex, some host animals exhibited increased seizure thresholds, decreased seizure severity, and decreased seizure-associated mortality in a maximum electroconvulsive shock model, a traditional assay for anti-epileptic drug screening (*68*). Transplantation of interneurons into the adult cortex also reduced the power in local field potential recordings used to monitor seizure-like electrical activity induced by focal administration of the convulsive drug 4-aminopyridine to the cortex (*69*). This effect was largely independent of the number of cells that survived in the host cortex, which may corroborate other studies indicating that small numbers and large numbers of transplanted interneurons exert equally strong effects on neuronal inhibition (*40*).

Interneuron transplantation has been found to restore synaptic inhibition and rescue seizure phenotypes in mouse models of acquired epilepsy. In one study, MGE interneurons were transplanted into the adult hippocampus after the ablation of hippocampal interneurons with saporin (*31*). Interneuron transplantation restored local synaptic inhibition and reduced the treated animals' susceptibility to pharmacologically induced seizures. In another study designed to evaluate the clinical potential of interneuron transplantation to limit spontaneous seizures, transplants were performed into animals with acquired epilepsy secondary to drug-induced status epilepticus (*32*). Using a well-characterized rodent model of temporal lobe epilepsy, the most common form of epilepsy in adults, these experiments showed that interneurons transplanted into the adult hippocampus migrate and integrate into host circuits as functional, mature interneurons that comprise the subtypes of interneurons derived from the MGE. Transplantation into the hippocampus, but not the amygdala, reduced spontaneous seizure frequency by approximately 90% in animals monitored by videoelectroencephalography more than 60 days after transplantation. Because behavioral and cognitive comorbidities frequently occur in temporal lobe epilepsy patients, the effects of interneuron transplantation on host behavior were also studied. Transplantation into the hippocampus reduced behavioral comorbidities present in the temporal lobe epilepsy model.

Together, these studies indicate that transplantation of a relatively small and locally restricted population of cortical interneurons can improve seizure phenotypes. This effect has been observed in models characterized by interneuron dysfunction (*31*), in genetic mutant models (*39*), and in models characterized by the pathology of other cell populations (*32*). Although the exact mechanism of seizure suppression remains unknown, transplanted interneurons likely constrain seizure activity by forming new inhibitory synapses and increasing "surround inhibition" (*70*). Other mechanisms may be involved, such as structural rearrangements of host circuitry, the secretion of neuropeptides or trophic factors, or the modulation of inflammation. It remains unclear, however, whether transplanted interneurons can integrate into neural circuits affected by long-standing epilepsy, or whether they exert a long-lasting effect on seizure phenotypes.

Interneuron transplantation has also been explored as a cell-based treatment for Parkinson's disease, a neurodegenerative condition characterized by movement abnormalities, cognitive and behavioral decline, and autonomic dysregulation. The motor symptoms of Parkinson's disease arise from the loss of dopaminergic neurons in the substantia nigra of the midbrain. This results in an imbalance of excitation and inhibition of the striatum, a basal ganglia structure that modulates motor commands. MGE interneurons were transplanted into rats that previously received 6-hydroxydopamine

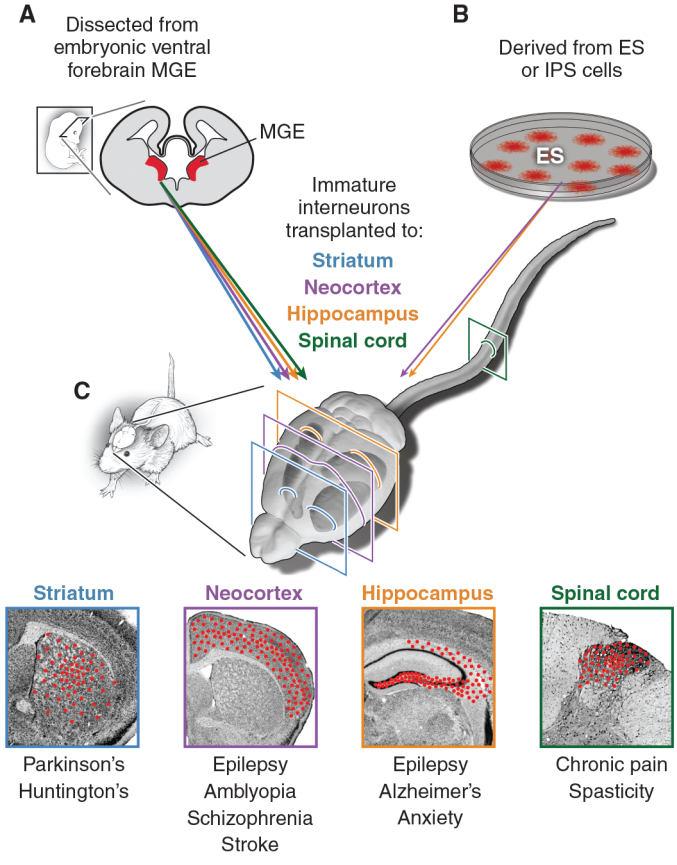

Fig. 3. Sources of immature interneurons for transplantation and therapeutic targets. (**A** and **B**) Immature interneurons can be transplanted (A) directly from the medial ganglionic eminence (MGE) of the embryonic ventral forebrain, or (B) from in vitro systems in which immature interneurons are generated from embryonic stem (ES) or induced pluripotent stem (IPS) cells. (**C**) Interneuron transplantation has been studied in diverse regions of the central nervous system, including the striatum, neocortex, hippocampus, and spinal cord. Depending on the site of transplantation, interneurons have been shown to modify disease phenotypes in animal models of Parkinson's disease, epilepsy, schizophrenia, anxiety disorder, and chronic pain. Interneuron transplantation may also be a method for therapeutically modifying neural circuits in conditions such as Huntington's disease, amblyopia, stroke, Alzheimer's disease, and spasticity.

lesions of the substantia nigra, a manipulation that yields a model of the motor symptoms of Parkinson's disease (*30*). Transplanted cells migrated, differentiated into GABAergic interneurons, and survived for more than 12 months in the damaged striatum, and they reduced Parkinsonian-like motor behaviors. Transplantation also increased motor activity in otherwise intact wild-type hosts, indicating that it also affects striatal-dependent motor behaviors in the intact brain. Although the mechanisms that underlie these effects are unknown, it is hypothesized that transplanted GABAergic interneurons introduce new inhibition to striatal circuits affected by the loss of brainstem dopaminergic inputs, thereby reducing the striatum's inhibitory influence on motor commands. Regardless of the exact mechanism, these experiments suggest that transplanted interneurons can modify a disease phenotype secondary to the dysfunction of an entirely different cell population.

As discussed above, MGE interneurons exert disease-modifying effects when transplanted into the neocortex, hippocampus, and striatum—three structures that are normally populated by these cells. MGE interneurons have also been shown to survive, integrate, and ameliorate disease symptoms when transplanted into the spinal cord, a structure containing GABAergic interneurons that originate in the spinal cord and express morphologies different from those of cortical interneurons. In these experiments, MGE interneurons were transplanted into a model of neuropathic pain elicited by peripheral nerve injury (*34*). In this model, inhibitory circuits in the dorsal horn of the spinal cord were disrupted, and as a result, non-noxious stimuli became painful (allodynia) while pain behaviors provoked by normally painful stimuli were increased (hyperalgesia). When transplanted into the dorsal spinal cord 1 week after peripheral nerve injury, MGE interneurons developed molecular phenotypes characteristic of GABAergic cortical interneurons. After approximately 2 weeks, the transplanted cells became responsive to stimuli delivered via peripheral nerves, and they made projections onto neurons that ascend to the brainstem, as indicated by activity-dependent gene expression and retrograde tracer studies. Finally, transplantation reduced behavioral measures of mechanical hypersensitivity, a hallmark of neuropathic pain. As was observed in other studies (*40*, *69*), there was no correlation between transplanted interneuron number and functional effect. Additionally, transplantation did not affect baseline pain thresholds in the absence of nerve injury, which suggests that transplanted interneurons may not functionally alter all spinal cord circuits. These experiments indicate that interneuron transplantation can modify neuropathic pain, a sensory disorder of the spinal cord; however, it remains to be determined whether interneuron transplantation can ameliorate motor disorders of the spinal cord characterized by increased tone, such as spasticity or incontinence.

In addition to its impressive effects in animal models of neurologic disease, interneuron transplantation has been shown to affect behavioral phenotypes common to some psychiatric disorders. Transplantation of MGE interneurons to the mouse neonatal prefrontal cortex, a brain structure involved in numerous cognitive and executive behavioral functions in rodents and humans, prevents phencyclidine-induced schizophreniform deficits in adult mice (*71*). By contrast, transplantation into the occipital cortex, a region involved in visual processing, does not prevent phencyclidine-induced deficits. These findings are consistent with post mortem studies of schizophrenic brains, which show altered chemical and molecular differentiation of interneurons in the prefrontal cortex (*62*, *64*).

Interneuron transplantation can also reduce anxiety-like behaviors in wild-type rodents. At 30 and 60 days after transplantation, but not 15 days, transplant recipients were less likely to avoid exposed areas of an elevated plus maze, a behavior indicative of diminished anxiety (*72*). Likewise, aggressive behaviors were diminished in epileptic mice that received interneuron transplants to the adult hippocampus, but not the amygdala (*32*). Moreover, while transplantation to both structures reduced hyperactivity in adult epileptic animals, it did not produce some of the anxiolytic effects observed after transplantation to wild-type neonatal animals (*72*). This finding could be attributed to differences between the transplant recipients (epileptic versus wild-type), time of transplantation (adult versus neonate), and structures targeted (hippocampus and amygdala versus neocortex). Further experiments may better define the behavioral effects of transplantation to different brain regions and may determine whether transplantation can reduce abnormal behaviors when performed after their onset.

Finally, it has yet to be determined whether interneuron transplantation, through its effects on host brain plasticity (*43*), can enhance functional recovery after injury to the central nervous system. A number of insults, such as stroke, traumatic brain injury, viral encephalitis, and anoxic brain injury, elicit focal neuronal cell death and produce secondary motor, sensory, and behavioral impairments. By inducing temporally restricted windows of brain plasticity (*43*), interneuron transplantation may enhance the brain's capacity to undergo functional recovery after such injuries. In these scenarios, interneuron transplantation would not be used to replace damaged neurons, but instead would be used to facilitate the reorganization of normal, spared neural circuits to compensate for ones damaged by injury. Although this application of interneuron transplantation has yet to be tested, there are a number of intuitive disease contexts that await study, including amblyopia (a form of blindness secondary to impaired eye movements in early life) and neonatal hypoxia-ischemia. In both conditions, ocular dominance plasticity is disrupted and vision is impaired (*54*, *73*). By inducing new ocular dominance plasticity in the visual cortex, transplanted interneurons may enable normal vision to develop in these conditions.

The Production of Cortical Interneurons in Vitro

The clinical potential of interneuron transplantation has thus far been investigated using cells from the rodent embryonic ventral forebrain. Ultimately, though, human applications will likely require transplantation of human cells. Although it has been suggested that substantial numbers of human cortical interneurons originate outside the ventral telencephalon (*74*), recent analyses of fetal brains provide evidence that the vast majority of primate cortical interneurons are in fact produced in the ventral telencephalon, at least through the second trimester of gestation (*75*, *76*). As in the developing rodent, the human ventral telencephalon contains distinct progenitor domains (medial, caudal, and lateral ganglionic eminences) marked by similar region-specific transcription factor expression (*75*, *76*). It remains to be seen, however, whether the morphogenetic factors that specify these progenitor domains are conserved between rodents and primates (*77*–*79*).

In vitro, cortical interneuron precursors have typically been produced from mouse and human embryonic stem cells (ESCs) through a two-stage process. First, ESCs are grown and differentiated on flat surfaces coated with cell matrix or fibroblasts (*80*–*82*) or as spherical aggregates [embryoid bodies (*83*, *84*)]. In this stage, undifferentiated ESCs are directed toward central nervous system progenitor identities through the use of serum-free media and mesendodermal signaling antagonists (*83*, *84*). Second, through the timed and scaled application of morphogens that confer a ventral identity, forebrain progenitor-like cells are directed toward ventral and then MGE- and CGE-like precursor phenotypes (*81*, *83*–*90*). To improve the efficiency and fidelity of ventral telencephalon-like precursor derivation, fluorescence-activated cell sorting (FACS) has been used to select for cells engineered to express fluorescent proteins under the control of forebrain-specific (*83*, *84*, *86*) and MGE-specific genetic promoters (*81*, *88*, *89*, *91*, *92*). Additionally, there has been progress toward the generation of specific cortical interneuron subtypes through the introduction of specific transcription factors into ESC-derived progenitors in vitro (*93*). Through these methods, researchers can now produce mouse and human interneurons that, after transplantation into the rodent brain, behave in a manner similar to interneurons transplanted from the mouse embryonic MGE.

The engraftment in vivo of ESC-derived interneurons was first demonstrated by the transplantation of fluorescently sorted mouse cells into the wild-type mouse brain (*81*). After differentiation in vitro, interneurons were purified by FACS to isolate those that expressed green fluorescent protein under the control of *Lhx6*, a promoter active in postmitotic interneurons of the MGE. This method of purification has overcome two key obstacles to the application of ESC-derived cell therapies: (i) the difficulty of selecting a specific and highly enriched donor population, and (ii) the need to exclude mitotically active cells, which could be tumorigenic. After FACS, the

purified population constituted just 2% of the initial population grown in vitro—a finding that highlights the challenge of directing cultured cells to an interneuron precursor-like identity. The transplanted cells migrated more than 2 mm, developed morphologies and electrophysiological properties of interneurons, and expressed some molecular markers characteristic of interneurons (GABA, somatostatin, parvalbumin, and neuropeptide Y, but not calretinin). The survival of the transplanted population at 1 month, however, was considerably lower than that observed in corresponding experiments using primary mouse MGE cells (approximately 2% versus 20%, respectively) (*33*, *40*, *81*). This reduced viability has been observed in other studies as well (*87*, *89*), which suggests that in vitro systems could select for and yield cells highly dependent on a specific set of conditions not present in vivo.

Mouse ESC-derived interneurons have been studied in a disease model of temporal lobe epilepsy (*87*). Unlike other studies (*81*, *91*), these experiments did not use FACS to enrich for interneuron precursor-like cells prior to transplantation. Nonetheless, the ESC-derived cells migrated throughout the host hippocampus, and after 2 to 3 months approximately 90% of them expressed neuronal markers. One host animal, however, developed a transplant-derived teratoma, indicating that extended differentiation protocols and selection of postmitotic neurons may be required to avoid the transplantation of tumorigenic cell types (*86*, *89*). Approximately half of the transplanted cells developed a GABAergic phenotype, yet relatively few of them (≤10%) expressed interneuron subtype-specific markers (somatostatin, parvalbumin, and calretinin). Although a moderate fraction of the transplanted cells had electrophysiological properties of mature cortical interneurons, these cells demonstrated reduced frequencies and amplitudes of excitatory synaptic events relative to interneurons of the host brain, which suggests that their integration into host circuits was limited. Further studies are needed to determine whether these results reflect a limitation of cells produced in vitro, or whether their integration was affected by the altered physiology of the epileptic host. Transplanted ESC-derived interneurons nearly doubled the GABAergic population of the hippocampus, which was partially depleted by pilocarpine-induced seizures. Transplantation did not, however, reduce mossy fiber sprouting (a correlate of neuronal reorganization in the epileptic hippocampus). Unfortunately, the seizure phenotype of these transplant recipients was not assessed.

Finally, experiments using human ESCs and induced pluripotent stem cells have provided proof of concept that human cortical interneurons can be produced in vitro, while also elucidating challenges specific to the use of human cells (*88*, *89*). In these studies, the development of ESC-derived human MGE-like interneurons was tracked for up to 7 months, both in vitro, on mouse feeder layers and brain slices, and in vivo, after transplantation to the postnatal mouse cortex. In one study, transplanted human ESC-derived interneurons exhibited immature phenotypes (unipolar or bipolar morphologies and expression of Dcx and Nkx2.1) 2 months after transplantation (*88*). When examined 7 months after transplantation (*89*), large fractions (as many as 50 to 75%) of the transplanted cells expressed one or more molecular markers characteristic of interneuron subtype maturation (somatostatin, calretinin, and calbindin); developed highly branched morphologies; and down-regulated expression of Dcx and Nkx2.1, two markers of immature interneurons. Essentially all cells expressed electrophysiological properties of mature interneurons and demonstrated excitatory synaptic currents, which suggests that they integrated into the host mouse cortex (*89*). Tumor formation was not noted (*89*), and transplanted interneurons dispersed 1 to 2 mm from the site of injection. Transplanted human ESC-derived interneurons (*88*, *89*) survived and expressed interneuron markers in greater numbers than did cells derived from mouse ESCs (*87*). For reasons that are unclear, however, very few of the transplanted human cells developed into mature fast-spiking, parvalbumin-expressing interneurons, despite the use of culture conditions and fluorescence purification methods expected to favor the production and selection of this cell type (*88*, *89*).

When transplanted into the postnatal mouse brain, human ESC-derived interneurons exhibit a protracted maturation similar to that of endogenous interneurons in the neonatal human cortex; this result suggests that pluripotent stem cell–derived interneuron development parallels endogenous human interneuron development (*88*, *89*). Thus, the time course of cellular maturation was not altered by transplantation into the neonatal mouse cortex, in which endogenous interneurons mature within 6 weeks of their production (*36*). These findings support the notion that interneuron maturation is more likely defined by intrinsic, organism-specific developmental programs, which, in human cells, play out over an extended time course. When cocultured on mouse cortical feeder layers, human ESC–derived interneurons may mature more quickly than cells cocultured on human cortical feeder layers (*88*), which suggests that environmental factors can influence their rate of maturation in vitro. Ultimately, the clinical application of human interneuron transplantation will likely require the development of cell culture systems that preserve, or possibly accelerate, the cellular mechanisms governing interneuron maturation.

The modification of neural circuits, for either therapeutic or experimental purposes, is possible through the transplantation of ventral telencephalon interneurons, a cell population that has a unique capacity to navigate and integrate into the postnatal nervous system. Given the central role of inhibition in neural circuit assembly and function, these studies of interneuron transplantation may be a prelude to the precise and directed adjustment of dysfunctional circuits in a number of disease settings. Ultimately, the generation of interneuron cell populations for transplantation, as well as the rational application of interneuron transplantation strategies, will benefit from a better understanding of this unique cell type's development.

References and Notes

1. J. Altman, Autoradiographic investigation of cell proliferation in the brains of rats and cats. *Anat. Rec.* **145**, 573–591 (1963). doi: 10.1002/ar.1091450409; pmid: 14012334
2. M. S. Kaplan, J. W. Hinds, Neurogenesis in the adult rat: Electron microscopic analysis of light radioautographs. *Science* **197**, 1092–1094 (1977). doi: 10.1126/science.887941; pmid: 887941
3. S. A. Goldman, F. Nottebohm, Neuronal production, migration, and differentiation in a vocal control nucleus of the adult female canary brain. *Proc. Natl. Acad. Sci. U.S.A.* **80**, 2390–2394 (1983). doi: 10.1073/pnas.80.8.2390; pmid: 6572982
4. C. Lois, A. Alvarez-Buylla, Long-distance neuronal migration in the adult mammalian brain. *Science* **264**, 1145–1148 (1994). doi: 10.1126/science.8178174; pmid: 8178174
5. P. S. Eriksson *et al.*, Neurogenesis in the adult human hippocampus. *Nat. Med.* **4**, 1313–1317 (1998). doi: 10.1038/3305; pmid: 9809557
6. E. Gould, A. Beylin, P. Tanapat, A. Reeves, T. J. Shors, Learning enhances adult neurogenesis in the hippocampal formation. *Nat. Neurosci.* **2**, 260–265 (1999). doi: 10.1038/6365; pmid: 10195219
7. D. R. Kornack, P. Rakic, The generation, migration, and differentiation of olfactory neurons in the adult primate brain. *Proc. Natl. Acad. Sci. U.S.A* **98**, 4752–4757 (2001). doi: 10.1073/pnas.081074998; pmid: 11296302
8. V. Pencea, K. D. Bingaman, L. J. Freedman, M. B. Luskin, Neurogenesis in the subventricular zone and rostral migratory stream of the neonatal and adult primate forebrain. *Exp. Neurol.* **172**, 1–16 (2001). doi: 10.1006/exnr.2001.7768; pmid: 11681836
9. O. Lindvall *et al.*, Grafts of fetal dopamine neurons survive and improve motor function in Parkinson's disease. *Science* **247**, 574–577 (1990). doi: 10.1126/science.2105529; pmid: 2105529
10. F. H. Gage, Transplantation in the future. *Prog. Brain Res.* **200**, 7–13 (2012). doi: 10.1016/B978-0-444-59575-1.00001-6; pmid: 23195412
11. S. B. Dunnett, A. Björklund, Introduction (part II). *Prog. Brain Res.* **201**, 3–5 (2012). doi: 10.1016/B978-0-444-59544-7.00017-2; pmid: 23186706
12. S. A. Anderson, D. D. Eisenstat, L. Shi, J. L. Rubenstein, Interneuron migration from basal forebrain to neocortex: Dependence on Dlx genes. *Science* **278**, 474–476 (1997). doi: 10.1126/science.278.5337.474; pmid: 9334308
13. Y. Kawaguchi, Y. Kubota, GABAergic cell subtypes and their synaptic connections in rat frontal cortex. *Cereb. Cortex* **7**, 476–486 (1997). doi: 10.1093/cercor/7.6.476; pmid: 9276173
14. S. J. Pleasure *et al.*, Cell migration from the ganglionic eminences is required for the development of hippocampal GABAergic interneurons. *Neuron* **28**, 727–740 (2000). doi: 10.1016/S0896-6273(00)00149-5; pmid: 11163262
15. S. Nery, G. Fishell, J. G. Corbin, The caudal ganglionic eminence is a source of distinct cortical and subcortical cell populations. *Nat. Neurosci.* **5**, 1279–1287 (2002). doi: 10.1038/nn971; pmid: 12411960
16. Q. Xu, I. Cobos, E. De La Cruz, J. L. Rubenstein, S. A. Anderson, Origins of cortical interneuron subtypes. *J. Neurosci.* **24**, 2612–2622 (2004). doi: 10.1523/JNEUROSCI.5667-03.2004; pmid: 15028753
17. S. J. B. Butt *et al.*, The temporal and spatial origins of cortical interneurons predict their physiological subtype. *Neuron* **48**, 591–604 (2005). doi: 10.1016/j.neuron.2005.09.034; pmid: 16301176
18. C. Wonders, S. A. Anderson, Cortical interneurons and their origins. *Neuroscientist* **11**, 199–205 (2005). doi: 10.1177/1073858404270968; pmid: 15911869

19. H. Wichterle, D. H. Turnbull, S. Nery, G. Fishell, A. Alvarez-Buylla, In utero fate mapping reveals distinct migratory pathways and fates of neurons born in the mammalian basal forebrain. *Development* **128**, 3759–3771 (2001). pmid: 11585802
20. O. Marín, J. L. Rubenstein, Cell migration in the forebrain. *Annu. Rev. Neurosci.* **26**, 441–483 (2003). doi: 10.1146/annurev.neuro.26.041002.131058; pmid: 12626695
21. M. Yozu, H. Tabata, K. Nakajima, The caudal migratory stream: A novel migratory stream of interneurons derived from the caudal ganglionic eminence in the developing mouse forebrain. *J. Neurosci.* **25**, 7268–7277 (2005). doi: 10.1523/JNEUROSCI.2072-05.2005; pmid: 16079409
22. G. Bartolini, G. Ciceri, O. Marín, Integration of GABAergic interneurons into cortical cell assemblies: Lessons from embryos and adults. *Neuron* **79**, 849–864 (2013). doi: 10.1016/j.neuron.2013.08.014; pmid: 24012001
23. H. Markram *et al*., Interneurons of the neocortical inhibitory system. *Nat. Rev. Neurosci.* **5**, 793–807 (2004). doi: 10.1038/nrn1519; pmid: 15378039
24. O. Isacson *et al*., Neural grafting in a rat model of Huntington's disease: Striosomal-like organization of striatal grafts as revealed by acetylcholinesterase histochemistry, immunocytochemistry and receptor autoradiography. *Neuroscience* **22**, 481–497 (1987). doi: 10.1016/0306-4522(87)90348-4; pmid: 2823174
25. A. M. Graybiel, F. C. Liu, S. B. Dunnett, Intrastriatal grafts derived from fetal striatal primordia. I. Phenotypy and modular organization. *J. Neurosci.* **9**, 3250–3271 (1989). pmid: 2477513
26. P. Pakzaban, T. W. Deacon, L. H. Burns, O. Isacson, Increased proportion of acetylcholinesterase-rich zones and improved morphological integration in host striatum of fetal grafts derived from the lateral but not the medial ganglionic eminence. *Exp. Brain Res.* **97**, 13–22 (1993). doi: 10.1007/BF00228813; pmid: 7907548
27. M. Olsson, K. Campbell, K. Wictorin, A. Björklund, Projection neurons in fetal striatal transplants are predominantly derived from the lateral ganglionic eminence. *Neuroscience* **69**, 1169–1182 (1995). doi: 10.1016/0306-4522(95)00325-D; pmid: 8848105
28. M. Olsson, C. Bentlage, K. Wictorin, K. Campbell, A. Björklund, Extensive migration and target innervation by striatal precursors after grafting into the neonatal striatum. *Neuroscience* **79**, 57–78 (1997). doi: 10.1016/S0306-4522(96)00606-9; pmid: 9178865
29. H. Wichterle, J. M. Garcia-Verdugo, D. G. Herrera, A. Alvarez-Buylla, Young neurons from medial ganglionic eminence disperse in adult and embryonic brain. *Nat. Neurosci.* **2**, 461–466 (1999). doi: 10.1038/8131; pmid: 10321251
30. V. Martínez-Cerdeño *et al*., Embryonic MGE precursor cells grafted into adult rat striatum integrate and ameliorate motor symptoms in 6-OHDA-lesioned rats. *Cell Stem Cell* **6**, 238–250 (2010). doi: 10.1016/j.stem.2010.01.004; pmid: 20207227
31. I. Zipancic, M. E. Calcagnotto, M. Piquer-Gil, L. E. Mello, M. Alvarez-Dolado, Transplant of GABAergic precursors restores hippocampal inhibitory function in a mouse model of seizure susceptibility. *Cell Transplant.* **19**, 549–564 (2010). doi: 10.3727/096368910X491383; pmid: 20144261
32. R. F. Hunt, K. M. Girskis, J. L. Rubenstein, A. Alvarez-Buylla, S. C. Baraban, GABA progenitors grafted into the adult epileptic brain control seizures and abnormal behavior. *Nat. Neurosci.* **16**, 692–697 (2013). doi: 10.1038/nn.3392; pmid: 23644485
33. M. Alvarez-Dolado *et al*., Cortical inhibition modified by embryonic neural precursors grafted into the postnatal brain. *J. Neurosci.* **26**, 7380–7389 (2006). doi: 10.1523/JNEUROSCI.1540-06.2006; pmid: 16837585
34. J. M. Bráz *et al*., Forebrain GABAergic neuron precursors integrate into adult spinal cord and reduce injury-induced neuropathic pain. *Neuron* **74**, 663–675 (2012). doi: 10.1016/j.neuron.2012.02.033; pmid: 22632725
35. J. L. Hanover, Z. J. Huang, S. Tonegawa, M. P. Stryker, Brain-derived neurotrophic factor overexpression induces precocious critical period in mouse visual cortex. *J. Neurosci.* **19**, RC40 (1999). pmid: 10559430
36. Y. Gonchar, Q. Wang, A. Burkhalter, Multiple distinct subtypes of GABAergic neurons in mouse visual cortex identified by triple immunostaining. *Front. Neuroanat.* **1**, 3 (2007). pmid: 18958197
37. M. Fogarty *et al*., Spatial genetic patterning of the embryonic neuroepithelium generates GABAergic interneuron diversity in the adult cortex. *J. Neurosci.* **27**, 10935–10946 (2007). doi: 10.1523/JNEUROSCI.1629-07.2007; pmid: 17928435
38. C. P. Wonders *et al*., A spatial bias for the origins of interneuron subgroups within the medial ganglionic eminence. *Dev. Biol.* **314**, 127–136 (2008). doi: 10.1016/j.ydbio.2007.11.018; pmid: 18155689
39. S. C. Baraban *et al*., Reduction of seizures by transplantation of cortical GABAergic interneuron precursors into Kv1.1 mutant mice. *Proc. Natl. Acad. Sci. U.S.A.* **106**, 15472–15477 (2009). doi: 10.1073/pnas.0900141106; pmid: 19706400
40. D. G. Southwell, R. C. Froemke, A. Alvarez-Buylla, M. P. Stryker, S. P. Gandhi, Cortical plasticity induced by inhibitory neuron transplantation. *Science* **327**, 1145–1148 (2010). doi: 10.1126/science.1183962; pmid: 20185728
41. M. Inan, J. Welagen, S. A. Anderson, Spatial and temporal bias in the mitotic origins of somatostatin- and parvalbumin-expressing interneuron subgroups and the chandelier subtype in the medial ganglionic eminence. *Cereb. Cortex* **22**, 820–827 (2012). doi: 10.1093/cercor/bhr148; pmid: 21693785
42. H. Taniguchi, J. Lu, Z. J. Huang, The spatial and temporal origin of chandelier cells in mouse neocortex. *Science* **339**, 70–74 (2013). doi: 10.1126/science.1227622; pmid: 23180771
43. D. G. Southwell *et al*., Intrinsically determined cell death of developing cortical interneurons. *Nature* **491**, 109–113 (2012). doi: 10.1038/nature11523; pmid: 23041929
44. T. Du, Q. Xu, P. J. Ocbina, S. A. Anderson, NKX2.1 specifies cortical interneuron fate by activating Lhx6. *Development* **135**, 1559–1567 (2008). doi: 10.1242/dev.015123; pmid: 18339674
45. R. Klein *et al*., Targeted disruption of the trkB neurotrophin receptor gene results in nervous system lesions and neonatal death. *Cell* **75**, 113–122 (1993). doi: 10.1016/0092-8674(93)90683-H; pmid: 8402890
46. S. Kimura *et al*., The T/ebp null mouse: Thyroid-specific enhancer-binding protein is essential for the organogenesis of the thyroid, lung, ventral forebrain, and pituitary. *Genes Dev.* **10**, 60–69 (1996). doi: 10.1101/gad.10.1.60; pmid: 8557195
47. Q. Xu *et al*., Sonic hedgehog signaling confers ventral telencephalic progenitors with distinct cortical interneuron fates. *Neuron* **65**, 328–340 (2010). doi: 10.1016/j.neuron.2010.01.004; pmid: 20159447
48. J. J. Palop, L. Mucke, Amyloid-β-induced neuronal dysfunction in Alzheimer's disease: From synapses toward neural networks. *Nat. Neurosci.* **13**, 812–818 (2010). doi: 10.1038/nn.2583; pmid: 20581818
49. M. P. J. Dekkers, Y.-A. Barde, Programmed cell death in neuronal development. *Science* **340**, 39–41 (2013). doi: 10.1126/science.1236152; pmid: 23559240
50. R. R. Buss, W. Sun, R. W. Oppenheim, Adaptive roles of programmed cell death during nervous system development. *Annu. Rev. Neurosci.* **29**, 1–35 (2006). doi: 10.1146/annurev.neuro.29.051605.112800; pmid: 16776578
51. V. Hamburger, R. Levi-Montalcini, Proliferation, differentiation and degeneration in the spinal ganglia of the chick embryo under normal and experimental conditions. *J. Exp. Zool.* **111**, 457–501 (1949). doi: 10.1002/jez.1401110308; pmid: 18142378
52. R. Levi-Montalcini, The development to the acoustico-vestibular centers in the chick embryo in the absence of the afferent root fibers and of descending fiber tracts. *J. Comp. Neurol.* **91**, 209–241, t3 (1949). doi: 10.1002/cne.900910204; pmid: 15408222
53. V. Nikoletopoulou *et al*., Neurotrophin receptors TrkA and TrkC cause neuronal death whereas TrkB does not. *Nature* **467**, 59–63 (2010). doi: 10.1038/nature09336; pmid: 20811452
54. T. K. Hensch, Critical period plasticity in local cortical circuits. *Nat. Rev. Neurosci.* **6**, 877–888 (2005). doi: 10.1038/nrn1787; pmid: 16261181
55. T. K. Hensch *et al*., Local GABA circuit control of experience-dependent plasticity in developing visual cortex. *Science* **282**, 1504–1508 (1998). doi: 10.1126/science.282.5393.1504; pmid: 9822384
56. M. Fagiolini *et al*., Specific $GABA_A$ circuits for visual cortical plasticity. *Science* **303**, 1681–1683 (2004). doi: 10.1126/science.1091032; pmid: 15017002
57. S. Sugiyama *et al*., Experience-dependent transfer of Otx2 homeoprotein into the visual cortex activates postnatal plasticity. *Cell* **134**, 508–520 (2008). doi: 10.1016/j.cell.2008.05.054; pmid: 18692473
58. J. A. Gordon, M. P. Stryker, Experience-dependent plasticity of binocular responses in the primary visual cortex of the mouse. *J. Neurosci.* **16**, 3274–3286 (1996). pmid: 8627365
59. T. Pizzorusso *et al*., Reactivation of ocular dominance plasticity in the adult visual cortex. *Science* **298**, 1248–1251 (2002). doi: 10.1126/science.1072699; pmid: 12424383
60. M. Kato, W. B. Dobyns, X-linked lissencephaly with abnormal genitalia as a tangential migration disorder causing intractable epilepsy: Proposal for a new term, "interneuronopathy". *J. Child Neurol.* **20**, 392–397 (2005). doi: 10.1177/08830738050200042001; pmid: 15921244
61. J. L. R. Rubenstein, M. M. Merzenich, Model of autism: Increased ratio of excitation/inhibition in key neural systems. *Genes Brain Behav.* **2**, 255–267 (2003). doi: 10.1034/j.1601-183X.2003.00037.x; pmid: 14606691
62. D. A. Lewis, T. Hashimoto, D. W. Volk, Cortical inhibitory neurons and schizophrenia. *Nat. Rev. Neurosci.* **6**, 312–324 (2005). doi: 10.1038/nrn1648; pmid: 15803162
63. H.-T. Chao *et al*., Dysfunction in GABA signalling mediates autism-like stereotypies and Rett syndrome phenotypes. *Nature* **468**, 263–269 (2010). doi: 10.1038/nature09582; pmid: 21068835
64. O. Marín, Interneuron dysfunction in psychiatric disorders. *Nat. Rev. Neurosci.* **13**, 107–120 (2012). pmid: 22251963
65. L. Verret *et al*., Inhibitory interneuron deficit links altered network activity and cognitive dysfunction in Alzheimer model. *Cell* **149**, 708–721 (2012). doi: 10.1016/j.cell.2012.02.046; pmid: 22541439
66. E. Rossignol, Genetics and function of neocortical GABAergic interneurons in neurodevelopmental disorders. *Neural Plast.* **2011**, 649325 (2011). doi: 10.1155/2011/649325; pmid: 21876820
67. Y. Ben-Ari, Neuro-archaeology: Pre-symptomatic architecture and signature of neurological disorders. *Trends Neurosci.* **31**, 626–636 (2008). doi: 10.1016/j.tins.2008.09.002; pmid: 18951639
68. M. E. Calcagnotto *et al*., Effect of neuronal precursor cells derived from medial ganglionic eminence in an acute epileptic seizure model. *Epilepsia* **51**, 71–75 (2010). doi: 10.1111/j.1528-1167.2010.02614.x; pmid: 20618405
69. E. De la Cruz *et al*., Interneuron progenitors attenuate the power of acute focal ictal discharges. *Neurotherapeutics* **8**, 763–773 (2011). doi: 10.1007/s13311-011-0058-9; pmid: 21748528
70. R. M. Richardson, N. M. Barbaro, A. Alvarez-Buylla, S. C. Baraban, Developing cell transplantation for temporal lobe epilepsy. *Neurosurg. Focus* **24**, E17 (2008). doi: 10.3171/FOC/2008/24/3-4/E16; pmid: 18341393
71. D. H. Tanaka, K. Toriumi, K. Kubo, T. Nabeshima, K. Nakajima, GABAergic precursor transplantation into the prefrontal cortex prevents phencyclidine-induced cognitive deficits. *J. Neurosci.* **31**, 14116–14125 (2011). doi: 10.1523/JNEUROSCI.2786-11.2011; pmid: 21976496
72. M. F. Valente *et al*., Postnatal transplantation of interneuronal precursor cells decreases anxiety-like behavior in adult mice. *Cell Transplant.* **22**, 1237–1247 (2013). doi: 10.3727/096368912X657422; pmid: 23031356
73. S. Failor *et al*., Neonatal cerebral hypoxia-ischemia impairs plasticity in rat visual cortex. *J. Neurosci.* **30**, 81–92 (2010). doi: 10.1523/JNEUROSCI.5656-08.2010; pmid: 20053890

74. K. Letinic, R. Zoncu, P. Rakic, Origin of GABAergic neurons in the human neocortex. *Nature* **417**, 645–649 (2002). doi: 10.1038/nature00779; pmid: 12050665
75. D. V. Hansen *et al*., Non-epithelial stem cells and cortical interneuron production in the human ganglionic eminences. *Nat. Neurosci.* **16**, 1576–1587 (2013). doi: 10.1038/nn.3541; pmid: 24097039
76. T. Ma *et al*., Subcortical origins of human and monkey neocortical interneurons. *Nat. Neurosci.* **16**, 1588–1597 (2013). doi: 10.1038/nn.3536; pmid: 24097041
77. J. M. Hébert, G. Fishell, The genetics of early telencephalon patterning: Some assembly required. *Nat. Rev. Neurosci.* **9**, 678–685 (2008). doi: 10.1038/nrn2463; pmid: 19143049
78. R. V. Hoch, J. L. R. Rubenstein, S. Pleasure, Genes and signaling events that establish regional patterning of the mammalian forebrain. *Semin. Cell Dev. Biol.* **20**, 378–386 (2009). doi: 10.1016/j.semcdb.2009.02.005; pmid: 19560042
79. A. L. Goulburn, E. G. Stanley, A. G. Elefanty, S. A. Anderson, Generating GABAergic cerebral cortical interneurons from mouse and human embryonic stem cells. *Stem Cell Res.* **8**, 416–426 (2012). doi: 10.1016/j.scr.2011.12.002; pmid: 22280980
80. Q.-L. Ying, A. G. Smith, Defined conditions for neural commitment and differentiation. *Methods Enzymol.* **365**, 327–341 (2003). doi: 10.1016/S0076-6879(03)65023-8; pmid: 14696356
81. A. M. Maroof, K. Brown, S.-H. Shi, L. Studer, S. A. Anderson, Prospective isolation of cortical interneuron precursors from mouse embryonic stem cells. *J. Neurosci.* **30**, 4667–4675 (2010). doi: 10.1523/JNEUROSCI.4255-09.2010; pmid: 20357117
82. S. M. Chambers *et al*., Highly efficient neural conversion of human ES and iPS cells by dual inhibition of SMAD signaling. *Nat. Biotechnol.* **27**, 275–280 (2009). doi: 10.1038/nbt.1529; pmid: 19252484
83. K. Watanabe *et al*., Directed differentiation of telencephalic precursors from embryonic stem cells. *Nat. Neurosci.* **8**, 288–296 (2005). doi: 10.1038/nn1402; pmid: 15696161
84. K. Watanabe *et al*., A ROCK inhibitor permits survival of dissociated human embryonic stem cells. *Nat. Biotechnol.* **25**, 681–686 (2007). doi: 10.1038/nbt1310; pmid: 17529971
85. X.-J. Li *et al*., Coordination of sonic hedgehog and Wnt signaling determines ventral and dorsal telencephalic neuron types from human embryonic stem cells. *Development* **136**, 4055–4063 (2009). doi: 10.1242/dev.036624; pmid: 19906872
86. T. Danjo *et al*., Subregional specification of embryonic stem cell-derived ventral telencephalic tissues by timed and combinatory treatment with extrinsic signals. *J. Neurosci.* **31**, 1919–1933 (2011). doi: 10.1523/JNEUROSCI.5128-10.2011; pmid: 21289201
87. X. Maisano *et al*., Differentiation and functional incorporation of embryonic stem cell-derived GABAergic interneurons in the dentate gyrus of mice with temporal lobe epilepsy. *J. Neurosci.* **32**, 46–61 (2012). doi: 10.1523/JNEUROSCI.2683-11.2012; pmid: 22219269
88. A. M. Maroof *et al*., Directed differentiation and functional maturation of cortical interneurons from human embryonic stem cells. *Cell Stem Cell* **12**, 559–572 (2013). doi: 10.1016/j.stem.2013.04.008; pmid: 23642365
89. C. R. Nicholas *et al*., Functional maturation of hPSC-derived forebrain interneurons requires an extended timeline and mimics human neural development. *Cell Stem Cell* **12**, 573–586 (2013). doi: 10.1016/j.stem.2013.04.005; pmid: 23642366
90. S. Cambray *et al*., Activin induces cortical interneuron identity and differentiation in embryonic stem cell-derived telencephalic neural precursors. *Nat. Commun.* **3**, 841 (2012). doi: 10.1038/ncomms1817; pmid: 22588303
91. A. L. Goulburn *et al*., A targeted NKX2.1 human embryonic stem cell reporter line enables identification of human basal forebrain derivatives. *Stem Cells* **29**, 462–473 (2011). doi: 10.1002/stem.587; pmid: 21425409
92. Y.-J. J. Chen *et al*., Use of "MGE enhancers" for labeling and selection of embryonic stem cell-derived medial ganglionic eminence (MGE) progenitors and neurons. *PLOS ONE* **8**, e61956 (2013). doi: 10.1371/journal.pone.0061956; pmid: 23658702
93. E. Au *et al*., A modular gain-of-function approach to generate cortical interneuron subtypes from ES cells. *Neuron* **80**, 1145–1158 (2013). doi: 10.1016/j.neuron.2013.09.022; pmid: 24314726

Acknowledgments: We thank S. Baraban for comments on the manuscript. We apologize to colleagues whose work we could not include because of space limitations. This work was supported by the NIH (R01-EY02874 to M.P.S., HD032116, NS28478 to A.A.-B., MH049428 to J.L.R., NS78326 and NS14627 to A.I.B.), by the California Institute of Regenerative Medicine (RC1-00346 and TR3-05606 to A.R.K., RB2-01602 to J.L.R., and TR2-01749 to A.A.-B.) and by the JG Bowes Foundation. A.A.-B., A.R.K., J.L.R., C.R.N.; Founders and shareholders, Neurona Therapeutics; M.S. Scientific Advisory Board of the Allen Institute for Brain Science. Related research in the authors' laboratories is funded by the National Institutes of Health (A.I.B., M.P.S., A.R.K., J.L.R., A.A.-B.), National Institute of Mental Health (J.L.R.), and California Institute for Regenerative Medicine (C.R.N., A.I.B., M.P.S., A.R.K., J.L.R., A.A.-B.). Patents related to this work: 20020151066 (UC Regents, issued 2000, Production of GABAergic Cells)—J.L.R., M. Mione, S. Anderson, T. Stuehmer, K. Yun; 20090311222 (UC Regents, 2006-pending, Transplantation of Neural Cells)—S. Baraban, J.L.R., A.A.-B.; 20130202568 (UC Regents, 2008-pending, Ameliorating Nervous System Disorders)—A.R.K., J.L.R., S. Baraban, A.A.-B.; 2013155222 A2 (UC Regents, 2012-pending, Brain-Specific Enhancers for Cell-Based Therapy)—V. Axel, J.L.R., Y.-J. Chen, L. Pennacchio, D. Vogt, A.R.K.; 61783594 (UC Regents, 2013-pending, In Vitro Production of Medial Ganglionic Eminence Precursor Cells)—C.R.N., J.L.R., A.R.K.

10.1126/science.1240622

function relationship of ESF1 is consistent with other cysteine-rich peptides, such as those involved in cell signaling of the stomatal cell lineage (*24*), and further supports their signaling role during early embryogenesis. Moreover, we argue that ESF1 regulation of early suspensor growth arose from parental conflict (*35*) and provides a maternal advantage over embryo growth at a critical stage when parental investment determines the fate of the offspring. ESF1 peptides are not imprinted like the related maternally expressed MEG1 peptides in maize (*8*, *36*), but are maternally deposited in the central cell gamete and early in the endosperm, which may be indicative of their immediate requirement at the onset of fertilization. Thus, plants appear to have evolved multiple independent strategies in the form of embryonic and extraembryonic factors, including mobile RNAs and peptides, to maternally control early embryogenesis.

Methods Summary

All plant material used in this study was derived from the wild-type *Columbia* (*Col*-0) accession and mutant alleles *cdka*;1 (*30*), *kpl*-1 (*31*), *ssp*-2 (*28*), *CA-YDA*, and *yda*-2991 (*29*). Details of transgenic lines can be found in the supplementary materials and methods. Microarray analysis was performed on wild-type developing siliques collected after manual pollination (*14*). Quantitative polymerase chain reaction analysis was performed as described in the supplementary materials and methods, with oligonucleotides listed in table S6. Details of histochemical and structural biochemical analyses of ESF1 peptides are fully described in the supplementary materials and methods. Sequence of the codon-optimized synthetic *ESF1* gene constructs is listed in table S7.

References and Notes

1. S. Lau, D. Slane, O. Herud, J. Kong, G. Jürgens, *Annu. Rev. Plant Biol.* **63**, 483–506 (2012).
2. M. D. Nodine, D. P. Bartel, *Nature* **482**, 94–97 (2012).
3. J. J. Petricka, J. M. Van Norman, P. N. Benfey, *Cold Spring Harb. Perspect. Biol.* **1**, a000497 (2009).
4. T. Kawashima, R. B. Goldberg, *Trends Plant Sci.* **15**, 23–30 (2010).
5. V. L. Dodeman, G. Ducreux, M. Kreis, *J. Exp. Bot.* **48**, 1493–1509 (1997).
6. E. C. Yeung, D. W. Meinke, *Plant Cell* **5**, 1371–1381 (1993).
7. D. Weijers, J. P. Van Hamburg, E. Van Rijn, P. J. Hooykaas, R. Offringa, *Plant Physiol.* **133**, 1882–1892 (2003).
8. L. M. Costa *et al.*, *Curr. Biol.* **22**, 160–165 (2012).
9. L. Katsir, K. A. Davies, D. C. Bergmann, T. Laux, *Curr. Biol.* **21**, R356–R364 (2011).
10. S. Kiyohara, S. Sawa, *Plant Cell Physiol.* **53**, 1989–1999 (2012).
11. E. Marshall, L. M. Costa, J. Gutierrez-Marcos, *J. Exp. Bot.* **62**, 1677–1686 (2011).
12. S. Okuda *et al.*, *Nature* **458**, 357–361 (2009).
13. S. Sprunck *et al.*, *Science* **338**, 1093–1097 (2012).
14. M. Tesfaye *et al.*, *PLOS ONE* **8**, e58992 (2013).
15. I. Moore, M. Samalova, S. Kurup, *Plant J.* **45**, 651–683 (2006).
16. H. Breuninger, E. Rikirsch, M. Hermann, M. Ueda, T. Laux, *Dev. Cell* **14**, 867–876 (2008).
17. I. Blilou *et al.*, *Nature* **433**, 39–44 (2005).
18. E. H. Rademacher *et al.*, *Dev. Cell* **22**, 211–222 (2012).
19. J. Friml *et al.*, *Nature* **426**, 147–153 (2003).
20. M. G. Heisler *et al.*, *Curr. Biol.* **15**, 1899–1911 (2005).
21. S. Ohki, M. Takeuchi, M. Mori, *Nat. Commun.* **2**, 512 (2011).
22. I. Beets *et al.*, *Science* **338**, 543–545 (2012).
23. A. Garelli, A. M. Gontijo, V. Miguela, E. Caparros, M. Dominguez, *Science* **336**, 579–582 (2012).
24. S. Ohki, K. Dohi, A. Tamai, M. Takeuchi, M. Mori, *J. Biomol. NMR* **42**, 271–277 (2008).
25. S. S. Sugano *et al.*, *Nature* **463**, 241–244 (2010).
26. G. Cornilescu, F. Delaglio, A. Bax, *J. Biomol. NMR* **13**, 289–302 (1999).
27. P. J. Simpson, H. Xie, D. N. Bolam, H. J. Gilbert, M. P. Williamson, *J. Biol. Chem.* **275**, 41137–41142 (2000).
28. M. Bayer *et al.*, *Science* **323**, 1485–1488 (2009).
29. W. Lukowitz, A. Roeder, D. Parmenter, C. Somerville, *Cell* **116**, 109–119 (2004).
30. M. K. Nowack *et al.*, *Nat. Genet.* **38**, 63–67 (2006).
31. M. Ron, M. Alandete Saez, L. Eshed Williams, J. C. Fletcher, S. McCormick, *Genes Dev.* **24**, 1010–1021 (2010).
32. S. J. Aw, Y. Hamamura, Z. Chen, A. Schnittger, F. Berger, *Development* **137**, 2683–2690 (2010).
33. W. E. Friedman, *Am. J. Bot.* **81**, 1468–1486 (1994).
34. Z. Zhang, T. Laux, *Sex. Plant Reprod.* **24**, 161–169 (2011).
35. R. L. Trivers, *Am. Zool.* **14**, 249–264 (1974).
36. J. F. Gutiérrez-Marcos *et al.*, *Plant Cell* **16**, 1288–1301 (2004).

Acknowledgments: We thank H. Prescott, A. Sarmiento, D. Garcia, and E. Caamaño for technical assistance. We also thank T. Laux, W. Lukowitz, I. Moore, B. Scheres, A. Schnittger, M. Bayer, and D. Weijers for seed stocks and valuable suggestions. We acknowledge funding from the Royal Society, ESF/RTD Framework COST action (FA0903), and Biotechnology and Biological Sciences Research Council grants (BB/F008082, BB/L003023/1 and BB/L003023). The work at the University of Minnesota was supported by NSF award IOB-0516811. NMR experiments were partly supported by Nanotechnology Platform Program of the Ministry of Education, Culture, Sports, Science and Technology (MEXT), Japan. K.S. and M.T. acknowledge the Minnesota Supercomputing Institute for computational resources and systems support used in microarray analysis. M.T. and K.S. performed microarray experiments and data analysis. E.M validated the array data, generated most transgenic lines, and conducted genetic analyses. L.M.C designed and performed genetic experiments, generated the LhG4 transactivation lines, and performed immunodetection. S.L.O. and R.P. performed the ovule culture experiments. K.B. identified the suspensor-specific *At2g30560* gene and generated pGRP-GUS:GFP lines. M.M. expressed ESF1 peptides. M.M., Y.U. and S.O. purified synthetic wild-type and mutant ESF1 peptides and performed solution NMR structural analysis. J.G-M., K. V., S.O., and M.M. conceived and supervised the study. J.G-M. and L.M.C. wrote the paper with input from S.O. All authors have reviewed and approved the paper, and the authors disclose no conflicts of interest.

Supplementary Materials

www.sciencemag.org/content/344/6180/168/suppl/DC1
Materials and Methods
Figs. S1 to S13
Tables S1 to S7
References (*37*–*52*)

10 July 2013; accepted 4 March 2014
10.1126/science.1243005

Flies Evade Looming Targets by Executing Rapid Visually Directed Banked Turns

Florian T. Muijres,[1] Michael J. Elzinga,[1] Johan M. Melis,[1,2] Michael H. Dickinson[1]*

Avoiding predators is an essential behavior in which animals must quickly transform sensory cues into evasive actions. Sensory reflexes are particularly fast in flying insects such as flies, but the means by which they evade aerial predators is not known. Using high-speed videography and automated tracking of flies in combination with aerodynamic measurements on flapping robots, we show that flying flies react to looming stimuli with directed banked turns. The maneuver consists of a rapid body rotation followed immediately by an active counter-rotation and is enacted by remarkably subtle changes in wing motion. These evasive maneuvers of flies are substantially faster than steering maneuvers measured previously and indicate the existence of sensory-motor circuitry that can reorient the fly's flight path within a few wingbeats.

Flies are among the most agile flying animals and have served as a model for many features of sensory physiology (*1*), muscle mechanics (*2*, *3*), and aerodynamics (*4*–*7*). Among their most impressive flight behaviors are evasive maneuvers, as witnessed by anyone who has attempted to swat them. The evasive takeoff behaviors of flies have been thoroughly investigated, and evidence suggests that they can quickly determine the direction of a looming threat and bias their jump in the opposite direction (*8*). Although the escape maneuvers of flying flies have recently been observed (*9*), they have not been systematically analyzed and it is not known whether, or how, they detect and evade a rapidly approaching object.

Like aircraft, the angular orientation of a flying insect can be specified by its rotation about three orthogonal axes: the yaw, pitch, and roll axes (Fig. 1C). For an insect flying steadily, the yaw axis is vertical, whereas the pitch and roll axes lie in the horizontal plane. Yaw—that is, rotation about the yaw axis—will simply change a fly's orientation in the horizontal plane. Pitch will cause the head to tilt either up or down, whereas roll will cause the body to rotate to the left or right. A combination of both roll and pitch will bank the body with respect to the horizontal plane. Previous studies suggest that flies change course without banking by creating torque about their yaw axis (*10*–*12*). It is not known, however, whether flies or other insects employ this same strategy during fast evasive maneuvers.

[1]University of Washington, Box 351800, 24 Kincaid Hall, Seattle, WA 98195–1800, USA. [2]Faculty of Aerospace Engineering, Delft University of Technology, 2600 GB Delft, Netherlands.
*Corresponding author. E-mail: flyman@uw.edu

Using three high-speed cameras operating at 7500 frames per second, we captured escape responses of the fruit fly *Drosophila hydei,* as they flew within a cylindrical arena (Fig. 1A) (*13*). Flies were backlit in each camera view using custom-built arrays of infrared (IR) light-emitting diodes (LEDs) (850 nm), an essential feature of the set-up because it allowed us to visualize the flies without interfering with their ability to see visual stimuli provided by an LED display (fig. S1). The LED display surrounded the arena and consisted of a 40 by 192 (height by circumference) array of green (565 nm) LEDs (*14*). Before and after each trail, all the green LEDs were turned on to provide illumination within the arena (70 lux). When triggered, the display was programmed to generate a dark expanding circle, with a Michelson contrast of 93% (*14*).

In each trial, both the looming stimulus and image capture were triggered automatically when a fly flew directly through the focus region of the three cameras at the center of the arena (*7*). The captured images during escape reactions were analyzed using a custom machine vision tracking system that was designed for analyzing *Drosophila* flight kinematics (*15*). In this system, the body and wings are tracked separately by projecting a fly body model and two wing models onto the three camera images using a direct linear transformation method for calibration (Fig. 1B) (*13*). We captured and digitized a total of 92 trials consisting of 3566 wingbeats, from which we determined heading, flight speed, and acceleration in both laboratory and fly frames of reference, as well as three angular measurements defining body position (pitch, roll, and yaw) (Fig. 1C) and three angular measurements for each of the two wings (stroke angle, deviation, and rotation) (Fig. 1D) (*13*).

Once they detected the looming threat, flies altered their flight path in a remarkably fast and accurate manner. Figure 1E shows a set of under-sampled photomontages of several trials taken by the downward-facing camera (see also movies S1 to S6). Visual inspection of the sixth image in each sequence immediately illustrates a major finding of our study; flies direct themselves away from the stimulus by quickly banking, and not yawing, their bodies. In addition, after changing their flight course, the animals quickly rotate back to attain a horizontal attitude and accelerate away from the looming threat. An animation of one example trial demonstrating the salient features of an evasive maneuver is shown in movie S7.

To examine the directional tuning and aerodynamics of the evasive maneuvers in more detail, we mirrored all sequences in which the flies performed a left-directed turn in response to the stimulus and aligned them with all the right-directed turns. Because the primary goal of our analysis was to elucidate the biomechanical basis of evasive maneuvers rather than the psychophysics of looming detection (*16*–*19*), we aligned all of our sequences to the start of the motor response rather than to the stimulus onset. The visual-motor delay during the escape response was on average 61 ± 21 ms (mean ± SD, n = 92 trials) (*13*), which is consistent with previous measurements in *D. melanogaster* (*8*, *17*).

The escape sequences consisted of two components: a rapid change in flight direction, $\Delta\sigma$, and an increase in flight speed, ΔU (Fig. 2, A and B), both of which depended strongly on the initial angular position of the looming stimulus in the fly's frame of reference, λ. Flies approached from the rear accelerated quickly, whereas animals approached from the front first slowed down while changing direction before speeding up (Fig. 2B). The directional tuning was most accurate when the stimulus loomed from the side ($\lambda \sim -90°$) (Fig. 2, G and H) and less accurate when the flies experienced looming directly in front or behind ($\lambda \sim -180°$ or 0°). Nevertheless, 80% of the flies were able to direct their escapes within a 90° sector directly opposite the azimuthal position of the stimulus (Fig. 2, G and H).

The total stroke-averaged aerodynamic force created by a flying animal may be estimated from its instantaneous acceleration, body mass, and gravity. To change heading and escape, a fly must direct the horizontal component of this force, σ_F, away from the threat, and a surprising feature of these maneuvers was the rapidity with which flies performed this task (Fig. 2C). Flies adjusted σ_F to within 95% of its final value within 7 ms (~1.3 wingbeats); this resulted in a peak turn rate, $\dot{\sigma}$, of 5300° s^{-1} (median, n = 92 trials, interquartile range = 3800 to 9000° s^{-1}). Flies also increased the magnitude of the aerodynamic force (Fig. 2D), but this change occurred more slowly than the change in direction.

Previous models of fly flight have assumed that the aerodynamic flight force vector created by the flapping wings is positioned roughly normal to the mean stroke plane at an orientation that remains relatively constant with respect to the body

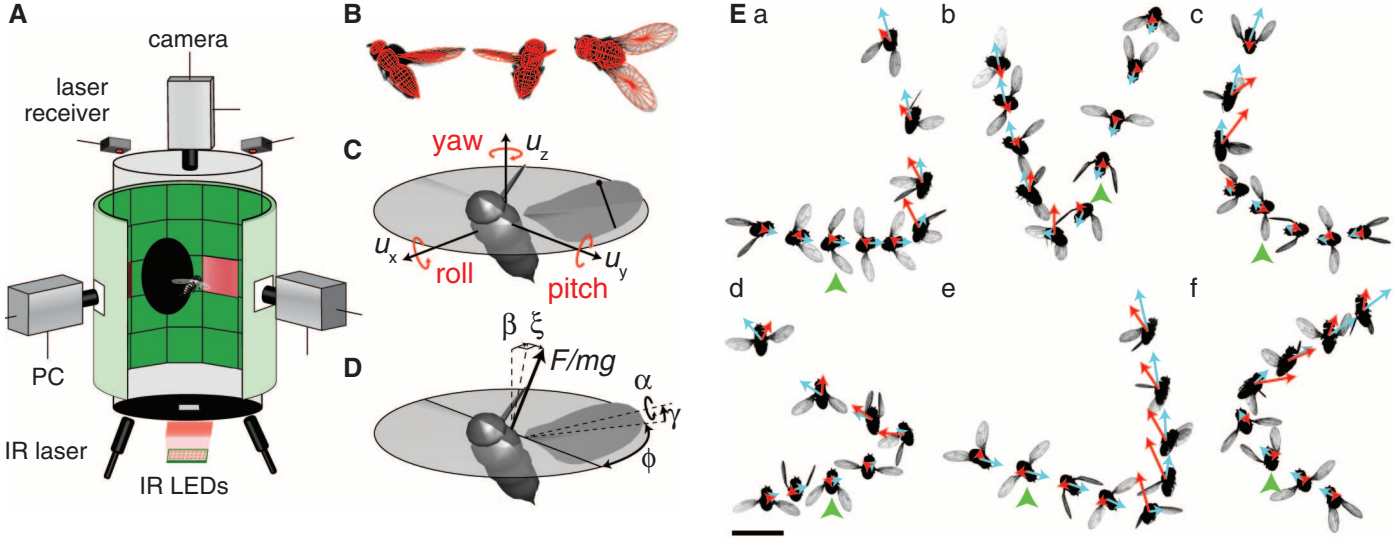

Fig. 1. Experimental setup, angle conventions, and example sequences. (**A**) When a fly passes through the crossed beams of the two IR lasers at the center of the arena, a looming stimulus is displayed on green LED panels and cameras are triggered. (**B**) Images of a fly in three camera views superimposed with a wireframe model after automated tracking. (**C** and **D**) *Drosophila* models in steady flight with a horizontal stroke plane. (C) Body dynamics are described by velocity vector [$\boldsymbol{U} = (u_x,u_y,u_z)$] and angular velocity vector [$\boldsymbol{\Omega} = (\omega_x,\omega_y,\omega_z)$], where ω_x, ω_y, and ω_z correspond to roll, pitch, and yaw rates, respectively. (D) Wingbeat kinematics are defined by stroke angle (ϕ), deviation angle (γ), and rotation angle (α). The orientation of the normalized force vector (F/mg, where mg is fly weight) in the body reference frame is defined by pitch (β) and roll (ξ) angles relative to a vector normal to the stroke plane. (**E**) Photomontages from the downward-facing camera of six flight sequences. Each image is shown at its correct spatial location but with variable time intervals. Horizontal components of velocity and acceleration vectors are shown in cyan and red, respectively. Looming stimulus direction and onset are indicated by green arrow. Scale bar in (E, part d), 5 mm (image), 1 m s^{-1} (velocity) and 25 m s^{-2} (acceleration).

axes (*20*–*22*). According to this so-called "helicopter model," flies change direction by rotating their whole body so that the total force vector points in the intended direction of motion. To test this assumption, we tracked the angular orientation of the aerodynamic force vector and found that it changed very little relative to the body throughout the maneuvers (Fig. 2, E and F). Thus, the helicopter model is largely valid, even during the rapid turns when the body undergoes large rotations. This analysis confirms the intuitive impression given by the raw image sequences presented in Fig. 1E and indicates that flies must alter direction primarily by banking their bodies.

Given the constraints of a force vector fixed to body coordinates, flies could employ two basic strategies for changing course. First, as suggested in some previous studies (*12*, *23*), flies might generate yaw torque to rotate their bodies around the vertical axis until they are aligned in the direction of intended motion. This yaw-based method is roughly equivalent to how airplanes make small course corrections in cruising flight using the tail rudder. Rather than using their legs or abdomen as a rudder, previous experiments suggest that flies generate yaw turns by differentially regulating the angle of attack of the wings during the upstroke and downstroke (*12*, *23*). Alternatively, flies might simultaneously pitch and roll their bodies until the aerodynamic force vector tilts in the direction of desired motion, analogous to a banked turn of an aircraft.

To differentiate between these two possibilities, we determined body orientation throughout the evasive maneuvers (Fig. 3 and fig. S2). As suggested in the raw images plotted in Fig. 1E, the early phase of the maneuvers is dominated by a coordinated change in roll and pitch, with only a modest change in yaw (although yaw increases later in the maneuver). The amount of roll and pitch generated by the flies varied significantly (linear regression, $P < 0.0001$) with the azimuthal position of the stimulus in a systematic way (Fig. 3, G to I), indicating that a fly actively controls these parameters to direct its motion away from the stimulus. The correlation between yaw and stimulus angle was also significant ($P = 0.0088$), but the regression slope was much weaker than those for roll and pitch.

The roll and pitch rotation at maximum force production can be combined into a single rotational vector with a direction, μ, in the horizontal plane (Fig. 3J). As shown in Fig. 3K, the orientation of this rotation axis varies linearly with the azimuthal position of the stimulus. If the fly rotated so as to direct its mean force vector directly away from the stimulus ($\sigma_F = 0°$) (Fig. 2C), the rotation axis would be related to the stimulus angle by the equation $\mu = -(\lambda + 90°)$. The flies' performance differs systematically from this prediction (Fig. 3K). Some authors have argued that bias or trial-by-trial stochasticity within escape headings might serve a functional role in evading the capture strategies of predators (*24*). In this case, however, we cannot exclude the alternative possibilities that flies are simply limited by biomechanical constraints or tolerate directional imprecision for the benefit of response speed.

Compared to a pure yaw maneuver, in which a fly could generate yaw torque in one direction and then coast to a stop via a combination of passive (*11*, *12*) and active (*25*) damping, a banked turn requires that an animal rotate first in one direction and then rotate back. Because passive damping can only asymptotically reduce roll and pitch rates and not reverse them, a banked turn thus requires active production of countertorque. Evidence for both phases of the maneuver (rotation and counter-rotation) is evident in the time histories of acceleration about the roll and pitch axes that exhibit a biphasic shape (Fig. 3, D to F). These plots underscore the brevity of the escape maneuvers, in which the production of peak torque and peak counter-torque is separated by only 3 to 4 wingbeats (Fig. 3, D to F). The rapidity with which a fly must alter stroke kinematics to bank in one direction and then rotate back is illustrated by movie S8. Both phases of the maneuver might be driven by a single feedforward program triggered by the visual stimulus or, alternatively, the counterturn might be elicited by reafferent feedback triggered by the initial rotation (*26*–*28*).

Immediately after a fly completes the counter-rotation portion of the maneuver, its body is misaligned with its direction of motion. This sideslip is readily apparent in the final frames of the photomontages in Fig. 1E (see also movies S1 to S6). To correct for this misalignment, flies must rotate about the yaw axis in the same direction as the previous change in heading. Due to the spatial limitations of our image capture volume, most flies were still in the process of this correction at the end of our recorded sequences (Fig. 3C). It is possible that this late correction in yaw (performed while maintaining a constant heading) is also part of the same feedforward program that generated the banked turn. However, the slower time course suggests that this late component might be triggered by visual cues, such as an offset in the pole of expansion of optic flow (*18*).

To investigate the aerodynamic basis of the escape maneuvers, we examined detailed changes in wing motion throughout each sequence. Ignoring deformations of the wing blade, which were small in our images, the position of a wing in each time step may be defined by three orthogonal rotational vectors (Fig. 1D). Of the 3566 wingbeats recorded in the 92 trials, we classified 1603 as steady, based on thresholds for low linear and angular acceleration of the body (*13*). The wing kinematics during steady flight exhibited remarkably low variability both in terms of stroke frequency

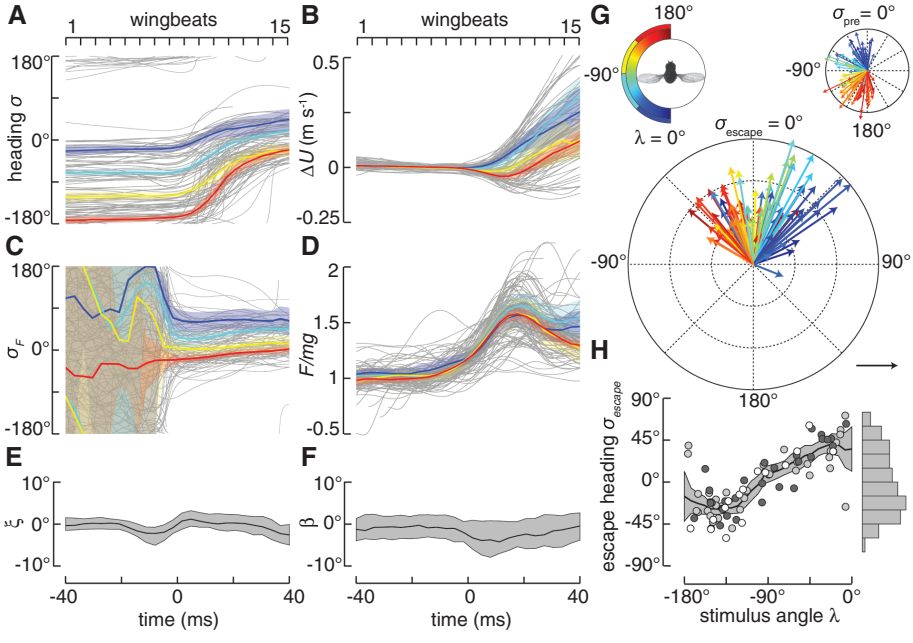

Fig. 2. Flies rapidly direct aerodynamic flight force away from looming stimulus. (**A** to **F**) Temporal dynamics of parameters throughout the maneuver: (A) σ, heading in the stimulus reference frame; (B) Δ*V*, change in flight speed; (C) σ_F, direction of horizontal aerodynamic force in stimulus reference frame; (D) *F*/*mg*, total normalized aerodynamic force. (E) Roll angle ξ and (F) pitch angle β of *F*/*mg* in the fly body frame (median and quartile range). In (A) to (D), thin gray lines indicate separate flight sequences; colored lines and shaded areas are average and 95% confidence intervals for four subsets of data in which the flies were approached from different 45°-wide azimuthal sectors [see upper left inset in (G)]. (**G**) Polar plots showing the flies' initial velocity and heading, σ_{pre}, and escape velocity and heading, σ_{escape}. Vectors are scaled to the black vector in lower right (0.2 m s^{-1}). The color of the vector encodes the initial azimuthal position of the stimulus in the fly's field of view (see inset at upper left). (**H**) Escape heading versus initial stimulus direction. Data for fast (black), moderate (gray), and slow (white) expanding stimuli are combined. Solid line and gray area indicate average and 95% confidence intervals, respectively; histogram shows distribution of σ_{escape}.

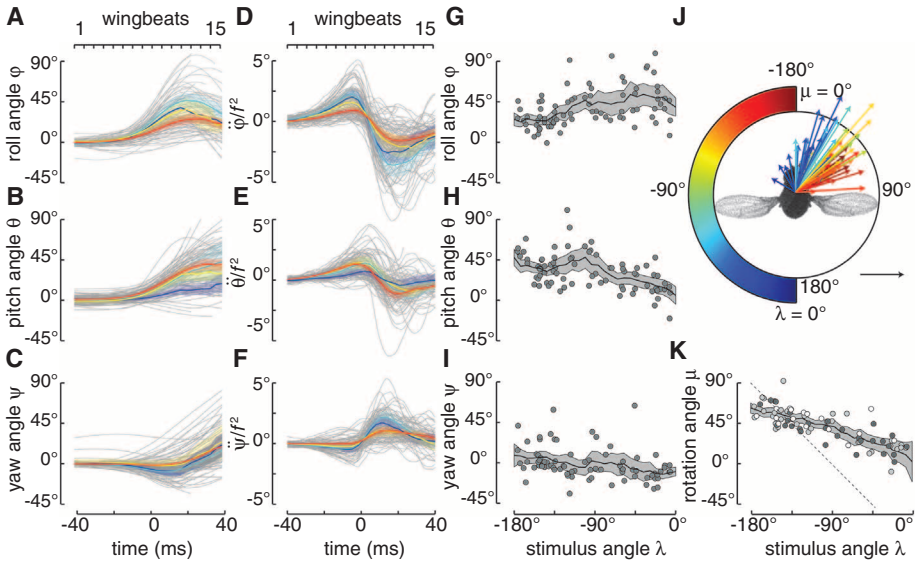

Fig. 3. Flies avoid stimulus by performing banked turns. (**A** to **C**) Time history of body angles aligned to start of motor response: (A) roll φ; (B) pitch θ; (C) yaw ψ. (**D** to **F**) Time history of the corresponding body angle accelerations, normalized by the square of wingbeat frequency *f*: $\ddot{\varphi}/f^2$, $\ddot{\theta}/f^2$, and $\ddot{\psi}/f^2$, respectively. In (A) to (F), thin gray lines indicate separate flight sequences; colored lines and shaded areas are average and 95% confidence intervals, respectively, for the four azimuthal stimulus sectors, as in Fig. 2. (**G** to **I**) Body angles measured at the point of maximum force (*F/mg*), plotted against stimulus angle: (G) roll; (H) pitch; (I) yaw. (**J**) The resultant horizontal body rotation vector [(φ,θ) at maximum force production] plotted in the fly frame. Vectors are color coded by stimulus angle and scaled according to black (45°) calibration vector. (**K**) Angular orientation of horizontal body rotation vector plotted against stimulus angle. The dotted line represents $\mu = -(\lambda + 90°)$.

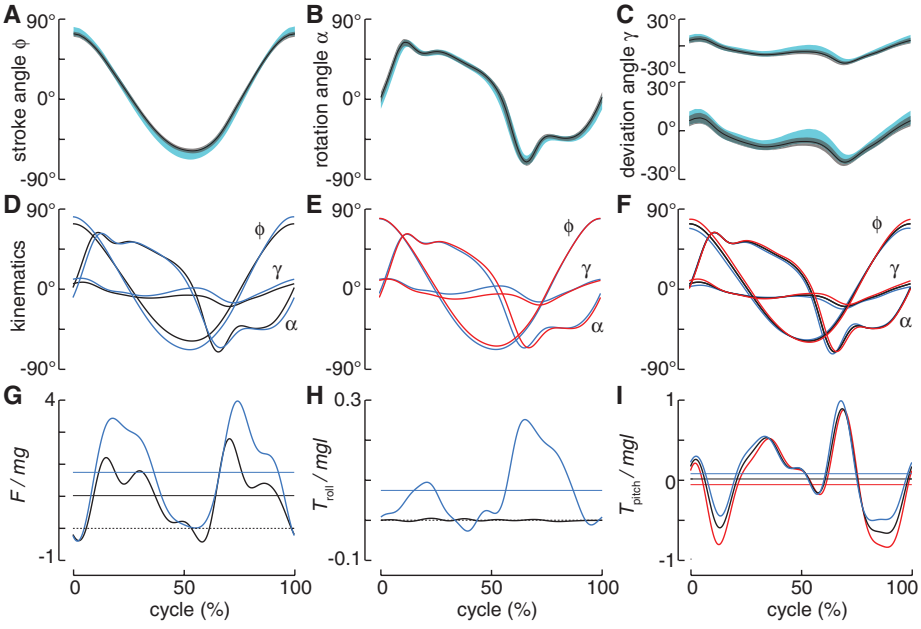

Fig. 4. Evasive maneuvers are controlled by subtle changes in wing motion. (**A** to **C**) Average (black) and quartile ranges (gray) of data from steady wingbeats; quartile ranges of data from unsteady wingbeats during escape maneuvers are indicated in cyan: (A) stroke angle; (B) rotation angle; (C) deviation angle. (**D**) Comparison of wing angles from steady wingbeats (black) and wingbeats producing peak flight force (blue). (**E**) Wing angles from left (blue) and right (red) wing of a wingbeat producing peak roll acceleration to the right. (**F**) Wing angles from steady wingbeats (black) and wingbeats generating peak nose-down (red) and nose-up (blue) pitch acceleration. (**G** to **I**) Time series of normalized forces *F/mg* and torques *T/mgl* (where *l* is mean wing length), measured using dynamically scaled robotic fly, for the kinematic patterns plotted in (D) to (F). [(G) to (I)] Steady data (black); (G) peak flight force (blue); (H) peak roll torque (blue); (I) peak nose-down torque (red) and peak nose-up torque (blue). The straight horizontal lines indicate average values over the stroke.

(188.7 ± 0.5 Hz, mean ± SD) and the time course of the three wing angles (Fig. 4, A to C). The wing motion during steady flight was also consistent with previous free-flight measurements of *D. melanogaster* (*7*, *23*).

Averaged time series changes in wing kinematics during the maneuvers are plotted in figs. S3 to S6, where the sequences are parsed into four groups according to initial stimulus angle. The biphasic pattern of changes in wing kinematics is consistent with the production of torque and countertorque derived from body kinematics. To determine more quantitatively how flies modulate wing motion to control forces and moments during the escape maneuvers, we analyzed the 1963 wingbeats that did not fulfill the steady flight criteria (hereafter called unsteady wingbeats). The mean and interquartile ranges for the three wing angles for all unsteady wingbeats are compared to the steady wingbeats in Fig. 4, A to C. The differences between steady and unsteady wingbeats are remarkably small, indicating that the changes in wing motion required to generate the rapid escape maneuvers are subtle, which underscores the remarkable precision of the fly's motor-control system despite the small number of motor neurons involved (*2*, *3*).

To determine which parameters of wing motion flies use to regulate flight force, roll, and pitch, we used a Fourier series to parameterize the time history of all three wing angles for each wingbeat (eq. S1). We then independently correlated (in three separate analyses) the amount of kinematic distortion in each stroke to the average linear acceleration, roll acceleration, or pitch acceleration generated during that stroke based on body motion (eq. S2). Based on these correlations, we could then reconstruct a prediction for the pattern of wing motion that would generate any arbitrary value of linear acceleration, roll acceleration, or pitch acceleration (eq. S3) (*13*).

In Fig. 4, D to F, we plot the time history for the three wing angles for steady flight superimposed with the pattern of wing motion that corresponds to the generation of peak flight force, peak roll acceleration, and peak pitch acceleration, where the peak value was defined as approximately 3 standard deviations from the mean value over all wingbeats (F/mg =1.6, $\ddot{\phi}/f^2 = 3°$, $\ddot{\theta}/f^2 = 2°$, respectively). To estimate the aerodynamic forces and moments generated by these different patterns of wing motion, we played them through a dynamically scaled robot (*25*, *29*). As a first test of the feasibility of our methods, we measured the forces and moments generated by the steady pattern of wing motion. The averaged aerodynamic force closely matched (102%) the average body weight of the flies (Fig. 4G). Next, we measured the forces and moments generated by the kinematic patterns corresponding to peak linear and angular accelerations. In all cases, the alterations in wing kinematics generate the expected qualitative change in the forces and moments, illustrating how flies regulate flight force, roll torque, and pitch torque through small coordinated changes

in all three components of wing motion (Fig. 4, G to I; Fig. 5; and movies S9 to S11).

To provide a more quantitative test of whether the kinematic changes we measured were actually sufficient to produce the forces and moments generated by the flies, we used the results of our Fourier parameterization to construct a set of time series for the three wing angles that represented a graded sequence from the steady flight pattern to the patterns that generated peak accelerations. Because these kinematic patterns were originally derived from correlations with body accelerations (eqs. S1 and S2), the resulting stroke-averaged forces and moments for each pattern generated by the robot could be explicitly compared to the measured free-flight values derived from body kinematics. For our analysis of flight force, we also included wingbeat frequency as an independent control parameter. Because modulating frequency alone (which is the same for both wings) cannot alter roll or pitch acceleration, it was excluded from these analyses through normalization of angular accelerations with stroke frequency squared.

The stroke-averaged flight forces generated by the dynamically scaled robot matched those derived from body acceleration almost exactly throughout the entire range of kinematic distortion (Fig. 6A), providing a strong quantitative validation of our analysis method, despite several simplifying assumptions (such as the fact that the wing kinematics were replayed on a stationary robot). The pitch and roll moments generated by the robot could not be explicitly compared to corresponding free-flight values without knowledge of the moment of inertia around these two axes. As an alternative method for testing the reliability of our method, we used the ratio of measured normalized torque (from the robot) to measured normalized angular acceleration (from the flight sequences) to derive estimates of the normalized moments of inertia. The empirically derived radian-based estimates (I_{roll} f^2/mgl = 1.43 and I_{pitch} f^2/mgl = 2.06) are roughly twice the values expected from a simple rigid body model (*29*, *30*), suggesting that the beating wings and associated added fluid mass contribute to rotational inertia.

After verifying that the coordinated distortions of the three wing angles generated the expected changes in flight forces and torques, we then used our approach to characterize the influence of each wing kinematic parameter in isolation. In these experiments, we played a set of kinematic sequences through our dynamically scaled robot in which only one of the four kinematic parameters was varied, while the other variables were held constant at the steady flight pattern. This exercise allowed us to explicitly examine the relative importance of each kinematic parameter on flight control, as well as determine whether the parameters interact in a nonlinear manner. We found that all kinematic parameters contribute substantially to the modulation of flight force, roll, and pitch control. Increases in stroke amplitude and frequency exerted the strongest influence on total flight force, with stroke deviation playing a more minor role (Fig. 6A). Together, these three kinematic changes act to increase wing velocity as well as create a stronger plunging motion at the start of each stroke (Fig. 5A). Curiously, the modulation of wing rotation alone causes a decrease in force production rather than an increase. The modulation of stroke amplitude and wing rotation contribute nearly equally in the regulation of roll, with wing deviation having a minor effect (Fig. 6B). Stroke amplitude also played the largest role in regulation of pitch, followed by wing deviation and wing rotation (Fig. 6C). For all cases (force, roll, and pitch), summing the forces or moments created by modulating the independent kinematic parameters in isolation accurately predicted values generated when all parameters were modulated simultaneously, indicating a remarkable degree of linearity (Fig. 6, A to C).

Previous studies on free-flying flies suggested that yaw torque is generated by a regulation of wing rotation (*12*), effectively changing the relative aerodynamic angle of attack during the upstroke and downstroke. In our study of banked turns, we also found that wing rotation was an important control parameter, although its contribution was relatively minor. In addition, the primary changes we measured in wing rotation were associated with shifts in timing, possibly modulating rotational lift (*5*) rather than angle of attack during upstroke

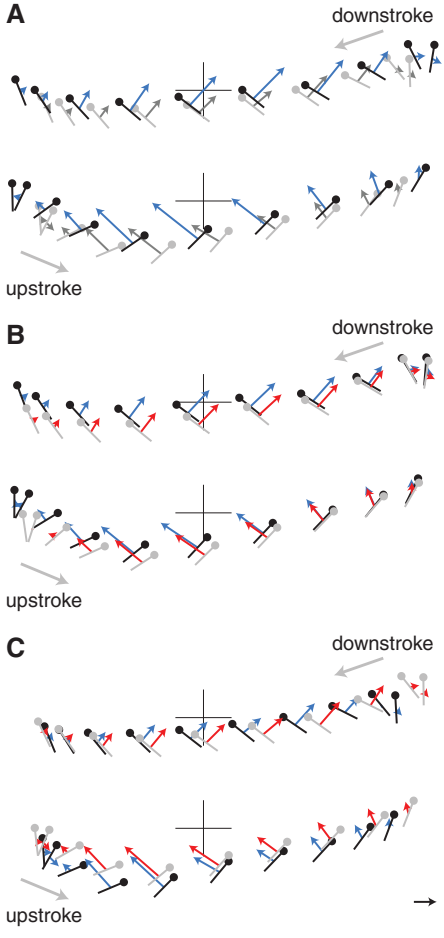

Fig. 5. Instantaneous aerodynamic forces superimposed on projections of the wing chord for wingbeats generating peak force, roll acceleration, and pitch acceleration. Data are equivalent to those in Fig. 4, D to I; see Fig. 1C for wing chord definition; vectors are scaled to the black vector in lower right (F/mg = 1). The cross in each panel defines the wing hinge location and is a 10° reference scale for stroke and deviation angles. (**A**) Comparison between steady wingbeat (gray) and wingbeat producing peak force (black chord, blue vector). (**B**) Forces created by the upward-rotating wing (black chord, blue vector) and the downward-rotating wing (gray chord, red vector) during peak roll acceleration. (**C**) Comparison between wingbeats generating peak nose-down pitch (black chord, red vector) and peak nose-up pitch (gray chord, blue vector).

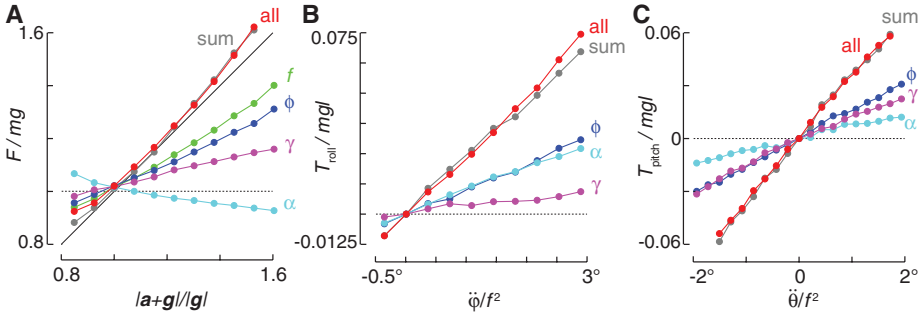

Fig. 6. Wingbeat average forces and torques responsible for linear and angular body accelerations, measured by replaying on the robotic fly a graded series of kinematic patterns that represent the measured distortion in wing motion from steady flight to peak values of linear and angular acceleration. In each case, the abscissa indicates normalized free-flight body accelerations, and the ordinate indicates the normalized force or torques resulting from the distorted wingbeat patterns (*13*). In all panels, red indicates data in which all kinematic parameters were modulated simultaneously. The effects of altering kinematic patterns in isolation are shown in green (wingbeat frequency f), blue (stroke angle ϕ), turquoise (rotation angle α), and magenta (deviation angle γ). The gray data indicate the linear sum of the forces or moment generated by these independent modulations. (**A**) Flight force versus linear acceleration. The thin black line shows the expectation for 100% weight support. (**B**) Roll torque versus roll acceleration. (**C**) Pitch torque versus pitch acceleration.

heating, the system develops a triclinic (T) stripe-like ordered state around 223 K, which reverts to the NC state at $T = 283$ K (*11*). Further nearby equilibrium states are revealed upon application of external pressure (*12*) or doping (*13*), both of which make *1T*-TaS_2 superconducting.

To induce the HST, we use a single sub–35-fs write (W) pulse from an amplified Ti-sapphire laser at 800 nm with energy $U_W \approx 1$ mJ/cm^2. After a HST is induced at 1.5 K, the four-probe resistance $r(T)$ drops approximately three orders of magnitude and remains in this state indefinitely (verified up to 1 week) at this temperature (Fig. 1B). Upon heating, $r(T)$ is approximately constant up to 60 K, whereupon it starts increasing; above $T_H \sim 100$ K, it merges approximately with the virgin $r(T)$ curve corresponding to the C state. The current-voltage characteristics remain linear throughout. Empirically we found that the H state can be completely erased (E) by a train of 10^4 50-ps pulses, each with energy $U_E \approx 1$ mJ/cm^2. Alternatively, Joule heating can be used for erasure by passing a current of ~0.1 mA through the device (*14*). In both cases, the system reverts to the C state. Stable switching can also be achieved at intermediate temperatures up to $T \sim 70$ K (*14*). The effect is entirely reversible from cycle to cycle and from sample to sample, irrespective of the sample growth batch, and there appears to be no limit on the number of W-E cycles that can be performed. [See supplementary materials for experimental details on thermal protocols, including aging effects (*15*), and a description of the laser lithography used to manufacture the contacts.]

To gain insight into the microscopic nature of the hidden state, we investigated the single-particle and collective excitations by pump-probe spectroscopy, with the pump and probe pulse energies kept low (<10 μJ/cm^2 and <1 μJ/cm^2, respectively) to ensure minimal disturbance of either state. The sample reflectivity $R(T)$ was simultaneously recorded by the probe beam. In Fig. 2, we show the transient reflectivity $\Delta R/R$ of *1T*-TaS_2. In the virgin C state, we observed oscillations due to the coherent excitation of the amplitude mode (AM) and phonons that were superimposed on a background from exponentially decaying single-particle (SP) excitations across the gap (*16*). The spectrum $S(\omega)$ obtained by Fourier transformation shows a strong AM at 2.46 THz and weaker phonon modes at 2.1, 2.18, 3.2, and 3.85 THz (Fig. 2B). The HST modified the $\Delta R/R$ (Fig. 2A) and the SP signal was substantially reduced. In the spectrum after the HST (Fig. 2B), the AM peak at 2.46 THz disappears in favor of a new mode at 2.39 THz; intensities of modes at 3.10 THz and 3.85 THz are reduced, and some additional spectral intensity appears between 2 and 2.5 THz. Upon heating, the spectrum of the H state remains unchanged until ~70 K; above 70 K, it gradually returns to the C state. Concurrent with the switching of the AM and phonons, we observed a switching of reflectivity R at 800 nm (Fig. 2D). All the observations display typical threshold behavior as a function of U_W; below threshold fluence, the resistivity, AM frequency, and reflectivity revert to the C state values after the W pulse. Close to threshold fluence, the AM shows bimodal behavior (fig. S5D), which we interpret as incomplete switching. We observed no intermediate shift of the AM in different samples, indicating distinct two-phase behavior. The H state spectrum is quite different from the NC state spectrum (Fig. 2, A and B) or the T state spectrum (*14*), indicating that it is not related to the equilibrium states.

We emphasize some notable features of the HST: (i) After photoexcitation, the H state spontaneously orders below T_H, as indicated by the narrowness of the AM peak and the fact that no partial frequency shift is observed even when incomplete switching is caused by near-threshold excitation. (ii) The switching occurs only with short pulses, and the threshold increases with increasing τ_W (Fig. 2C). (Note that the threshold can no longer be achieved with $\tau_W > 4$ ps at any U_W that we tried.) (iii) The H state is stable until erased or heated above ~70 K. Note that T_H has no special importance under equilibrium conditions and is relevant only for describing the transition from the H state to the C state.

To understand these unusual phenomena, we first introduce a scenario for switching based on the current understanding of the electronic ordering in *1T*-TaS_2 (*11*, *15*, *17*, *19*), and then describe a phenomenological model consistent with the data. The relevant electronic states of *1T*-TaS_2 in the C state that are within reach of our 1.5-eV laser photons are shown in Fig. 3C. They are formed predominantly from a single Ta *d* band, which is split into subbands by the formation of

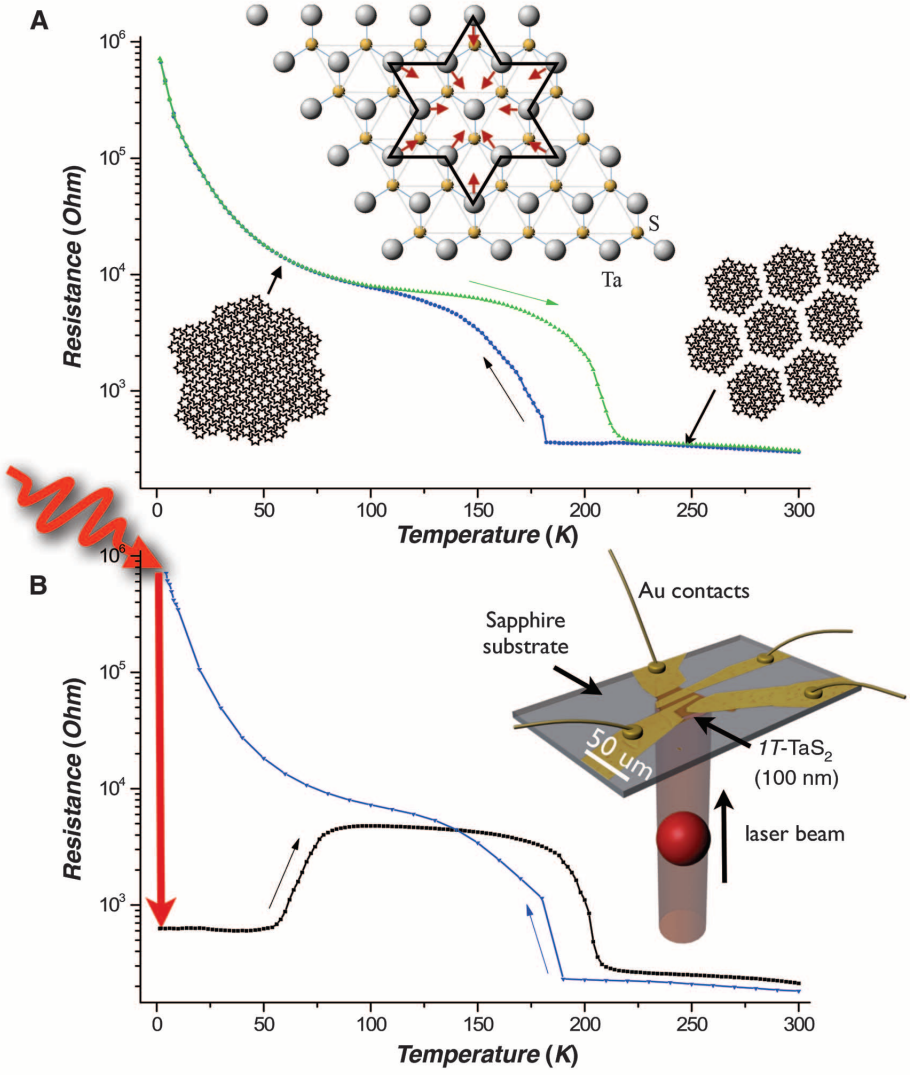

Fig. 1. Resistivity switching of *1T*-TaS_2 by a 35-fs laser pulse at 800 nm. (**A**) Temperature dependence of the four-probe resistance $r(T)$ on temperature cycling; blue and green curves are measured on cooling and warming, respectively. The sketches show the lattice distortions associated with an individual polaron (top) and their ordering in the NC (high T) and C (low T) states. (**B**) The drop of r at 1.5 K after a single pulse with $U_W > U_T$, where U_T is the threshold fluence (red arrow); the blue curve is the resistance measured on cooling. Upon heating, the resistance reverts between 60 and 100 K (black curve). Inset: Schematic of the sample and contacts.

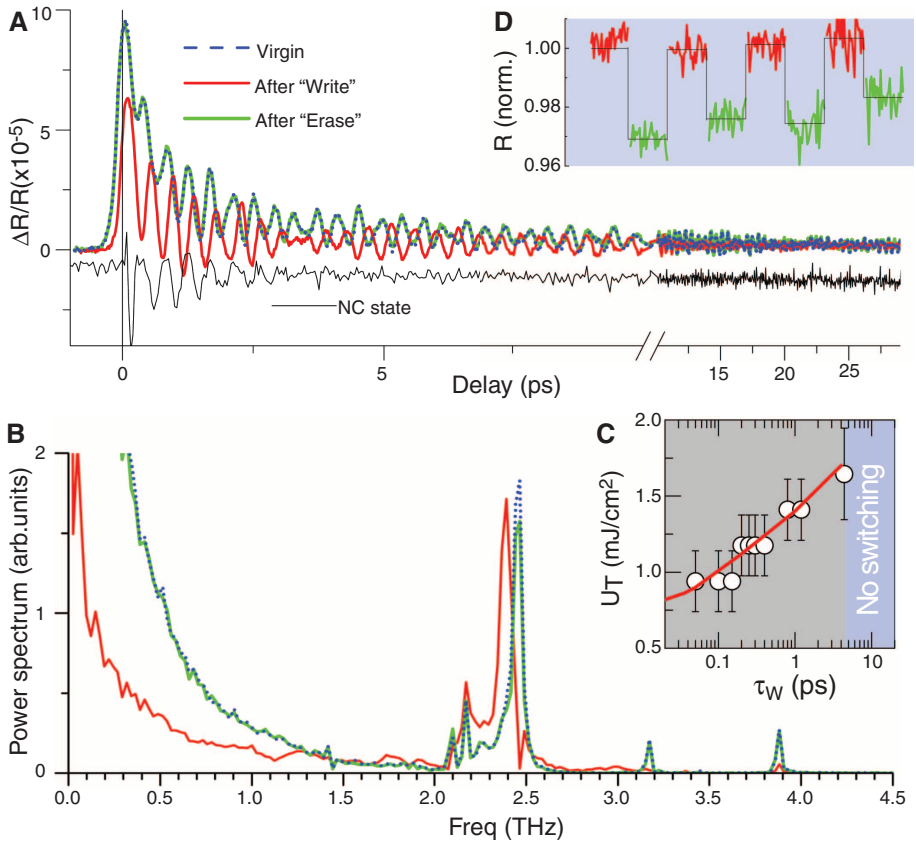

Fig. 2. Spectral signatures of the HST process. (**A**) Transient reflectivity $\Delta R(t)/R$ of 1*T*-TaS_2 in the virgin state (blue dashed line), after exposure to a 50-fs W pulse (red line), and after an E pulse (green line). Black line: data in the NC state at 220 K recorded upon cooling (offset for clarity). (**B**) The corresponding Fourier-transformed power spectra $S(\omega)$ using the same color notation. (**C**) Switching threshold fluence U_T as a function of pulse length τ_W measured optically with pump-probe experiments. The red line is predicted by the model calculation (*14*). (**D**) Reflectivity at 800 nm recorded with the photodiode during a sequence of alternating W and E pulses. (The noise is from the laser.)

a CDW depicted in Fig. 1A. Six of these subbands are filled with 12 electrons per new large unit cell, forming a manifold of occupied states up to 0.4 eV below E_F (Fig. 3C, in blue). The 13th leftover electron is localized on the central Ta atom, causing inward radial displacements of 12 neighbors in the shape of a star of David (*9*, *14*, *16*), thus forming a self-localized polaron. The 13th electron gives rise to a half-filled narrow metallic band straddling the Fermi level; this band is further split by the Coulomb interaction into upper and lower Hubbard bands (Fig. 3C, green) (*18*), whereby the upper band merges with the manifold of unoccupied subbands above E_F while the lower one is ~0.2 eV below E_F. This is well above the top of the valence band at −0.4 eV, which makes the C state a Mott insulator in the form of a polaronic crystal (*12*, *17*, *18*).

Photoexcitation initially creates equal numbers of electrons (*e*) and holes (*h*) by an interband transition, followed by rapid intraband thermalization via scattering within the *e*-*h* population and with the lattice, as well as transitions between different bands, reaching states near the Fermi level and melting the C order on a time scale on the order of 50 fs (*20*–*23*). The maximum effective electronic temperature reached in the process is T_e ~ 1000 K; the lattice reaches ~150 K within 3 to 5 ps, whereupon the electrons and lattice are in quasi-equilibrium. [See (*14*) for temperature measurements and model estimates.]

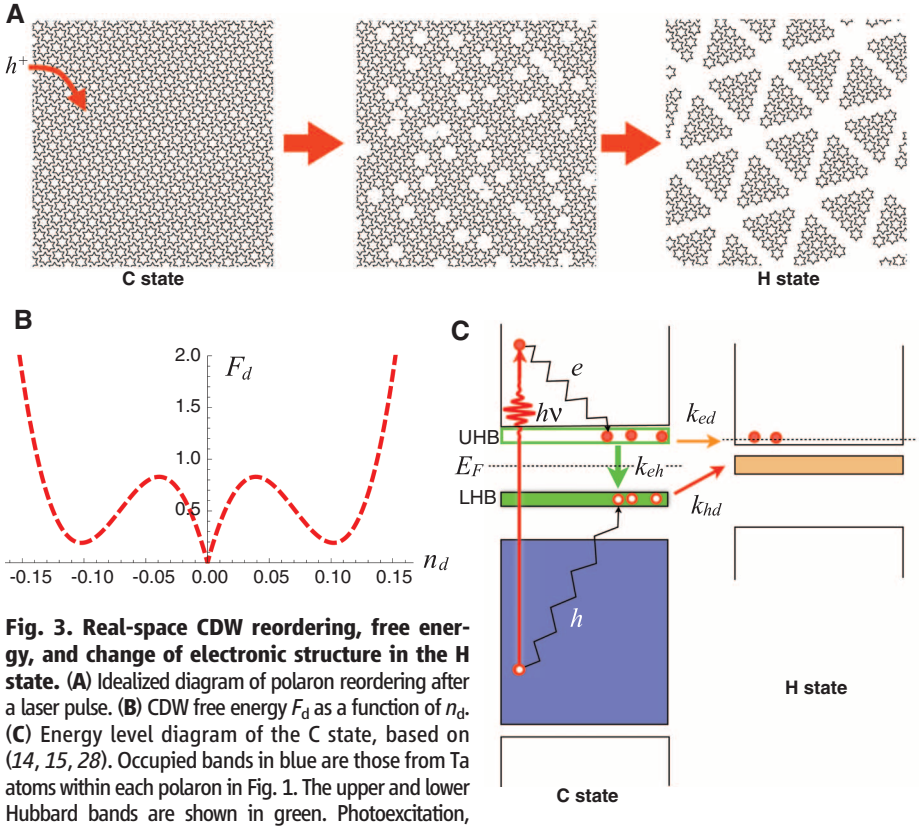

Fig. 3. Real-space CDW reordering, free energy, and change of electronic structure in the H state. (**A**) Idealized diagram of polaron reordering after a laser pulse. (**B**) CDW free energy F_d as a function of n_d. (**C**) Energy level diagram of the C state, based on (*14*, *15*, *28*). Occupied bands in blue are those from Ta atoms within each polaron in Fig. 1. The upper and lower Hubbard bands are shown in green. Photoexcitation, initial energy relaxation, and subsequent relaxation processes of the *e* and *h* are shown. k_{ed}, k_{eh}, and k_{hd} are the rates for transitions of electrons to defect states, electrons to hole states, and holes to defect states, respectively.

However, the large asymmetry of the band structure in this compound (*17*) can also lead to a photodoping effect: The electrons and holes scatter and lose energy at different rates, leading to a transient imbalance of their respective populations, n_e and n_h, within less than 5 ps.

A photodoped hole in this system annihilates with the localized 13th electron; this process removes the charge at the center of the polaron, leaving a void in the place of the polaronic distortion. Because some of the 13th electrons have been annihilated by holes, not all ions in these regions are charge-compensated, and they have an excess charge. Yet these regions cannot conduct because the remaining 12 electrons are in filled states within the gap formed by the long-range CDW (Fig. 3C). The excess charge will be screened by the electrons, which are now transferred to the delocalized bands. At a sufficiently high concentration n_v, these voids are expected to aggregate by diffusion into domain walls. The overall state becomes conducting via the band states released by the annihilated polarons, which, if ordered, would form a new ordered structure of polaron clusters separated by domain walls, as indicated schematically in Fig. 3A. We can also imagine that photoexcited electrons could squeeze into the structure in between the polarons, creating interstitials with a concentration n_i (*11*). Together with voids with a concentration n_v, the total "intrinsic defect" concentration $n_d = n_v - n_i$ may have either sign. Overall charge conservation $n_h + n_v = n_e + n_i$ gives the imbalance of the current carriers, $n_d = n_e - n_h$.

The value of n_d is related to deviations $\delta q/\pi \approx -n_d$ of the CDW wave vector q with respect to the C state. Conventionally, photodoping is a transient effect, so once *e-h* symmetry is recovered, the voids and domain walls disappear and the C state is restored. However, if the voids can be stabilized by collectively ordering into a long-range ordered state, the final state is different from the original one. The free energy $F_d(n_d)$ appropriate for the formation of the charge-ordered state outlined above (*19*) needs to include the effect of repulsion between the domain walls and between their crossings (*19*, *25*, *26*), and should reproduce the first-order nature of the transition (*19*, *26*). Values of $F_d(n_d)$ based on these considerations and existing models (*19*, *26*) are plotted in Fig. 3B. The time dependencies of concentrations $n_e(t)$ and $n_h(t)$ are calculated in (*14*).

The model (*14*) is consistent with the main experimental observations, namely the appearance of a switching threshold for the W pulse fluence, its critical pulse-length dependence, the threshold temperature for the E cycle, the high conductance, and the remarkable stability of the H state. The switching is caused by relatively weak and short pulses, which—considering the large change in resistance and optical reflectivity—has potential for device applications. The effect will also stimulate the search for new generations of room-temperature nonvolatile memory elements in electronically ordered materials. As a memory element switchable by 35-fs pulses, our device is already comparable to the current speed record of 40 fs in magnetic materials (*28*).

References and Notes

1. S. Koshihara, Y. Tokura, T. Mitani, G. Saito, T. Koda, *Phys. Rev. B* **42**, 6853–6856 (1990).
2. K. Nasu, *Photoinduced Phase Transitions* (World Scientific, Singapore, 2004).
3. H. Okamoto *et al.*, *Phys. Rev. B* **70**, 165202 (2004).
4. A. Cavalleri *et al.*, *Phys. Rev. Lett.* **87**, 237401 (2001).
5. S. Tomimoto, S. Miyasaka, T. Ogasawara, H. Okamoto, Y. Tokura, *Phys. Rev. B* **68**, 035106 (2003).
6. N. Takubo *et al.*, *Phys. Rev. Lett.* **95**, 017404 (2005).
7. K. Nasu, H. Ping, H. Mizouchi, *J. Phys. Condens. Matter* **13**, R693–R721 (2001).
8. G. Yu, C. H. Lee, A. J. Heeger, N. Herron, E. M. McCarron, *Phys. Rev. Lett.* **67**, 2581–2584 (1991).
9. D. Fausti *et al.*, *Science* **331**, 189–191 (2011).
10. A. Zakery, S. R. Elliott, *Optical Nonlinearities in Chalcogenide Glasses and Their Applications* (Springer, New York, 2007).
11. R. Thomson, B. Burk, A. Zettl, J. Clarke, *Phys. Rev. B* **49**, 16899–16916 (1994).
12. B. Sipos *et al.*, *Nat. Mater.* **7**, 960–965 (2008).
13. L. J. Li *et al.*, *Eur. Phys. Lett.* **97**, 67005 (2012).
14. See supplementary materials on *Science* Online.
15. T. Ishiguro, H. Sato, *Phys. Rev. B* **44**, 2046–2060 (1991).
16. J. Demsar, L. Forro, H. Berger, D. Mihailovic, *Phys. Rev. B* **66**, 041101 (2002).
17. K. Rossnagel, N. V. Smith, *Phys. Rev. B* **73**, 073106 (2006).
18. E. Tosatti, P. Fazekas, *J. Phys. Colloq.* **37**, C4-165–C4-168 (1976).
19. K. Nakanishi, H. Shiba, *J. Phys. Soc. Jpn.* **43**, 1839–1847 (1977).
20. J. C. Petersen *et al.*, *Phys. Rev. Lett.* **107**, 177402 (2011).
21. S. Hellmann *et al.*, *Phys. Rev. Lett.* **105**, 187401 (2010).
22. L. Perfetti *et al.*, *New J. Phys.* **10**, 053019 (2008).
23. M. Eichberger *et al.*, *Nature* **468**, 799–802 (2010).
24. F. Clerc *et al.*, *J. Phys. Condens. Matter* **19**, 355002 (2007).
25. W. McMillan, *Phys. Rev. B* **14**, 1496–1502 (1976).
26. P. Bak, *Rep. Prog. Phys.* **45**, 587 (1982).
27. N. Dean *et al.*, *Phys. Rev. Lett.* **106**, 016401 (2011).
28. A. Kirilyuk, A. V. Kimel, T. Rasing, *Rev. Mod. Phys.* **82**, 2731–2784 (2010).

Acknowledgments: Supported by the Slovenian Research Agency, European restructuring funds (CENN Nanocenter), and European Research Council advanced grant TRAJECTORY. A European patent application PCT/SI2013/000056 has been submitted. We thank L. Forro, V. V. Kabanov, N. Kirova, P. Monceau, E. Tossatti, and E. Tutis for valuable discussions.

Supplementary Materials

www.sciencemag.org/content/344/6180/177/suppl/DC1
Materials and Methods
Supplementary Text
Figs. S1 to S10
Table S1
References (*29*–*55*)

6 June 2013; accepted 13 March 2014
10.1126/science.1241591

Entangled States of More Than 40 Atoms in an Optical Fiber Cavity

Florian Haas, Jürgen Volz,* Roger Gehr, Jakob Reichel,† Jérôme Estève†

Multiparticle entanglement enables quantum simulations, quantum computing, and quantum-enhanced metrology. Yet, there are few methods to produce and measure such entanglement while maintaining single-qubit resolution as the number of qubits is scaled up. Using atom chips and fiber-optical cavities, we have developed a method based on nondestructive collective measurement and conditional evolution to create symmetric entangled states and perform their tomography. We demonstrate creation and analysis of entangled states with mean atom numbers up to 41 and experimentally prove multiparticle entanglement. Our method is independent of atom number and should allow generalization to other entangled states and other physical implementations, including circuit quantum electrodynamics.

For entanglement-enabled technologies as well as from a fundamental point of view, an important goal is to scale up the number of entangled particles in many-qubit systems. In a bottom-up approach, individual addressing and universal quantum gates allow full control on the quantum state, and, in principle, any entangled state can be produced. However, because the number of gate operations scales up with particle number, experiments based on this method (such as ion traps) are currently limited to less than 20 entangled qubits (*1*).

Many important entangled states can be produced in a "top-down" approach with collective interactions or quantum nondemolition (QND) measurements, the complexity of which does not increase with particle number. In atomic ensembles, spin-squeezed (*2*, *3*) and twin Fock states (*4*) have been produced by collisional interactions; collective QND measurement (*5*–*8*) and cavity-mediated interactions (*9*) have been used to produce spin squeezing and have been proposed for Schrödinger cats (*10*) and Dicke states, including twin Fock states (*11*). However, state-of-the-art QND measurements in ensembles are still far from the single-particle resolution that would be required, for example, to reach the Heisenberg limit of quantum metrology (*12*). Moreover, the full quantum state of a system cannot be experimentally determined

Laboratoire Kastler Brossel, École Normale Supérieure, Université Pierre et Marie Curie–Paris 6, CNRS, 24 Rue Lhomond, 75005 Paris, France.

*Present address: Vienna Center for Quantum Science and Technology, Atominstitut, Vienna University of Technology, 1020 Vienna, Austria.

†Corresponding author. E-mail: esteve@lkb.ens.fr (J.E.); jakob.reichel@ens.fr (J.R.)

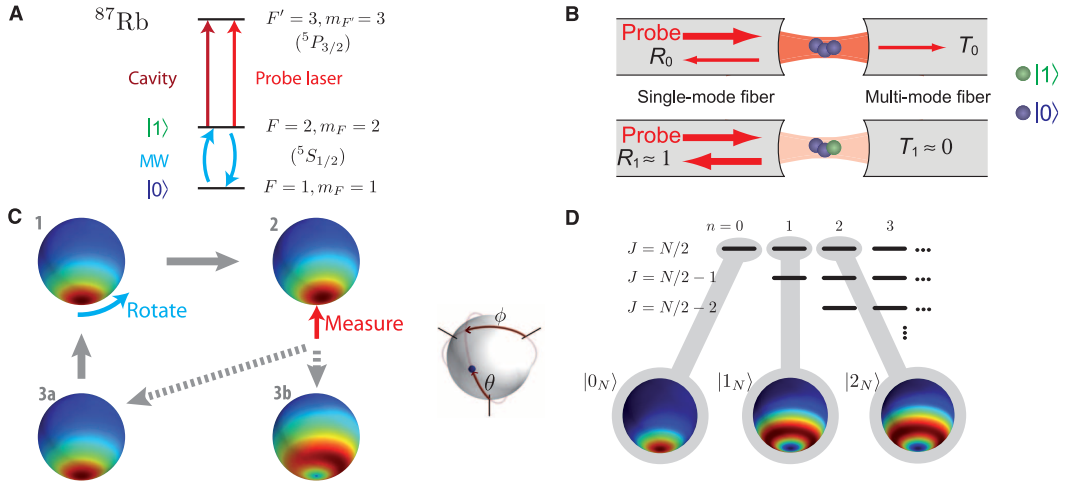

Fig. 1. Cavity-assisted generation of entanglement. (**A**) Relevant level scheme of ^{87}Rb. A resonant 6.8 GHz microwave allows applying arbitrary rotations to the atomic qubit. The cavity and probe laser are resonant with the transition $|1\rangle \rightarrow |F' = 3, m_{F'} = 3\rangle$, where F' and $m_{F'}$ denote the hyperfine and magnetic sublevels of the excited state, respectively. (*21*). MW, microwave pulse. (**B**) Principle of the collective QND measurement based on the normal-mode splitting. *R*, reflection; *T*, transmission. (**C**) Preparation sequence of the W state. The asymmetry in 3b originates from the nonzero contribution of higher-order Dicke states, which is due to the finite value of *p*. (**D**) The spin states with norm *J* and *z* component $-J + n$, where $2J \geq n \geq 0$, form a basis for the total atomic pseudospin (with this notation, *n* is the number of atoms in $|1\rangle$). In the symmetric subspace ($J = N/2$), the atomic state is fully characterized by its Husimi *Q* distribution, measured in our experiment. Shown are calculated distributions for the $|0_N\rangle$, $|1_N\rangle$, and $|2_N\rangle$ Dicke states.

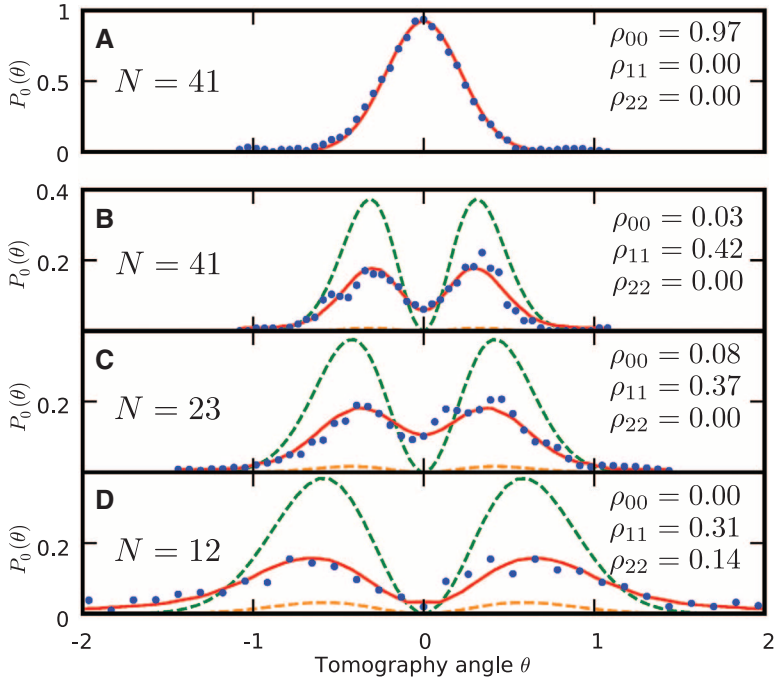

Fig. 2. Tomography of coherent and W states. (**A**) Tomography of a coherent state $|0_N\rangle$ (the initial state before the W state preparation). From a fit (red line), we obtain the number of atoms, $N = 41$. (**B** to **D**) Tomography of W states with 41, 23, and 12 atoms, respectively. Each point corresponds to ~50 measurements. For each atom number, the red curve results from a maximum likelihood state reconstruction taking into account all known imperfections of the tomography technique (*21*). For comparison, the dashed green lines show the theoretical $P_0(\theta)$ for an ideal W state, and the dashed orange lines indicate that of a statistical mixture in which one known atom among *N* is in $|1\rangle$. For each *N*, the populations of the $|0_N\rangle$ state and the first and second Dicke states $|1_N\rangle$ and $|2_N\rangle$ are indicated, as deduced from the state reconstruction.

nor efficiently analyzed beyond 10 to 20 qubits, in general (*13*), so that new methods that specifically identify and characterize relevant forms of entanglement in large systems are required.

Here, we use a cavity-based measurement that distinguishes one particular many-particle quantum state from the orthogonal subspace of all other states. This allows us to prepare many-body entangled states projectively and to directly measure their quasiprobability distribution with high resolution. Consider an ensemble of *N* atoms, all strongly coupled to a single mode of a high-finesse cavity (*14*–*18*) (Fig. 1, A and B). The cavity and probe beam are tuned for detecting the hyperfine state, $|0\rangle$ or $|1\rangle$ (*19*). Transmission through the cavity is observed only when all *N* atoms are in $|0_N\rangle \equiv |0\ldots0\rangle$. A single atom in $|1\rangle$ makes the cavity fully reflecting (*20*), and no further substantial changes occur when more than one atom is in $|1\rangle$. Due to the very strong coupling of the atom-resonator system (*21*), this is true for all atomic positions, so that the atoms are indistinguishable when probed by the cavity mode. Furthermore, we set the probe power such that the total probability for a spontaneous emission event is much smaller than one (*19*), limiting the amount of atom-distinguishing information that leaks into the environment. Thus, to good approximation, measuring the cavity transmission is a projective measurement with two eigenvalues: high transmission corresponding to $|0_N\rangle$ and low transmission to the orthogonal subspace containing all other states, where at least one atom is in $|1\rangle$. This measurement enables the generation of multiparticle entanglement as follows: Atoms are prepared in a premeasurement state $|\Psi\rangle$, then are measured as described. Low transmission signals preparation of $|0_N\rangle$ (meaning that the cycle must be repeated), whereas high transmission prepares the system in $|\xi\rangle \equiv c(\mathbb{1} - |0_N\rangle\langle 0_N|)|\Psi\rangle$, where *c* is a normalization factor. For a suitable choice of $|\Psi\rangle$, $|\xi\rangle$ can have interesting nonclassical properties. Here, we prepare a $|\xi\rangle$ that is a good approximation of

$$|1_N\rangle \equiv \frac{1}{\sqrt{N}}(|10\ldots0\rangle + |010\ldots0\rangle + \ldots + |00\ldots1\rangle) \quad (1)$$

known as the W state or the first Dicke state. It represents a fundamental class of entangled states (*22*), which are robust against particle loss and enable some meteorological gain over nonentangled states (*23*).

To obtain the W state, we start from $|0_N\rangle$ and apply a weak coherent microwave pulse on the qubit transition. If the excitation probability *p* is small, this prepares $|\Psi\rangle = \sqrt{1-p}|0_N\rangle + \sqrt{p}|1_N\rangle$. Measuring $|\Psi\rangle$ as described either projects back onto $|0_N\rangle$ or prepares $|1_N\rangle$. Low transmission heralds successful preparation, and the state is then available for further experiments. Figure 1C shows the expected evolution during the sequence.

Note that the system is always in a known, pure state, as in a quantum feedback scheme, and in contrast to single-photon heralded schemes (*24*, *25*).

To fully characterize the produced state, we have developed a tomography technique that measures the Husimi Q distribution of the total spin (*26*). In the ideal sequence (Fig. 1C), the state evolves inside the symmetric subspace, which contains the states with maximum pseudo-spin $J = N/2$ (Fig. 1D). In this subspace, which is spanned by the Dicke states and can be represented on a generalized Bloch sphere, the Q function is defined as $Q(\theta,\phi) = (N+1)/(4\pi)\, P_0(\theta,\phi)$ (*26*), where $P_0(\theta,\phi) = \langle 0_N | R^{\dagger}_{\theta,\phi} \rho R_{\theta,\phi} | 0_N \rangle$ is the probability that all atoms are in $|0_N\rangle$ after a rotation $R_{\theta,\phi}$ of the state with density matrix ρ. This expression shows that a direct measurement of Q is obtained by combining a rotation $R_{\theta,\phi}$ (performed with a microwave pulse here) with the measurement described above. Indeed, the probability to obtain high transmission for a given state measures its overlap with $|0_N\rangle$ (*21*, *27*). This method strongly differs from marginal distribution measurements (*3*, *28*) and is similar to one developed in quantum optics (*29*). Note that our binary individual measurement is sufficient to distinguish all symmetric states in the tomography when performed with a sufficient number of repetitions. For states outside the symmetric subspace ($J < N/2$), spin conservation under $R_{\theta,\phi}$ entails that they never transform into $|0_N\rangle$ and, thus, have a zero contribution to the measured P_0 for all (θ,ϕ) (Fig. 1D) (*21*). Therefore, the norm of Q of a given state yields its probability of lying in the symmetric subspace, whereas the shape of $Q(\theta,\phi)$ fully characterizes the symmetric part of the state.

In our experiment, a small atom number is prepared from an ultracold ensemble close to quantum degeneracy and trapped in a single antinode of a one-dimensional intracavity optical lattice, where each atom is strongly coupled to the resonant cavity mode (*15*, *21*). Figure 2A shows the tomography curve $P_0(\theta) \equiv P_0(\theta, \phi = 0)$ for $|0_N\rangle$, the state before the preparation sequence. The measured curve is well approximated by the expected $\cos^{2N}(\theta/2)$, from which we deduce the mean number of atoms N that contribute to the state. Because of our atom number preparation (*21*), we expect the prepared atom number to follow a binomial distribution with SD σ = 4.2, 3.6, and 2.8 for N = 41, 23, and 12.

Applying the entanglement preparation method [see (*21*) for experimental details], the tomography results $P_0(\theta)$ of the prepared W states for N = 41, 23, 12 are shown in Fig. 2, B to D. The curves feature the characteristic central dip expected for the nonclassical W state. The nonzero value for $\theta = 0$ indicates some remnant population in $|0_N\rangle$, which is below 10% for all atom numbers. In addition, the curves have a high contrast, indicating a population in the symmetric subspace above 40% for all atom numbers. This clearly sets them apart from their classical counterparts, the statistical mixtures of all states with one localized excitation, $\{|100\ldots\rangle, |010\ldots\rangle, \ldots\}$ (orange curves in Fig. 2, B to D). For those states, the symmetric subspace population is only $1/N$, so that the maximum value of $P_0(\theta)$ is small.

Because of the rotational symmetry of the state, a fair estimate of the W state fidelity is obtained from the single polar cut $\phi = 0$ of the Q distribution. In fact, we expect that other cuts do not contain additional information because of a slow drift of the magnetic field during the long acquisition time of our data (several days), which randomizes the phases between the different Dicke states. This can be seen in the symmetry of the tomography data shown in Fig. 2 [$P_0(-\theta) \approx P_0(\theta)$]. We also measured $P_0(\theta, \phi = \pi/2)$ and verified that it is very similar to $P_0(\theta,0)$. To partially reconstruct the density matrix ρ in the Dicke basis, we make the simplifying assumption that ρ is purely diagonal and deduce the populations ρ_{ii} using a maximum likelihood algorithm. We have checked that this assumption does not overestimate the fidelity ρ_{11}, nor does it underestimate ρ_{00} for our data (*21*). The red solid lines in Fig. 2 show the tomography curves corresponding to the reconstructed density matrices displayed as insets, where we truncated the basis to the first three Dicke states (0 to 2 atoms in $|1\rangle$) (*21*). A fidelity ρ_{11} of 0.42, 0.37, and 0.31 was obtained for N = 41, 23, and 12. The 1σ error is below 0.1 in all cases (*21*).

One important limit to the fidelity is false-positive detection during preparation (atoms detected in $|1_N\rangle$ although they are in $|0_N\rangle$). Discarding runs with ambiguous measurement results reduces this error and increases fidelity, at the cost of reducing success probability. To decide whether the cavity is in the high- or low-transmission state, we analyze both the reflected and transmitted photon numbers, N_R and N_T, and compare to predefined thresholds. Figure 3A shows the count distribution of N_R (*21*). All data was acquired using $N_T = 0$, $N_R \geq 4$ as the criterion signaling successful preparation, leaving room for postselection using a higher threshold $N_{R,min}$. Figure 3B shows the fidelity as a function of $N_{R,min}$, confirming that this is an important contribution to the preparation error. The data shown in Fig. 2 correspond to values of $N_{R,min}$ [slightly different for each atom number (*21*)] such that the fraction of successful runs is ~10%.

Knowing how much entanglement is present in a many-particle state is difficult, even when the full density matrix is known. We now establish criteria for entanglement in the vicinity of the W state by solely comparing the two populations ρ_{00} and ρ_{11}. Bipartite entanglement being extremely difficult to prove with a W state (*30*), we rather look for multipartite entanglement and for the minimal number of entangled atoms. A state with density matrix ρ contains, at most, k entangled particles if ρ can be decomposed as a convex sum of density matrices $\rho_1 \otimes \ldots \otimes \rho_M$, where each ρ_i corresponds to a density matrix containing, at most, k atoms, and $M \leq N$ (*30*).

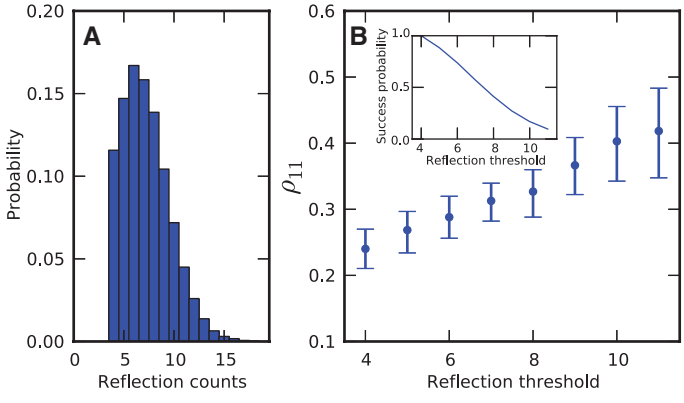

Fig. 3. Fidelity control of a W state with 41 atoms. (**A**) Distribution of counts in reflection during successful state preparation. The count rate in transmission is always zero, otherwise the preparation step is repeated. (**B**) Fidelity of the prepared W state and success probability as functions of the reflection threshold $N_{R,min}$. The data shown in Fig. 2B corresponds to $N_{R,min} = 11$, for which the preparation success is 9%. Error bars indicate 1 SD.

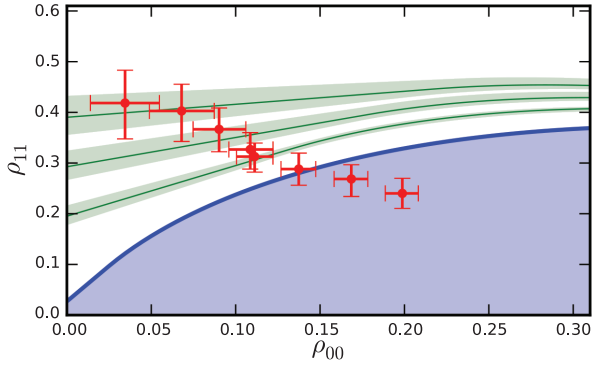

Fig. 4. Multipartite entanglement for a W state with 41 atoms. Fully separable states lie within the blue shaded area. From bottom to top, the green curves show the bound for k-separable states with k = 8, 12, and 16. A state above a bound contains at least $k + 1$ entangled particles. Shaded areas limit the bounds when varying the atom number from 37 to 45. The red points are the data from Fig. 3B, showing the increase of the minimal number of entangled particles with increasing $N_{R,min}$. Error bars indicate 1 SD.

Starting from this expression, we first calculate the upper bound for ρ_{11} as a function of ρ_{00} for a fully separable state with $k = 1$ (*21*). The bound, which is tight, is shown as the solid thick blue line in Fig. 4. Any state corresponding to a point outside the blue shaded region necessarily contains at least two-particle entanglement. The calculation can be extended to larger k, and the green lines show the bounds for $k = 8$, 12, and 16. The experimental state with the highest fidelity of 0.42 lies ~1 SD above the $k = 12$ curve, indicating that it contains at least 13 entangled atoms.

In our present setup, fidelity is limited by decoherence due to differential light shifts in the dipole trap (*21*) and a probability of ~0.2 for spontaneous emission from $|1\rangle$ during the QND detection. For large atom numbers, spontaneous emission from $|0\rangle$ will eventually become dominant. Simulations show that, with state-of-the-art optical cavities, the entanglement process can be scaled up to ensembles with $N > 10^4$. Because our method relies only on coherent evolution and collective QND measurement, it can be adapted to many systems and, in particular, to other forms of cavity quantum electrodynamics, including addressable qubits such as ions in optical cavities (*31*) or superconducting qubits in microwave cavities (*32*), as long as they are indistinguishable by cavity measurement. Furthermore, by including multiple rotations and QND detection intervals, or by combining it with other entanglement schemes such as cavity-induced spin squeezing (*6*), our scheme can be extended to a large range of entangled states. In combination with the inherent single-particle resolution, this makes it possible to investigate the fundamental limits of metrologically relevant forms of entanglement and could considerably enhance the precision of interferometric devices based on quantum metrology. In addition, our method is well suited to investigate quantum Zeno dynamics (*33*), where permanent QND observation of a degenerate eigenvalue limits the coherent evolution of the system to a given subspace, enabling preparation of a large variety of entangled states (*34*).

References and Notes

1. T. Monz *et al*., *Phys. Rev. Lett.* **106**, 130506 (2011).
2. C. Gross, T. Zibold, E. Nicklas, J. Estève, M. K. Oberthaler, *Nature* **464**, 1165–1169 (2010).
3. M. F. Riedel *et al*., *Nature* **464**, 1170–1173 (2010).
4. B. Lücke *et al*., *Science* **334**, 773–776 (2011).
5. J. Appel *et al*., *Proc. Natl. Acad. Sci. U.S.A.* **106**, 10960–10965 (2009).
6. M. H. Schleier-Smith, I. D. Leroux, V. Vuletić, *Phys. Rev. Lett.* **104**, 073604 (2010).
7. J. G. Bohnet *et al*., Reduced back-action for phase sensitivity 10 times beyond the standard quantum limit. http://arxiv.org/abs/1310.3177 (2013).
8. M. Koschorreck, M. Napolitano, B. Dubost, M. W. Mitchell, *Phys. Rev. Lett.* **104**, 093602 (2010).
9. I. D. Leroux, M. H. Schleier-Smith, V. Vuletić, *Phys. Rev. Lett.* **104**, 073602 (2010).
10. S. Massar, E. S. Polzik, *Phys. Rev. Lett.* **91**, 060401 (2003).
11. A. Kuzmich, N. P. Bigelow, L. Mandel, *Europhys. Lett.* **42**, 481–486 (1998).
12. V. Giovannetti, S. Lloyd, L. Maccone, *Science* **306**, 1330–1336 (2004).
13. V. Vedral, *Nature* **453**, 1004–1007 (2008).
14. H. J. Kimble, *Phys. Scr.* **T76**, 127 (1998).
15. Y. Colombe *et al*., *Nature* **450**, 272–276 (2007).
16. F. Brennecke *et al*., *Nature* **450**, 268–271 (2007).
17. T. P. Purdy *et al*., *Phys. Rev. Lett.* **105**, 133602 (2010).
18. S. Brakhane *et al*., *Phys. Rev. Lett.* **109**, 173601 (2012).
19. J. Volz, R. Gehr, G. Dubois, J. Estève, J. Reichel, *Nature* **475**, 210–213 (2011).
20. A. D. Boozer, A. Boca, R. Miller, T. E. Northup, H. J. Kimble, *Phys. Rev. Lett.* **97**, 083602 (2006).
21. Materials and methods are available as supplementary materials on *Science* Online.
22. W. Dür, G. Vidal, J. I. Cirac, *Phys. Rev. A* **62**, 062314 (2000).
23. L. Pezzé, A. Smerzi, *Phys. Rev. Lett.* **102**, 100401 (2009).
24. C. W. Chou *et al*., *Nature* **438**, 828–832 (2005).
25. T. Chanelière *et al*., *Nature* **438**, 833–836 (2005).
26. F. T. Arecchi, E. Courtens, R. Gilmore, H. Thomas, *Phys. Rev. A* **6**, 2211–2237 (1972).
27. R. Gehr *et al*., *Phys. Rev. Lett.* **104**, 203602 (2010).
28. S. L. Christensen *et al*., Quantum interference of a single spin excitation with a macroscopic atomic ensemble. http://arxiv.org/abs/1309.2514 (2013).
29. J. M. Raimond *et al*., *J. Phys. B* **38**, S535–S550 (2005).
30. O. Gühne, G. Tóth, *Phys. Rep.* **474**, 1–75 (2009).
31. B. Casabone *et al*., *Phys. Rev. Lett.* **111**, 100505 (2013).
32. J. A. Mlynek *et al*., *Phys. Rev. A* **86**, 053838 (2012).
33. P. Facchi, S. Pascazio, *Phys. Rev. Lett.* **89**, 080401 (2002).
34. J. M. Raimond *et al*., *Phys. Rev. Lett.* **105**, 213601 (2010).

Acknowledgments: We thank G. Semerjian for help with the calculations on the entanglement criterion and B. Huard for discussions. This work was supported by the European Union Information and Communication Technologies project QIBEC (Quantum Interferometry with Bose-Einstein Condensates) (GA 284584) and the Integrating Project AQUTE (Atomic Quantum Technologies) (GA 247687). F.H. acknowledges a scholarship by Institut Francilien de Recherche sur les Atomes Froids. Author contributions: F.H. and J.V. performed the experiment; R.G. made contributions in its early stages; and F.H., J.V., J.R., and J.E. contributed to data analysis and interpretation, as well as to the manuscript.

Supplementary Materials

www.sciencemag.org/content/344/6180/180/suppl/DC1
Materials and Methods
Figs. S1 to S6
References (*35*–*37*)

25 November 2013; accepted 12 March 2014
Published online 27 March 2014;
10.1126/science.1248905

Unfolding the Laws of Star Formation: The Density Distribution of Molecular Clouds

Jouni Kainulainen,[1]* Christoph Federrath,[2] Thomas Henning[1]

The formation of stars shapes the structure and evolution of entire galaxies. The rate and efficiency of this process are affected substantially by the density structure of the individual molecular clouds in which stars form. The most fundamental measure of this structure is the probability density function of volume densities (ρ-PDF), which determines the star formation rates predicted with analytical models. This function has remained unconstrained by observations. We have developed an approach to quantify ρ-PDFs and establish their relation to star formation. The ρ-PDFs instigate a density threshold of star formation and allow us to quantify the star formation efficiency above it. The ρ-PDFs provide new constraints for star formation theories and correctly predict several key properties of the star-forming interstellar medium.

The formation of stars is an indivisible component of our current picture of galaxy evolution. It also represents the first step in defining where new planetary systems can form. The physics of how the interstellar medium (ISM) is converted into stars is strongly affected by the density structure of individual molecular clouds (*1*). This structure directly affects the star-formation rates (*SFRs*) and efficiencies (*SFEs*) predicted by analytic models (*2*–*5*). Inferring this structure observationally is challenging because observations only probe projected column densities. Hence, the key parameters of star-formation models remain unconstrained. Here, we present a technique that allows us to quantify the grounding measure of the molecular cloud density structure: the probability density function of their volume density (ρ-PDF).

The *SFRs* of molecular clouds are estimated in analytic theories from the amount of gas in the clouds above a critical density, ρ_{crit} (*2*–*5*)

$$SFR = \frac{\varepsilon_{core}}{\phi} \int_{s_{crit}}^{\infty} \frac{t_{ff}(\rho_0)}{t_{ff}(\rho)} \frac{\rho}{\rho_0}\, p(s)\mathrm{d}s \qquad (1)$$

where $s = \ln(\rho/\rho_0)$ is the logarithmic, mean-normalized density, and $s_{crit} = \ln(\rho_{crit}/\rho_0)$. We use the number density, $n = \rho/\overline{\mu} m_p$, where $\overline{\mu}$ is the mean molecular mass and m_p is the proton mass, as the measure of density. The parameter ε_{core} in Eq. 1 is the core-to-star efficiency, giving the fraction of gas above s_{crit} that collapses into a star. The $t_{ff}(\rho)$ is the free-fall time of pressureless gas that approximates the star-formation time scale, and ϕ is the ratio of the free-fall time to the actual star-formation time scale. The critical density, commonly referred to as the (volume) density threshold of star formation, indicates that stars form only above that density. Generally, the critical density depends on gas properties (*2*–*5*), but theoretical considerations suggest that it could be relatively constant under typical molecular cloud conditions (*5*).

[1]Max-Planck-Institute for Astronomy, Königstuhl 17, 69117 Heidelberg, Germany. [2]Monash Centre for Astrophysics, School of Mathematical Sciences, Monash University, Vic 3800, Australia.
*Corresponding author. E-mail: jtkainul@mpia.de

The decisive density structure of molecular clouds is encapsulated in the function $p(s)$ describing the probability of a volume dV to have a log density between [s, s + ds]—the ρ-PDF. In current understanding, the ρ-PDF is determined by supersonic turbulence that induces a log-normal ρ-PDF (*6*–*9*):

$$p(s) = \frac{1}{\sigma_s\sqrt{2\pi}} e^{\frac{(s-\mu)^2}{2\sigma_s^2}} \quad (2)$$

where μ and σ_s are the mean and width, respectively. The ρ-PDF width is linked to the turbulent gas properties through $\sigma_s^2 = \ln\left(1 + b^2 M_s^2 \frac{\beta}{\beta+1}\right)$ (*10*), where M_s (sonic Mach number) is a measure of the turbulence energy, b is a parameter related to the turbulence driving mechanism (*9*), and β is the ratio of thermal to magnetic pressures.

Despite their decisive role for star formation, the ρ-PDF function and the critical density are not observationally well-constrained. Instead, studies have measured their two-dimensional (2D) counterparts: the column density PDFs (*11*, *12*) and the column density threshold of star formation (*13*, *14*). We must, however, accept that these cannot be used in the theories based on Eq. 1 because of the nontrivial transformation between the volume and column densities (*15*, *16*). An analytic technique to estimate ρ-PDFs from column densities exists (*16*) but is not widely applied because of its stringent requirements for the isotropy of the data. A technique exploiting molecular line observations also exists (*17*), but it samples the ρ-PDF sparsely, hampering the determination of its shape. To overcome the problem, some studies have derived *SFRs* using the mean densities of the clouds instead (*18*). Even though reasonably successful in predicting *SFRs*, the approach does not connect the processes shaping the ISM to *SFRs* as directly as do the theories using Eq. 1. Consequently, exactly how those processes control star formation remains unknown.

To make progress, we developed an approach to estimate the ρ-PDF functions and the critical density from column density data (*19*). We represent the data as a set of hierarchical, 3D structures. First, we decompose the column density maps with wavelet filtering so as to describe the structure at different spatial scales. Then, substantial structures are identified at the different scales, and their 3D geometries are modeled with prolate spheroids. We chose this shape based on tests against numerical simulations (*19*). It allows modeling of both elongated, filament-like structures that are common in molecular clouds, and near-spherical shapes that represent small-scale, clumpy structures. The inclination angles of the spheroids are not known and are assumed to be zero. This leads to a high uncertainty in the densities of individual structures, but we show that when averaged over numerous structures, the ρ-PDF is reconstructed reasonably well (supplementary text). The masses of the structures are calculated from the column densities at their respective scales. Last, the hierarchical cloud structure is modeled by placing the overlapping structures inside each other's, allowing modeling of complicated, asymmetric structures. The volumes (dV) and masses—and hence densities (dρ)—of all structures are known, which yields the ρ-PDF.

We tested the technique with 14 numerical simulations of magneto-hydrodynamic, self-gravitating turbulence (*19*, *20*). The ρ-PDFs are reasonably well recovered under various physical conditions (figs. S5 to S10) (*19*). The important ρ-PDF parameters, the mean and width, have about 10 and 20% uncertainty, respectively (supplementary text).

With this technique in hand, we derived ρ-PDFs for molecular clouds. As observational data, we used column density maps derived from dust extinction mapping (*11*). We derived ρ-PDFs for 16 molecular clouds closer than 260 pc (Fig. 1 and figs. S1 to S3). The derived ρ-PDFs probe the range of volume densities from 80 to 5×10^4 cm^{-3}. The sensitivity of our technique decreases above ~3×10^4 cm^{-3} because the extinction maps cover a limited dynamic range of column densities (*19*). The ρ-PDFs closely follow log-normal functions, as predicted with turbulence theory (Eq. 2), and their widths vary between σ_s = [1.2, 2.0] (table S1).

Having quantified the ρ-PDFs, we can establish the relationship between the clouds' density structure and their star-formation activity. As a measure of this activity, we adopted the number of young stellar objects, N_{YSO}, in the clouds (*19*). This number was used to estimate the mean star-formation surface densities, $\Sigma_{SFR} = \frac{N_{YSO} <M>}{A \times 2My}$, where A is the cloud area, 2 million years (My) is the star-formation time scale (*13*, *14*, *21*), and $<M>$ = 0.5 $M_\odot$ is the mean stellar mass. We show that the ρ-PDF widths correlate with Σ_{SFR} (Fig. 2A). This correlation invokes two possible interpretations. One is that the clouds' density structures evolve with time, characterized by the widening of their ρ-PDFs and consequent increase of Σ_{SFR}. Another interpretation is that the initial conditions of cloud formation set the clouds' density structures, which then control the Σ_{SFR}. Distinguishing between these scenarios with the available observational data is difficult (supplementary text).

Once we had quantified the ρ-PDFs and assessed their relation to star formation, we could estimate the critical density of star formation. Our sample includes three clouds on the verge of star formation; they have either formed only one star, or no stars at all. The mean of the highest log densities probed by the ρ-PDFs of these clouds is $s = 4.2 \pm 0.3$, which corresponds to a volume density of $(5 \pm 2) \times 10^3$ cm^{-3} (*19*). This threshold does not depend strongly on the spatial resolution of the data we used (*19*). We interpreted these values as the critical densities in the clouds of our sample, noting that cloud-to-cloud variations may exist (*5*). Previously, the critical volume density based on analyses of observed column densities has been suggested to be ~10^4 cm^{-3} (*13*) and $(6.1 \pm 4.4) \times 10^3$ cm^{-3} (*22*) in nearby clouds. The observational estimates of the critical density are generally smaller than analytical model predictions that indicate (2 to 5) × 10^4 cm^{-3} (*5*). The reason for this discrepancy remains unknown.

The ρ-PDFs and critical density allow us to infer the *SFE* of star-forming gas. Following

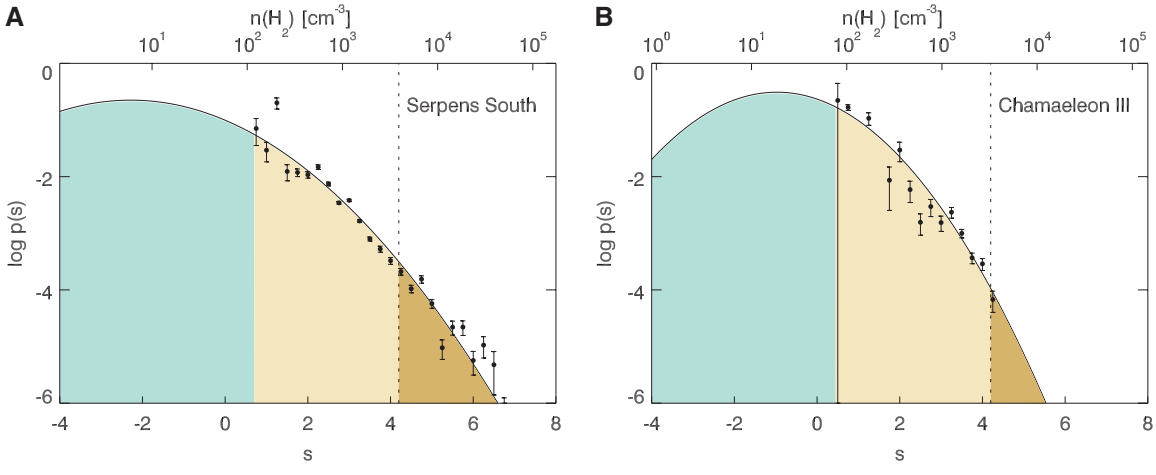

Fig. 1. ρ-PDFs of two molecular clouds. (A) The star-forming Serpens South cloud. **(B)** The non–star-forming Chamaeleon III cloud. The solid lines show fits of log-normal models. Dark brown indicates the star-forming gas. Light brown indicates the major structures enveloping star-forming gas. Green indicates the relatively nonstructured gas.

Eq. 1, only the gas above s_{crit} participates in star formation. The mass of the star-forming gas is then $M_{sf} = M(s > s_{crit}) = M_{cloud} \int_{s_{crit}}^{\infty} \frac{\rho}{\rho_0} p(s) ds$ (table S1). The *SFE* of the gas above s_{crit} (referred to as dense gas) is $SFE(\text{dense gas}) = \frac{M_{stars}}{M_{stars} + M_{sf}}$, yielding the average of 16^{+20}_{-9}% for our sample. The *SFE*(dense gas) is independent of the fraction of star-forming gas in the clouds (Fig. 2B), indicating that it is independent of the density structure of the clouds' lower-density regions (supplementary text).

The *SFE*(dense gas) we derive using volume densities is somewhat higher than an estimate based on column densities. We estimated the efficiencies also from the column densities, using $N = 6.3 \times 10^{21}$ cm^{-2} as the critical value (*13*). This yielded a mean efficiency of 6^{+11}_{-4}%. The masses of star-forming gas estimated from volume densities are lower than those estimated from column densities, yielding higher *SFEs*. This difference results from the fact that when measured from column densities, M_{sf} contains a contribution from a diffuse envelope that surrounds the dense (star-forming) gas. Our volume density technique removes this component. In addition, when estimated from column densities the *SFE* correlates with the dense gas mass fraction (Fig. 2B). This correlation is likely artificial; the relative contribution of the envelopes to the M_{sf} is larger when the dense gas fraction is lower.

The constraints we derived for the ρ-PDF, critical density, and *SFE* provide insight to the mass range of star-forming molecular clouds. Suppose the lowest possible mass of a star is given by the hydrogen-burning limit, 0.08 $M_\odot$. A simplistic calculation suggests that a minimum mass for a maternal molecular cloud to form a star is then on the order of 30 $M_\odot$ (*19*). This coincides with the mass range (5 to 50 $M_\odot$) of the smallest known star-forming molecular clouds, globules (*23*).

We similarly estimated the mass of a cloud likely to form high-mass (>20 $M_\odot$) stars. The mass required for a natal molecular cloud to have a 95% probability to form a high-mass star is $\sim 7^{+14}_{-5} \times 10^4$ $M_\odot$ (*19*). This is in agreement with the fact that from the solar neighborhood clouds, only Orion A, whose mass is 10^5 $M_\odot$ (*11*), is forming high-mass stars. For only a 50% probability to form a high-mass star, the same calculation yields a cloud mass of $1.5^{+3.4}_{-0.7} \times 10^4$ $M_\odot$ (*19*).

The ρ-PDFs can also help us to understand star formation on scales larger than individual molecular clouds. Our sample represents almost all molecular gas closer than 260 pc. The total ρ-PDF of the sample (fig. S4) indicates that ~2.5% of this gas is above the star formation threshold. If we hypothesize that the total ρ-PDF is close to the average ρ-PDF of the Milky Way gas, a *SFR* of ~3 $M_\odot$/year follows for the Milky Way (*19*). This agrees with other *SFR* estimates for the Milky Way (*24*–*26*). It is difficult to estimate how close the ρ-PDF of our sample is to the galactic mean; the galactic ρ-PDF is not generally known. Some works suggest that the turbulence properties are universal (*27*) and that the mean surface densities of gas do not depend strongly on the galactic environment (*28*). This implies that the ρ-PDF of molecular gas may not vary much in general. Some observations have indicated that the ρ-PDFs of massive clouds may substantially differ from the local clouds (*29*). However, it is not known how representative such clouds are, or what the relationship is between density and star formation in them. Albeit simplistic, our estimate of the Milky Way *SFR* lays out the possibility that the *SFRs* of entire galaxies are imprinted on their ρ-PDFs when averaged over scales of hundreds of parsecs.

With our approach to estimate molecular cloud ρ-PDFs, we were able to derive fundamental quantities that characterize star formation. The results provide an observationally established basis for predicting *SFRs* of molecular clouds, and they may also lead to a better understanding of the *SFRs* of entire galaxies.

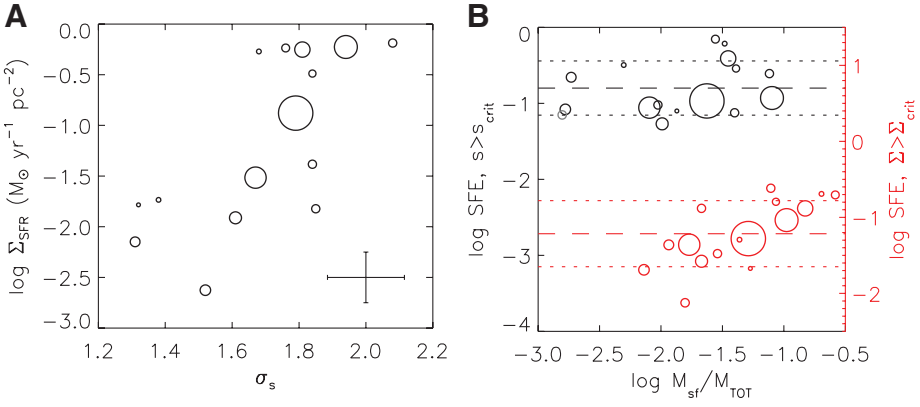

Fig. 2. Relationship between the star formation and molecular cloud density structure. (**A**) *SFR* surface densities (Σ_{SFR}) as a function of the ρ-PDF width (σ_s). The symbol sizes reflect the cloud masses, spanning the range from 0.07×10^4 to 3.6×10^4 $M_\odot$. The error bar indicates the 1σ statistical uncertainty. (**B**) *SFE* of the star-forming gas as a function of the dense gas mass fraction (black circles, the left *y* axis). The *SFEs* of the gas above the critical column density of $N = 6.3 \times 10^{21}$ cm^{-2} are also shown (red circles, the right *y* axis). The dashed line shows the mean, and dotted lines are the SD.

References and Notes

1. P. Hennebelle, E. Falgarone, *Astron. Astrophys. Rev.* **20**, 55–112 (2012).
2. M. R. Krumholz, C. F. McKee, *Astrophys. J.* **630**, 250–268 (2005).
3. P. Padoan, Å. Nordlund, *Astrophys. J.* **730**, 40–50 (2011).
4. P. Hennebelle, G. Chabrier, *Astrophys. J.* **743**, L29–L33 (2011).
5. P. Padoan *et al.*, in *Protostars and Planets VI*, H. Beuther, R. S. Klessen, C. P. Dullemond, T. Henning, Eds. (University of Arizona Space Science Series); http://arxiv.org/abs/1312.5365v1.
6. E. Vazquez-Semadeni, *Mon. Not. R. Astron. Soc.* **423**, 681–692 (1994).
7. P. Padoan, Å. Nordlund, B. J. T. Jones, *Mon. Not. R. Astron. Soc.* **288**, 145–152 (1997).
8. J. Scalo, E. Vazquez-Semadeni, D. Chappell, T. Passot, *Astrophys. J.* **504**, 835–853 (1998).
9. C. Federrath, R. S. Klessen, W. Schmidt, *Astrophys. J.* **688**, L79–L82 (2008).
10. F. Z. Molina, S. C. O. Glover, C. Federrath, R. S. Klessen, *Mon. Not. R. Astron. Soc.* **423**, 2680–2689 (2013).
11. J. Kainulainen, H. Beuther, T. Henning, R. Plume, *Astron. Astrophys.* **508**, L35–L38 (2009).
12. N. Schneider *et al.*, *Astrophys. J.* **766**, L17–L23 (2013).
13. C. J. Lada, M. Lombardi, J. F. Alves, *Astrophys. J.* **724**, 687–693 (2010).
14. A. Heiderman, N. J. Evans, *Astrophys. J.* **723**, 1019–1037 (2010).
15. J. Fischera, M. A. Dopita, *Astrophys. J.* **611**, 919–927 (2004).
16. C. M. Brunt, C. Federrath, D. J. Price, *Mon. Not. R. Astron. Soc.* **405**, L56–L60 (2010).
17. A. Ginsburg, C. Federrath, J. Darling, *Astrophys. J.* **779**, 50 (2014).
18. M. R. Krumholz, A. Dekel, C. F. McKee, *Astrophys. J.* **745**, 69 (2012).
19. Materials and methods are available as supplementary materials on *Science* Online.
20. C. Federrath, R. S. Klessen, *Astrophys. J.* **761**, 156 (2012).
21. N. J. Evans *et al.*, *Astrophys. J. Suppl. Ser.* **181**, 321–350 (2009).
22. N. J. Evans II, A. Heiderman, N. Vutisalchavakul, *Astrophys. J.* **782**, 114 (2014).
23. R. Launhardt *et al.*, *Astrophys. J. Suppl. Ser.* **188**, 139–177 (2010).
24. T. P. Robitaille, B. A. Whitney, *Astrophys. J.* **710**, L11–L15 (2010).
25. N. Murray, M. Rahman, *Astrophys. J.* **709**, 424–435 (2010).
26. R. Diehl *et al.*, *Nature* **439**, 45–47 (2006).
27. M. Heyer, C. Brunt, *Astrophys. J.* **615**, L45–L48 (2004).
28. J. Roman-Duval, J. M. Jackson, M. Heyer, J. Rathborne, R. Simon, *Astrophys. J.* **723**, 492–507 (2010).
29. J. Kainulainen, J. C. Tan, *Astron. Astrophys.* **549**, A53 (2013).

Acknowledgments: We thank H. Beuther, P. Clark, and A. Stutz for discussions. J.K. acknowledges the Deutsche Forschungsgemeinschaft priority program 1573 ("ISM-SPP"), and C.F. acknowledges the Discovery Projects Fellowship from the Australian Research Council (grant DP110102191). We acknowledge supercomputing time at Leibniz-Rechenzentrum (grant pr32lo), Jülich Supercomputing Centre (grant hhd20), and Partnership for Advanced Computing in Europe (grant pr89mu). This work is based on publicly available data from the 2 Micron All Sky Survey (http://irsa.ipac.caltech.edu/Missions/2mass.html).

Supplementary Materials

www.sciencemag.org/content/344/6180/183/suppl/DC1
Materials and Methods
Supplementary Text
Figs. S1 to S9
Table S1
References (*30*–*57*)

19 November 2013; accepted 17 March 2014
10.1126/science.1248724

Toughening Elastomers with Sacrificial Bonds and Watching Them Break

Etienne Ducrot,[1,2,3] Yulan Chen,[4] Markus Bulters,[5] Rint P. Sijbesma,[4] Costantino Creton[1,2,3]*

Elastomers are widely used because of their large-strain reversible deformability. Most unfilled elastomers suffer from a poor mechanical strength, which limits their use. Using sacrificial bonds, we show how brittle, unfilled elastomers can be strongly reinforced in stiffness and toughness (up to 4 megapascals and 9 kilojoules per square meter) by introducing a variable proportion of isotropically prestretched chains that can break and dissipate energy before the material fails. Chemoluminescent cross-linking molecules, which emit light as they break, map in real time where and when many of these internal bonds break ahead of a propagating crack. The simple methodology that we use to introduce sacrificial bonds, combined with the mapping of where bonds break, has the potential to stimulate the development of new classes of unfilled tough elastomers and better molecular models of the fracture of soft materials.

Elastomers are widely used in industrial applications such as tires, seals, gloves, and dampers for their ability to deform reversibly to large strains. Yet currently, maintaining this large deformability imposes an upper limit in stiffness. Above a Young's modulus of around 1 to 1.5 MPa, unfilled elastomers are brittle, limiting applications. This limitation is particularly severe at high temperatures and for rubbers with a low entanglement density. Fracture of simple elastomers has been described by Lake and Thomas (*1*, *2*), who predicted that the threshold fracture toughness (minimum energy necessary to break the elastomer) should scale with $N_c^{1/2}$, where N_c is the number of monomers between cross-links. In essence, the more cross-linked (and the stiffer) the elastomer, the more brittle it becomes. To circumvent this limitation, rubbers have been toughened by adding nanofillers and by making the elastomers more viscoelastic (*3*). It was found that optimized nanofillers impart a large increase in stiffness at small strain and cause highly dissipative processes to be active at large strains, effectively increasing both stiffness and strain at break (*4*). However, incorporating nanofillers introduces constraints in terms of processing and safety and requires careful dispersion. Alternatively, increasing the viscoelastic character of the elastomer is used to increase fracture toughness through molecular friction (*5*), but this method only works over a limited temperature range.

Many empirical strategies have been tried to increase simultaneously the strength and stiffness of unfilled elastomers by introducing heterogeneities in the network. The multimodal distribution of molecular weights between cross-links has been extensively tried on silicones, but the gains in stiffness at low strains only result in moderate increases in toughness (*6*–*8*). Another strategy has been to prestretch a partially cross-linked elastomer and further cross-link it in the stretched state (*9*). This improves the strength of the elastomer in the prestretching direction but decreases the initial tensile modulus and leads to very anisotropic properties. Knowledge-based strategies to increase fracture toughness while retaining full reversibility of deformation and low viscoelasticity have been limited by the lack of understanding of where and how energy is dissipated as a crack propagates. This micromechanical knowledge has been developed decades ago for materials with a yield stress, such as metals (*10*) and glassy polymers (*11*, *12*), in which dissipation of energy is localized and visible in a plastically deformed zone. However, for soft materials (gels, rubbers, or soft adhesives) there is typically no well-defined yield stress, and the origin of dissipation of energy during crack propagation remains an open question. Recent work has shown hydrogels with toughness in excess of 100 to 1000 times that of regular (very brittle) gels while maintaining a reasonable extensibility and recoverability of the strain (*13*, *14*). Hydrogels are very soft [Young's modulus (E) 1 to 100 kPa] molecular sponges full of water and thus are quite different materials from the hydrophobic and fully water-insoluble elastomers. The increase in toughness has been attributed there to the early fracture of "weak or overstressed" bonds (either intrinsically weaker than the main bonds, or loaded more than the main bonds) introduced in the bulk of the material by means of the synthetic method (*13*, *15*–*17*).

Our elastomers are obtained through sequential free-radical polymerizations. First, a well–cross-linked rubbery network is synthesized by means of ultraviolet (UV) polymerization in the presence of solvent. After drying, the rubber sheet referred to as "single network" (SN) is then swollen with a second monomer, UV initiator, and a small amount of cross-linker, effectively isotropically stretching the chains of the network. A second UV polymerization is performed on this swollen network, until all monomer is consumed. Varying the degree of cross-linking of the first network controls the level of swelling from a swelling ratio (Q) = 3.3 to 5 and effectively controls the level of prestretch of the first network chains and their volume fraction in the network (fig. S1). The double networks will be referred to as "DN." To obtain even lower-volume fractions of first network and higher levels of prestretch, the second step can be repeated on the DN. The presence of chains of the second network decrease the elastic component of the free energy per unit volume, allowing us to stretch first network chains further. The third polymerization step results in a material in which the first network chains only represent 5 to 10 weight percent (wt %) and are highly stretched, whereas the chains polymerized during the second step are lightly stretched, and those polymerized during the third step are entangled, lightly cross-linked, and loosely connected by chain transfer reactions (fig. S2 and table S3). These triple networks will be referred to as TN. It should be noted that because of the nature of the monomers used (acrylates), chain transfer reactions to the polymer likely occur during the second and third polymerization, effectively loosely connecting the networks with each other and affecting stress transfer between the networks.

In our example, the first network is made from ethyl acrylate and butanediol diacrylate cross-linker, and the second and third steps have

Table 1. Composition and properties of the materials of the study. Shown are the temperature of the experiment T, weight fraction of first network $\phi_{wt\%}^{1st}$, Young's modulus E (in MPa), and true stress at break σ_T^{break} (in MPa). Dashes indicate that the measurement was not done for that network.

Sample	T (°C)	SN EA_x			DN EA_xMA			TN EA_xMAMA		
First network		$\phi_{wt\%}^{1st}$	E	σ_T^{break}	$\phi_{wt\%}^{1st}$	E	σ_T^{break}	$\phi_{wt\%}^{1st}$	E	σ_T^{break}
$EA_{0.5}$	60	100	0.8	0.5	20	1.3	8	6	2.2	22
EA_1	60	100	1.5	0.5	30	2	6.5	10	4.2	29
EA_2	60	100	2.3	0.5	35	2.3	3	—	—	—
		SN $EA_{0.5}$			DN $EA_{0.5}EA$			TN $EA_{0.5}EAEA$		
$EA_{0.5}$	20	100	0.6	1.2	20	0.8	10	5	1.5	16

[1]École Supérieure de Physique et de Chimie Industrielles de la Ville de Paris (ESPCI) ParisTech, UMR 7615, 10, Rue Vauquelin, 75231 Paris Cédex 05, France. [2]CNRS, UMR 7615, 10, Rue Vauquelin, 75231 Paris Cédex 05, France. [3]Sorbonne-Universités, Université Pierre et Marie Curie (UPMC) Université Paris 06, UMR 7615, 10, Rue Vauquelin, 75231 Paris Cédex 05, France. [4]Institute for Complex Molecular Systems, Eindhoven University of Technology, Post Office Box 513, 5600 MB Eindhoven, Netherlands. [5]DSM Ahead, Urmonderbaan 22, 6167 RD Geleen, Netherlands.

*Corresponding author. E-mail: costantino.creton@espci.fr

been carried out with methyl acrylate. However, similar networks have been obtained with sequential polymerizations by using two methyl acrylate networks or two and three ethyl acrylate networks with similar results (fig. S3 and table S1). A summary of the properties and nomenclature of the materials is shown in Table 1. Three cross-linker concentrations in the first network are presented here (table S1). $EA_{0.5}$ is cross-linked at 1.45 mole percent (mol %) of monomer, EA_1 two times more (2.81 mol %), and EA_2 four times more (5.81 mol %). Their corresponding DN and TN are referred to as EA_xMA if the second network is made of MA or EA_xEA if the second monomer is EA, and referred to as EA_xMAMA if the third network is made of MA or EA_xEAEA if the third monomer is EA.

As an example of the mechanical properties of SN, DN, and TN elastomers, the stress strain curves at 60°C [45°C above the glass transition temperature (T_g) of the PMA] in uniaxial extension are shown in Fig. 1A for EA_1, EA_1MA, and EA_1MAMA. The elastic modulus of the elastomer increases by a factor of up to 3.5, whereas the true stress at break increases by a factor of 58. The effect of changing the cross-linker concentration in the first network on the properties of the DN elastomer is shown in Fig. 1B, and the effect of changing the second and third monomer for the DN and TN materials [at equal temperature difference from Tg. ($T - T_g$)] is shown in Fig. 1C. In principle, such a striking increase in strength could be due to plasticity in large strain, leading to permanent deformation upon unloading.

However, as shown in Fig. 2A the material unloads with no detectable hysteresis for the EA_1MA DN, and as shown in Fig. 2B, there is a substantial hysteresis during the first cycle but no measurable hysteresis for the subsequent cycles to the same strain for the $EA_{0.5}MAMA$ TN. The residual deformation after each cycle remains below 6% for the DN and TN, and the modulus after each cycle remains nearly constant for the TN, showing that the damage is very moderate (fig. S4). Although substantial hysteresis occurs in the material in cyclic extension, the modulus does not decrease much. This suggests that unlike what was observed for gels, most of the initial modulus is due to the second and third network, and the chains of the first network simply limit the maximum extensibility.

The increase in strain and stress at break suggests that the fracture toughness of the elastomers should also increase. We carried out crack propagation experiments on single-edged notched samples (fig. S5) at a low nominal strain rate of 0.025 s^{-1} at 60°C and 20°C for all prepared networks and used the large-strain approximation of Greensmith (*18*) to extract the critical energy release rate G_c. The results are presented in Fig. 3 as a function of the elastic modulus. The fracture toughness G_c increases from ~50 J/m^2 to 2000 to 5000 J/m^2 from the SN and the TN. These values of fracture toughness for materials that also have a high elastic modulus and low loading rate is in the range of some filled elastomers or of the best tough hydrogels. We are aware of one unfilled elastomer that has a comparable combination of properties—namely, natural rubber, which reaches a G_c value of 2 to 10 kJ/m^2 in comparable conditions (*19*). But, this behavior is due to strain-induced crystallization, which is difficult to reproduce in other elastomers.

We hypothesize that the origin of the toughening mechanism is similar to that of Gong and coworkers (*15*, *20*, *21*)—that the fracture of covalent bonds in the primary-minority network controls the stress level (and hence the stiffness), whereas the second- and third-majority networks prevent large cracks from forming. From macroscopic evidence, Gong and coworkers could assess that bonds actually break near the crack tip.

We found that we can directly see where and when sacrificial bonds break as the material is deformed by using a chemoluminescent

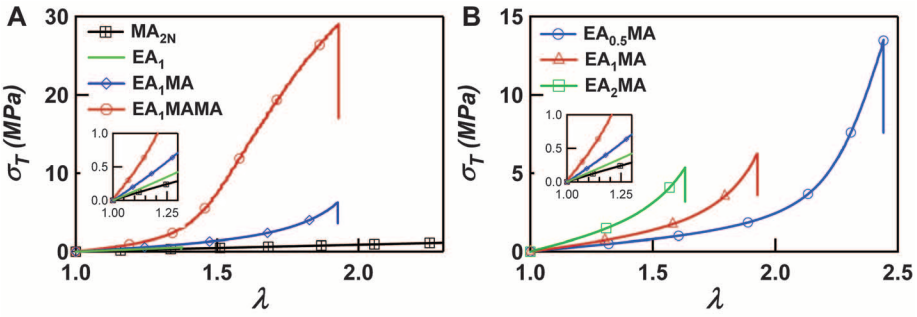

Fig. 1. Mechanical behavior of tough elastomers in uniaxial tension. (**A**) True stress/stretch curves of the EA_1, EA_1MA, EA_1MAMA, and PMA second network alone at 60°C. (**B**) Effect of changing the level of cross-linker in the EA first network on the EA_xMA DN. (**C**) Comparisons between $EA_{0.5}MA$[MA] and $EA_{0.5}EA$[EA] at equivalent $T - T_g$. Solid lines represent the TN, and dashed lines represent the DN.

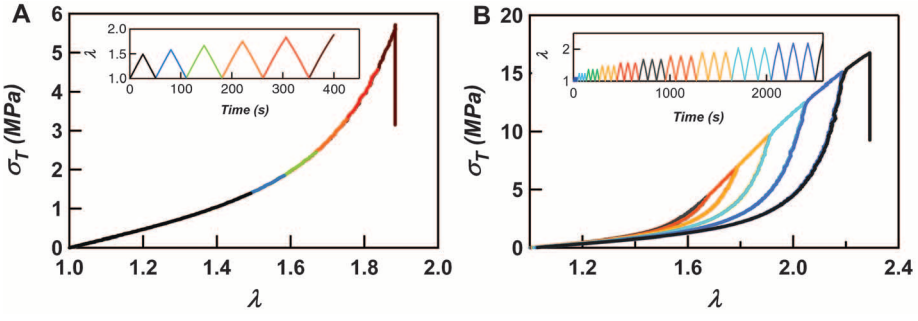

Fig. 2. Step-cycle loading-unloading curves of multiple network elastomers at 60°C. (**A**) Stress-strain curve of a single sample of EAMA elastomer submitted to a step-cycle loading. (Inset) The applied stretch as a function of time. All curves follow the same path on the σ-λ curve for this elastomer. (**B**) The same graph for a single sample of $EA_{0.5}MAMA$ network. In this case, each *n*th cycle follows a different path when λ of the *n*th cycle exceeds the maximum value of λ of the $(n - 1)$ cycle. Despite the damage in large strain, the initial modulus is nearly the same for all cycles (fig. S4).

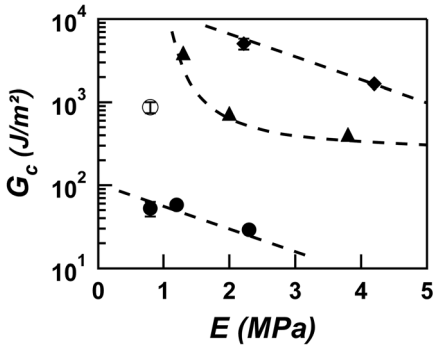

Fig. 3. Fracture toughness of multiple network elastomers. Shown is the fracture toughness G_c from single-edge notch tests at 60°C versus initial modulus for SN (solid circles), DN (triangles), and TN (diamonds) of various cross-linker concentrations in the first network EA_x[MA[MA]], second network alone MA_{2N} (open circle). The dashed lines are to guide the eyes. Error bars show SD; sample size, $n = 3$ repeats per experiment.

cross-linker, bis(adamantyl)-1,2-dioxetane bisacrylate (BADOBA) (fig. S6) (*22*), which is able to emit light when it breaks. If a sufficient force is applied to the BADOBA, the dioxetane group breaks into two ketones, one of which is in the excited state, as shown schematically in Fig. 4A. Relaxation to the ground state emits a photon in the bright blue range of the spectrum (emission maximum Λ_{max} = 420 nm). Because MA-based networks need to be tested at 60°C and the BADOBA is insufficiently stable at 60°C for the duration of a mechanical test, we chose fully EA-based networks and prepared a SN of $EA_{0.5}$, a DN of $EA_{0.5}EA$, and a TN of $EA_{0.5}EAEA$. In all of these networks, the first network was cross-linked with BADOBA. Uniaxial tensile cycles and fracture tests were filmed with a sensitive camera able to detect single photons at 50 images per second (fig. S7). The load-unload cycles of an $EA_{0.5}EA$ DN is shown in Fig. 4B, together with the corresponding light emission signal as a function of λ, and the same data for the TN network is shown in Fig. 4, C and D. A video of the luminescence of TN under cyclic extension is presented in movie S1. Bond breakage only occurs above a certain value of λ, and only for the first cycle, because subsequent cycles to the same value of λ are fully elastic. This data demonstrate that the first-cycle hysteresis (fig. S8) is due to the irreversible breakage of bonds homogeneously in the whole sample. Comparing the mechanical data of Fig. 4, B and C, with that of Fig. 1C, the replacement of the BDA with the BADOBA only has a small weakening effect on the mechanical properties of the elastomers, strongly suggesting that although the chemoluminescent bond is a bit weaker than a C-C bond (150 kJ/mol versus 350 kJ/mol) (*23*), it really acts as a marker and does not modify the mechanism itself. The power-law correlation between the cumulative mechanical hysteresis and the total emitted light for a given value of λ is shown in Fig. 4E.

Having established that the intensity of blue light is directly connected to the mechanical hysteresis, the next step was to use it to map bond breakage during fracture experiments. The image of the luminescence around the tip of a propagating crack is shown in Fig. 5 for the EA-based SN, DN, and TN. A video of the crack propagation in the TN followed by chemoluminescence is presented in movie S2. Because scales are identical and the signal is proportional to the number of photons per pixel, the intensity can be compared; the bond breakage is very localized in front of the crack tip (practically one pixel) for the SN, is still localized at the crack tip but more intense for the DN, and extends over a large region in the material for the TN. A precise integration of the luminescence over the whole region is not possible because of the high dynamic range, leading to a saturation of the camera sensor. However, these results show that the same mechanism detected by the hysteresis in uniaxial tension is active at the crack tip. This result is in qualitative agreement with post mortem observations on fractured gels (*20*) and with two models proposed respectively by Tanaka (*24*) and Brown (*25*), predicting that the dual population of co-continuous networks creates a yielding mechanism and a damage zone where the yield stress is controlled by the stress to break the first network bonds, and the size of the zone is controlled by the extensibility of the second network chains.

However, the intensity mapping provides much more precise information. It shows that an increase in degree of prestretching of the chains and a decrease in their volume fraction leads to a much

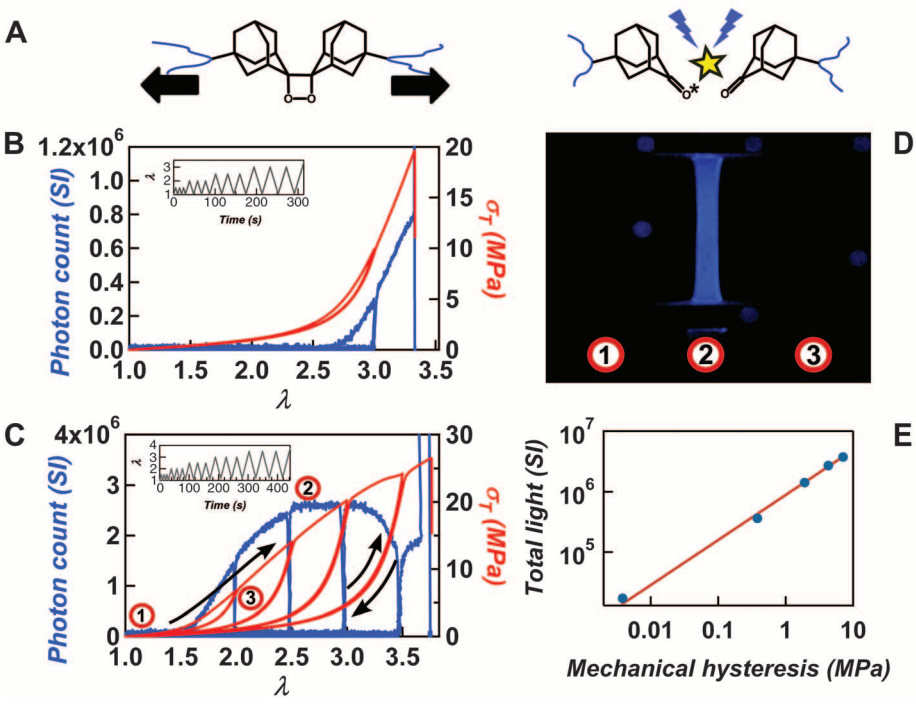

Fig. 4. Chemoluminescent molecules to detect bond breakage. (**A**) Schematic of the chemoluminescence process, bond breakage of the dioxetane cross-linker, and light emission. (**B**) Step-cycle test for a single sample of the DN network showing mechanical stress-strain curves (red) and light emission curves measured with image analysis (blue) for the same sample. A slight amount of bond breakage is observed at high strain. (**C**) Step-cycle test for a single sample of the TN network showing light emission (in blue) and stress (in red). Light emission is zero during unloading and reloading, until λ of the *n*th cycle exceeds the maximum value of λ of the (*n* − 1) cycle. (**D**) Image of the luminescence of TN under loading at various steps of the experiment [reported in (C)]: (1) near the beginning of the test, (2) on the first loading at λ ~ 2.6, and (3) on reloading at λ ~ 1.7. (**E**) Cumulative light emitted during the cycles as a function of the mechanical hysteresis in TN. The mechanical hysteresis is defined as sum of the integrals under load-unload cycles, and the total light is the sum of the emitted light for that level of mechanical hysteresis. The total light varies as the mechanical hysteresis to the power 0.75.

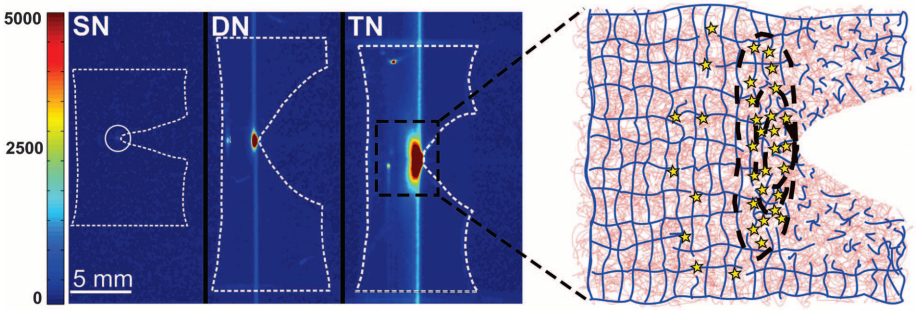

Fig. 5. Mapping of where bonds break during crack propagation. Intensity-colorized images of propagating cracks on notched samples containing dioxetane cross-linker in the first network, showing the light emission due to the breakage of bonds in SN, DN, and TN samples. The size and geometry of the sample are shown with a white dashed line. Vertical lines in the DN and TN image are due to detector artifacts; in DN and TN, spots far from the crack tip are due to reflection of the light on surface inhomogeneities and do not correspond to a local light emission. (Right) Schematic of the sacrificial bond-breaking mechanism in front of the crack tip for the DN and TN; the first network is represented in blue, and the second and third networks are in red.

larger dissipative volume ahead of the crack tip and to a tougher material, therefore guiding materials design. It also shows the dynamic shape of the damage zone, allowing a quantitative comparison with more advanced damage models (*26*).

A family of tough, stiff unfilled elastomers with less than 6% of residual deformation after strains up to 150%, and negligible viscoelasticity, can be obtained from ordinarily brittle elastomers. The toughening mechanism relies on the dissipation of energy due to bond breakage of a variable fraction of sacrificial prestretched chains inside the material. By varying the volume fraction, monomer type, and cross-linking level of the prestretched chains, the properties of the materials can be tuned over a wide range, and design can be guided by the concomitant use of chemoluminescent molecules to reveal where and when bonds break during fracture. The methodology can be used both to develop better models of fracture of soft materials and to guide design of other families of soft materials than polyacrylics, which have ordinarily poor mechanical properties but much better resistance to temperature, UV, or chemicals.

References and Notes

1. G. J. Lake, P. B. Lindley, *J. Appl. Polym. Sci.* **9**, 1233–1251 (1965).
2. G. J. Lake, A. G. Thomas, *Proc. R. Soc. Lond. A Math. Phys. Sci.* **300**, 108–119 (1967).
3. A. N. Gent, *Langmuir* **12**, 4492–4496 (1996).
4. G. Heinrich, M. Kluppel, T. A. Vilgis, *Curr. Opin. Solid St. M.* **6**, 195–203 (2002).
5. B. N. J. Persson, O. Albohr, G. Heinrich, H. Ueba, *J. Phys. Condens. Matter* **17**, R1071–R1142 (2005).
6. B. D. Viers, J. E. Mark, *J. Macromol. Sci. Part A Pure Appl. Chem.* **44**, 131–138 (2007).
7. G. D. Genesky, C. Cohen, *Polymer (Guildf.)* **51**, 4152–4159 (2010).
8. G. D. Genesky, B. M. Aguilera-Mercado, D. M. Bhawe, F. A. Escobedo, C. Cohen, *Macromolecules* **41**, 8231–8241 (2008).
9. N. K. Singh, A. J. Lesser, *Macromolecules* **44**, 1480–1490 (2011).
10. G. E. Dieter, *Mechanical Metallurgy* (McGraw Hill, New York, ed. 2, 1976).
11. H. R. Brown, *Macromolecules* **24**, 2752–2756 (1991).
12. E. J. Kramer, L. L. Berger, *Adv. Polym. Sci.* **91**, 1–68 (1990).
13. J. P. Gong, Y. Katsuyama, T. Kurokawa, Y. Osada, *Adv. Mater.* **15**, 1155–1158 (2003).
14. Y. Tanaka *et al.*, *J. Phys. Chem. B* **109**, 11559–11562 (2005).
15. R. E. Webber, C. Creton, H. R. Brown, J. P. Gong, *Macromolecules* **40**, 2919–2927 (2007).
16. J.-Y. Sun *et al.*, *Nature* **489**, 133–136 (2012).
17. Y. H. Na *et al.*, *Macromolecules* **39**, 4641–4645 (2006).
18. H. W. Greensmith, *J. Appl. Polym. Sci.* **7**, 993–1002 (1963).
19. K. Sakulkaew, A. G. Thomas, J. J. C. Busfield, *Polym. Test.* **30**, 163–172 (2011).
20. Q. M. Yu, Y. Tanaka, H. Furukawa, T. Kurokawa, J. P. Gong, *Macromolecules* **42**, 3852–3855 (2009).
21. T. Nakajima, T. Kurokawa, S. Ahmed, W.- Wu, J. P. Gong, *Soft Matter* **9**, 1955–1966 (2013).
22. Y. Chen *et al.*, *Nat. Chem.* **4**, 559–562 (2012).
23. P. Lechtken, *Chem. Ber.* **109**, 2862–2870 (1976).
24. Y. Tanaka, *Europhys. Lett.* **78**, 56005 (2007).
25. H. R. Brown, *Macromolecules* **40**, 3815–3818 (2007).
26. X. Wang, W. Hong, *Soft Matter* **7**, 8576–8581 (2011).

Acknowledgments: We gratefully acknowledge the financial support of DSM Ahead, Geleen, Netherlands and many helpful discussions with the researchers of their Materials Science Center. We also thank E.J. Kramer and H.R. Brown for their insightful comments and critical reading of the manuscript, and D. Martina for his friendly and efficient help in setting up the camera for the chemoluminescence experiments. Last, we thank W. Fresquet from Andor Technology for lending us the camera.

Supplementary Materials

www.sciencemag.org/content/344/6180/186/suppl/DC1
Materials and Methods
Supplementary Text
Figs. S1 to S7
Tables S1 to S3
Reference (*27*)
Movies S1 to S2

13 November 2013; accepted 6 March 2014
10.1126/science.1248494

Mitosis Inhibits DNA Double-Strand Break Repair to Guard Against Telomere Fusions

Alexandre Orthwein,[1] Amélie Fradet-Turcotte,[1] Sylvie M. Noordermeer,[1] Marella D. Canny,[1] Catherine M. Brun,[1] Jonathan Strecker,[1,2] Cristina Escribano-Diaz,[1] Daniel Durocher[1,2]*

Mitotic cells inactivate DNA double-strand break (DSB) repair, but the rationale behind this suppression remains unknown. Here, we unravel how mitosis blocks DSB repair and determine the consequences of repair reactivation. Mitotic kinases phosphorylate the E3 ubiquitin ligase RNF8 and the nonhomologous end joining factor 53BP1 to inhibit their recruitment to DSB-flanking chromatin. Restoration of RNF8 and 53BP1 accumulation at mitotic DSB sites activates DNA repair but is, paradoxically, deleterious. Aberrantly controlled mitotic DSB repair leads to Aurora B kinase–dependent sister telomere fusions that produce dicentric chromosomes and aneuploidy, especially in the presence of exogenous genotoxic stress. We conclude that the capacity of mitotic DSB repair to destabilize the genome explains the necessity for its suppression during mitosis, principally due to the fusogenic potential of mitotic telomeres.

We hypothesized that the inactivation of mitotic double-strand break (DSB) repair (*1*–*3*) might be caused by the failure to recruit the DSB repair factors BRCA1 and 53BP1 to DNA damage sites during mitosis (*4*–*7*). 53BP1 and BRCA1 promote DSB repair by nonhomologous end joining (NHEJ) and homologous recombination, respectively (*8*). Both proteins accumulate at DSB sites downstream of a common pathway consisting of the ataxia telangiectasia mutated–dependent phosphorylation of H2AX (forming γ-H2AX) followed by MDC1, RNF8, and RNF168 recruitment (*8*). RNF168 ubiquitylates H2A (*9*, *10*), which triggers the recruitment of 53BP1 (*11*) and also BRCA1 (*12*). Mitosis severs this pathway upstream of RNF8 recruitment to DSB sites as the formation of γ-H2AX and MDC1 ionizing radiation (IR)–induced foci, which denote accumulation at break sites, are unaffected by mitotic entry (*4*).

To elucidate how mitosis blocks RNF8 recruitment to DSB sites, we tested whether the RNF8-MDC1 interaction (*13*–*15*) is disabled in mitosis (see supplementary materials and methods). We observed that whereas RNF8 and MDC1 interact in asynchronously dividing cells after irradiation, their interaction is suppressed during M (mitotic) phase (Fig. 1A and fig. S1A; details of all synchronization and treatments are depicted in fig. S2). Because RNF8 recognizes redundant, phosphorylated epitopes on MDC1, we assessed whether mitosis inhibits the ability of RNF8 to recognize phospho-MDC1. MDC1-derived phosphopeptides that encompass its Thr^{752} (T752) phosphorylation site (pT752) are unable to retrieve RNF8 from mitotic extracts, whereas they readily retrieve RNF8 from extracts of asynchronously dividing cells (Fig. 1B and fig. S1B). This inhibition is due to cyclin-dependent kinase 1 (CDK1)–dependent phosphorylation, because pretreating mitotic extracts with PP1, a Ser/Thr phosphatase, or treating cells with the CDK1 inhibitor RO-3306 before harvesting restored the RNF8-pT752 interaction (Fig. 1B).

To test whether CDK1 could directly inhibit the RNF8-MDC1 interaction, recombinant human and mouse RNF8 proteins fused to glutathione *S*-transferase (GST) were subjected to phosphorylation by CDK1-cyclin B or CDK2-cyclin A before pull-down assays with pT752. CDK1, but not CDK2, could phosphorylate RNF8, which suppressed the ability of RNF8 to bind to pT752 (fig. S1, C to E). The reconstitution of the CDK1-dependent inhibition of the RNF8-pT752 interaction identified T198 as the main CDK1 site on RNF8 (fig. S1F). An antibody against the phosphorylated T198 residue (RNF8 pT198) confirmed a mitosis-specific phosphorylation of T198 (Fig. 1C and fig. S1G). Mutation of T198 to alanine (yielding RNF8 T198A) rendered the RNF8-pT752 interaction insensitive to CDK1 in pull-down assays (fig. S1E). In contrast, the T198E (E, Glu) mutation, which mimics T198 phosphorylation, constitutively inhibited RNF8 binding to phosphopeptides (fig. S1E).

We tested whether the RNF8-T198A mutation restored RNF8 recruitment to DSB sites in mitotic U2OS cells. Reintroduction of wild-type (WT) RNF8

[1]The Lunenfeld-Tanenbaum Research Institute, Mount Sinai Hospital, 600 University Avenue, Toronto, Ontario M5G 1X5, Canada. [2]Department of Molecular Genetics, University of Toronto, Ontario M5S 3E1, Canada.

*Corresponding author. E-mail: durocher@lunenfeld.ca

in RNF8-depleted cells (fig. S3) enabled the formation of IR-induced foci in interphase but not in mitosis (Fig. 1, D and E, and fig. S4). In contrast, RNF8-T198A accumulated at DSB sites in both cell cycle phases (Fig. 1, D and E, and fig. S4). Conversely, the RNF8-T198E mutation suppressed IR-induced focus formation in interphase (Fig. 1D and fig. S4). RNF8-T198 phosphorylation is therefore the main mechanism by which mitosis suppresses RNF8 recruitment to DSB sites.

In the same experiments, we tested whether the T198A mutation restored BRCA1 and 53BP1 accumulation at mitotic DSB sites. Reintroducing RNF8-T198A restored BRCA1 recruitment to DSB sites but failed to restore 53BP1 IR-induced focus formation during M phase (Fig. 1, D and E). These results indicate that in addition to RNF8 phosphorylation, mitotic cells inactivate the recruitment of 53BP1 via a second inhibitory mechanism.

To identify this additional regulatory step, we mapped mitotic phosphorylation sites on 53BP1 by mass spectrometry. This approach identified a number of sites and, among them, T1609 and S1618 (S, Ser) that map to the 53BP1 ubiquitination-dependent recruitment (UDR) motif (Fig. 2A and fig. S5). The UDR allows 53BP1 to bind to ubiquitylated H2A and is necessary for its accumulation at DSB sites (*11*). Immunoblotting of extracts derived from cells released from a double-

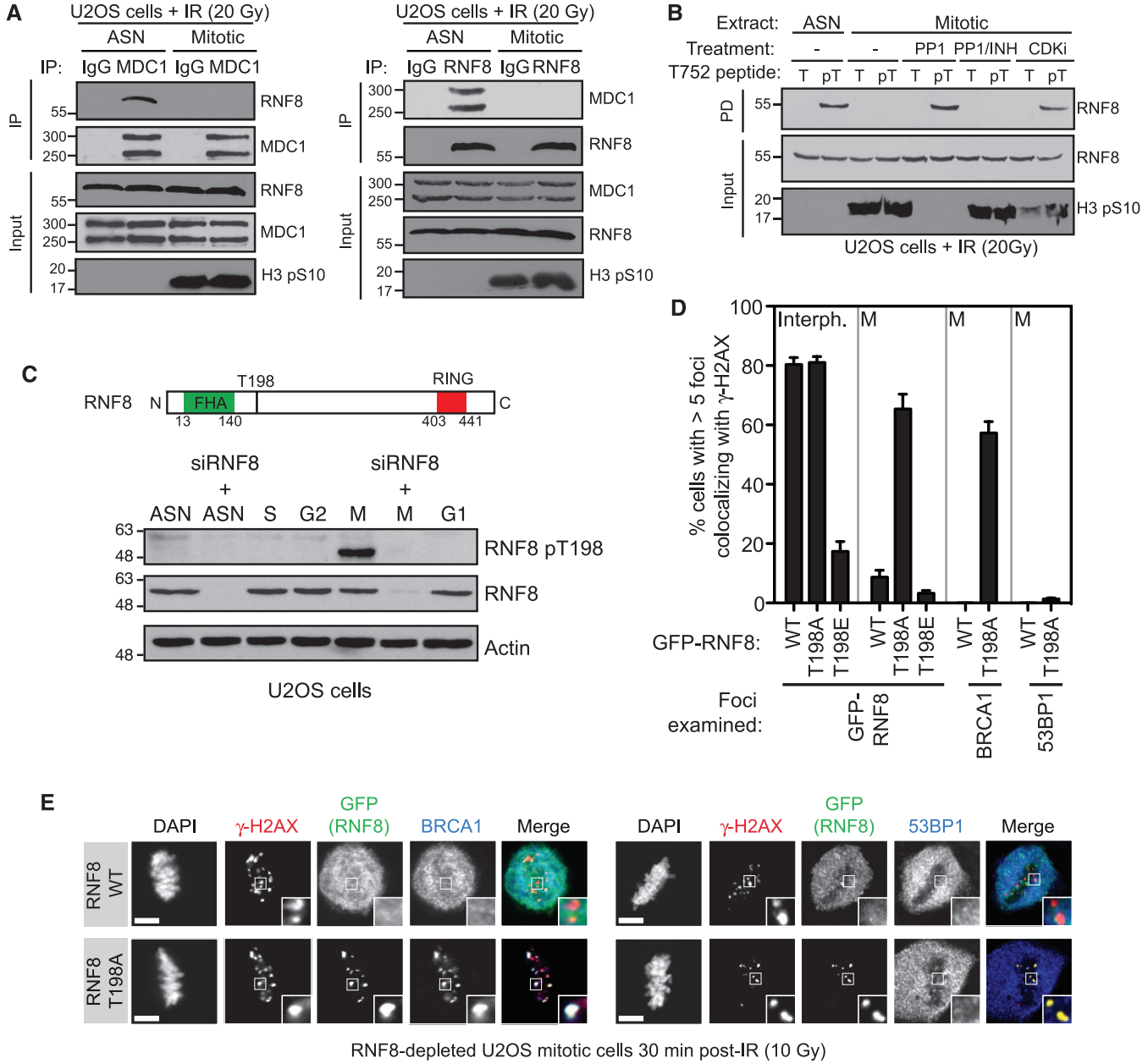

Fig. 1. Mitotic cells inactivate the RNF8-MDC1 interaction through phosphorylation. (**A**) Immunoprecipitation (IP) of MDC1 or RNF8 from asynchronous (ASN) and mitotic U2OS cell extracts. IgG, immunoglobulin G. (**B**) Pull-down (PD) assay of RNF8 from ASN or mitotic extracts with unphosphorylated (T) or phosphorylated (pT) peptides encompassing the MDC1 T752 residue. INH, phosphatase inhibitor cocktail; CDKi, CDK inhibitor. (**C**) (Top) RNF8 domain organization. FHA, forkhead-associated domain; N, N terminus; C, C terminus. (Bottom) Whole-cell extracts of U2OS cells released from a double-thymidine block were probed using an antibody against RNF8 pT198. siRNF8, small interfering RNA against RNF8. (**D**) RNF8-depleted U2OS cells stably expressing green fluorescent protein (GFP)–RNF8 or its mutants were synchronized by double-thymidine block before release and irradiation (10 Gy). Interphase (Interph.) and mitotic (M) cells were processed for GFP, γ-H2AX, and BRCA1 or 53BP1 immunofluorescence [mean ± SD (error bars); $N = 3$ biological replicates]. (**E**) Representative micrographs of (D). Scale bars, 5 μm. DAPI, 4′,6-diamidino-2-phenylindole.

thymidine block confirmed that both sites are simultaneously phosphorylated in mitosis (Fig. 2A and fig. S6A). T1609 is likely a target of a proline-directed kinase such as CDK1 or p38, whereas S1618 is a PLK1 target (*16*). Using a recombinant 53BP1 protein fragment comprising the Tudor and UDR motifs (*11*), we confirmed that CDK1 could phosphorylate T1609 and that PLK1 targets S1618 (fig. S6, B and C). No substantial phosphorylation of the 53BP1 Tudor-UDR fragment was observed in the T1608/S1619A (TASA) double mutant (fig. S6, B and C). These results indicate that the 53BP1 UDR is phosphorylated in mitosis by proline-directed kinases, such as CDK1, and PLK1.

To test the importance of the mitotic phosphorylation of the UDR, we assessed the ability of the 53BP1 Tudor-UDR to interact with nucleosome core particles (NCPs) containing a dimethylated H4 Lys^{20} (K20) mimic (H4Kc20me2) and H2A K15-ubiquitin, as previously reported (*11*). The 53BP1 Tudor-UDR protein binds specifically to such dually modified NCPs (Fig. 2B and fig. S7). However, upon CDK1 and PLK1 phosphorylation, NCP binding was abrogated (Fig. 2B and fig. S7). The inhibition required both kinases (fig. S7) and the T1609/S1618 residues (Fig. 2B). Conversely, phosphomimetic mutations that convert T1609 and S1608 to glutamic acid led to the inhibition of 53BP1 binding to RNF168-ubiquitylated NCPs that was strongest with the T1609E/S168E (TESE) double mutant (fig. S7).

The T1609A, T1609E, S1618A, and TASA mutations have little to no impact on 53BP1 focus formation in interphase cells (fig. S8, A and B). However, the TESE mutation profoundly

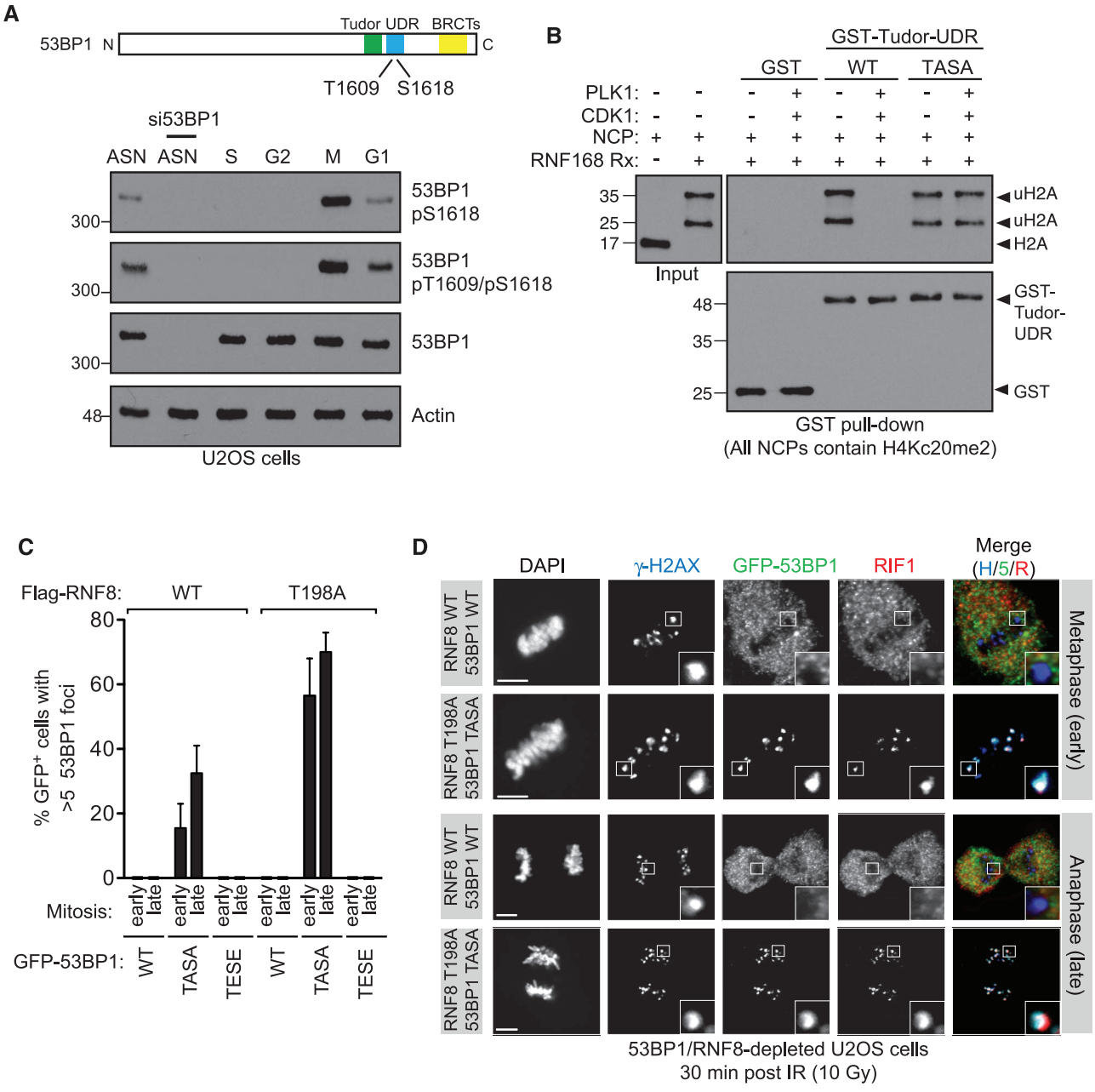

Fig. 2. Mitotic cells inactivate 53BP1 by phosphorylating the UDR. (**A**) (Top) 53BP1 domain organization. BRCTs, BRCA1 C-terminal domains. (Bottom) Extracts from U2OS cells released from a G_1/S block were probed by immunoblotting for S1618 and simultaneous T1609/S1618 phosphorylation. (**B**) Pull-down assay of RNF168-ubiquitylated NCPs with the indicated GST-Tudor-UDR constructs. Where indicated, the GST-Tudor-UDR was preincubated with CDK1 or PLK1 before the binding assays. (**C**) Quantitation of GFP-53BP1 focus-positive cells expressing the indicated Flag-RNF8 and GFP-53BP1 constructs in early or late mitosis [mean ± SD (error bars); $N = 3$]. (**D**) Representative micrographs of (E). Scale bar, 5 μm.

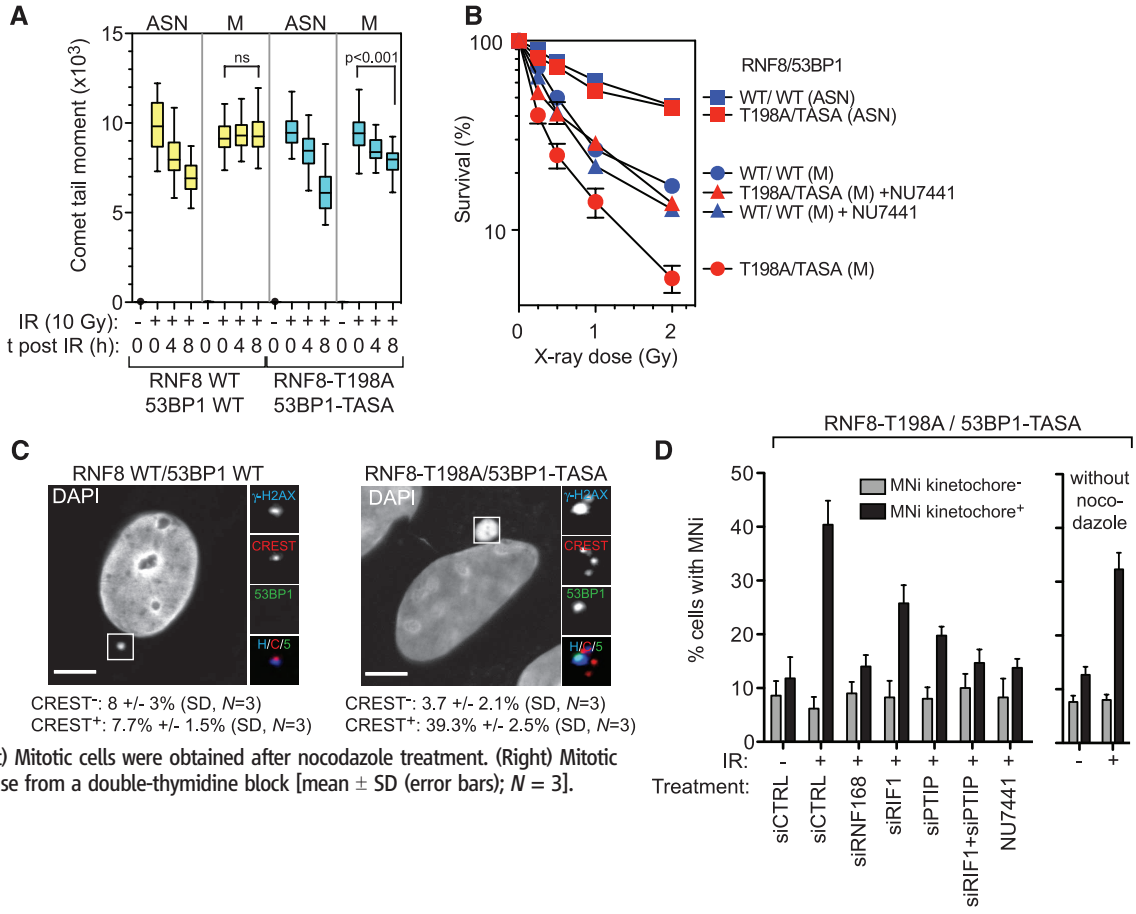

Fig. 3. Reactivation of mitotic DSB repair is deleterious. (**A**) Neutral comet analysis of asynchronously dividing or mitotic U2OS cells stably expressing the indicated Flag-RNF8 and GFP-53BP1 proteins before and after irradiation with a 10-Gy dose (N = 30). Statistical significance was determined by one-way analysis of variance (ANOVA). ns, not significant; t, time. (**B**) Clonogenic survival assays of the cells described in (A) in the presence or absence of NU7441 [mean ± SD (error bars); $N \geq 3$]. (**C**) Formation of MNi in U2OS cells stably expressing the indicated proteins after irradiation (0.5 Gy) and released from the mitotic block. Scale bars, 5 μm. (**D**) Quantitation of MNi formation in mitotic U2OS cells stably expressing RNF8-T198A/53BP1-TASA and treated as indicated. (Left) Mitotic cells were obtained after nocodazole treatment. (Right) Mitotic cells were obtained after release from a double-thymidine block [mean ± SD (error bars); N = 3].

affects 53BP1 recruitment to DSB sites (fig. S8, A and B) and the ability of 53BP1 to restore IR resistance in *53bp1*$^{-/-}$ DT40 avian cells (fig. S8, C and D). Together, these results indicate that T1609/S1618 phosphorylation inhibits 53BP1 accumulation and function at DSB sites. When mitotic cells expressing the combination of RNF8-T198A and 53BP1-TASA mutants were irradiated, 53BP1 recruitment to DSB sites was restored nearly to the level observed for the WT protein in interphase cells (Fig. 2, C and D). Under these conditions, RIF1, a 53BP1 effector during NHEJ (*17*–*21*), was also recruited to DSB sites (Fig. 2D). We therefore conclude that the block to 53BP1 recruitment in mitosis is the result of RNF8 phosphorylation on T198 and 53BP1 phosphorylation on T1609/S1618.

We next assessed whether the combination of RNF8-T198A and 53BP1-TASA mutants restored DSB repair in mitosis, using the neutral comet assay. Asynchronously dividing cells expressing RNF8-T198A and 53BP1-TASA displayed DSB repair kinetics that were comparable to WT cells (Fig. 3A and fig. S9A). As expected (*1*, *2*), M-phase cells expressing WT proteins did not repair their chromosomal breaks over the duration of the experiment (Fig. 3A). In contrast, the RNF8-T198A/53BP1-TASA–expressing mitotic cells clearly repaired DSBs over time (Fig. 3A). In two orthogonal assays, γ-H2AX focus formation/dissolution and TUNEL (terminal deoxynucleotidyl transferase–mediated deoxyuridine triphosphate nick end labeling), we confirmed that expression of RNF8-T198A and 53BP1-TASA reactivated mitotic DSB repair (fig. S9, B to D). These results demonstrate that RNF8 pathway restoration reactivates DSB repair in mitotic cells.

Cells in M phase are hypersensitive to IR, presumably because they inactivate DSB repair (*4*). To test whether mitotic DSB repair affects IR sensitivity, we carried out clonogenic survival assays with low doses of radiation [0.25 to 2 grays (Gy)]. As expected, mitotic cells were more IR-sensitive than their asynchronously dividing counterparts (Fig. 3B). Asynchronously dividing cells expressing RNF8-T198A/53BP1-TASA had a clonogenic survival profile identical to that of WT RNF8/53BP1-expressing cells. In stark contrast, RNF8-T198A/53BP1-TASA–expressing mitotic cells displayed marked IR hypersensitivity compared with mitotic cells expressing WT proteins (Fig. 3B). To determine whether mitotic DSB repair was responsible for the increased IR-sensitivity of the RNF8-T198A/53BP1-TASA cells, we treated cells with the DNA-PKcs inhibitor NU7441 to inhibit NHEJ, the DSB repair pathway mediated by 53BP1. NU7441 rescued the IR hypersensitivity of RNF8-T198A/53BP1-TASA–expressing mitotic cells to the levels of those expressing their WT counterparts (Fig. 3B). These results indicate that mitotic DSB repair leads to IR hypersensitivity and is therefore deleterious.

Repair of DSBs during cell division might be harmful due to defective chromosome segregation. To test this hypothesis, we monitored the formation of micronuclei (MNi), as they are caused by the mis-segregation of chromosomes or their fragments (*22*). We subjected mitotic cells expressing various combinations of RNF8 (wild type or T198A) and 53BP1 (wild type or TASA) proteins to a 0.5-Gy x-ray dose. Cells were released from the mitotic block and analyzed 6 hours later. In cells expressing RNF8-T198A/53BP1-TASA, we observed a selective and marked increase in CREST (i.e., kinetochore)–positive MNi, indicative of whole-chromosome mis-segregation, without a concomitant increase in kinetochore-negative MNi (Fig. 3, C and D). This increase was independent of the synchronization procedure but stimulated by irradiation and RNF168, which recruits 53BP1 to DSB sites (Fig. 3D and fig. S10). Furthermore, the combined depletion of RIF1 and PTIP, the 53BP1 effectors in DSB repair (*17*–*21*, *23*), along with the inhibition of DNA-PKcs, suppressed the formation of kinetochore-positive MNi (Fig. 3D). These results indicate that the reactivation of mitotic DSB repair impairs chromosome segregation, causing aneuploidy.

Together, PTIP and RIF1 promote telomere fusions (*23*), a chromosome rearrangement that

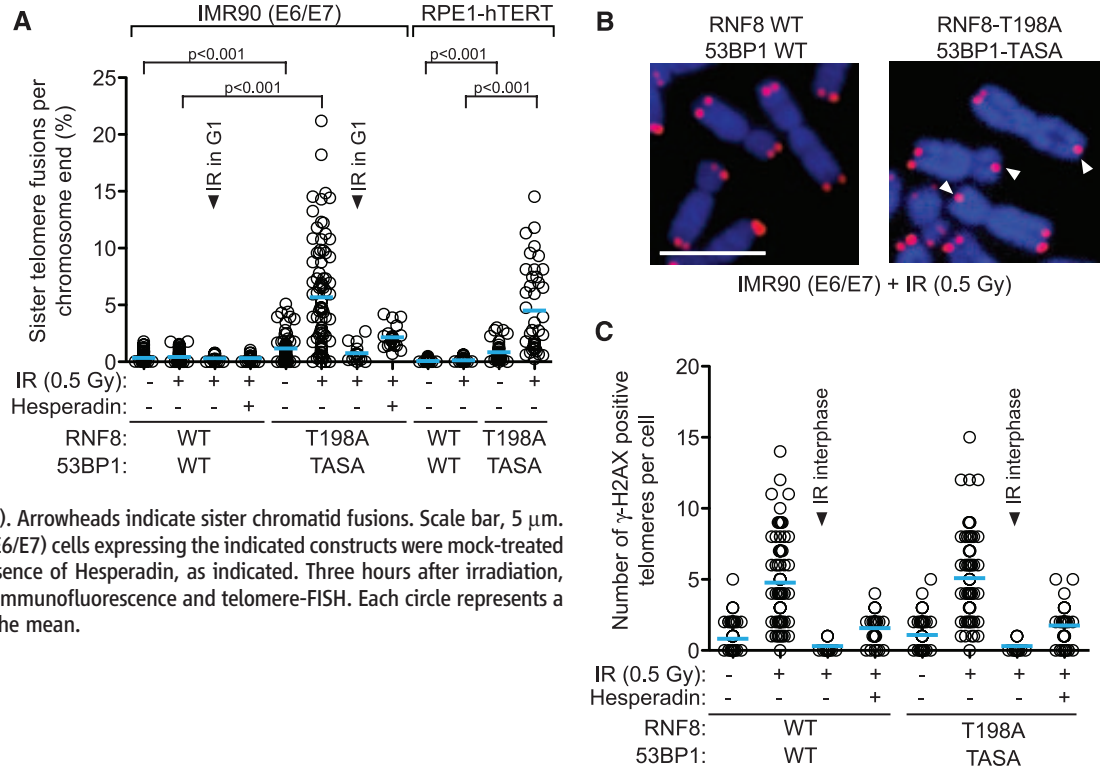

Fig. 4. Mitotic DSB repair causes telomere fusions. (A) RNF8- and 53BP1-depleted IMR90 (E6/E7) or RPE1-hTERT metaphase cells expressing the indicated constructs were exposed to IR (0.5 Gy) and collected 3 hours later. Mitotic spreads were subjected to telomere-FISH and counterstained with DAPI. Where indicated, the irradiation was carried out with cells blocked in G_1, and metaphases were collected after release. Hesperadin is an Aurora B kinase inhibitor. Each circle represents a counted cell; blue bars indicate the mean. Statistical significance was determined by one-way ANOVA. **(B)** Representative micrographs of (A). Arrowheads indicate sister chromatid fusions. Scale bar, 5 μm. **(C)** Mitotic or interphase IMR90 (E6/E7) cells expressing the indicated constructs were mock-treated or irradiated (0.5 Gy) in the presence of Hesperadin, as indicated. Three hours after irradiation, cells were processed for γ-H2AX immunofluorescence and telomere-FISH. Each circle represents a counted cell; blue bars indicate the mean.

generates dicentric chromosomes. To assess whether mitotic DSB repair produces telomere fusions, we examined metaphase telomeres by fluorescence in situ hybridization (FISH) in telomerase-negative (IMR90 E6/E7) and -positive (RPE1-hTERT) cells. We observed an increase that was greatly stimulated after IR treatment in telomere fusions in untreated RNF8-T198A/53BP1-TASA mitotic cells, but not in interphase cells (Fig. 4, A and B, and fig. S11, A to C). The presence of telomere fusions was confirmed by Southern blotting and BAL-31 nucleolytic digestion (fig. S11, D and E). RNF8-T198A/53BP1-TASA also produced high levels of NHEJ-dependent dicentrics, identified as anaphase bridges containing two kinetochores (fig. S12, A and B). Together, these results suggest that the aneuploidy caused by mitotic DSB repair is the consequence of sister telomere fusions.

Because telomeres normally inhibit DSB repair (*24*), our results inferred that mitotic telomeres might be prone to deprotection and that genotoxic stress stimulates telomere uncapping. The irradiation of mitotic, but not interphase, cells induced telomere uncapping, as measured by γ-H2AX colocalization with telomeres, independently of the RNF8 and 53BP1 status (Fig. 4C and fig. S13). This phenomenon was reminiscent of the recently described Aurora B kinase–dependent telomere uncapping seen during prolonged mitoses (*25*). In support of the possibility that mitotic and genotoxic stress causes mitotic telomere uncapping via a common mechanism, we found that telomere deprotection (Fig. 4C and fig. S13) and fusions (Fig. 4A) were also dependent on Aurora B activity, as they were suppressed by hesperadin treatment.

We conclude that cells must suppress DSB repair in mitosis because M-phase telomeres are prone to fusions. We propose that mitotic telomeres exist in an underprotected state due to Aurora B–dependent repression of Shelterin activity. This condition can transition to a fully deprotected state, either as a low-frequency spontaneous event or at high frequency after mitotic or genotoxic stress. Because mitotic inhibition of DSB repair has been observed in a number of metazoan species, it appears that cells have not been able to evolve a better solution to the problem caused by underprotected mitotic telomeres other than transiently inactivating this major genome-maintenance pathway.

References and Notes

1. R. E. Zirkle, W. Bloom, *Science* **117**, 487–493 (1953).
2. C. L. Rieder, R. W. Cole, *J. Cell Biol.* **142**, 1013–1022 (1998).
3. A. M. Heijink, M. Krajewska, M. A. T. M. van Vugt, *Mutat. Res.* **750**, 45–55 (2013).
4. S. Giunta, R. Belotserkovskaya, S. P. Jackson, *J. Cell Biol.* **190**, 197–207 (2010).
5. M. A. van Vugt *et al.*, *PLOS Biol.* **8**, e1000287 (2010).
6. W. Zhang, G. Peng, S. Y. Lin, P. Zhang, *J. Biol. Chem.* **286**, 35899–35905 (2011).
7. G. Nelson, M. Buhmann, T. von Zglinicki, *Cell Cycle* **8**, 3379–3383 (2009).
8. S. Panier, D. Durocher, *Nat. Rev. Mol. Cell Biol.* **14**, 661–672 (2013).
9. F. Mattiroli *et al.*, *Cell* **150**, 1182–1195 (2012).
10. M. Gatti *et al.*, *Cell Cycle* **11**, 2538–2544 (2012).
11. A. Fradet-Turcotte *et al.*, *Nature* **499**, 50–54 (2013).
12. S. P. Jackson, D. Durocher, *Mol. Cell* **49**, 795–807 (2013).
13. M. S. Huen *et al.*, *Cell* **131**, 901–914 (2007).
14. N. K. Kolas *et al.*, *Science* **318**, 1637–1640 (2007).
15. N. Mailand *et al.*, *Cell* **131**, 887–900 (2007).
16. K. Grosstessner-Hain *et al.*, *Mol. Cell. Proteomics* **10**, M111.008540 (2011).
17. M. Zimmermann, F. Lottersberger, S. B. Buonomo, A. Sfeir, T. de Lange, *Science* **339**, 700–704 (2013).
18. L. Feng, K. W. Fong, J. Wang, W. Wang, J. Chen, *J. Biol. Chem.* **288**, 11135–11143 (2013).
19. C. Escribano-Díaz *et al.*, *Mol. Cell* **49**, 872–883 (2013).
20. M. Di Virgilio *et al.*, *Science* **339**, 711–715 (2013).
21. J. R. Chapman *et al.*, *Mol. Cell* **49**, 858–871 (2013).
22. M. Fenech *et al.*, *Mutagenesis* **26**, 125–132 (2011).
23. E. Callen *et al.*, *Cell* **153**, 1266–1280 (2013).
24. A. Sfeir, T. de Lange, *Science* **336**, 593–597 (2012).
25. M. T. Hayashi, A. J. Cesare, J. A. Fitzpatrick, E. Lazzerini-Denchi, J. Karlseder, *Nat. Struct. Mol. Biol.* **19**, 387–394 (2012).

Acknowledgments: All primary data are archived at the Lunenfeld-Tanenbaum Research Institute. We thank R. Szilard and Durocher lab members for critically reading the manuscript; A. Nussenzweig, J. Karlseder, D. Xu, J. Lukas, A.-C. Gingras, W. Dunham, M. Cook, A. Rosebrock, L. Harrington, F. Rossiello, F. d'Adda di Fagagna, S. Lawo, and L. Pelletier for reagents or technical advice; and D. Chowdhury for the pT1609/pS1618 antibody and for sharing unpublished data. A.O. and A.F.-T. received postdoctoral fellowships from the Canadian Institutes of Health Research (CIHR); S.M.N. is a scholar of the EIRR21st training program; C.M.B. received a fellowship from the Swiss National Science Foundation; J.S. received a doctoral award from the CIHR; and D.D. is the Thomas Kierans Chair in Mechanisms of Cancer Development and a Canada Research Chair (Tier 1). The work was supported by CIHR grant MOP89754 and by the Krembil Foundation.

Supplementary Materials

www.sciencemag.org/content/344/6180/189/suppl/DC1
Materials and Methods
Figs. S1 to S13
References (*26*–*29*)

4 November 2013; accepted 12 March 2014
Published online 20 March 2014;
10.1126/science.1248024

A Developmental Switch of Axon Targeting in the Continuously Regenerating Mouse Olfactory System

Limei Ma,[1] Yunming Wu,[1] Qiang Qiu,[1] Hayley Scheerer,[1] Andrea Moran,[1] C. Ron Yu[1,2]*

The mammalian olfactory system has the natural capacity to regenerate throughout the animal's life span. Despite constant neurogenesis, olfactory sensory neurons project to precise, stereotypical positions in the brain. Here, we identify a critical period of olfactory sensory axon targeting during postnatal development in mouse. Perturbing axon projection beyond postnatal day 7 permanently disrupts targeting specificity of the sensory neurons. In addition, we find that the establishment of the convergence map requires perinatal sensory neurons. Late-born neurons appear to connect with prospective glomeruli based on homotypic interactions among neurons expressing the same odorant receptor. Our results reveal a developmental switch in axon guidance and a mechanism of circuit integration of adult-born neurons.

Neural regeneration holds the potential to repair dysfunctional or damaged nervous systems. A key step that must be achieved for an effective cure is to allow new neurons to make precise and functional connections. Adult neurogenesis in mammals occurs in the olfactory epithelium, dentate gyrus of the hippocampus, and subventricular zone of the lateral ventricle (*1*–*3*). In olfactory epithelium, sensory neurons are continuously generated to replace aging cells and in response to axonal or peripheral damages (*4*–*7*). These neurons must project to the olfactory bulb and establish precise and functional connections with a glomerulus containing axons expressing the same olfactory receptor (OR) gene (*6*, *8*). This regenerative capacity is essential in maintaining the topographic map in the bulb and consistency in odor perception. Here, we show that axon-targeting mechanisms used for the initial establishment differ from those used for subsequent maintenance of the olfactory map.

The topographic projection from the olfactory epithelium to the bulb is established perinatally in mouse (*8*, *9*). Beginning at embryonic day 17, olfactory sensory neurons expressing the same OR gene converge onto the same glomerulus (*8*–*12*). In the olfactory epithelium, neurogenesis peaks around postnatal day 14 (P14), gradually subsides, and continues at a steady rate after weaning at P21 (*2*). The newly generated sensory neurons project into existing glomeruli to maintain constant innervation of the bulb (*13*). Although some evidence supports lifelong plasticity of the olfactory map (*3*, *14*), other evidence suggests that the sensory neuron projection may not be properly

[1]Stowers Institute for Medical Research, 1000 East 50th Street, Kansas City, MO 64110, USA. [2]Department of Anatomy and Cell Biology, University of Kansas Medical Center, 3901 Rainbow Boulevard, Kansas City, KS 66160, USA.

*Corresponding author. E-mail: cry@stowers.org

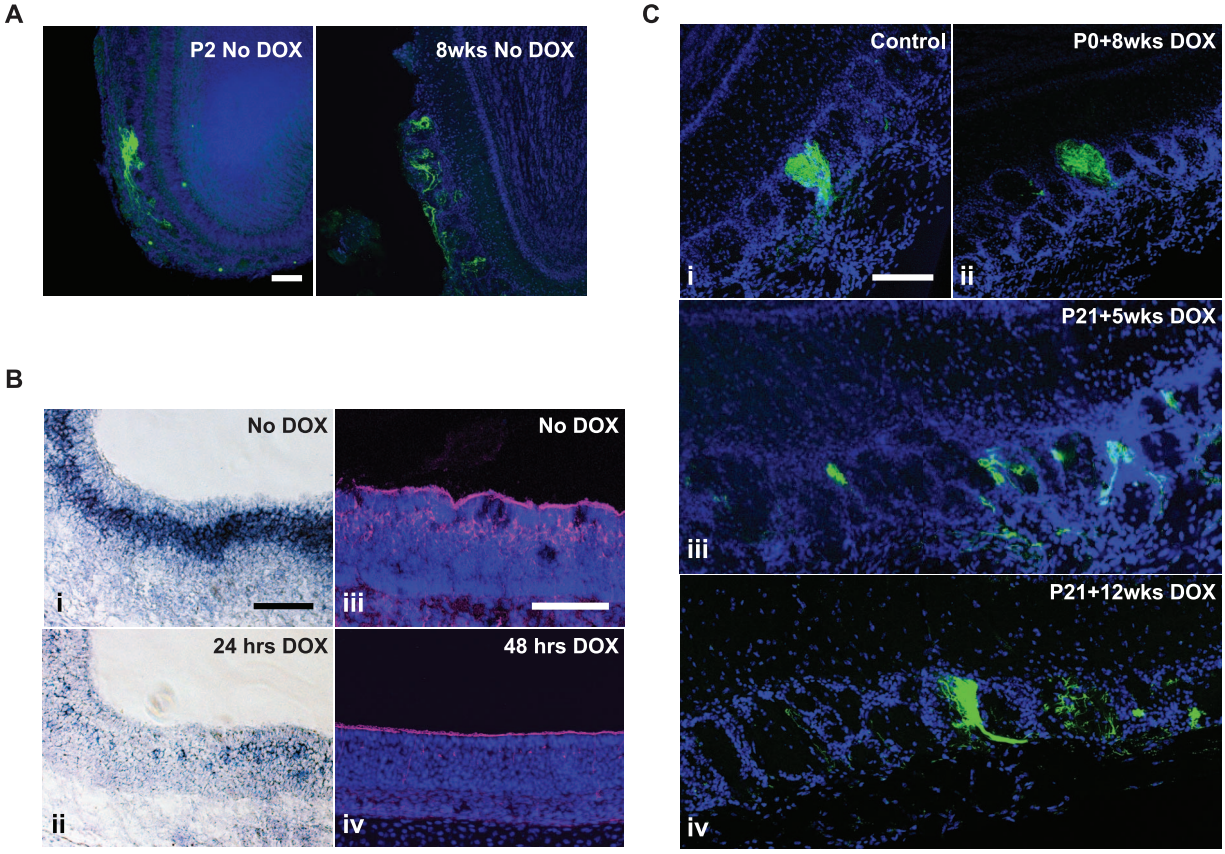

Fig. 1. Silencing spontaneous activity of olfactory sensory neurons during postnatal development permanently alters axonal projection. (**A**) Representative images of *P2-GFP* glomeruli in Kir2.1 mice showing divergent projection patterns in postnatal day 2 (P2) and adult (8-week-old, 8wks) mice. (**B**) In situ hybridization using antisense riboprobe against Kir2.1 (i and ii, purple) and immunofluorescent staining of Kir2.1 protein (iii and iv, red) in the olfactory epithelium of Kir2.1 mice treated with or without doxycycline (DOX) diet. Duration of treatment is indicated. (**C**) Representative images of *P2-GFP* neuron projection in the olfactory bulb from (i) controls, Kir2.1 mice treated with doxycycline (ii) at P0 for 8 weeks, (iii) at P21 for 5 weeks, and (iv) at P21 for 12 weeks. Green: GFP; blue: 4′,6′-diamidino-2-phenylindole (DAPI). Scale bars, 100 μm.

reestablished after damage to the olfactory epithelium or large-scale axotomy (*5*, *15*).

In mice carrying *OMP-IRES-tTA:tetO-Kir2.1-IRES-tauLacZ* alleles (Kir2.1 mice)—in which OMP is the olfactory marker protein; IRES, the internal ribosome entry site; tTA, tetracycline-controlled transcription activator; and tetO, a promoter that drives expression of the fusion protein tau–β-galactosidase—ectopically expressed Kir2.1 channels in the olfactory sensory neurons suppressed neural activity and led to erroneous innervation of multiple glomeruli by neurons expressing the same OR (Fig. 1A and fig. S1A) (*16*). Kir2.1 transgene expression could be effectively turned off by feeding mice a doxycycline diet, so that Kir2.1 transcript and protein levels were drastically reduced within 48 hours of treatment (Fig. 1B). After doxycycline treatment, odor-evoked responses imaged from the dorsal bulb (*17*, *18*) were restored (fig. S1B).

We were curious about whether doxycycline treatment would restore the stereotypic convergence pattern. In mice fed with doxycycline from P21 onward, axons expressing the same OR gene continued to project to multiple glomeruli throughout the course of treatment (Fig. 1C, iii and iv). Thus, suppressing neural activity till P21 led to persistent changes in projection pattern (fig. S1C). In contrast, when Kir2.1 mice were fed doxycycline from birth, neurons expressing the same OR projected into a single glomerulus (Fig. 1C, ii). It appeared that a time window existed between birth and P21 (weaning) during which developing olfactory sensory neurons could reestablish a convergence map.

In a time-course experiment, we quantified the eventual number of glomeruli innervated by a single type of sensory neurons in mice treated with doxycycline at different postnatal ages (fig. S2A). We examined sensory neurons expressing ORs projecting to different regions of the olfactory bulb, including *M72* (*M72-IRES-tauGFP*), *P2* (*P2-IRES-GFP*), and *MOR28* (*MOR28-IRES-GFP*), all tagged with the gene for green fluorescent protein (GFP) (fig. S2B) (*16*, *19*, *20*). As demonstrated with the *M72* receptor (Fig. 2A), the number of glomeruli increased significantly when mice were treated with doxycycline later than P5 (Fig. 2B and fig. S2C). Although the degree of divergence differs for each OR and the olfactory bulb follows a dorsal-ventral progression in the expression of guidance cues (*21*, *22*), we did not find an obvious difference in the transition period for the three ORs (Fig. 2B and fig. S2C). The projection patterns were most sensitive to deprivation of neural activity after P5. Because Kir2.1 expression was suppressed within 48 hours, we reasoned that the plasticity in restoring the map began to diminish after P7. Before P7, olfactory axons had the capacity to reestablish converging projection patterns when activity was restored.

During the first postnatal week, mitral cells in the olfactory bulb, which receive input from the sensory neurons, prune their dendrites from innervating multiple glomeruli to a single one (*23*). We examined mitral cell dendritic morphology in Kir2.1 mice by retrograde lipophilic dye labeling and found that mitral cells completed the pruning process by P7 in both control and mutant mice (Fig. 2C). Thus, the divergent sensory axon projection had little impact on postsynaptic cell dendritic development. The regulation of sensory axon projection appears independent from mitral cell development.

Is the permanent change in sensory neuron projection the result of electrical silencing or does it reflect an intrinsic developmental program revealed by this perturbation? To address this question, we examined *OMP-IRES-tTA:tetO-LBR* (LBR) mice, in which ectopic expression of lamin B receptor in the sensory neurons led to disregulated OR gene expression and multiglomerular projection (*24*). In these mice, axon projection returned to normal in mice fed with doxycycline beginning at P0 (Fig. 3A). In contrast, we observed multiglomerular projection patterns in mice fed with doxycycline at later stages (Fig. 3A). The number of *P2* glomeruli in LBR mice followed a similar time course to that found in Kir2.1 animals (Fig. 3B). Thus, using independent methods to perturb sensory axon projection, we observed the same critical period of olfactory map formation.

It is not known whether mistargeted axons reorganize to restore convergence, or the sensory neurons are replaced by newly generated neurons

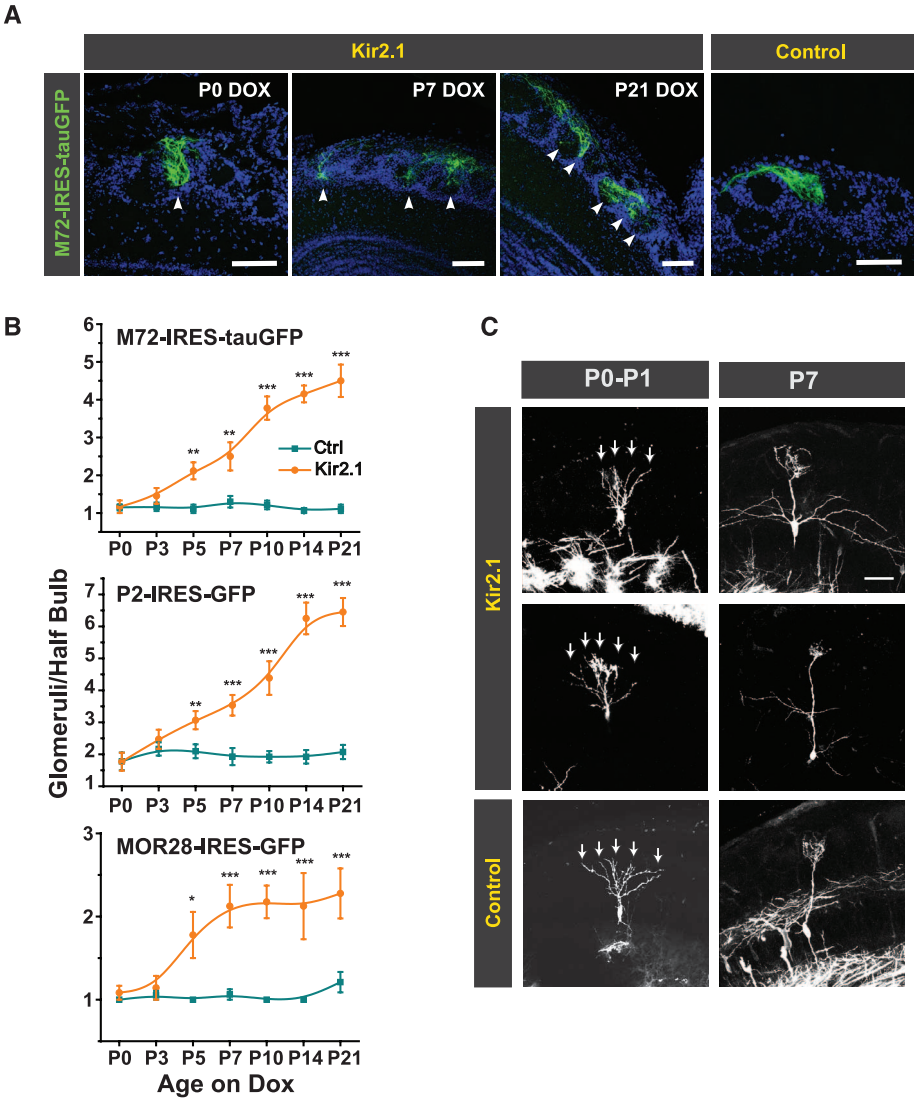

Fig. 2. Critical period of olfactory axon convergence. (**A**) Representative images of *M72-GFP* neuron projection in coronal olfactory bulb sections from control and Kir2.1 mice treated with doxycycline starting at different postnatal dates. Green: GFP; blue: DAPI. Arrowheads indicate the glomeruli receiving the *M72-GFP* axon inputs. (**B**) Quantification of the *M72*, *P2*, and *MOR28* glomeruli in Kir2.1 mice and control littermates treated with doxycycline at different postnatal stages. Two-sample, one-way Student's *t* test is applied for statistical analysis. **P* < 0.05, ***P* < 0.01, ****P* < 0.001 (*t* test). Error bars, SEM. (**C**) Olfactory axon convergence is independently regulated from the mitral cells. Representative image of retrograde DiI labeling of mitral cells in Kir2.1 and control mice during perinatal period (P0 to P1) and P7. Arrows indicate the branches of the primary dendrite of the labeled mitral cells. Scale bars, 100 μm.

that form the single glomerulus convergence. We tested whether neurons generated after birth were able to reestablish the convergence patterns by ablating early neurons using transgenically expressed diphtheria toxin (*3*, *25*) in *OMP-IRES-tTA:tetO-DTA* (DTA) mice. Doxycycline feeding beginning at P0 resulted in normal projection of olfactory axons (Fig. 3C). However, treatment after P3 resulted in projections to multiple glomeruli (Fig. 3C). This observation suggested that sensory neurons present at birth were required to establish the converging projection pattern. Late-born neurons were not able to restore convergence.

In a previous study, neurons expressing the *P2* receptor were ablated, and the newly generated neurons continued to converge their axons onto single glomerular locations (*3*). In this case, a small percentage of *P2* axons remained intact. It is possible that existing axonal tracts acted to guide the new axons via a presorting mechanism (*26*) mediated by homotypic interactions (*19*, *27*). We hypothesized that perturbing the projection of sensory neurons expressing one OR type would affect only neurons of the same type. We tested this hypothesis using the *OMP-IRES-tTA:tetO-M71-IRES-tauLacZ* mice (*28*), in which a large population of neurons ectopically expressed the *M71* OR (fig. S3, A and B).

In these animals, sensory neurons expressing endogenous *M71* (*M71-IRES-tauGFP*) were found to project to multiple glomeruli in the dorsal region of the bulb (Fig. 4A). In animals fed doxycycline after P7, neurons expressing endogenous M71 receptor continued to project to multiple glomeruli (Fig. 4B, bottom). In contrast, doxycycline feeding before P3 rescued the single-glomerulus projection pattern (Fig. 4B, top). Note that neurons expressing *M72* or *MOR28* receptor maintained single-glomerulus convergence patterns in the *M71* transgenic mice (Fig. 4C). Thus, perturbation of axons by ectopic *M71* expression only affected endogenous M71 neurons (fig. S3C). This result demonstrated that homotypic interaction was sufficient to redirect axon routing before, but not after, P7.

The regenerative capacity of the olfactory system makes it an unlikely system to be regulated by a developmental critical period. Our study demonstrates that, during the perinatal stage, sensory axons have the reorganizational capacity to ensure the segregation of axons expressing different ORs. Early axons appear to have the ability to correct erroneous projections (*9*, *11*) and provide the track for late-born neurons to follow. Late-born neurons appear to interact with existing paths through homotypic affinity, possibly by using guidance molecules, such as Kirrels and ephrins, which provide identity code for the olfactory sensory neurons expressing different ORs (*27*, *29*). Ectopic tracks, formed as a result of suppressing neural activity or lamin B receptor overexpression, divert the axons to innervate ectopic glomeruli persistently. These results imply that different mechanisms are used for establishment of the olfactory map than are used for maintenance of

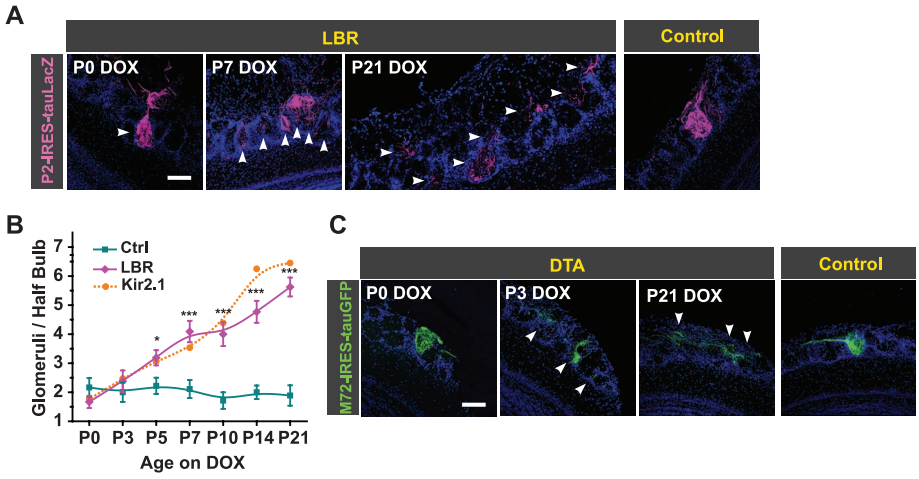

Fig. 3. Establishment of axon convergence requires perinatal olfactory sensory neurons. (**A**) Representative images of *P2-tauLacZ* axon projection in olfactory bulb sections from *OMP-tTA:tetO-LBR* and control mice treated with doxycycline beginning at P0, P7, or P21. Analyses are performed 8 to 12 weeks after doxycycline treatment. Magenta: LacZ; blue: DAPI. (**B**) Quantification of the *P2-tauLacZ* glomeruli in the LBR mice treated with doxycycline at different postnatal stages. The average number of *P2-GFP* glomeruli in Kir2.1 mice is shown by dotted line (Fig. 2B). Two-sample, one-way Student's *t* test is applied for statistical analysis. **P* < 0.05, ***P* < 0.01, and ****P* < 0.001 with *t* test. (**C**) Representative images of *M72-tauGFP* neuron projection in olfactory bulb sections from *OMP-tTA:tetO-DTA* and control mice. Doxycycline diet starts at P0, P3, or P21 as marked. Green: GFP; blue: DAPI. Arrowheads indicate the glomeruli receiving the *P2* (A) or *M72* (C). Scale bars, 100 μm.

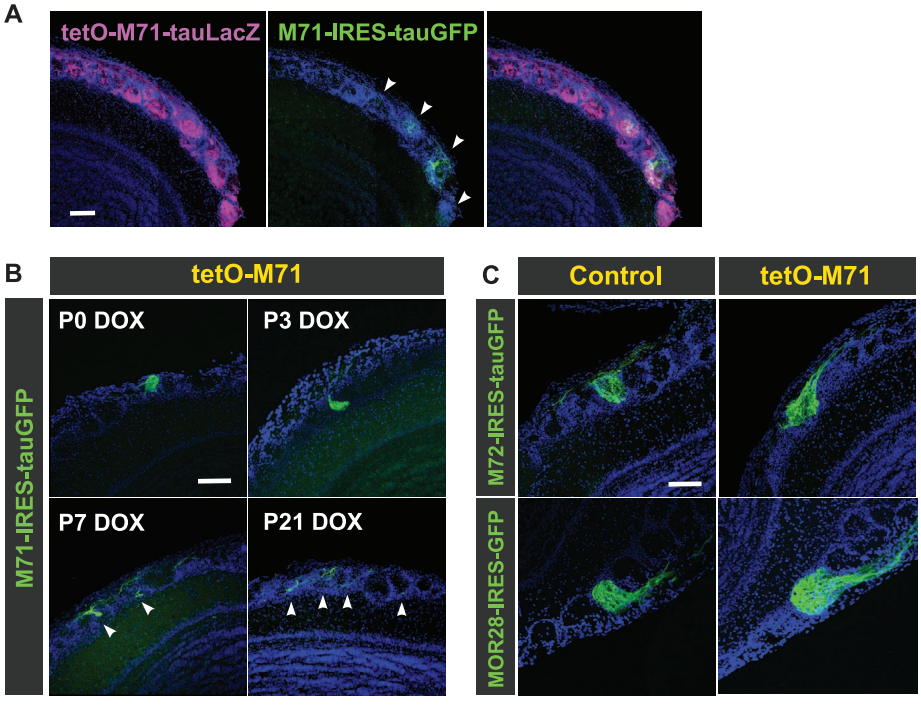

Fig. 4. Homotypic interaction among olfactory sensory neurons expressing the same OR. (**A**) Ectopic expression of *M71* receptor gene perturbs projection of olfactory sensory neurons expressing endogenous *M71* receptor (*M71-IRES-tauGFP*). Coronal olfactory bulb section of *OMP-IRES-tTA:tetO-M71* mice without doxycycline treatment is shown. Magenta: LacZ; green: GFP; blue: DAPI. (**B**) Coronal bulb sections from *tetO-M71* mice treated with doxycycline beginning at P0, P3, P7, and P21. Arrowheads indicate the glomeruli receiving endogenous *M71-IRES-tauGFP* axons. (**C**) Ectopic expression of *M71* does not alter projection of neurons expressing other OR genes. Representative images of *M72-IRES-tauGFP* and *MOR28-IRES-GFP* neuron projection in coronal bulb sections from *tetO-M71* and control mice treated with doxycycline beginning at P14 and P21, respectively. Scale bars, 100 μm.

the map. Although transient ectopic glomeruli may be generated during normal postnatal development, they are pruned in adult animals (*30*, *31*). The pruning process may reflect a refinement process at a later postnatal stage.

Our study puts the olfactory system in line with other sensory systems in that it undergoes a change in circuit plasticity during the critical period of development (*32*). Although, traditionally, the discussions of critical period have focused on how sensory deprivation affects the development of neural circuits, our study reveals an intrinsic developmental program that unfolds whether or not neural activity is perturbed. Even though the olfactory system is regulated by a critical period, late-generated neurons adopt a different strategy for axon projection. Thus, a developmental critical period may function to restrict the reorganization of the neural circuit and to maintain an established map.

References and Notes

1. G. L. Ming, H. Song, *Annu. Rev. Neurosci.* **28**, 223–250 (2005).
2. A. Mackay-Sim, P. Kittel, *J. Neurosci.* **11**, 979–984 (1991).
3. J. A. Gogos, J. Osborne, A. Nemes, M. Mendelsohn, R. Axel, *Cell* **103**, 609–620 (2000).
4. R. M. Costanzo, *Ciba Found. Symp.* **160**, 233–242, discussion 243–248 (1991).
5. R. M. Costanzo, *Chem. Senses* **25**, 199–205 (2000).
6. R. M. Costanzo, *Chem. Senses* **30** (suppl. 1), i133–i134 (2005).
7. P. P. Graziadei, G. A. Monti Graziadei, *Ann. N.Y. Acad. Sci.* **457**, 127–142 (1985).
8. P. Mombaerts *et al.*, *Cell* **87**, 675–686 (1996).
9. S. J. Royal, B. Key, *J. Neurosci.* **19**, 9856–9864 (1999).
10. M. S. Bailey, A. C. Puche, M. T. Shipley, *J. Comp. Neurol.* **415**, 423–448 (1999).
11. S. M. Potter *et al.*, *J. Neurosci.* **21**, 9713–9723 (2001).
12. A. Bulfone *et al.*, *Neuron* **21**, 1273–1282 (1998).
13. A. Mackay-Sim, P. W. Kittel, *Eur. J. Neurosci.* **3**, 209–215 (1991).
14. P. Mombaerts, *Annu. Rev. Cell Dev. Biol.* **22**, 713–737 (2006).
15. J. A. John, B. Key, *Chem. Senses* **28**, 773–779 (2003).
16. C. R. Yu *et al.*, *Neuron* **42**, 553–566 (2004).
17. T. Bozza, J. P. McGann, P. Mombaerts, M. Wachowiak, *Neuron* **42**, 9–21 (2004).
18. L. Ma *et al.*, *Proc. Natl. Acad. Sci. U.S.A.* **109**, 5481–5486 (2012).
19. P. Feinstein, P. Mombaerts, *Cell* **117**, 817–831 (2004).
20. G. Barnea *et al.*, *Science* **304**, 1468 (2004).
21. K. T. Nguyen-Ba-Charvet, T. Di Meglio, C. Fouquet, A. Chédotal, *J. Neurosci.* **28**, 4244–4249 (2008).
22. H. Takeuchi *et al.*, *Cell* **141**, 1056–1067 (2010).
23. D. M. Lin *et al.*, *Neuron* **26**, 69–80 (2000).
24. E. J. Clowney *et al.*, *Cell* **151**, 724–737 (2012).
25. P. Lee *et al.*, *Proc. Natl. Acad. Sci. U.S.A.* **95**, 11371–11376 (1998).
26. T. Imai *et al.*, *Science* **325**, 585–590 (2009).
27. S. Serizawa *et al.*, *Cell* **127**, 1057–1069 (2006).
28. A. Fleischmann *et al.*, *Neuron* **60**, 1068–1081 (2008).
29. T. Imai, H. Sakano, *Eur. J. Neurosci.* **34**, 1647–1654 (2011).
30. D. J. Zou *et al.*, *Science* **304**, 1976–1979 (2004).
31. H. B. Treloar, P. Feinstein, P. Mombaerts, C. A. Greer, *J. Neurosci.* **22**, 2469–2477 (2002).
32. T. K. Hensch, *Nat. Rev. Neurosci.* **6**, 877–888 (2005).

Acknowledgments: We thank L. Nay, E. S. Gillespie, and the Laboratory Animal Services at the Stowers Institute for technical assistance and S. Lomvardas, R. Axel, N. Ryba, and P. Mombaerts for sharing transgenic mice. We appreciate helpful discussions with H. Taniguchi, H. Sakano, Y. Zou, and members of the Yu lab. This work fulfills, in part, requirements for Y.W.'s Ph.D. thesis with the Open University, United Kingdom. This work is supported by funding from Stowers Institute.

Supplementary Materials

www.sciencemag.org/content/344/6180/194/suppl/DC1
Materials and Methods
Figs. S1 to S3
Reference (*33*)

21 November 2013; accepted 28 February 2014
10.1126/science.1248805

A Critical Period Defined by Axon-Targeting Mechanisms in the Murine Olfactory Bulb

Lulu Tsai* and Gilad Barnea†

The olfactory system remains plastic throughout life because of continuous neurogenesis of sensory neurons in the nose and inhibitory interneurons in the olfactory bulb. Here, we reveal that transgenic expression of an odorant receptor has non–cell autonomous effects on axons expressing this receptor from the endogenous gene. Perinatal expression of transgenic odorant receptor causes rerouting of like axons to new glomeruli, whereas expression after the sensory map is established does not lead to rerouting. Further, chemical ablation of the map after rerouting does not restore the normal map, even when the transgenic receptor is no longer expressed. Our results reveal that glomeruli are designated as targets for sensory neurons expressing specific odorant receptors during a critical period in the formation of the olfactory sensory map.

Critical periods are epochs of increased brain plasticity when neural circuits are especially sensitive to shaping by stimuli. In the olfactory system, enhanced plasticity is not confined to early development; rather, it is maintained throughout adult life (*1*). This prolonged plasticity is achieved by the continuous generation of the inhibitory granule cells that migrate into the olfactory bulb and integrate into the circuits and by the generation of olfactory sensory neurons (OSNs) that incorporate into the circuits throughout life (*2*, *3*). Although we know that plasticity is retained in the mature olfactory system, does a critical period exist in the formation of the sensory map in the olfactory bulb?

In mice, each OSN expresses only one of the ~1300 odorant receptor (OR) genes (*4*–*7*) from only one allele (*8*). The OSNs that express the same OR are randomly dispersed within a broad zone in the main olfactory epithelium in the nose (*9*, *10*). In the olfactory bulb, the first olfactory center in the brain, the axons of OSNs expressing the same OR converge on spatially fixed neuropil structures called glomeruli (*9*–*11*). Further, ORs actively participate in the axon guidance of OSNs to particular glomeruli (*12*, *13*). In the glomeruli, the axons synapse with the dendrites of mitral and tufted cells, the projection neurons in the bulb. Each projection neuron receives input from a single glomerulus and sends its axon to the olfactory cortex. Thus, an olfactory sensory map is formed in the bulb. In this map, the identity of each odor is encoded by the combination of glomeruli that it activates (*3*). In contrast to the somatosensory, auditory, and visual maps, neighboring relations between peripheral sensory neurons are not maintained in the olfactory sensory map. Because OSNs continue to integrate into the circuits throughout life, the challenge of axon guidance persists in adulthood (*3*).

We devised a strategy for ectopic expression of a specific OR, MOR28, in a temporally controlled manner using the tetracycline response element (tetO) to drive its expression. The tetO promoter is activated by the tetracycline-controlled transcription activator tTA, which is inhibited by the antibiotic doxycycline. When doxycycline is removed, expression from the tetO promoter is induced within days (*14*–*16*). A similar approach for inducing ectopic expression of ORs was previously used (*17*–*19*). Our strategy involved the use of three alleles (fig. S1A). In the first, designated *OMP-IRES-tTA*, the olfactory marker protein (OMP) drives expression of tTA in all OSNs (*16*). In the second, designated *tetO::MOR28-IRES-tau-LacZ* (TO28), tetO drives the expression of MOR28 and the fusion protein tau–β-galactosidase (β-gal). To distinguish between the OSNs that express MOR28 from its endogenous genomic locus (endogenous MOR28 OSNs) versus OSNs that express MOR28 from the transgene (transgenic MOR28 OSNs), we introduced a third allele, designated *MOR28-IRES-GFP*. OSNs that express MOR28 from this allele also express green fluorescent protein (GFP) (*20*). Thus, GFP expression marks OSNs expressing MOR28 from its endogenous locus. Because β-gal and GFP are exogenous to mice, staining for each identifies transgenic or endogenous MOR28 OSNs, respectively (fig. S1B).

Department of Neuroscience, Brown University, Providence, RI 02912, USA.

*Present address: Department of Biology, Drexel University, Philadelphia, PA 19104, USA.
†Corresponding author. E-mail: gilad_barnea@brown.edu

This strategy enabled us to induce transgene expression at different developmental points.

We generated two founder lines for the TO28 transgene. In the presence of the *OMP-IRES-tTA* allele, animals from these lines express the transgene only in a small fraction of OSNs, presumably because of position effect variegation. In one of these lines, designated TO28L, the transgene is expressed in ~1% of OSNs, and in the other, designated TO28H, the transgene is expressed in ~5% of OSNs. In both lines, the transgene is expressed throughout the olfactory epithelium, both within and outside the characteristic MOR28 zone of expression (Fig. 1, A and B, and fig. S1B).

Normally, MOR28-expressing OSNs converge on two symmetrical pairs of glomeruli per mouse, one medial and one lateral, all located in the posterior-ventral part of the bulb (*13, 16, 20, 21*). In both transgenic MOR28 lines, visualization of the projection patterns of transgene-expressing OSNs revealed that they converged on multiple glomeruli that were scattered throughout the bulb. The positions and numbers of these glomeruli varied significantly between animals and also between the two bulbs within the same animal (Fig. 1, C to F). We counted the ectopic glomeruli in sectioned bulbs from both lines and observed 46.8 ± 8.33 β-gal–positive glomeruli per animal (n = 5) in TO28L and 103.25 ± 13.85 glomeruli per animal (n = 4) in TO28H (fig. S1C).

In animals that express transgenic MOR28, the endogenous MOR28 axons innervated more than the regular four glomeruli. These glomeruli were always coinnervated by transgenic MOR28 fibers, and they were confined to areas within 650 μm of the typical locations of the wild-type glomeruli (Fig. 1, G and H). In some cases, only a few transgenic MOR28 fibers innervated a glomerulus mainly innervated by endogenous MOR28 fibers, likely the wild-type MOR28 glomerulus (Fig. 1G). In other cases, the transgenic MOR28 fibers and the endogenous MOR28 axons innervated multiple glomeruli. However, the mixing between the two neuronal populations was extensive, and we could not determine which of the glomeruli was the wild-type MOR28 glomerulus (Fig. 1H). Because the endogenous MOR28 axons do not express transgenic MOR28 (fig. S1B), this phenotype is non–cell autonomous and is likely the result of homotypic attraction between the endogenous and transgenic MOR28 fibers (*19*, *22*). We refer to the glomeruli that contain both endogenous and transgenic MOR28 axons as rerouted-MOR28 glomeruli. Roughly the same numbers of rerouted-MOR28 glomeruli are observed in the two TO28 lines: 3.14 ± 0.55 (n = 7) in TO28L and 4.8 ± 0.86 (n = 5) in TO28H (fig. S1D).

We examined whether rerouted-MOR28 glomeruli could be formed throughout the lifetime of the animal, or whether they could only be formed during a specific developmental period. To determine this, we used doxycycline to silence the tetO promoter in mice capable of TO28 expression (mice bearing both the transgene and the *OMP-IRES-tTA* driver). Pregnant females were fed doxycycline from conception to allow the embryos to form wild-type glomerular maps. We then removed doxycycline from the diet at P0, P7, or P14 to allow transgene expression. Mice were maintained on a doxycycline-free diet to enable continuous transgene expression and were examined after 15 weeks or 32 weeks without the drug, nearly 3 times the half-life of OSNs (fig. S2A). Whereas transgenic MOR28 axons formed ectopic glomeruli and also innervated the wild-type MOR28 glomeruli, endogenous MOR28 axons almost never formed rerouted-MOR28 glomeruli (Fig. 2, A to D, and fig. S3A, and C to F). When doxycycline was removed at P0 or P7, rerouted glomeruli were observed in 1 out of 9 mice, or 1 out of 17, respectively. Rerouting was never observed (0 out of 9 mice) when doxycycline

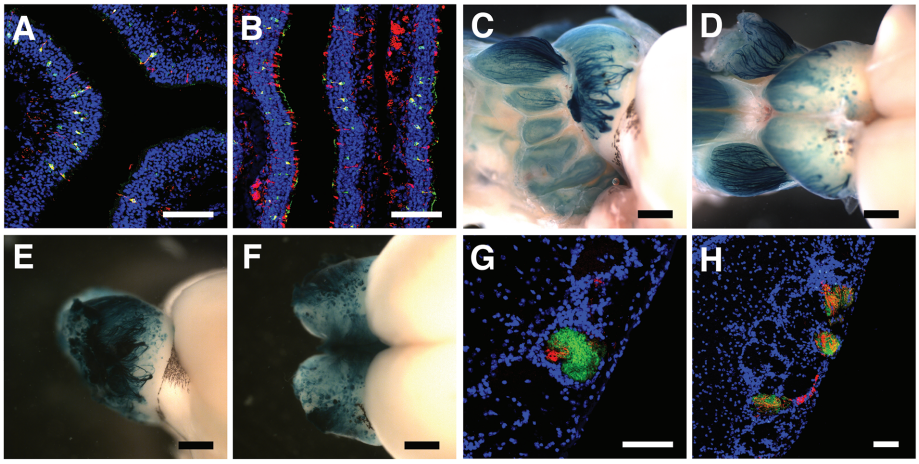

Fig. 1. Ectopic expression of MOR28 results in formation of two types of ectopic glomeruli. Staining with antibodies against MOR28 (green) and β-gal (red) reveal ectopic expression of MOR28 in the olfactory epithelia from two lines: (**A**) TO28L expresses MOR28 in ~1% of OSNs and (**B**) TO28H expresses MOR28 in ~5% of OSNs. Lateral and dorsal views of whole-mount preparations from TO28L (**C** and **D**) and TO28H (**E** and **F**) stained with X-gal to reveal the distribution of ectopic glomeruli. (**G** and **H**) Bulb sections from TO28L were stained with antibodies against GFP (green) to reveal endogenous MOR28, and β-gal (red) to reveal transgenic MOR28. In some cases, the abundance of green fibers identifies the wild-type MOR28 glomerulus (G). In others, axons expressing endogenous MOR28 innervate multiple rerouted-MOR28 glomeruli (H). Scale bars: for (C) to (F), 1 mm; all other images, 100 μm.

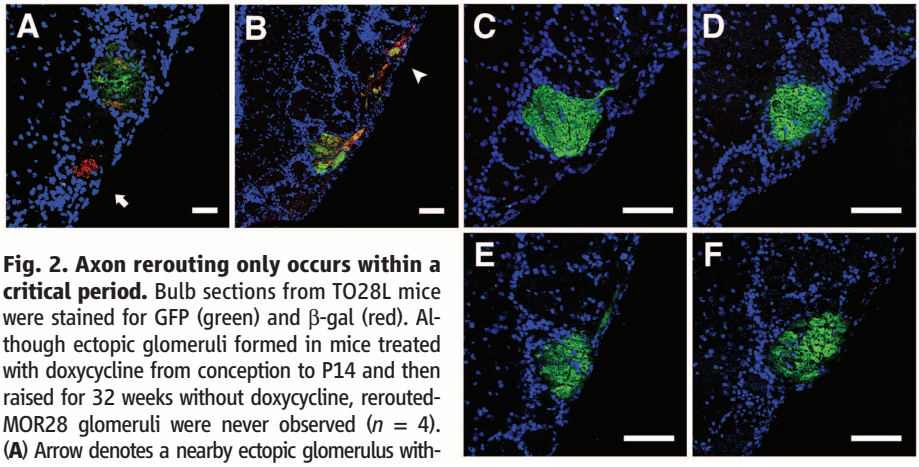

Fig. 2. Axon rerouting only occurs within a critical period. Bulb sections from TO28L mice were stained for GFP (green) and β-gal (red). Although ectopic glomeruli formed in mice treated with doxycycline from conception to P14 and then raised for 32 weeks without doxycycline, rerouted-MOR28 glomeruli were never observed (n = 4). (**A**) Arrow denotes a nearby ectopic glomerulus without rerouted-MOR28 axons. In mice raised without doxycycline (n = 7), both rerouted-MOR28 glomeruli (3.14 ± 0.55) and ectopic glomeruli were observed. (**B**) Arrowhead indicates the edge of a second rerouted glomerulus that is shown in fig. S2C. Rerouted-MOR28 glomeruli were not observed in (**C**) control littermates treated with doxycycline until P14 (n = 2) or (**D**) never exposed to doxycycline (n = 4). (**E**) TO28L mice maintained on a doxycycline diet before and after OSN ablation never exhibited rerouted glomeruli (n = 2). (**F**) Mice that expressed TO28L only postnatally did not form rerouted glomeruli even after OSN ablation (n = 5). Scale bars, 100 μm.

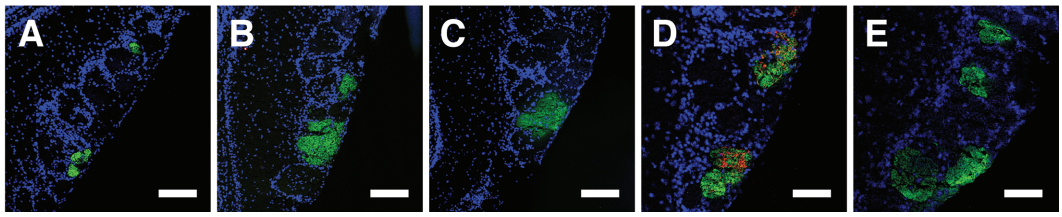

Fig. 3. Rerouted-MOR28 glomeruli are maintained even without continuous transgene expression. (**A** to **C**) TO28L mice and control littermates were raised without doxycycline until P60 and treated with doxycycline for >5 months thereafter. Bulb sections were stained for GFP (green) and β-gal (red). Rerouted-MOR28 glomeruli were observed (A) after 21 weeks, and (B) even after 32 weeks in doxycycline-fed mice, when transgenic MOR28 fibers were no longer present. (C) No rerouted-MOR28 glomeruli were observed in controls after 21 weeks on doxycycline. (**D** and **E**) TO28L mice were raised without doxycycline until P60, when OSNs were ablated. The mice were analyzed after 2 months recovery with or without doxycycline. (D) Mice that expressed the transgene before and after OSN ablation exhibited rerouted glomeruli (3.6 ± 0.98, n = 5). (E) In mice that expressed the transgene only before ablation, transgenic MOR28 fibers were no longer present, but endogenous MOR28 axons still innervated multiple glomeruli (3 ± 1.15, n = 3). Scale bars, 100 μm.

was removed at P14 (fig. S3B). We conclude that there is a critical period for the formation of rerouted-MOR28 glomeruli that ends at birth or shortly thereafter.

Among the many differences between the developing and adult olfactory systems is the fraction of OSNs that are immature with outgrowing axons. In embryos, most OSNs are immature, and their axons target the glomeruli within a short period of time. Thus, outgrowing axons do not contact many established axonal tracts. By contrast, at any given time in the adult, only rare OSN axons are actively growing along established tracts made up of mature OSN axons. We therefore tested whether the abundance of immature OSNs with outgrowing axons underlies the critical period for the formation of rerouted-MOR28 glomeruli. Mice capable of TO28 expression were treated with doxycycline beginning at conception to suppress the formation of rerouted-MOR28 glomeruli. As the mice were taken off doxycycline, they were also treated with methimazole, which causes OSN ablation (*23*). We empirically determined the peak effect of methimazole on MOR28-expressing neurons and found that 5 days after injection only 0.2% of these OSNs remain (fig. S2B). Thus, this paradigm enabled us to examine synchronized regrowth of 99.8% of the axons in the adult. When regrowth occurred in the presence of transgenic MOR28 axons (n = 5 mice), ectopic glomeruli were formed, but we still never observed rerouted-MOR28 glomeruli (Fig. 2, E and F, and fig. S3A). These data indicate that the developmental mechanisms available perinatally, when the olfactory map is established, are not available for regeneration in the adult after olfactory neuron ablation.

We next examined whether continuous transgene expression is required for the maintenance of rerouted-MOR28 glomeruli. Mice expressing the transgene developed until 2 months of age to allow ectopic and rerouted-MOR28 glomeruli to form. These mice were then treated with doxycycline for 21 weeks, or nearly twice the half-life of OSNs, to allow for substantial turnover of MOR28-expressing OSNs (fig. S4). Although no axon fibers expressing transgenic MOR28 were observed at this point, endogenous MOR28 axons continued to innervate the rerouted-MOR28 glomeruli (Fig. 3, A to C). Thus, rerouted-MOR28 glomeruli, once formed, were not dependent on persistent expression of transgenic MOR28.

Finally, we examined whether the rerouted-MOR28 glomeruli would still be targeted by newly growing endogenous MOR28 axons after OSN ablation. Mice expressing TO28L were allowed to form ectopic and rerouted-MOR28 glomeruli until 2 months of age. The OSNs were then ablated by methimazole injection, and the mice were treated with doxycycline for 2 months to allow the glomerular map to be restored without expression of transgenic MOR28 (fig. S4). These mice exhibited as many rerouted-MOR28 glomeruli as mice that were not treated with doxycycline after OSN ablation (Fig. 3, D and E). These results suggest that the previously formed rerouted-MOR28 glomeruli, or the tracts leading to them, are marked as targets for endogenous MOR28 axons.

We have shown that OSNs expressing a particular OR are affected non–cell autonomously by other OSNs that express the same OR. This supports the notion that homotypic attraction exists between OSNs expressing the same OR (*19*, *22*). It is unclear whether these interactions are directly mediated by the axonal OR itself (*13*), or by any of the cell adhesion molecules implicated in OSN guidance (*3*). A role for OR-mediated, non–cell autonomous interactions in glomerular formation adds a layer of complexity to the prevailing model that focuses on cell-autonomous mechanisms by which ORs affect guidance (*3*, *24*). Homotypic attraction between OSNs leads to convergence of like axons on the same glomeruli. This is in contrast to the homotypic repulsion between neurons expressing the same splice form of the adhesion molecule DSCAM1 in *Drosophila* and self-avoidance between neurites expressing the same type of protocadherin in mammals (*25*, *26*). Should similar non–cell autonomous mechanisms participate in the organization of other circuits, it would pose a challenge for the development of neuronal regeneration therapies.

The confinement of rerouted-MOR28 glomeruli to areas within 650 μm of the typical locations of the wild-type glomeruli and the cap in the number of rerouted-MOR28 glomeruli in the two founder lines suggest that axon rerouting can occur only within a "neighborhood" of glomeruli. This "neighborhood" likely corresponds to the area where the final sorting of axons expressing the same OR into discrete glomeruli occurs (*3*).

What is the nature of the guidance signal? It is formally possible that the axons of the ~30 endogenous MOR28 OSNs per mouse remaining after methimazole ablation serve as the structural substrate of the memory for the tract to the rerouted-MOR28 glomeruli. However, a model in which the few residual endogenous MOR28 OSNs act as "pioneers" is unlikely in view of the sparse distribution of these neurons. Alternatively, fragments of the axons of the dead neurons could mark the tracts to the glomeruli. In this case, the axons of regenerating OSNs would follow this trail to the correct glomerulus by interacting with these fragments. As another possibility, axons may leave molecular traces in the surrounding extracellular matrix, or may induce expression of specific marks in postsynaptic neurons. Regardless of the precise mechanism, our results show that these marks are put in place only during a developmental critical period. This may ensure the stability of the olfactory sensory map in spite of the continuous regeneration of OSNs throughout life.

References and Notes

1. T. K. Hensch, *Annu. Rev. Neurosci.* **27**, 549–579 (2004).
2. A. Carleton, L. T. Petreanu, R. Lansford, A. Alvarez-Buylla, P.-M. Lledo, *Nat. Neurosci.* **6**, 507–518 (2003).
3. K. Mori, H. Sakano, *Annu. Rev. Neurosci.* **34**, 467–499 (2011).
4. R. Vassar, J. Ngai, R. Axel, *Cell* **74**, 309–318 (1993).
5. K. J. Ressler, S. L. Sullivan, L. B. Buck, *Cell* **73**, 597–609 (1993).
6. K. Raming *et al.*, *Nature* **361**, 353–356 (1993).
7. X. Zhang, S. Firestein, *Nat. Neurosci.* **5**, 124–133 (2002).
8. A. Chess, I. Simon, H. Cedar, R. Axel, *Cell* **78**, 823–834 (1994).
9. R. Vassar *et al.*, *Cell* **79**, 981–991 (1994).
10. K. J. Ressler, S. L. Sullivan, L. B. Buck, *Cell* **79**, 1245–1255 (1994).
11. P. Mombaerts *et al.*, *Cell* **87**, 675–686 (1996).
12. F. Wang, A. Nemes, M. Mendelsohn, R. Axel, *Cell* **93**, 47–60 (1998).

13. G. Barnea *et al.*, *Science* **304**, 1468 (2004).
14. M. Gossen, H. Bujard, *Proc. Natl. Acad. Sci. U.S.A.* **89**, 5547–5551 (1992).
15. J. A. Gogos, J. Osborne, A. Nemes, M. Mendelsohn, R. Axel, *Cell* **103**, 609–620 (2000).
16. C. R. Yu *et al.*, *Neuron* **42**, 553–566 (2004).
17. M. Q. Nguyen, Z. Zhou, C. A. Marks, N. J. P. Ryba, L. Belluscio, *Cell* **131**, 1009–1017 (2007).
18. A. Fleischmann *et al.*, *Neuron* **60**, 1068–1081 (2008).
19. M. Q. Nguyen, C. A. Marks, L. Belluscio, N. J. P. Ryba, *J. Neurosci.* **30**, 9271–9279 (2010).
20. B. M. Shykind *et al.*, *Cell* **117**, 801–815 (2004).
21. A. Tsuboi *et al.*, *J. Neurosci.* **19**, 8409–8418 (1999).
22. A. Vassalli, A. Rothman, P. Feinstein, M. Zapotocky, P. Mombaerts, *Neuron* **35**, 681–696 (2002).
23. E. B. Brittebo, *Pharmacol. Toxicol.* **76**, 76–79 (1995).
24. A. Nakashima *et al.*, *Cell* **154**, 1314–1325 (2013).
25. J. L. Lefebvre, D. Kostandinov, W. V. Chen, T. Maniatis, J. R. Sanes, *Nature* **488**, 517–521 (2012).
26. S. L. Zipursky, W. B. Grueber, *Annu Rev Neurosci.* **36**, 547–568 (2013).

Acknowledgments: We thank R. Axel, E. Morrow, and members of the Barnea laboratory for critical reading of the manuscript. We thank R. Y. Korsak and M. Talay for artwork for the figures. This work was supported by NIH grants T32GM007601 (L.T.) and 5R01MH086920 (G.B.), as well as by funds from the Pew Scholar in the Biomedical Sciences program.

Supplementary Materials

www.sciencemag.org/content/344/6180/197/suppl/DC1
Materials and Methods
Supplementary Text
Figs. S1 to S4
Reference (*27*)

21 November 2013; accepted 28 February 2014
10.1126/science.1248806

Acquisition of Germ Plasm Accelerates Vertebrate Evolution

Teri Evans,[1] Christopher M. Wade,[1] Frank A. Chapman,[2] Andrew D. Johnson,[1]* Matthew Loose[1]*

Primordial germ cell (PGC) specification occurs either by induction from pluripotent cells (epigenesis) or by a cell-autonomous mechanism mediated by germ plasm (preformation). Among vertebrates, epigenesis is basal, whereas germ plasm has evolved convergently across lineages and is associated with greater speciation. We compared protein-coding sequences of vertebrate species that employ preformation with their sister taxa that use epigenesis and demonstrate that genes evolve more rapidly in species containing germ plasm. Furthermore, differences in rates of evolution appear to cause phylogenetic incongruence in protein-coding sequence comparisons between vertebrate taxa. Our results support the hypothesis that germ plasm liberates constraints on somatic development and that enhanced evolvability drives the evolution of germ plasm.

The germ line of metazoans is established early in development with the specification of primordial germ cells (PGCs). Among vertebrates, the conserved mechanism for PGC specification involves their induction from pluripotent cells by extracellular signals, a process referred to as epigenesis (*1*, *2*). However, in several lineages of vertebrates, an alternative mechanism evolved, termed preformation. Here, PGCs are determined by inheritance of germ plasm. Preformation evolved by convergence, which suggests that it may confer a selective advantage. Accordingly, the evolution of germ plasm is associated with morphological innovations and enhanced numbers of species within individual clades (*1*, *3*, *4*). Why this derived mode of PGC specification evolved repeatedly in vertebrates is unknown.

The best-studied contrast of epigenesis and preformation is within amphibians. The PGCs of urodele amphibians (salamanders) are specified by epigenesis, whereas in its sister lineage, anurans (frogs), PGCs contain germ plasm (*5*). Using the axolotl (*Ambystoma mexicanum*) as a model urodele, the ancestral gene regulatory networks (GRNs) for pluripotency and mesoderm specification in vertebrates were identified (*6*, *7*). These GRNs were conserved through the evolution of mammals (*6*, *7*), which also employ epigenesis (*8*). In contrast, in frogs the master regulators of pluripotency as employed in mammals have been deleted (*6*, *9*, *10*), and the GRN for mesoderm underwent expansions of key regulatory molecules (*7*, *11*). Similar genetic innovations evolved in the GRNs for zebrafish development (*12*), which also uses preformation (*13*). The correlation of germ plasm with genetic change has been proposed to result from the relaxation of constraints on somatic development imposed by maintaining the PGC induction pathway (*1*, *3*, *4*). To investigate this possibility, we compiled available expressed sequence tag, mRNA and cDNA sequences from vertebrates (fig. S1A and table S1) identifying ortholog pairs shared between sister taxa with different modes of PGC specification and an appropriate mammal and outgroup sequence (*14*) (fig. S1B). To increase sequence numbers from organisms using epigenesis, we generated transcriptomes from the axolotl and an Acipenseriforme, *Acipenser ruthenus* (the sterlet) (*14*), identifying 82,954 sequence clusters across all vertebrates. All analyses were performed with protein coding DNA sequence, excluding the saturated third position (*14*) (figs. S2 and S3).

Of the 56 published gene trees involving an anuran and a urodele, 29 do not recapitulate the known species phylogeny (table S2). The majority of the incongruent gene trees group urodele

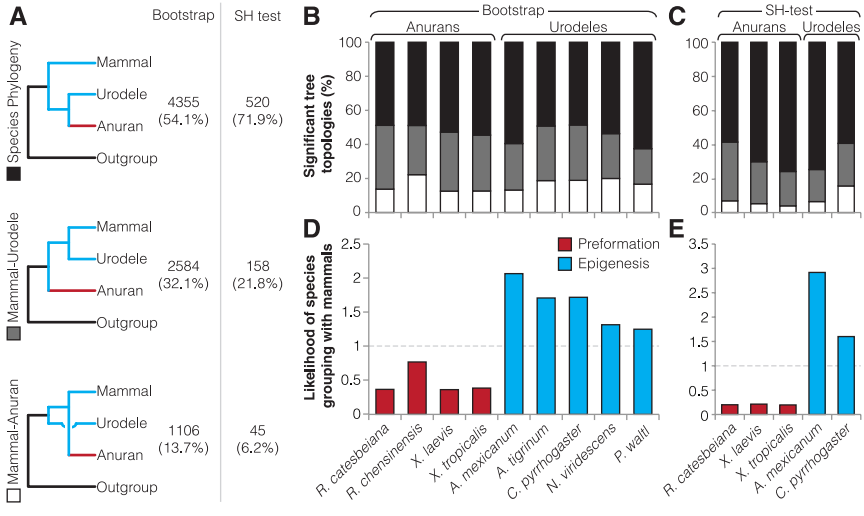

Fig. 1. Amphibian four-taxon tree topologies. (A) Number of significant trees by bootstrapping (>70%) and SH test ($P < 0.05$) for each topology rooted with a Teleostei sequence. (**B** and **C**) The proportions of species phylogeny (black), mammal-urodele (gray), and mammal-anuran (white) topologies per species. (**D** and **E**) The likelihood of each species grouping with mammals when the tree is incongruent; species using preformation are shown in red, those using epigenesis in blue. Dashed lines indicate equal probability of species grouping with mammal or outgroup. [(B) to (E)] Only species with >20 significant trees are shown. The results excluding the transcriptome are shown in fig. S4.

[1]School of Life Sciences, University of Nottingham, Nottingham, NG7 2UH, UK. [2]Program of Fisheries and Aquatic Sciences, University of Florida, Gainesville, FL 32653–3071, USA.

*Corresponding author. E-mail: matt.loose@nottingham.ac.uk (M.L.); andrew.d.johnson@nottingham.ac.uk (A.D.J.)

and mammal species together, both of which undergo epigenesis, to the exclusion of anurans. We generated unrooted four-taxon trees to investigate the extent of this incongruity (*14*), presenting trees rooted on the known outgroup (a Teleostei sequence) (Fig. 1A). Within these trees, 54.1% (4355 of 8045) of amphibian sequences show the expected species phylogeny (>70% bootstrap), grouping anuran with urodele. The majority of the remainder [32.1% (2584 of 8045)] incongruently group urodeles with mammals (Fig. 1A). The Shimodaira-Hasegawa (SH) test reduces the number of significant trees overall ($P < 0.05$), increasing the proportion of trees reflecting the species phylogeny (*14*). Orthology groups that do not reflect the species phylogeny (28%) are three times as likely to place the urodele sequence with the mammal (Fig. 1A, fig. S4A, and table S3). We next considered each amphibian species in turn, grouping them by mode of PGC specification (Fig. 1, B and C). We show that when a tree is incongruent, any given anuran sequence is less likely than its orthologous urodele sequence to group with mammals (Fig. 1, D and E). These results do not depend on the inclusion of the urodele transcriptome data (fig. S4).

Within Actinopterygii (ray-finned fishes), Teleostei (teleosts) use preformation, whereas Acipenseriformes (sturgeons and paddlefish), which maintain primitive embryological and adult traits, most likely have retained epigenesis (*1*, *4*, *13*). We identified 19,394 trees with >70% bootstrap support, of which 68.2% (13,233) reflect the species phylogeny. The majority of the remainder [24.5% (4757)] incongruently group Acipenseriformes with mammals (Fig. 2A). The SH test reduces the total, but still Acipenseriforme sequences are 5 times as likely to group with mammals when the species phylogeny is not obtained (Fig. 2A). Subdividing the data by species reveals a clear distinction between Teleostei and Acipenseriformes; in incongruent trees, Acipenseriformes are more likely to group with a mammal (Fig. 2, B to E). This is true for all 59 Teleostei analyzed with bootstrap-supported trees and 22 of 23 Teleostei supported by the SH test (fig. S5, A and B, and table S4). These results remain true even if the transcriptome data are excluded (fig. S5, C and D)

We next investigated the sauropsids (reptiles and birds), determining four-taxon tree topologies. In sauropsids, preformation evolved independently in lepidosaurs (lizards and snakes) and in archosaurs (crocodiles and birds) (*15*–*18*). The lepidosaurs, which experienced a change in the rate of evolution (*19*), and archosaurs, separated ~280 million years ago (*20*). The turtle lineage (testudines), using epigenesis, is closer to the archosaurs than lepidosaurs (*21*). Thus, we analyzed the sauropsids in two subdivisions—the archosaurs and testudines, and the lepidosaurs. Within these groups, we compared birds (preformation) with crocodiles and testudines (epigenesis) and similarly snakes (preformation) with Gekkota and Iguanidae lizards (epigenesis) (*15*–*18*). Within the sauropsids, almost all the four-taxon trees support the expected species phylogeny and do not subdivide by the mode of germ cell specification in this analysis (fig. S6 and table S5), although the total number of sequence comparisons was low (fig. S1A).

Nonetheless, among the amphibians and actinopterygians, but not the sauropsids, when in an incongruent tree, species using epigenesis are more likely to group with mammals (Figs. 1,2). Such incongruent phylogenies may be driven by differences in the rate of sequence evolution (*19*, *22*), and organisms that have acquired preformation are typically more speciose than those using epigenesis (*3*, *4*). We therefore used three-taxon multiple alignments to determine how the relative rate of sequence evolution differs between sister taxa. Among amphibian species, 32.3% of sequences are evolving at significantly different rates ($P < 0.05$), of which 87% show urodele sequences evolving slower than anurans (Fig. 3A and fig. S7B). Within the actinopterygians, ~50% of sequences evolve at significantly different rates ($P < 0.05$), with almost all showing that Acipenseriforme sequences are slower than Teleostei (Fig. 3B and fig. S7, A and B). Furthermore, in the sauropsids, ~20 to 25% of sequences are evolving at significantly different rates, with the majority of slow-evolving sequences in organisms using epigenesis ($P < 0.05$) (Fig. 3, C and D). Thus, sauropsid sequences exhibit differences in the rate of sequence evolution that correlate with the mode of PGC specification.

Combining these data across classes, 56% (69,165 of 121,373) of all analyses show no significant difference in the rate of sequence evolution (Fig. 3E and table S6). Only 2319 of 121,373 relative-rate tests (<2%) showed a sequence derived from an organism with epigenesis evolving faster than its ortholog. The remaining 41.1% of comparisons (49,898 of 121,373) suggest that sequences from organisms using epigenesis are evolving more slowly. Ranking each species by the proportion of slower-evolving sequences separates organisms using epigenesis from those using preformation, regardless of taxonomic class (fig. S7F).

To investigate functional properties of sequences showing accelerated rates of evolution and incongruent phylogenies, we mapped our results to the mouse and zebrafish genomes (see supplementary text). The proportion of sequences showing evidence of accelerated evolution is significantly higher among genes expressed early in development (chi-square test, $P < 0.05$) and decreases in genes expressed at later stages (fig. S8). Previous reports demonstrate that early genes are under the highest levels of developmental

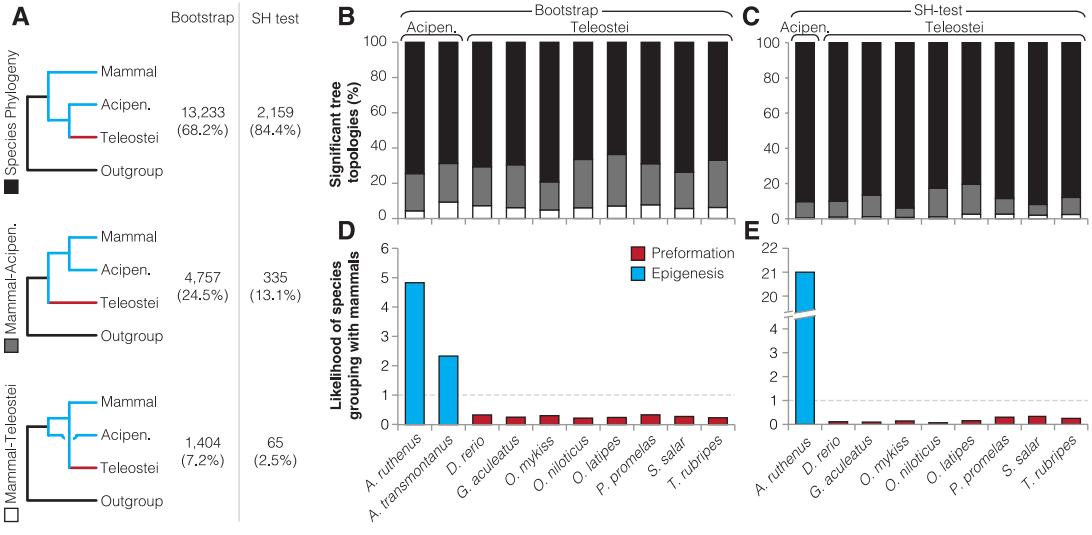

Fig. 2. Actinopterygian four-taxon tree topologies. (**A**) Number of significant trees by bootstrapping (>70%) and SH test ($P < 0.05$) for each topology, rooted with an amphioxus sequence. (**B** and **C**) The proportion of species phylogeny (black), Mammal-Acipenseriforme (gray) and Mammal-Teleostei (white) topologies per species. (**D** and **E**) The likelihood of each species grouping with mammals when the tree is incongruent; species using preformation are shown in red, those using epigenesis in blue. Dashed lines indicate equal probability of species grouping with mammal or outgroup. [(B) to (E)] Only Acipenseriformes with >20 significant trees and eight Teleostei species are shown; the results for all species are in fig. S5, A and B. The results excluding the transcriptome are shown in fig. S5, C and D.

constraint (*23*), and our data suggest that early genes are the most likely to evolve at faster rates in species employing preformation. Together, this supports the hypothesis that the evolution of germ plasm liberates constraints on early development (*1*, *4*).

We next considered the correlation of results where individual sequences had been tested for both rate and incongruent tree topologies (table S11). All four-taxon trees were rooted on species using preformation, yet our preceding analyses suggest that these outgroups also have accelerated rates of evolution compared with their sister taxa (Fig. 4A). Because tree reconstruction may fail as a consequence of two long branches clustering (long-branch attraction)(Fig. 4B) (*24*), we asked whether the incongruent trees were driven by the differences in rates observed in the outgroup sister taxa.

For the majority of amphibian four-taxon trees where the outgroup sister taxa differ in rate, the Teleostei sequence is evolving significantly faster than its Acipenseriforme ortholog [$P < 0.05$, (fig. S9A)]. We therefore rebuilt trees using Acipenseriformes as the outgroup. This increased the proportion of trees congruent with the species phylogeny at the expense of trees grouping urodele sequences with mammals (fig. S9B and table S12). Grouping sequences by both relative rate and tree topology revealed that the highest proportion of incongruent trees occur when the relative rate differs within amphibians (Fig. 4C). If rate differences drive incongruence, changing outgroup should only affect those trees where the outgroup rates differ. Where the actinopterygian sequences do not significantly differ in rate, proportions of incongruent trees remain similar as the outgroup species changes (Fig. 4, D and E, and table S13). Where actinopterygian sequences significantly differ in rate, the proportion of incongruent trees is reduced using an Acipenseriforme rather than a Telesotei outgroup ($P < 0.05$). The most dramatic change occurs when both amphibian and actinopterygian sequences significantly differ in rate ($P < 0.05$), suggesting that the faster rate of evolution in both anuran and Teleostei sequences drives the observed incongruence.

The natural history of vertebrates is punctuated with the repeated evolution of germ plasm associated with embryological innovations, gross morphological changes in adults, and enhanced speciation (*1*–*4*). Germ plasm functions to segregate PGCs from somatic cells at the inception of development, and we propose that this relaxes genetic constraints on the mechanisms that govern early somatic development (*4*). Our results identify a consistent bias in changes in the rate of sequence evolution in species using preformation compared with their sister taxa that use epigenesis. No other biological property correlates as well with the observed changes in rate (fig. S10). Sequences expressed during early development are under high levels of developmental constraint (*23*), and we show that these sequences exhibit a release of constraint in species using preformation. Taken together, these data suggest that the acquisition of germ plasm liberates developmental constraints, leading to increased rates of sequence evolution and enhanced speciation. They support the hypothesis that enhanced evolvability is responsible for the repeated evolution of germ plasm (*1*–*4*).

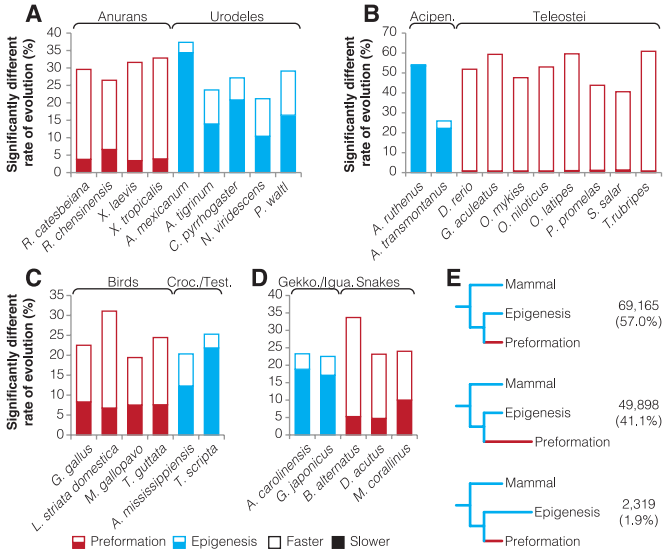

Fig. 3. Relative-rate test results. (**A** to **D**) Proportion of sequences evolving at significantly slower (filled) or faster (clear) rates in each species ($P < 0.05$; preformation shown in red, epigenesis in blue). (A) Amphibians. (B) Actinopterygians, including eight Teleostei species (all Teleostei shown in fig. S7G). (C) Archosaurs and Testudines. (D) Lepidosaurs. Only species with >20 significant sequences are shown. (**E**) Summary of relative-rate data across all vertebrates grouping species by epigenesis or preformation. [(A) (B), and (E)] Excluding transcriptomes are in figs. S7, C to E, respectively.

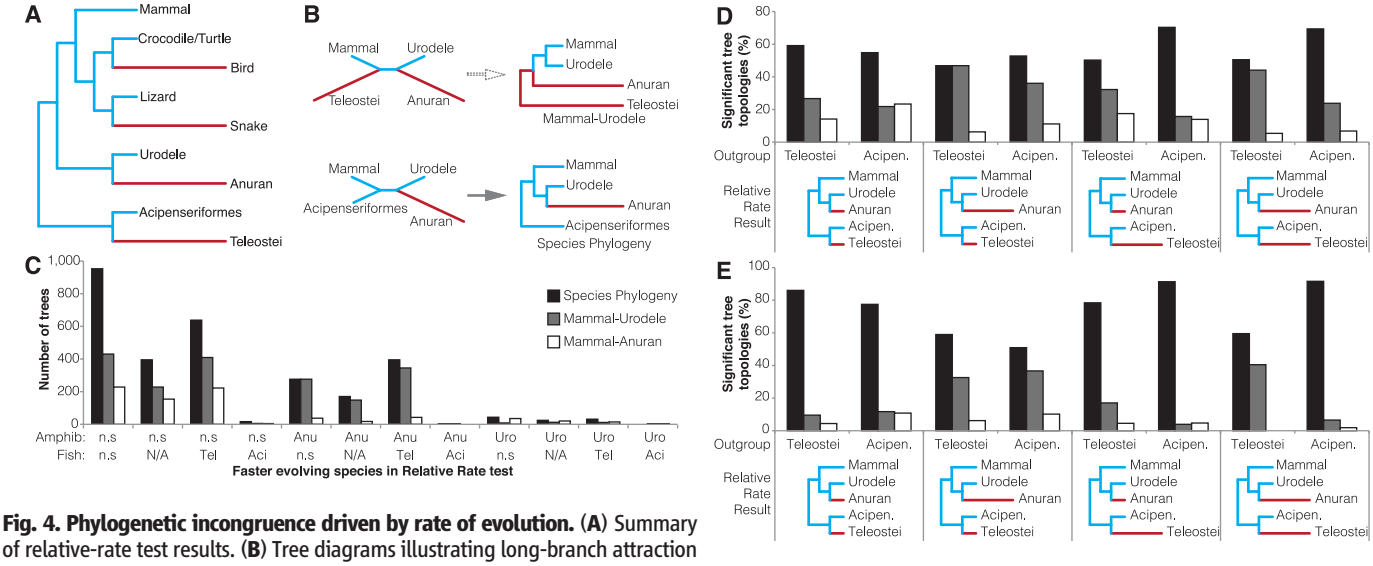

Fig. 4. Phylogenetic incongruence driven by rate of evolution. (**A**) Summary of relative-rate test results. (**B**) Tree diagrams illustrating long-branch attraction driven by outgroup choice in four-taxon trees. (**C**) Number of amphibian four-taxon tree topologies grouped by relative-rate differences between anurans and urodeles, and Teleostei and Acipenseriformes. n.s, not significant; N/A, not available; Anu, Anuran; Uro, Urodele; Tel, Telesotei; Aci, Acipenseriforme. (**D** and **E**) For the four common relative-rate test results between Amphibians and Actinopterygii, the proportions of Amphibian four-taxon tree topologies are shown when using Teleostei or Acipenseriforme outgroups. (D) Bootstrap trees. (E) SH test trees.

References and Notes

1. A. D. Johnson *et al.*, *Evol. Dev.* **5**, 414–431 (2003).
2. A. D. Johnson *et al.*, *Philos. Trans. R. Soc. Lond. B Biol. Sci.* **358**, 1371–1379 (2003).
3. B. I. Crother, M. E. White, A. D. Johnson, *J. Theor. Biol.* **248**, 322–330 (2007).
4. A. D. Johnson, E. Richardson, R. F. Bachvarova, B. I. Crother, *Reproduction* **141**, 291–300 (2011).
5. P. D. Nieuwkoop, L. A. Sutasurya, *Primordial Germ Cells in the Chordates, Embryogenesis and Phylogenesis* (Cambridge Univ. Press, Cambridge, 1979).
6. J. E. Dixon *et al.*, *Development* **137**, 2973–2980 (2010).
7. G. Swiers, Y. H. Chen, A. D. Johnson, M. Loose, *Dev. Biol.* **343**, 138–152 (2010).
8. H. G. Leitch, W. W. Tang, M. A. Surani, *Curr. Top. Dev. Biol.* **104**, 149–187 (2013).
9. S. Frankenberg, M. B. Renfree, *BMC Biol.* **11**, 56 (2013).
10. U. Hellsten *et al.*, *Science* **328**, 633–636 (2010).
11. M. Loose, R. Patient, *Dev. Biol.* **271**, 467–478 (2004).
12. X. Fan, S. T. Dougan, *Dev. Genes Evol.* **217**, 807–813 (2007).
13. E. Raz, *Nat. Rev. Genet.* **4**, 690–700 (2003).
14. Materials and methods are available as supplementary materials on *Science* Online.
15. R. F. Bachvarova, B. I. Crother, A. D. Johnson, *Evol. Dev.* **11**, 603–609 (2009).
16. R. F. Bachvarova *et al.*, *Evol. Dev.* **11**, 525–534 (2009).
17. J. Hubert, in *Biology of the Reptilia: Development A.*, C. Gans, F. Billet, P. F. A. Maderson, Eds. (John Wiley & Sons, New York, 1985), pp. 41–74.
18. N. Tsunekawa, M. Naito, Y. Sakai, T. Nishida, T. Noce, *Development* **127**, 2741–2750 (2000).
19. S. Hughes, D. Mouchiroud, *J. Mol. Evol.* **53**, 70–76 (2001).
20. S. B. Hedges, J. Dudley, S. Kumar, *Bioinformatics* **22**, 2971–2972 (2006).
21. Z. Wang *et al.*, *Nat. Genet.* **45**, 701–706 (2013).
22. L. M. Dávalos, A. L. Cirranello, J. H. Geisler, N. B. Simmons, *Biol. Rev. Camb. Philos. Soc.* **87**, 991–1024 (2012).
23. J. Roux, M. Robinson-Rechavi, *PLOS Genet.* **4**, e1000311 (2008).
24. M. J. Telford, R. R. Copley, *Curr. Biol.* **15**, R296–R299 (2005).

Acknowledgments: All data are available from the authors' Web site at www.nottingham.ac.uk/~plzloose/phyloinc and are deposited at http://datadryad.org (DOI:10.5061/dryad.rd70f). The authors thank B. Crother, G. Morgan, and M. Blythe for helpful discussion. Sequencing was carried out at the Genome Centre, Queen Mary, University of London by L. Bhaw-Rosun and M. Struegbig. This work was supported by the Biotechnology and Biological Sciences Research Council, Medical Research Council, and University of Nottingham.

Supplementary Materials

www.sciencemag.org/content/344/6180/200/suppl/DC1
Materials and Methods
Supplementary Text
Figs. S1 to S10
Tables S1 to S13
References (*25*–*78*)

4 December 2013; accepted 18 March 2014
10.1126/science.1249325

PINK1 Loss-of-Function Mutations Affect Mitochondrial Complex I Activity via NdufA10 Ubiquinone Uncoupling

Vanessa A. Morais,[1,2]* Dominik Haddad,[1,2] Katleen Craessaerts,[1,2] Pieter-Jan De Bock,[3,4] Jef Swerts,[1,2] Sven Vilain,[1,2] Liesbeth Aerts,[1,2] Lut Overbergh,[5] Anne Grünewald,[6] Philip Seibler,[6] Christine Klein,[6,7] Kris Gevaert,[3,4] Patrik Verstreken,[1,2] Bart De Strooper[1,2,8]*

Under resting conditions, *Pink1* knockout cells and cells derived from patients with *PINK1* mutations display a loss of mitochondrial complex I reductive activity, causing a decrease in the mitochondrial membrane potential. Analyzing the phosphoproteome of complex I in liver and brain from *Pink1*$^{-/-}$ mice, we found specific loss of phosphorylation of serine-250 in complex I subunit NdufA10. Phosphorylation of serine-250 was needed for ubiquinone reduction by complex I. Phosphomimetic NdufA10 reversed Pink1 deficits in mouse knockout cells and rescued mitochondrial depolarization and synaptic transmission defects in *pink*^{B9}-null mutant *Drosophila*. Complex I deficits and adenosine triphosphate synthesis were also rescued in cells derived from PINK1 patients. Thus, this evolutionary conserved pathway may contribute to the pathogenic cascade that eventually leads to Parkinson's disease in patients with PINK1 mutations.

Mutations in PINK1, a mitochondrial targeted Ser/Thr kinase, cause a monogenic form of Parkinson's disease (PD) (*1*, *2*). Loss of *PINK1* function mutations interfere with Parkin-mediated carbonyl cyanide m-chlorophenyl hydrazone (CCCP)–induced mitophagy (*3*–*5*) and mitochondrial fusion and fission defects (*4*). However, an early and invariant phenotype of PINK1 loss of function in different species is an enzymatic defect in mitochondrial complex I and a decrease in mitochondrial membrane potential ($\Delta\psi_m$) (*6*–*8*). In contrast to effects of PINK1 on toxin-induced mitophagy like CCCP (*4*, *5*, *9*), these complex I defects are observed in cell culture and *Drosophila* neurons under resting conditions with normal-appearing mitochondria (*6*, *8*). Because *Pink1*$^{-/-}$ mice display only subtle, and somewhat controversial, phenotypes of altered mitochondrial morphology (*6*, *8*, *10*, *11*), it remains unresolved to what extent decreased mitophagy, or, alternatively, primary complex I deficiency, or both, are involved in those defects (*6*). In *pink1* and *parkin Drosophila* models (*12*–*14*), phenotypes are more pronounced. Thorax muscle degeneration and flight deficits can be rescued by expression of the fission-promoting gene *drp1* or by ablating the fusion-promoting gene *opa1* (*15*, *16*), linking these molecules to the role of PINK1 and Parkin in fusion and fission defects. Intriguingly, other *pink1*-related phenotypes, such as defective neurotransmitter release, adenosine triphosphate (ATP) depletion, and loss of $\Delta\psi_m$, cannot be rescued efficiently in *Drosophila* neurons by fission gene *Drp1 (17, 18)* but can be rescued by genes restoring the proton motive force (*19*) or by NDi1, a yeast rotenone-insensitive reduced form of nicotinamide adenine dinucleotide (NADH)–quinone oxidoreductase (*17*). This suggests that two parallel molecular pathways are affected by *pink1* deficiency in flies, and both could be relevant to our understanding of the role of PINK1 in PD.

First, we confirmed the pathological relevance of the previously reported $\Delta\psi_m$ defects in *Pink1*$^{-/-}$ mice and *Drosophila* using human fibroblasts and two induced pluripotent stem (iPS) cell lines derived from PD patients with PINK1 mutations. Fibroblasts contained homozygous p.Q456X nonsense (L2122) or p.V170G missense (L1703) mutations (*20*), and iPS cells were derived from two PD patients with c.1366C>T; p.Q456X nonsense (L2122 and L2124) mutations. Integrity of the mitochondrial-targeted red fluorescent protein–labeled mitochondrial network was qualitatively and quantitatively (fragmented versus elongated) not different between control (L2134 and L2132) and patient (L1703 and L2122) fibroblasts (fig. S1, A and B). $\Delta\psi_m$ was significantly decreased in the patient fibroblasts as assessed by the electrochemical potentiometric dye tetramethyl rhodamine ethyl ester (TMRE) (fig. S1, C and D). Overall ATP content in these PINK1 mutant fibroblasts was also decreased when compared with age-matched controls (fig. S1E) (*20*). In neuronal differentiated iPS cells (L2124 and L2122) (*21*), $\Delta\psi_m$ and ATP content (fig. S1, F to H) were lowered compared with controls (L2134 and L2135), confirming that clinical mutations in the context of human cells and human neurons display similar deficits as cell lines derived from Pink1-null mice and flies.

Cells display a specific deficit in the enzymatic activity of complex I (*6*). Therefore, we immunocaptured complex I from isolated mouse mitochondria (Fig. 1, A and B) and obtained independent phosphoproteomes from three brain and three liver

[1]VIB Center for the Biology of Disease, 3000 Leuven, Belgium. [2]Center of Human Genetics, University Hospitals Leuven and Department of Human Genetics, KU Leuven, and Leuven Research Institute for Neuroscience and Disease (LIND), 3000 Leuven, Belgium. [3]Department of Medical Protein Research, VIB, 9000 Ghent, Belgium. [4]Department of Biochemistry, Ghent University, 9000 Ghent, Belgium. [5]Laboratory of Clinical and Experimental Endocrinology, KU Leuven, 3000 Leuven, Belgium. [6]Section of Clinical and Molecular Neurogenetics at the Department of Neurology, University of Lübeck, 23538 Lübeck, Germany. [7]Wellcome Trust Centre for Mitochondrial Research, Institute of Ageing and Health, Newcastle University, Newcastle upon Tyne NE2 4HH, UK. [8]University College London, Institute of Neurology, Queen Square, London, UK.

*Corresponding author. E-mail: bart.destrooper@cme.vib-kuleuven.be (B.D.S.); vanessa.morais@cme.vib-kuleuven.be (V.A.M.)

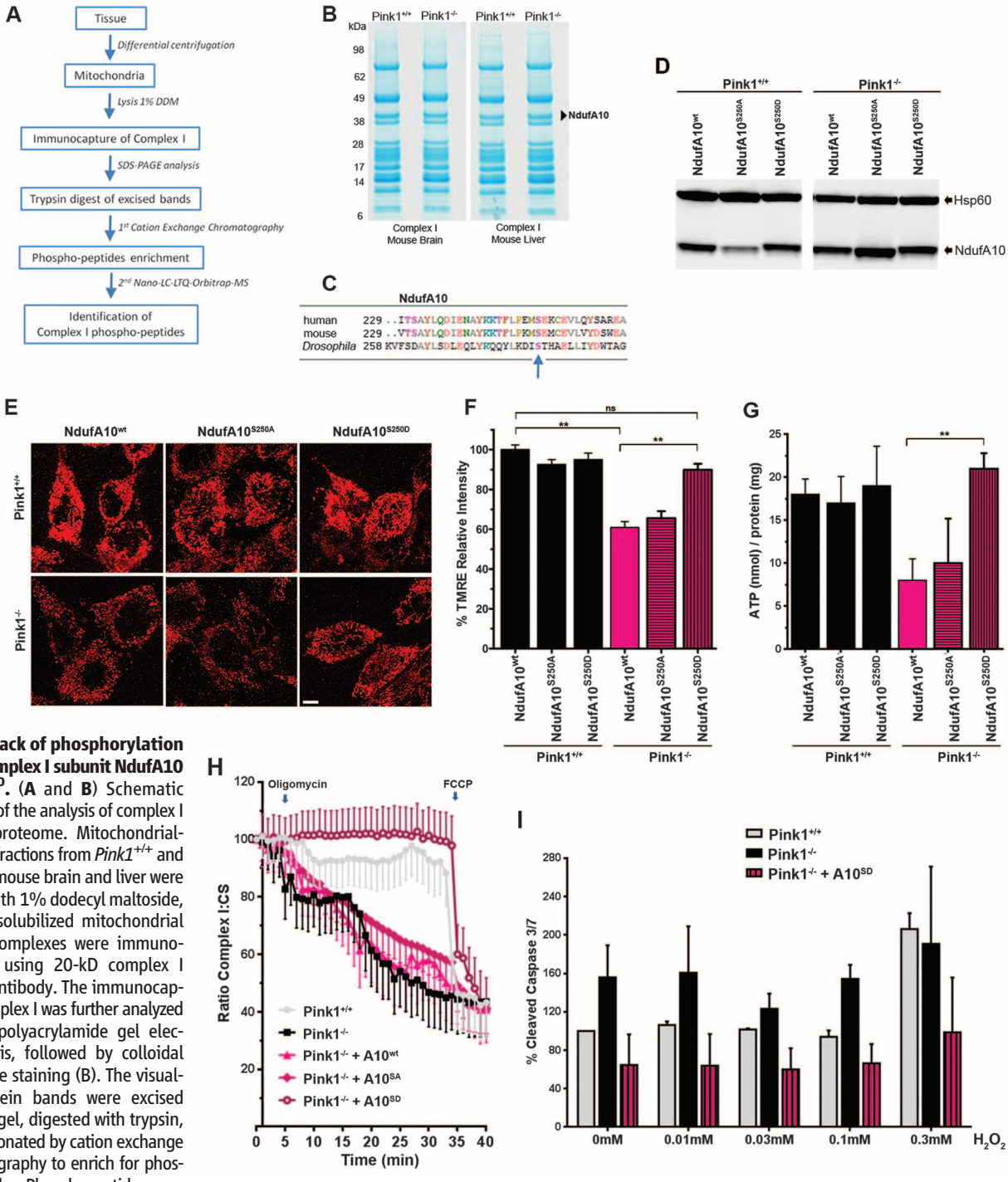

Fig. 1. Lack of phosphorylation of the complex I subunit NdufA10 at Ser^{250}. (**A** and **B**) Schematic overview of the analysis of complex I phosphoproteome. Mitochondrial-enriched fractions from *Pink1*$^{+/+}$ and *Pink1*$^{-/-}$ mouse brain and liver were treated with 1% dodecyl maltoside, and the solubilized mitochondrial protein complexes were immunocaptured using 20-kD complex I subunit antibody. The immunocaptured complex I was further analyzed on SDS–polyacrylamide gel electrophoresis, followed by colloidal Coomassie staining (B). The visualized protein bands were excised from the gel, digested with trypsin, and fractionated by cation exchange chromatography to enrich for phosphopeptides. Phosphopeptides were further analyzed by liquid chromatography–mass spectrometry on a Nano-LC-LTQ-Orbitrap-MS. (**C**) Alignment of human, mouse, and *Drosophila* NdufA10 revealed that the identified PINK1-dependent phosphoserine (in magenta) is conserved across species. (**D**) *Pink1*$^{+/+}$ and *Pink1*$^{-/-}$ MEFs were stably transduced with 3xFLAG-tagged wild-type NdufA10^{wt}, phosphorylation-deficient NdufA10^{S250A}, and phosphomimetic NdufA10^{S250D}. Expression levels were analyzed by immunoblotting of mitochondria-enriched fractions using antibodies to FLAG and Hsp60 (loading control). (**E**, **F**, and **G**) Phosphomimetic NdufA10^{S250D} restores the mitochondrial membrane potential and ATP levels in *Pink1*$^{-/-}$ MEFs. Cells were stably transduced with NdufA10 constructs as indicated and loaded with 10 nM TMRE (E), and quantification of TMRE intensity (F) over mitochondrial regions of interest was performed using ImageJ software. ATP levels were measured in cell lysates (G). Statistical analysis: Student's *t* test; **, $P < 0.01$; ns, not significant; mean ± SD; $n = 100$. Scale bar, 10 μm. (**H**) Live imaging of $\Delta\psi_m$ reveals that phosphomimetic NdufA10^{S250D} restores the mitochondrial membrane potential. Pink1$^{+/+}$, Pink1$^{-/-}$, and Pink1$^{-/-}$ expressing the phosphomimetic NdufA10 mutants' fibroblast cells were loaded with 10 nM TMRM in the presence of 2 μg/ml cyclosporine H. Sequential images of TMRM fluorescence were acquired every 60 s over a 40-min time course. TMRM fluorescence over mitochondrial regions of interest was measured. When indicated (arrows), 2 μg/ml oligomycin (an ATP synthase inhibitor) and 2 μM carbonyl cyanide 4-trifluoromethoxyphenylhydrazone (an uncoupler) were added. Mean ± SD; $n = 5$ independent experiments. (**I**) Phosphomimetic NdufA10 mutant protects Pink1-devoid cells from H_2O_2-induced apoptosis. Pink1$^{+/+}$, Pink1$^{-/-}$, and Pink1$^{-/-}$ fibroblasts expressing the phosphomimetic NdufA10 mutants were treated with increasing concentrations of H_2O_2, and after 4 hours apoptosis was determined using the luminescent cleaved Caspase-Glo 3/7 assay. Mean ± SD; $n = 3$ independent experiments.

preparations, covering 40 out of the 46 complex I subunits (table S1). Nine previously unknown phosphosites were identified (table S2), but they were present both in Pink1-deficient and wild-type tissue. Only Ser^{250} in complex I subunit NdufA10 (Fig. 1C and table S2) was lacking in knock-out material. In contrast, the unphosphorylated peptide was identified in three out of the six knock-out samples (fig. S2). The Ser^{250} is conserved from *Drosophila* to human, suggesting that it is functionally important (Fig. 1C). Consistent with this notion, stable transfection of phosphomimetic $NdufA10^{S250D}$ or wild-type $NdufA10^{wt}$, but not phosphorylation-deficient $NdufA10^{S250A}$, rescued the complex I activity defect in *NdufA10*-deficient HeLa cells (fig. S3, A and B).

To assess the role of this site in the context of Pink1, we stably transfected $Pink1^{+/+}$ and $Pink1^{-/-}$ mouse embryonic fibroblasts (MEFs) with $NdufA10^{wt}$, $NdufA10^{S250A}$, and $NdufA10^{S250D}$ (Fig. 1D). Although the defect in $\Delta\psi_m$ assessed by TMRE labeling was not rescued with $NdufA10^{wt}$ or $NdufA10^{S250A}$, $NdufA10^{S250D}$ completely restored $\Delta\psi_m$ and ATP levels (Fig. 1, E to G). No effects on $\Delta\psi_m$ were observed in $Pink1^{+/+}$ MEFs expressing the NdufA10 mutants (Fig. 1, E to G). Real-time imaging of $\Delta\psi_m$ with tetramethylrhodamine methyl ester (TMRM) further corroborated that $NdufA10^{S250D}$ restored this defect (Fig. 1H). Additionally, $NdufA10^{S250D}$ appeared to exert a protective effect toward previously reported susceptibility of $Pink1^{-/-}$ mutant cells to H_2O_2-induced apoptosis (Fig. 1I). Thus, a phosphomimetic mutation at Ser^{250} in NdufA10 is sufficient to restore the defect in $\Delta\psi_m$ in $Pink1^{-/-}$ mutant cells.

To study the physiological relevance of the PINK1-dependent phosphorylation event, we assessed to what extent *Drosophila pink1* mutant phenotypes could be rescued by expression of wild-type ($A10^{wt}$), phosphorylation-deficient ($A10^{SA}$), or phosphomimetic ($A10^{SD}$) NdufA10. We focused first on phenotypes dependent on complex I deficiency. $Pink1^{B9}$-null mutant *Drosophila* failed to maintain neurotransmitter release at neuromuscular junctions (NMJ) during high-frequency stimulation (10 Hz) (fig. S4A) (*6*), a defect that was fully rescued when expressing $A10^{SD}$ but not with $A10^{wt}$ or $A10^{SA}$ (Fig. 2A). Basal neurotransmitter release was not affected under the conditions tested (Fig. 2B). This deficit is caused by a defect in reserve pool (RP) vesicle mobilization (*6*), which can be assessed using FM 1-43, a lipophilic dye that labels these vesicles. Deficient loading of the RP vesicles was rescued upon expression of $A10^{SD}$ in $pink1^{B9}$ flies (Fig. 2C and fig. S4B) but not with $A10^{wt}$ or $A10^{SA}$. This phenotype was ATP dependent and was caused by a loss of $\Delta\psi_m$ in the mitochondria at the NMJ as assessed with JC-1, a green fluorescent potentiometric dye that shifts to red fluorescence as a function of a normal negative $\Delta\psi_m$ (*22*). Synaptic mitochondria of $pink1^{B9}$ mutants expressing $A10^{SD}$ showed red JC-1 aggregates comparable to control (Fig. 2D and fig. S4C), indicating restoration of the $\Delta\psi_m$, whereas $A10^{wt}$ or $A10^{SA}$ displayed similar weak signals as the $pink1^{B9}$ mutant. Also, ATP synthesis was restored upon expression of $A10^{SD}$ (Fig. 2F). $\Delta\psi_m$ was not disturbed in control $pink1^{rev}$ NMJs expressing NdufA10 mutants (fig. S5, A and B). Thus, the synaptic phenotype in $pink1^{B9}$ flies was significantly rescued by $A10^{SD}$. $Pink1^{B9}$ flies also show severe muscle degeneration and flight defects (*12*, *13*). These phenotypes were not rescued upon $A10^{SD}$ expression, suggesting that most likely they are linked to other PINK1 functions (fig. S5, C and D). Also, CCCP-induced Parkin recruitment was not restored in $Pink1^{-/-}$ cells expressing the

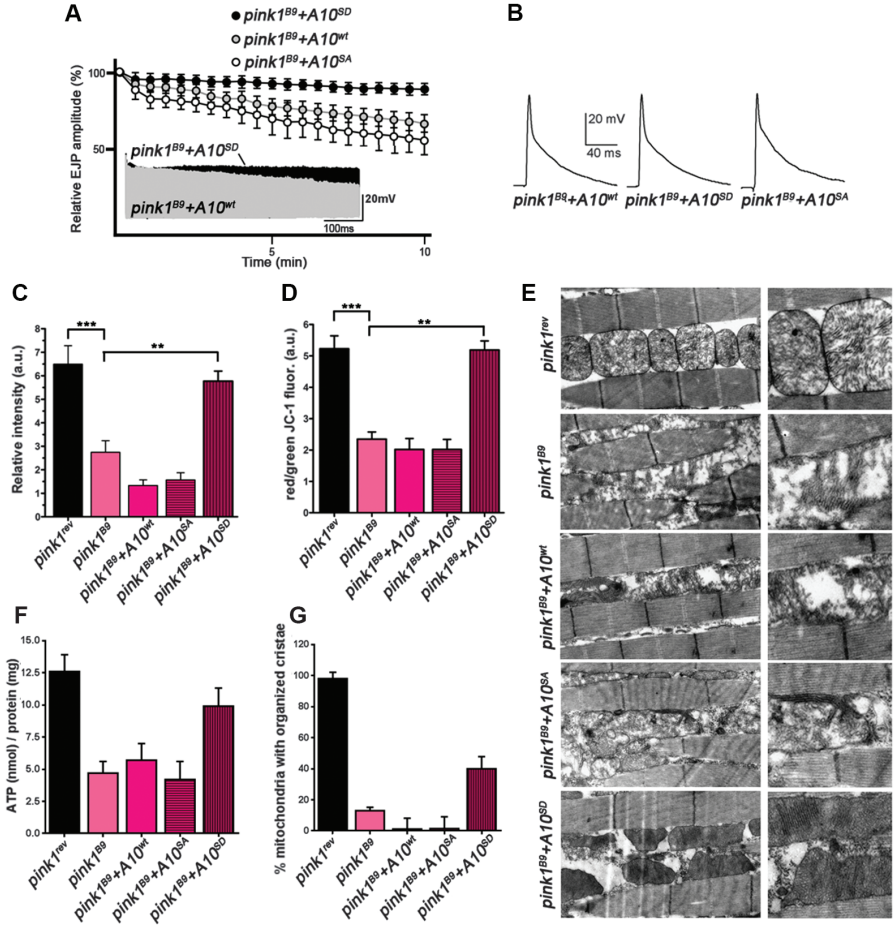

Fig. 2. Restoration of synaptic defects in *Drosophila pink1*^{B9} null mutants by expressing phosphomimetic NdufA10. (**A**) Relative excitatory junction potentials (EJPs) amplitudes measured in 2-mM Ca^{2+} during 10 min of 10-Hz stimulation in $pink1^{B9}$-null mutants expressing wild-type ($A10^{wt}$), phosphodeficient ($A10^{SA}$), and phosphomimetic ($A10^{SD}$) NdufA10 mutants. Inset represents an overlay of a raw data trace of EJPs recorded for 10 min at 10 Hz in 2-mM calcium of $pink1^{B9}$+$A10^{SD}$ (black) and $pink1^{B9}$+$A10^{wt}$ (gray). The deficit to maintain normal EJP amplitude during a 10-Hz stimulation train observed in $pink1^{B9}$ mutant expressing $A10^{wt}$ is restored when phosphomimetic $A10^{SD}$ is present. Mean ± SEM; n = 4 larvae for $A10^{wt}$, 7 for $A10^{SA}$, and 8 for $A10^{SD}$. (**B**) Traces of basal neurotransmitter release measured at 1 Hz in 2-mM Ca^{2+} in $pink1^{B9}$-null mutants expressing NdufA10 mutants. The average EJP amplitudes recorded are $pink1^{B9}$+$A10^{wt}$, 56.4 ± 1.9 mV; $pink1^{B9}$+$A10^{SA}$, 52.4 ± 2.1 mV; and $pink1^{B9}$+$A10^{SD}$, 57.0 ± 3.3 mV. Basal neurotransmitter release is not affected in $pink1^{B9}$ larvae expressing the NdufA10 mutants. (**C**) RP labeling at *Drosophila* larval NMJs in controls ($pink1^{REV}$) and *pink1* mutants ($pink1^{B9}$). Both the exo/endo cycling pool (ECP) and RP were labeled with FM1-43; after depolarization, only ECP vesicles, but not RP vesicles, were unloaded. Synapses were imaged after this unloading procedure. Quantification of fluorescence intensity of loaded RP vesicles was normalized to loading intensity of controls. The loading defect in $pink1^{B9}$ is restored upon expression of phosphomimetic NdufA10. (**D**) Quantification of mitochondrial membrane potential at NMJ boutons in controls ($pink1^{REV}$) and *pink1* mutants ($pink1^{B9}$) using the ratiometric dye JC-1, where the red JC-1 fluorescence emission to green emission (in the same area) is compared. The mitochondrial membrane potential was restored upon expression of phosphomimetic NdufA10. (**F**) Analysis of ATP levels in these mutant flies where decreased ATP content is restored in mutant flies expressing the phosphomimetic $A10^{SD}$. (**E** and **G**) Electron micrographs [(E), inset in right column] and corresponding quantification of mitochondria that have organized cristae independently of overall mitochondrial morphology (E) of adult fly muscle in controls ($pink1^{REV}$) and *pink1* mutants ($pink1^{B9}$) showing that cristae organization is partially restored in mutant flies expressing $A10^{SD}$. Statistical analysis: Student's t test; ***P < 0.001; **P < 0.01; *P < 0.05; mean ± SD; n = 8 larvae. Scale bar, 4.5 μm.

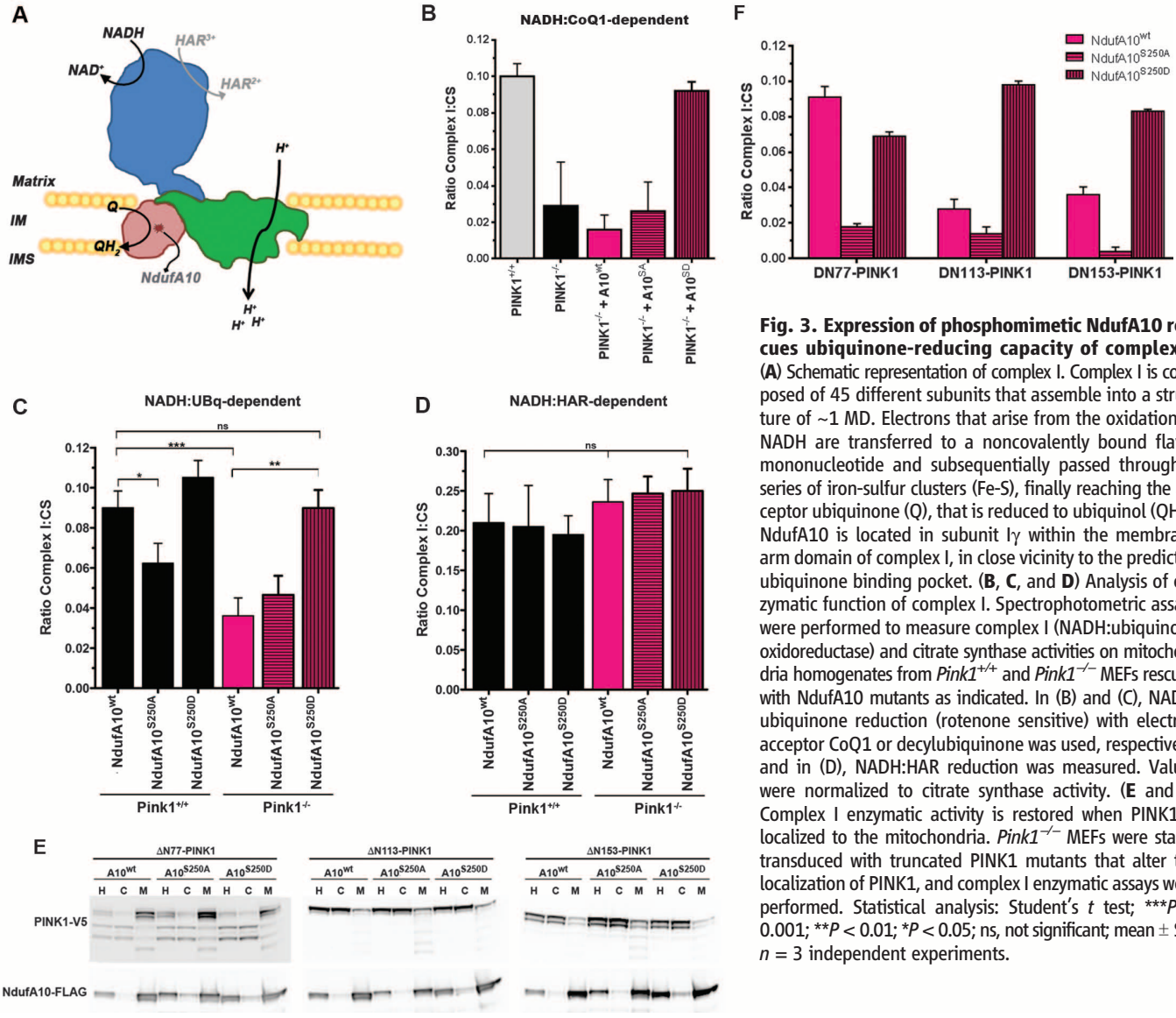

Fig. 3. Expression of phosphomimetic NdufA10 rescues ubiquinone-reducing capacity of complex I. (**A**) Schematic representation of complex I. Complex I is composed of 45 different subunits that assemble into a structure of ~1 MD. Electrons that arise from the oxidation of NADH are transferred to a noncovalently bound flavin mononucleotide and subsequentially passed through a series of iron-sulfur clusters (Fe-S), finally reaching the acceptor ubiquinone (Q), that is reduced to ubiquinol (QH_2). NdufA10 is located in subunit Iγ within the membrane arm domain of complex I, in close vicinity to the predicted ubiquinone binding pocket. (**B**, **C**, and **D**) Analysis of enzymatic function of complex I. Spectrophotometric assays were performed to measure complex I (NADH:ubiquinone oxidoreductase) and citrate synthase activities on mitochondria homogenates from *Pink1*$^{+/+}$ and *Pink1*$^{-/-}$ MEFs rescued with NdufA10 mutants as indicated. In (B) and (C), NADH: ubiquinone reduction (rotenone sensitive) with electron acceptor CoQ1 or decylubiquinone was used, respectively, and in (D), NADH:HAR reduction was measured. Values were normalized to citrate synthase activity. (**E** and **F**) Complex I enzymatic activity is restored when PINK1 is localized to the mitochondria. *Pink1*$^{-/-}$ MEFs were stably transduced with truncated PINK1 mutants that alter the localization of PINK1, and complex I enzymatic assays were performed. Statistical analysis: Student's *t* test; ***$P < 0.001$; **$P < 0.01$; *$P < 0.05$; ns, not significant; mean ± SD; $n = 3$ independent experiments.

phosphomimetic NdufA10^{S250D} mutant (fig. S5E), possibly ruling out an effect of NdufA10 on the mitophagy pathway. We investigated more closely the mitochondria in the flight muscles by performing electron microscopy. A10^{SD} improved cristae structural organization without rescuing overall mitochondria morphology (Fig. 2, E and G). Thus, the muscular degeneration in *Drosophila* appears to be mainly the result of mitochondrial fusion and fission defects caused by PINK1 deficiency (*16*); however, restoring complex I enzymatic activity aids cristae organization leading to improved bioenergetics but does not improve the mitochondria morphology or the muscular degeneration.

NdufA10 is located in subunit Iγ of complex I in close vicinity to the ND1 and ND3 subunits (*23*, *24*). We hypothesized that the identified phosphorylation site on NdufA10 could structurally influence the ubiquinone binding cavity. We performed enzymatic assays for complex I to assess the reduction of coenzyme Q1 (CoQ1) and decylubiquinone, a ubiquinone analog (Fig. 3A). Reduction of both electron acceptors, CoQ1 and decylubiquinone, was significantly affected in complex I prepared from *Pink1*$^{-/-}$ MEFs expressing NdufA10^{wt} but was restored with NdufA10^{S250D} (Fig. 3, B and C). The effect on complex I was specific for its ubiquinone reductase enzymatic function because another enzymatic assay that employs only the NADH-binding site of complex I, which is based on the reduction of the artificial substrate hexammineruthenium (HAR) (*25*) (Fig. 3A), was not affected in *Pink1*$^{-/-}$ cells or in *Pink1*$^{-/-}$-expressing NdufA10 mutants (Fig. 3D). Thus, NdufA10 is required for the binding and/or reduction of the physiological complex I substrate ubiquinone.

To determine whether PINK1 needs to be targeted to mitochondria to facilitate NdufA10 activity, we introduced PINK1 truncated mutants into the *Pink1*$^{-/-}$ MEFs (Fig. 3E). Amino acids between position 77 and 112 are sufficient to target PINK1 to the mitochondria (*26*). PINK1-ΔN77 was indeed targeted to the mitochondria, whereas the ΔN113 and ΔN153 were mainly present in non-mitochondrial fractions (Fig. 3E). Only ΔN77 restored complex I enzymatic activity (Fig. 3F). This and the association of PINK1 with the inner mitochondrial membrane, as shown with proteinase K protection assays and the extraction with sodium carbonate (fig. S6 and fig. S7, A and B), suggests that PINK1 needs to be targeted to the mitochondria to activate NdufA10, although more complex scenarios cannot be ruled out.

We finally investigated whether *Pink1*$^{-/-}$ cells expressing human wild-type or *PINK1* containing PD-causing mutations could be rescued with NdufA10^{S250D} (fig. S8A). NdufA10^{S250D} was able to restore fully the decylubiquinone reduction reaction in complex I from cells expressing PINK1 clinical mutants G309D and W437X or the artificial kinase inactive (KD) PINK1 mutant (Fig. 4A). Furthermore, $\Delta\psi_m$ was fully restored upon NdufA10^{S250D} expression in the cells expressing the PD-causing mutations (Fig. 4B).

We electroporated fibroblasts derived from *PINK1*-mutant patients and controls (fig. S1) with

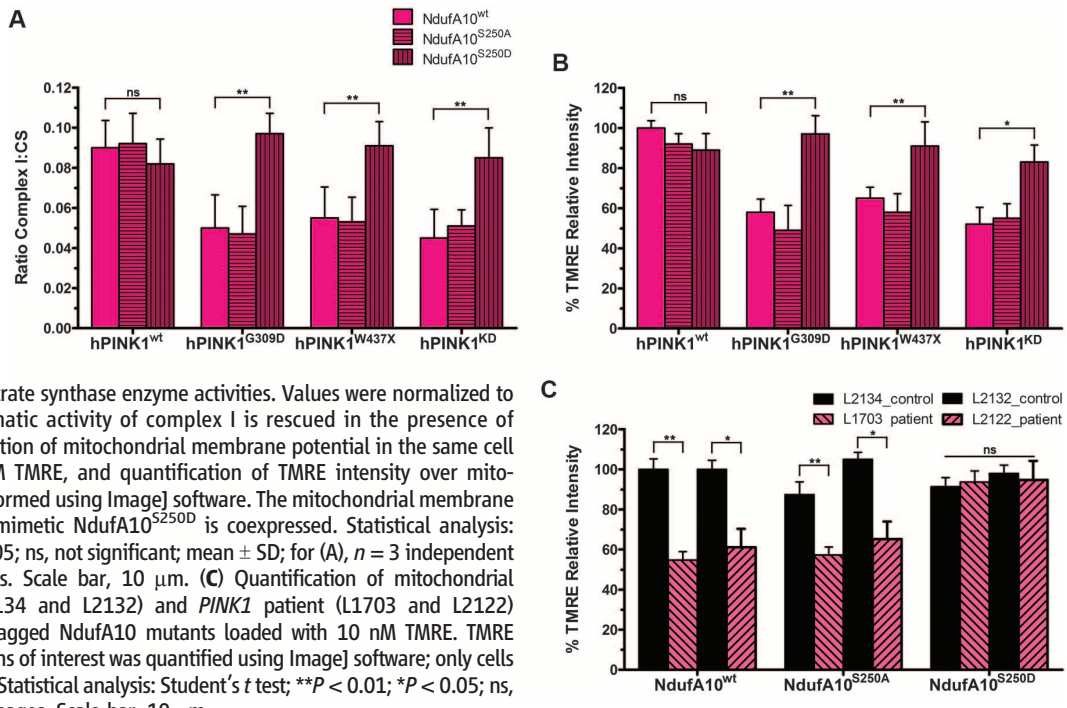

Fig. 4. Restoration of mitochondrial membrane potential deficits caused by PINK1 PD-causing mutations. (**A**) Respiratory chain measurements performed on mitochondria homogenates from *Pink1*$^{-/-}$ MEFs rescued with human PINK1 wild-type (wt) or PD-causing mutants or artificial kinase dead mutant (KD). The cells were stably transduced with NdufA10 phosphomimetic mutants and analyzed by spectrophotometric assays of complex I (NADH:ubiquinone oxidoreductase, rotenone sensitive) and citrate synthase enzyme activities. Values were normalized to citrate synthase activity. The enzymatic activity of complex I is rescued in the presence of NdufA10^{S250D} mutant. (**B**) Quantification of mitochondrial membrane potential in the same cell lines. Cells were loaded with 10 nM TMRE, and quantification of TMRE intensity over mitochondrial regions of interest was performed using ImageJ software. The mitochondrial membrane potential is restored when phosphomimetic NdufA10^{S250D} is coexpressed. Statistical analysis: Student's *t* test; **, $P < 0.01$; *, $P < 0.05$; ns, not significant; mean ± SD; for (A), $n = 3$ independent experiments; for (B), $n = 70$ images. Scale bar, 10 μm. (**C**) Quantification of mitochondrial membrane potential in control (L2134 and L2132) and *PINK1* patient (L1703 and L2122) fibroblasts electroporated with GFP-tagged NdufA10 mutants loaded with 10 nM TMRE. TMRE fluorescence over mitochondrial regions of interest was quantified using ImageJ software; only cells that were GFP positive were analyzed. Statistical analysis: Student's *t* test; **$P < 0.01$; *$P < 0.05$; ns, not significant; mean ± SD; $n = 80$ images. Scale bar, 10 μm.

green fluorescent protein (GFP)–tagged forms of the NdufA10 mutants, and the $\Delta\psi_m$ was rescued as assessed by TMRE in the patient-derived fibroblasts expressing GFP and NdufA10^{S250D} but not in those expressing NdufA10^{wt} or NdufA10^{S250A} (Fig. 4C). Thus, restoration of the pseudophosphorylation status of NdufA10 rescues complex I activity in cells harboring PD-causing mutations in *PINK1*.

Phosphorylation of Ser^{250} in NdufA10 regulates the ubiquinone reductase ability of complex I. Crystal structures from complex I reveal that subunits NdufS2 and NdufS7 are involved in electron donation to ubiquinone (*27*, *28*) and that contacts between the peripheral arm and membrane domain of complex I are mediated by NdufS2, ND1, and ND3, leading to the formation of a cavity capable of harboring the large hydrophobic substrate ubiquinone (*23*, *29*). NdufA10 is located close to ND1 and ND3; therefore, phosphorylation of this site could regulate the interaction of complex I with ubiquinone. Vitamin K_2, an alternative electron carrier for ubiquinone, can rescue the *pink1*^{B9} mutant phenotype in *Drosophila (19)*, in agreement with this hypothesis. Although the most parsimonious explanation for our observations is that PINK1 phosphorylates NdufA10, we have not been able to demonstrate such activity directly and therefore cannot rule out an indirect effect of PINK1 on this site. Nonetheless, our findings provide a molecular link between PINK1 dysfunction and activity of complex I. We conclude that PINK1 has dual functions in mitochondrial homeostasis. Under steady-state conditions, PINK1 is needed to maintain complex I and electron transport chain (ETC) activity. The clinical mutations create a latent situation where this phosphorylation is affected and ETC function becomes destabilized, as shown here under steady-state culture conditions. When additional stress is exerted—for example, in the presence of CCCP or other mitochondrial toxins—defects in mitophagy are also observed (*30*). Such a multiple-hit hypothesis for familial PD makes sense given the relatively late onset of the disease. Rescuing complex I activity by activating phosphorylation or inhibiting dephosphorylation of NdufA10 at residue Ser^{250} could thus potentially prevent or partially attenuate the disease.

References and Notes

1. E. M. Valente *et al.*, *Science* **304**, 1158–1160 (2004).
2. E. M. Valente *et al.*, *Ann. Neurol.* **56**, 336–341 (2004).
3. D. P. Narendra *et al.*, *PLOS Biol.* **8**, e1000298 (2010).
4. R. J. Youle, D. P. Narendra, *Nat. Rev. Mol. Cell Biol.* **12**, 9–14 (2011).
5. D. P. Narendra, R. J. Youle, *Antioxid. Redox Signal.* **14**, 1929–1938 (2011).
6. V. A. Morais *et al.*, *EMBO Mol. Med.* **1**, 99–111 (2009).
7. A. Y. Abramov *et al.*, *PLOS ONE* **6**, e25622 (2011).
8. C. A. Gautier, T. Kitada, J. Shen, *Proc. Natl. Acad. Sci. U.S.A.* **105**, 11364–11369 (2008).
9. D. Narendra, L. A. Kane, D. N. Hauser, I. M. Fearnley, R. J. Youle, *Autophagy* **6**, 1090–1106 (2010).
10. N. Exner *et al.*, *J. Neurosci.* **27**, 12413–12418 (2007).
11. A. K. Lutz *et al.*, *J. Biol. Chem.* **284**, 22938–22951 (2009).
12. J. Park *et al.*, *Nature* **441**, 1157–1161 (2006).
13. I. E. Clark *et al.*, *Nature* **441**, 1162–1166 (2006).
14. Y. Yang *et al.*, *Proc. Natl. Acad. Sci. U.S.A.* **103**, 10793–10798 (2006).
15. H. Deng, M. W. Dodson, H. Huang, M. Guo, *Proc. Natl. Acad. Sci. U.S.A.* **105**, 14503–14508 (2008).
16. Y. Yang *et al.*, *Proc. Natl. Acad. Sci. U.S.A.* **105**, 7070–7075 (2008).
17. S. Vilain *et al.*, *PLOS Genet.* **8**, e1002456 (2012).
18. W. Liu *et al.*, *Proc. Natl. Acad. Sci. U.S.A.* **108**, 12920–12924 (2011).
19. M. Vos *et al.*, *Science* **336**, 1306–1310 (2012).
20. A. Grünewald *et al.*, *Exp. Neurol.* **219**, 266–273 (2009).
21. P. Seibler *et al.*, *J. Neurosci.* **31**, 5970–5976 (2011).
22. P. Verstreken *et al.*, *Neuron* **47**, 365–378 (2005).
23. R. G. Efremov, R. Baradaran, L. A. Sazanov, *Nature* **465**, 441–445 (2010).
24. R. J. Janssen, L. G. Nijtmans, L. P. van den Heuvel, J. A. Smeitink, *J. Inherit. Metab. Dis.* **29**, 499–515 (2006).
25. V. D. Sled, A. D. Vinogradov, *Biochim. Biophys. Acta* **1141**, 262–268 (1993).
26. L. Silvestri *et al.*, *Hum. Mol. Genet.* **14**, 3477–3492 (2005).
27. L. A. Sazanov, P. Hinchliffe, *Science* **311**, 1430–1436 (2006).
28. J. M. Berrisford, L. A. Sazanov, *J. Biol. Chem.* **284**, 29773–29783 (2009).
29. M. A. Tocilescu, V. Zickermann, K. Zwicker, U. Brandt, *Biochim. Biophys. Acta* **1797**, 1883–1890 (2010).
30. N. Matsuda *et al.*, *J. Cell Biol.* **189**, 211–221 (2010).

Acknowledgments: This work was supported by the Fund for Scientific Research Flanders (FWO); research fund KU Leuven; the Hercules Foundation, Federal Office for Scientific Affairs (IAP P7/16); a Methusalem grant of the Flemish Government, VIB, Agentschap voor Innovatie door Wetenschap en Technologie (IWT), the European Research Council (ERC StG and AdG to P.V. and B.D.S.); the Queen Elisabeth Foundation; the Hermann and Lilly Schilling Foundation (to C.K.); the Deutsche Forschungsgemeinschaft (to A.G. and to C.K.); the Fritz Thyssen Foundation (to A.G.); and the StemBANCC consortium (to C.K.). B.D.S. is the Arthur Bax and Anna Vanluffelen chair for Alzheimer's disease. S.V. is supported by an FWO postdoctoral fellowship, and L.A. is supported by an IWT predoctoral fellowship. B.D.S., V.A.M., and P.V. are the inventors on a patent application comprising diagnostic assays measuring the phosphorylation status of NdufA10 and screening methods for compounds able to restore or increase the phosphorylation of NdufA10. B.D.S. is a paid consultant for the Alzheimer's disease research programs at Janssen Pharmaceutica, Envivo, and Remynd NV. The data reported in this paper are tabulated in the main paper and in the supplementary materials.

Supplementary Materials

www.sciencemag.org/content/344/6180/203/suppl/DC1
Materials and Methods
Figs. S1 to S8
Tables S1 and S2
References (*31*–*40*)

2 December 2013; accepted 11 March 2014
Published online 20 March 2014;
10.1126/science.1249161

Mapping the Cellular Response to Small Molecules Using Chemogenomic Fitness Signatures

Anna Y. Lee,[1,2]* Robert P. St.Onge,[3]* Michael J. Proctor,[3] Iain M. Wallace,[1] Aaron H. Nile,[4] Paul A. Spagnuolo,[5] Yulia Jitkova,[6] Marcela Gronda,[6] Yan Wu,[6] Moshe K. Kim,[7,8] Kahlin Cheung-Ong,[1,2] Nikko P. Torres,[1,7] Eric D. Spear,[9] Mitchell K. L. Han,[10] Ulrich Schlecht,[3] Sundari Suresh,[3] Geoffrey Duby,[11] Lawrence E. Heisler,[1] Anuradha Surendra,[1] Eula Fung,[3] Malene L. Urbanus,[2] Marinella Gebbia,[1] Elena Lissina,[1,2] Molly Miranda,[3] Jennifer H. Chiang,[12] Ana Maria Aparicio,[3] Mahel Zeghouf,[13] Ronald W. Davis,[3] Jacqueline Cherfils,[13] Marc Boutry,[11] Chris A. Kaiser,[9] Carolyn L. Cummins,[10] William S. Trimble,[7,8] Grant W. Brown,[1,7] Aaron D. Schimmer,[6] Vytas A. Bankaitis,[4] Corey Nislow,[1,2,12] Gary D. Bader,[1,2] Guri Giaever[1,2,10,12]†

Genome-wide characterization of the in vivo cellular response to perturbation is fundamental to understanding how cells survive stress. Identifying the proteins and pathways perturbed by small molecules affects biology and medicine by revealing the mechanisms of drug action. We used a yeast chemogenomics platform that quantifies the requirement for each gene for resistance to a compound in vivo to profile 3250 small molecules in a systematic and unbiased manner. We identified 317 compounds that specifically perturb the function of 121 genes and characterized the mechanism of specific compounds. Global analysis revealed that the cellular response to small molecules is limited and described by a network of 45 major chemogenomic signatures. Our results provide a resource for the discovery of functional interactions among genes, chemicals, and biological processes.

Chemical genomics is a powerful approach for understanding in vivo mechanisms of drug action. The ability to interpret molecular-level responses in a cellular context has led to therapies for intractable diseases (*1*). "Guilt-by-association" approaches allow mechanisms of untested compounds to be inferred on the basis of profile similarity to established drugs (*2*, *3*). Loss-of-function genetic screens provide direct mechanistic insight as they report genes that when deleted, confer drug sensitivity. Here, we used yeast genomic tools (*4*) in loss-of-function assays to systematically characterize the cellular response to small-molecule perturbation by screening 3250 compounds using a haploinsufficiency profiling (HIP) and homozygous profiling (HOP) chemogenomic platform (*5*–*7*). HIP exploits drug-induced haploinsufficiency (*8*), as measured by a growth or fitness defect (FD) observed in a heterozygous strain deleted for one copy of the drug's target gene. HIP identifies candidate protein targets by measuring the drug-induced FDs of ~1100 heterozygous strains representing the yeast essential genome (*5*, *6*). In the complementary HOP assay, drug-induced FDs are reported for ~4800 homozygous deletion strains, identifying the nonessential genes required to buffer the targeted pathways (*7*, *9*). Each combined HIPHOP profile provides a genome-wide view of the cellular response to a specific compound.

By prescreening 50,000 diverse druglike small molecules, we identified 3250 compounds that inhibited wild-type yeast growth (~95% of unknown mechanism; table S1 and fig. S1). Each compound was profiled genome-wide, and FDs were measured for each strain; larger scores representing a greater requirement for the deleted gene to resist chemical treatment (*10*). For example, the *Erg11*Δ/*ERG11* strain represents a "hit" as it had the largest FD in the fluconazole HIP profile and passed significance and specificity thresholds (*10*). Fluconazole inhibits the protein Erg11, thus demonstrating the ability of HIP to identify targets in vivo (Fig. 1A). Fluconazole HOP identified mechanisms that buffer the ergosterol pathway, including the requirement for iron (Fig. 1A). Gene Ontology (GO) enrichments are provided for each profile (fig. S2) (*10*). Additional relationships among genes, profiles, pathways, and compounds can be explored with the interactive online HIPHOP chemogenomic database http://chemogenomics.pharmacy.ubc.ca/HIPHOP/ (*10*).

In total, HIP identified 317 compounds that specifically perturb the function of 121 essential genes. To distinguish these compounds from drugs or credentialed chemical probes, we refer to them as "chemical-genetic probes," and to their interacting gene partners as "HIP hits" (*10*). Consistent with the ability of HIP to identify protein targets, these specific interactions were significantly enriched for established compound-target pairs (hypergeometric test $P < 10^{-4}$) including drugs approved by the U.S. Food and Drug Administration (e.g., rapamycin) and chemical probes (e.g., cerulenin) (table S2 and fig. S3). These drugs and probes target homologous proteins in yeast and mammalian cells, suggesting that some of our uncharacterized compounds may function similarly in mammalian cells, even though yeast required about fives times as much compound to inhibit growth by 20% [minimum 20% inhibitory concentration (IC_{20}) = ~244 nM, median = ~100 μM; fig. S4 and table S3]. This observation is consistent with published data (*11*, *12*) and reflective of yeast's robust xenobiotic defenses. Using quantitative growth assays (fig. S5 and table S2), we confirmed dose-dependent drug-induced haploinsufficiency for 63 compound-gene pairs, 54 of them novel (figs. S6 to S9). Specific chemical-genetic probes were tested for inhibitory activities in cell-free assays (IC_{50} range 1 to 500 μM, median = ~23 μM) and/or cell-based assays (IC_{50} range 30 nM to 100 mM, median = 60 μM). For example, we validated inhibitors of actin (0136-0228) and tubulin (1327-0036) in yeast and mammalian cell-based assays (IC_{50} range 30 nM to 100 μM) and in in vitro polymerization assays (IC_{50} range 20 to 25 μM; fig. S10). An in vitro assay suggested that compound 1327-0036 binds to the colchicine-binding site on the tubulin dimer (fig. S10). Another compound (3013-0144) perturbed the septin Cdc12 (IC_{50} = 1 μM), exhibiting about five times more activity than forchlorfenuron, a known septin inhibitor (*13*) (Fig. 1B). Three compounds that perturb Sec14, a conserved phosphatidylinositol transfer protein, were also biochemically validated (IC_{50} = ~1 μM; Fig. 1C), and we have recently shown that two additional inhibitors are effective in vivo and in vitro (*14*). The specificity of these compounds for Sec14 was further validated by demonstrating that suppressed double mutants *cki1*Δ *sec14*Δ (*15*) and *kes1*Δ *sec14*Δ (*16*) were resistant to these inhibitors (fig. S7). This experimental support provides encouraging proof-of-concept data and underscores the need for further characterization of putative protein inhibitors (see fig. S5 for the structures of all validated inhibitors).

Hierarchically clustering all HIPHOP profiles allowed classification of cellular response types into major (covering ~36% of profiles), minor (~40%), or unique (~24%) signatures. Each major response was defined by a characteristic gene signature in a cluster of more than four profiles, while most minor signatures were associated with three to four profiles (fig. S11 and table S4). Several minor signatures point to compelling biology,

[1]The Donnelly Centre, University of Toronto, Toronto, Ontario M5S 3E1, Canada. [2]Department of Molecular Genetics, University of Toronto, Toronto, Ontario M5S 1A8, Canada. [3]Department of Biochemistry, Stanford Genome Technology Center, Stanford University, Palo Alto, CA 94304, USA. [4]Department of Molecular and Cellular Medicine, College of Medicine, Texas A&M University Health Sciences Center, College Station, TX 77843–1114, USA. [5]School of Pharmacy, University of Waterloo, Kitchener, Ontario N2G 1C5, Canada. [6]Princess Margaret Cancer Centre, University Health Network, Toronto, Ontario M5G 2M9, Canada. [7]Department of Biochemistry, University of Toronto, Toronto, Ontario M5S 1A8, Canada. [8]Cell Biology Program, Hospital for Sick Children, University of Toronto, Toronto, Ontario M5G 1X8, Canada. [9]Department of Biology, Massachusetts Institute of Technology, Cambridge, MA 02142, USA. [10]Department of Pharmaceutical Sciences, Faculty of Pharmacy, University of Toronto, Toronto, Ontario M5S 3M2, Canada. [11]Institut des Sciences de la Vie, Université catholique de Louvain, B-1348 Louvain-la-Neuve, Belgium. [12]Faculty of Pharmaceutical Sciences, The University of British Columbia, Vancouver, British Columbia, V6T 1Z3, Canada. [13]Laboratoire d'Enzymologie et Biochimie Structurales, Centre National de la Recherche Scientifique (CNRS), Gif-sur-Yvette, France.

*These authors contributed equally to this work.
†Corresponding author. E-mail: g.giaever@ubc.ca

including a signature representing the response to three chemical-genetic probes that share a 2,5-dimethylpyrrole chemical moiety and putatively target the geranylgeranyltransferase complex *RAM2/CDC43* (table S2). Unique signatures (one to two profiles each) include distinctive drugs (e.g., methotrexate) and chemical-genetic probes (e.g., 0kpi-0099, fig. S12).

We focused on the highest-confidence major cellular response signatures, which represent ~70% of our chemical-genetic probes (*10*). Of these 45 signatures, 33 were enriched for known gene function, 40 represent ≥1 HIP hits, and 11 represent ≥2 compounds of known mechanism (Fig. 2). Five of these 11 signatures are enriched for compounds with similar bioactivity [hypergeometric test false discovery rate (FDR) ≤ 0.1; table S5], supporting mechanism prediction for related compounds (*10*) (Fig. 2). For example, the exosome signature compounds included four chemotherapeutics known to target this complex (hypergeometric test $P < 10^{-10}$; Fig. 3) (*5*, *6*), allowing a similar mechanism to be inferred for two additional compounds. Similarly, we predict DNA damage as the underlying mechanism for 20 uncharacterized compounds with the same signature as established DNA-damaging agents (table S5). Response signatures also provide hypotheses applicable to mammalian cells. For example, trichlorophene induced mitochondrial stress. Trichlorophene-treated immortalized human leukemia cells confirmed a mitochondrial-specific mechanism; exhibiting increased generation of mitochondrial reactive oxygen species and a reduction in reserve oxygen capacity (fig. S13). Signatures also yielded new information about well-characterized compounds; e.g., the tubulin inhibitors nocodazole and benomyl induced a signature containing tubulin biogenesis and *SWR1* complex genes, a biological link between cytoarchitecture and chromatin structure supported by genetic interaction data (*17*).

Our signatures are recognizable in other genome-wide data sets, supporting their biological relevance. Yeast large-scale genetic interaction data (*18*) revealed that our response signatures were observed in 12% of 380 genetic profiles that lacked GO enrichment (table S6). In some cases, the signatures provided annotation for uncharacterized genes. For example, genes known to genetically interact with *YPL109C* (*18*) are not enriched for any GO-based function, yet were significantly enriched for our ubiquinone biosynthesis and proteasome signature (hypergeometric test FDR ≤ 0.1), suggesting a related function. Our signatures also identify links between biological processes (fig. S14). For example, the ubiquinone biosynthesis and proteasome signature links these two processes by 38 gene pairs exhibiting correlated fitness, or "cofitness." Independent support for this observation is provided by nine genetic interactions (*18*) and one physical interaction (*17*) (table S7). Cofitness also supported a functional relationship between diphthamide biosynthesis and histone exchange in the *NEO1-PIK1* signature (table S7).

Approximately half (n = 28) of the major response signatures are associated with compounds significantly enriched for chemical moieties (hypergeometric test FDR ≤ 0.1; table S8 and Fig. 2), suggesting that specific molecular structural properties can drive a cellular response. For example, the *NEO1* and *NEO1-PIK1* signatures (Fig. 2) are characterized by *NEO1* haploinsufficiency induced by cationic amphiphilic drugs (CADs; fig. S15). CADs are associated with drug-induced phospholipidosis (DIPL), a human phospholipid storage disorder (*19*, *20*) caused by diverse therapeutics. At a cellular level, DIPL arises from the selective accumulation of CADs in the acidic vacuole and lysosome, in yeast and mammalian cells, respectively. Consistent with published yeast genetic studies, we confirmed that inhibition of yeast vacuolar adenosine triphosphatase by bafilomycin A alleviates the FD induced by CADs (*21*). Furthermore, we found that bafilomycin A rescued CAD-induced *NEO1* haploinsuffiency (Fig. 4A and fig. S8). Structural features of *NEO1* and *NEO1-PIK1* compounds proved predictive of response; a statistical structure-based model performed about seven times better than random in identifying compounds that induce *NEO1* haploinsufficiency (fig. S16; percentage of correct predictions in cross-validation = 99%) (*10*).

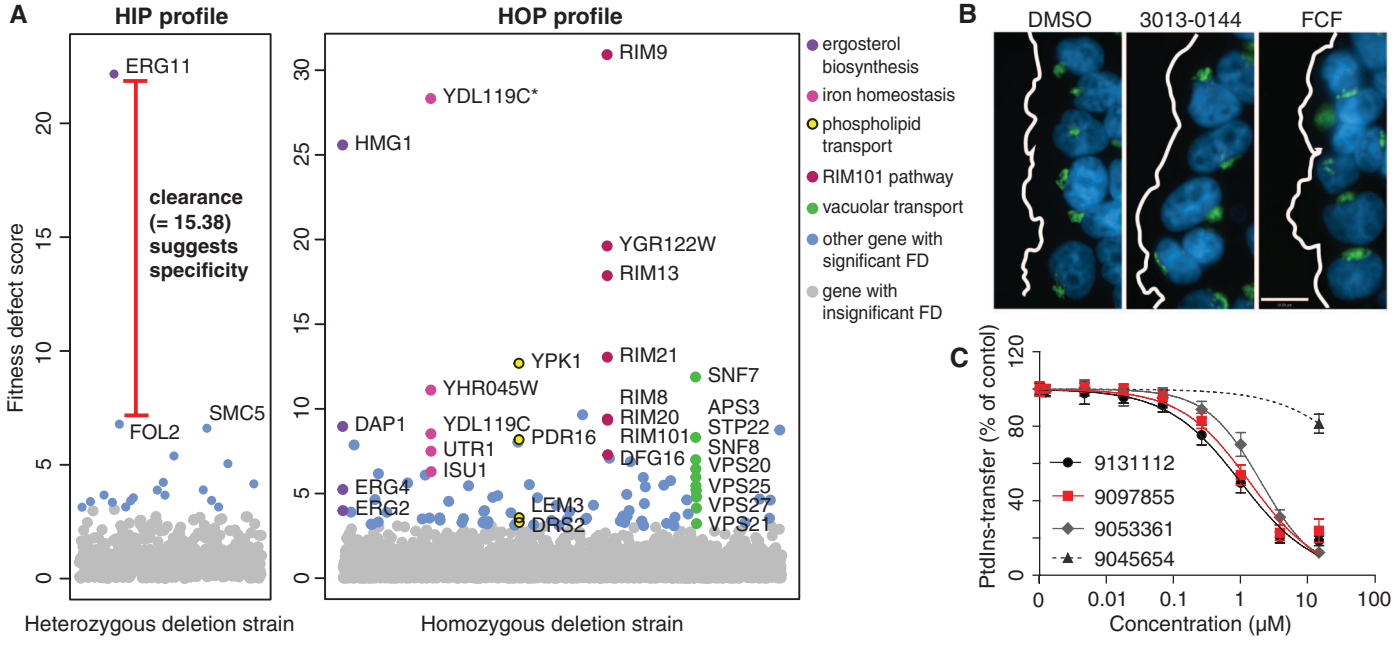

Fig. 1. Validation of chemical-genetic probes. (**A**) Fluconazole HIPHOP profile. Fitness defect (FD) scores plotted for each deletion strain. HIP (left) identifies the established drug target Erg11. HOP (right) identifies processes directly (e.g., sterol biosynthesis) and indirectly (e.g., iron ion homeostasis) related to *ERG11* function. Significant FDs (standard normal distribution $P \leq 0.001$) are labeled except those (blue) not covered by the highlighted processes; *, dubious gene overlapping labeled gene. (**B**) Cdc12 inhibitor. In a wound-healing assay, HeLa cells with dimethyl sulfoxide (DMSO), 1 μM 3013-0144, and 5 μM forchlorfenuron (FCF) were fixed and stained as described, with DNA stained blue and antibodies against the Golgi visualized via green fluorescence (*10*). DMSO-treated cells show the Golgi reoriented toward the wound edge (white line); in contrast, 3013-0144 inhibited Golgi reorientation as effectively as FCF (scale bar, 10 μm). (**C**) Dose-dependent inhibition of the phosphatidylinositol (PtdIns) transfer activity of purified recombinant Sec14 (*10*). Transfer of radiolabeled PtdIns as a percentage of the untreated control (y axis), measured in the presence of 9131112, 9097855, 9053361*, and 9045654 (an inactive derivative) at the indicated concentrations (x axis). Data are mean ± SD (N = 3). *9053361 did not qualify as a HIP hit, but was nonetheless validated.

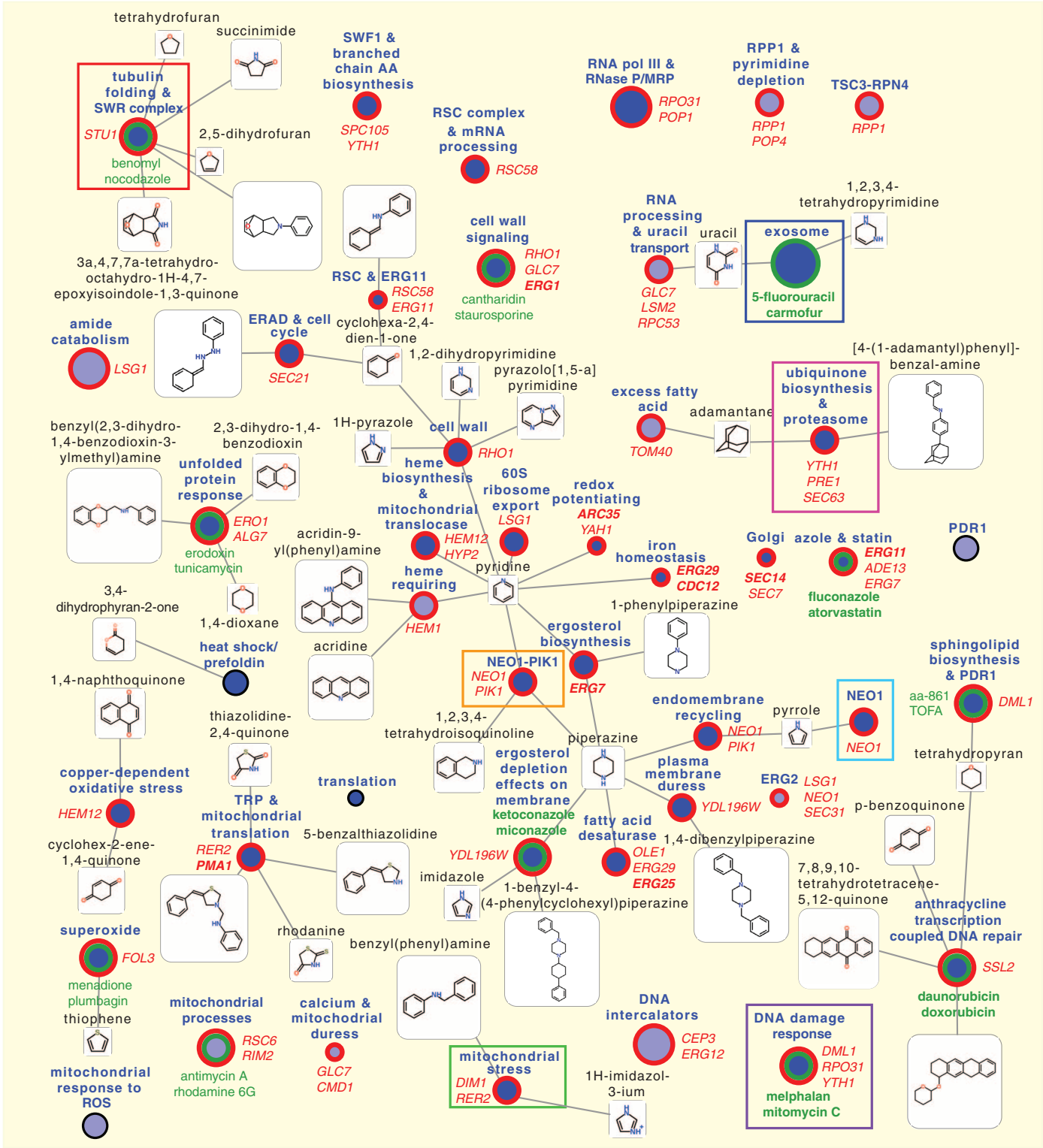

Fig. 2. The cellular response is defined by a network of chemogenomic response signatures. Each circular node represents a major signature; size is proportional to confidence in the signature (*10*). Node color: dark blue if GO enriched (hypergeometric test FDR ≤ 0.1), pale blue otherwise. Node border color: green, signature represents two or more compounds of known mechanism (select compound names are shown, and are in bold if they drive bioactivity class enrichment); red, signature represents chemical-genetic probes (select HIP hits are shown, and are in bold if validation data are provided). Signatures are connected to chemical moiety nodes where signature compounds are enriched (hypergeometric test FDR ≤ 0.1). Boxes indicate signatures discussed in the text. ERAD, endoplasmic reticulum–associated degradation; RNA pol III, RNA polymerase III; ROS, reactive oxygen species; TOFA, 5-tetradecoxyfuran-2-carboxylic acid; TRP, tryptophan.

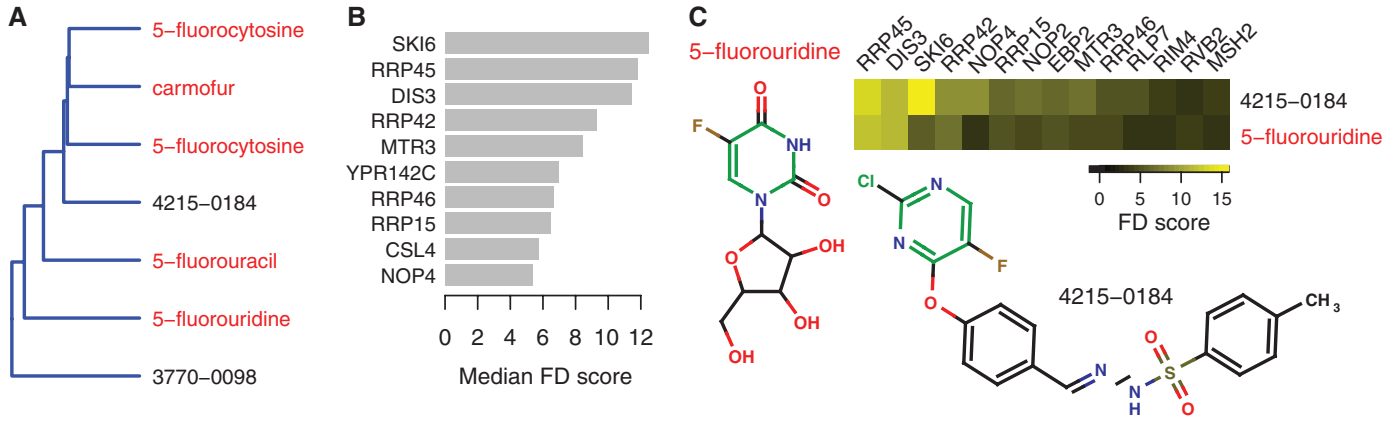

Fig. 3. Mechanism inference with the exosome signature. (**A**) Dendrogram of the exosome profiles extracted from the dendrogram of all HIPHOP profiles. Profiled compounds with established mechanisms are shown in red. (**B**) The exosome signature. For each gene in the signature, the bar plot indicates the median FD score across the exosome profiles. (**C**) Mechanism inferred by signature similarity. Scores of genes exhibiting significant fitness defects in the profiles of 5-fluorouridine and an uncharacterized compound (4215-0184) associated with the exosome signature. Both compounds contain a 5-fluoropyrimidine substructure (green). Guilt-by-association infers that 4215-0184 inhibits the exosome.

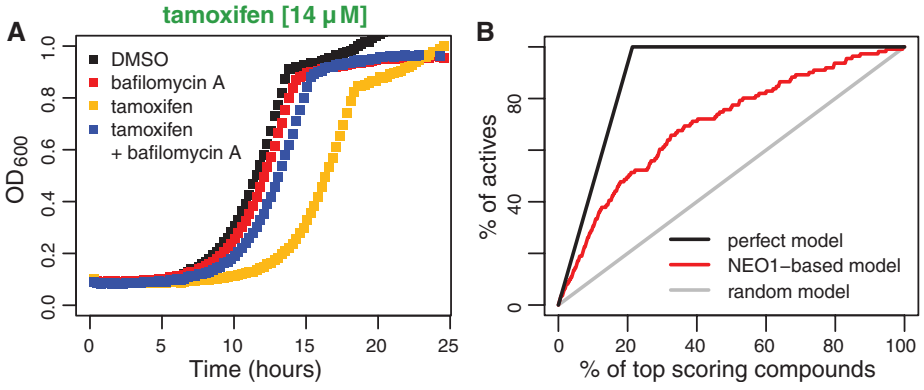

Fig. 4. *NEO1*-based signatures and drug-induced phospholipidosis (DIPL). (**A**) Rescue of CAD-induced *NEO1* haploinsufficiency. Tamoxifen-induced *NEO1* haploinsufficiency is rescued by bafilomycin A. Growth of the *neo1*Δ/*NEO1* strain treated with these compounds was monitored by measuring the optical density at 600 nm (OD_{600}) (*y* axis) for 24 hours (*x* axis). (**B**) Prediction of DIPL. The plot shows the percentage of DIPL-causing compounds (actives; *y* axis) identified among the top-scoring compounds (*x* axis).

Our yeast-based model suggests that haploinsufficiency of *NEO1*, and by extension, its human homologs (ATP9A and B), may prove useful as a biomarker to identify DIPL-causing compounds (Fig. 4B).

Our systems-level view of the cellular response to small molecules provides a resource for the exploration of multifaceted relationships among genes, biological processes, chemical structures, and response signatures. Although not previously captured by any existing GO category, in retrospect, we detect signatures present in other large-scale genomic data sets suggesting that they may be used to address the challenges of incomplete gene annotation and integration of diverse genome-wide data sets. It is likely that we have identified all major signatures (within similar chemical space in yeast), as we observed saturation in our screen. Reanalysis of our prior chemogenomic data set (*7*) revealed that ~60% of the 45 signatures could be detected (fig. S17 and table S4), and simulation demonstrates that 80% of our 45 major clusters would be identified after screening <30% of the compounds (fig. S18). We expect that these signatures therefore represent fundamental small-molecule response systems that are present across eukaryotic cells. Accordingly, we expect that many of our 317 chemical-genetic probes will be directly applicable to mammalian cell biology and may support novel targets as opportunities to pursue for therapeutic intervention (*5*, *22*, *23*).

References and Notes

1. P. M. Barrett, A. Alagely, E. J. Topol, *Hum. Mol. Genet.* **21** (R1), R66–R71 (2012).
2. J. Lamb *et al.*, *Science* **313**, 1929–1935 (2006).
3. F. Iorio *et al.*, *Proc. Natl. Acad. Sci. U.S.A.* **107**, 14621–14626 (2010).
4. G. Giaever *et al.*, *Nature* **418**, 387–391 (2002).
5. G. Giaever *et al.*, *Proc. Natl. Acad. Sci. U.S.A.* **101**, 793–798 (2004).
6. P. Y. Lum *et al.*, *Cell* **116**, 121–137 (2004).
7. M. E. Hillenmeyer *et al.*, *Science* **320**, 362–365 (2008).
8. G. Giaever *et al.*, *Nat. Genet.* **21**, 278–283 (1999).
9. A. B. Parsons *et al.*, *Nat. Biotechnol.* **22**, 62–69 (2004).
10. Materials and methods are available as supplementary material on *Science* Online.
11. I. M. Wallace *et al.*, *Chem. Biol.* **18**, 1273–1283 (2011).
12. N. P. Torres, A. Y. Lee, G. Giaever, C. Nislow, G. W. Brown, *Assay Drug Dev. Technol.* **11**, 299–307 (2013).
13. Q. Hu, W. J. Nelson, E. T. Spiliotis, *J. Biol. Chem.* **283**, 29563–29571 (2008).
14. A. H. Nile *et al.*, *Nat. Chem. Biol.* **10**, 76–84 (2014).
15. A. E. Cleves *et al.*, *Cell* **64**, 789–800 (1991).
16. M. Fang *et al.*, *EMBO J.* **15**, 6447–6459 (1996).
17. A. Chatr-aryamontri *et al.*, *Nucleic Acids Res.* **41**, D816–D823 (2013).
18. M. Costanzo *et al.*, *Science* **327**, 425–431 (2010).
19. N. Anderson, J. Borlak, *FEBS Lett.* **580**, 5533–5540 (2006).
20. M. J. Reasor, S. Kacew, *Exp. Biol. Med. (Maywood)* **226**, 825–830 (2001).
21. M. M. Rainey, D. Korostyshevsky, S. Lee, E. O. Perlstein, *Genetics* **185**, 1221–1233 (2010).
22. M. Škrtić *et al.*, *Cancer Cell* **20**, 674–688 (2011).
23. R. K. Blackman *et al.*, *PLOS ONE* **7**, e29798 (2012).

Acknowledgments: Supported by the National Human Genome Research Institute (RO1 003317-07) (C.N., G.G., and R.W.D.); Canadian Cancer Society Research Institute (#020380) (C.N. and G.G.); Canadian Institute for Health Research (MOP-81340) (G.G.), MOP-79368 (G.W.B.), and MOP-700724 (W.S.T.); Canadian Research Chair (G.G.); Charles H. Best Institute (A.Y.L.); Belgian National Fund for Scientific Research and the Interuniversity Poles of Attraction Program (M.B.); French National Research Agency (J.C.); Marie Curie Fellowship (I.M.W.); Leukemia and Lymphoma Society (A.D.S.); Robert A. Welch Foundation (V.A.B.); and NIH grants (GM103504) (G.D.B.) and GM44530 (V.A.B.). The data reported in this paper are tabulated in the supplementary materials, and access to the entire data set is available for query and in a variety of downloadable formats at http://chemogenomics.pharmacy.ubc.ca/HIPHOP/. The raw microarray data are archived in the ArrayExpress database (www.ebi.ac.uk/arrayexpress) under accession no. E-MTAB-2391.

Supplementary Materials

www.sciencemag.org/content/344/6180/208/suppl/DC1
Materials and Methods
Figs. S1 to S24
Tables S1 to S10
References (*24*–*65*)

26 December 2013; accepted 18 March 2014
10.1126/science.1250217

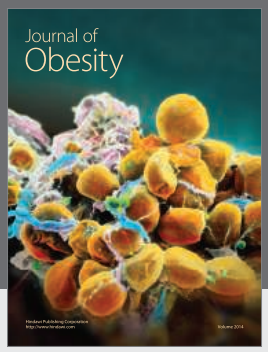

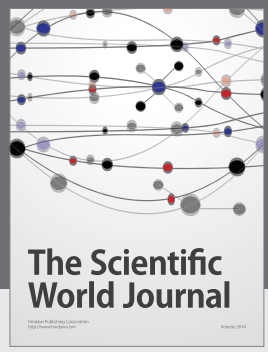

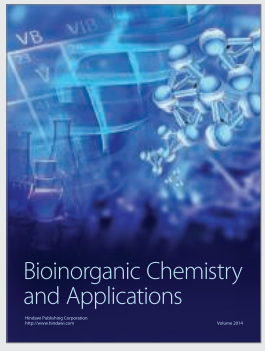

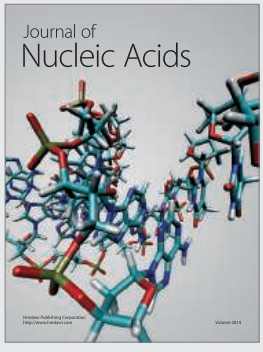

Hindawi

Submit your manuscripts at
http://www.hindawi.com

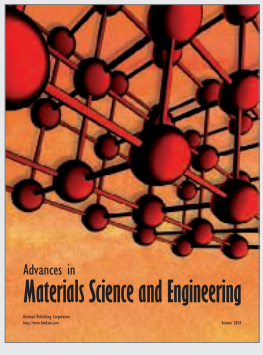

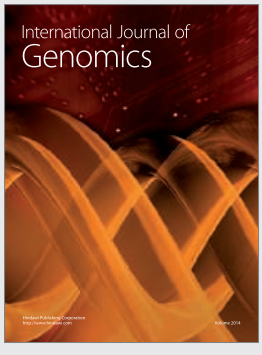

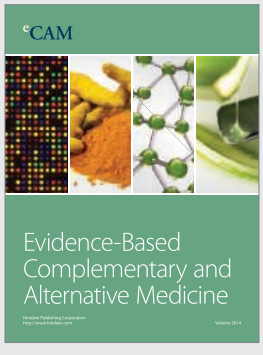

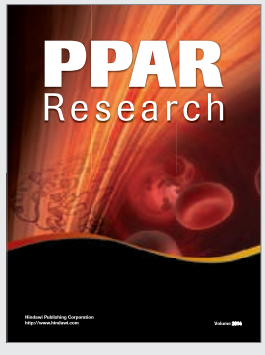

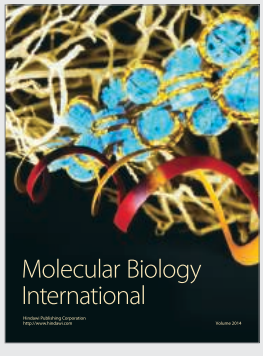

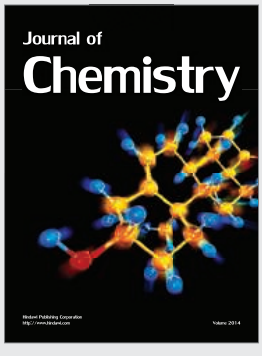

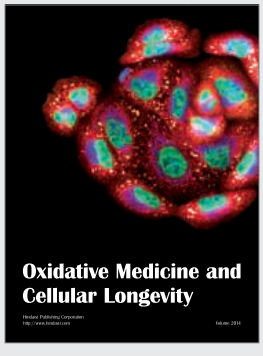

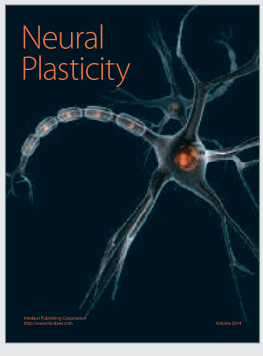

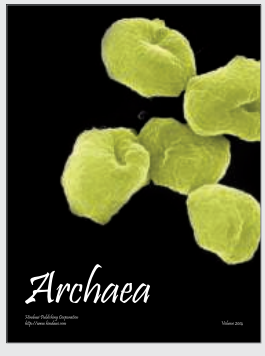

“WE’RE BRINGING A NEW PERSPECTIVE TO

cancer metabolism research

FIRST WE MADE IT POSSIBLE – NOW WE’VE MADE IT EASY.

XF technology provides the easiest and most comprehensive assessment of cancer cell metabolism, measuring glucose and glutamine metabolism, and fatty acid oxidation of cancer cells in a microplate, in real-time! ”

— David Ferrick, PhD,
CSO, Seahorse Bioscience

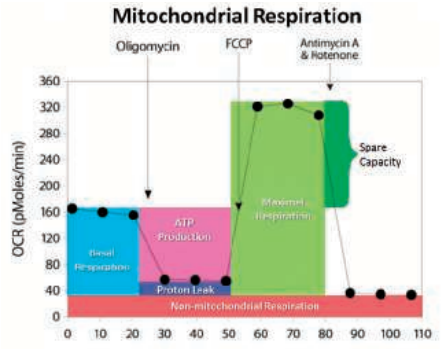

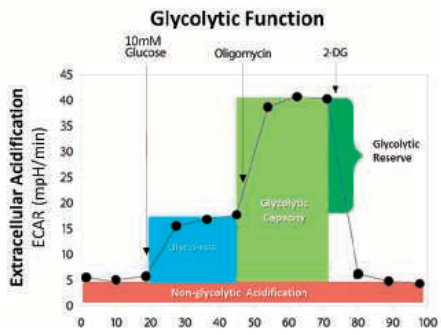

The Seahorse XF^{e} Extracellular Flux Analyzer

Measurements of cellular glycolysis are essential to understanding cancer, immune response, stem cell differentiation, aging, and cardiovascular and neurodegenerative diseases. The XF^{e} Analyzer and XF Glycolysis Stress Test Kit make it easy to measure the three key parameters of cellular glycolysis in a microplate: glycolysis, glycolytic capacity, and glycolytic reserve, revealing critical information not evident in mitochondrial respiration measurements alone.

See what’s possible.

Scan this QR code to view videos and see what the XF Analyzer can achieve.
Visit www.seahorsebio.com/science for more information!

Seahorse *Bioscience*

NEW ENGLAND BioLabs® Inc.

Clone with Confidence.

Whether you are performing your first cloning experiment, or constructing multi-fragment gene assemblies, NEB® has the solution for you. Our high quality reagents are available for every workflow, and include specialized enzymes, competent cells, and novel solutions – such as Gibson Assembly®. When you are looking to clone with confidence, think of NEB.

Explore the wise choice at **CloneWithNEB.com.**

Visit CloneWithNEB.com to view online tutorials describing various cloning workflows.

In a complicated world,
the future just got simpler.

The QX200™ AutoDG™ Droplet Digital™ PCR system is here.

Bio-Rad's Droplet Digital PCR (ddPCR™) systems gave scientists the power to unveil new discoveries through precise and absolute nucleic acid quantification. The new automated droplet generator simplifies the ddPCR workflow, making digital PCR both scalable and practical. Automated droplet generation minimizes hands-on time, eliminates user-to-user variability, and makes every droplet count.

Learn more at **bio-rad.com/info/simpleddpcr**

BIO-RAD

BLUE + GOLD = GREEN

From our alternative fuel research to our gold rating in the Sustainability Tracking Assessment and Rating System survey, UC San Diego is an evironmental leader.

2014 *U.S. News & World Report Rankings* for

Best Graduate Programs

UC San Diego

DEFINING THE FUTURE OF THE PUBLIC RESEARCH UNIVERSITY

#1 COGNITIVE PSYCHOLOGY

#1 BEHAVIORAL NEUROSCIENCE

#2 NEUROSCIENCE

#3 BIOENGINEERING

BD Horizon Brilliant™ Ultraviolet and the BD LSRFortessa™ X-20

Ultraviolet laser and reagents expand research capabilities and clarify results.

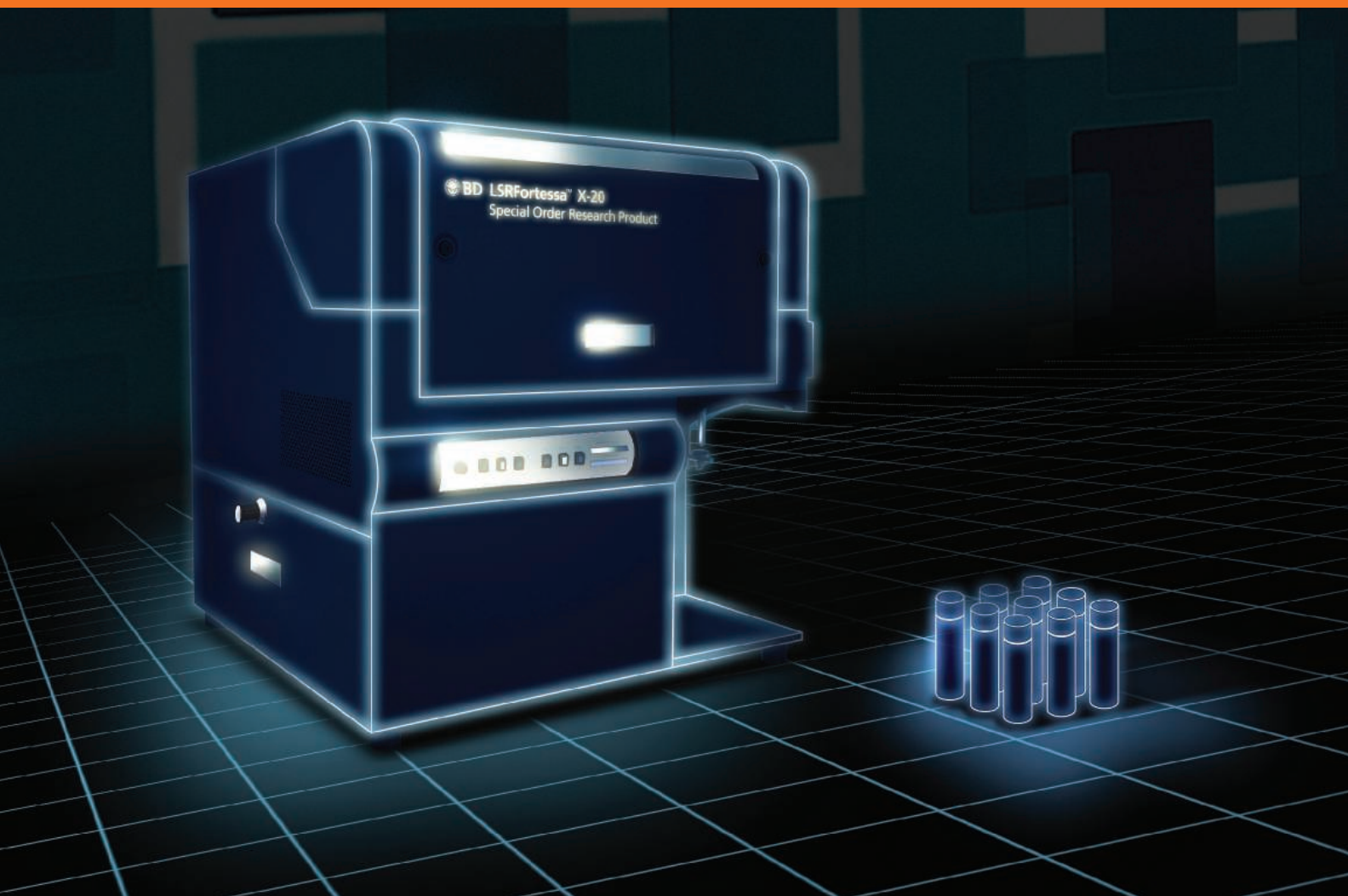

A whole new spectrum of choice.

BD Horizon Brilliant Ultraviolet reagents open a new world of choice and productivity for scientists who use multicolor flow cytometry in their research. By adding the ultraviolet range to panel design, markers can be spread over more lasers, reducing compensation requirements of the experiment.

Use of these new ultraviolet excitable dyes can reduce setup time because there is less need to adjust for compensation.

When the dyes are combined with a dedicated ultraviolet laser position, your options and capabilities are further expanded.

Find out how you can add a whole new spectrum of productivity to your research with BD Horizon Brilliant Ultraviolet dyes and the ultraviolet capable BD LSRFortessa X-20 special order analyzer. Tools and information available at **bdbiosciences.com/go/ultra.**

BD

Helping all people live healthy lives

BD Biosciences
2350 Qume Drive
San Jose, CA 95131
bdbiosciences.com

Research is still your favorite?

MAKE GREAT THINGS HAPPEN

Opportunities for natural scientists: Are you interested in exploring, researching, developing new ideas? Welcome to EMD. When it comes to innovations we are way out front. The spectrum of our pioneering research extends from specialist therapeutic areas, to analysis of microorganisms, all the way to liquid crystals for LCDs. We offer excellent development perspectives and challenging research projects in a team-oriented environment for committed and highly qualified experts. Join us and take part in shaping our diversified global business. Ready to tread new paths?

Merck KGaA, Darmstadt, Germany – with more than 300 years of progress and about 38,000 employees in over 60 countries, we are leading in chemicals and pharma.
Our subsidiaries in Canada and the United States operate under the umbrella brand EMD. With passion, dedication and innovative ideas, we pursue one global goal: to improve people's quality of life.
Like to join in? Welcome to the team!

come2emd.com

EMD

Go from this... ...to THIS

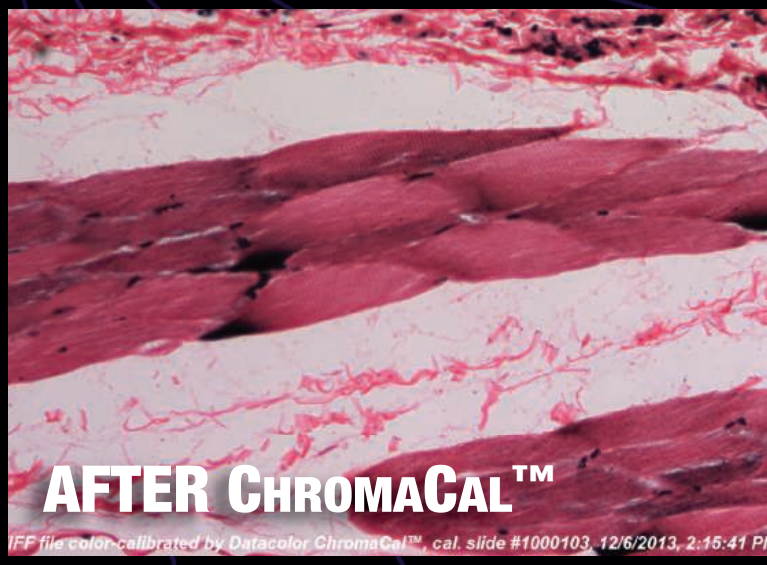

THE LATEST EMERGING TECHNOLOGY...

EMS has it.

Datacolor ChromaCal™
Color Calibration System for Optical Microscopy

datacolor ChromaCal™

An innovative new solution that enables researchers, scientists and technicians to establish and preserve the color integrity of their digital transmitted, brightfield microscopy images.

Datacolor ChromaCal integrates 3 components:

- **Color calibration microscope slide**
- **Proprietary software**
- **Computer monitor calibration sensor**

Together, the Datacolor ChromaCal system establishes a color profile for your microscopy system and applies that profile to your specimen images to ensure consistent and reliable color representation. The outcome is improved comparability of images and enhanced communication and collaboration for better decision making.

PLEASE CONTACT US FOR MORE INFORMATION...

Electron Microscopy Sciences

P.O. Box 550 • 1560 Industry Rd. • Hatfield, Pa 19440
Tel: (215) 412-8400 • Fax: (215) 412-8450
email: sgkcck@aol.com *or* stacie@ems-secure.com

www.emsdiasum.com

THE NEW EMS FULL LINE CATALOG IS COMING SOON.
RESERVE YOUR COPY TODAY!

Mirus

The Transfection Experts

A Transfection Breakthrough

NEW! *Trans*IT-X2™ Dynamic Delivery System

Achieve superior transfections with an advanced non-liposomal, polymeric system that effciently delivers DNA and/or RNA out of the endosome and into the cytoplasm, overcoming a critical barrier to nucleic acid delivery.

The *Trans*IT-X2™ Dynamic Delivery System gives researchers:

- **Efficiency**–superior broad spectrum expression
- **Delivery**–independent or simultaneous delivery of plasmid DNA and siRNA
- **Technology**–novel, non-liposomal, polymeric technology

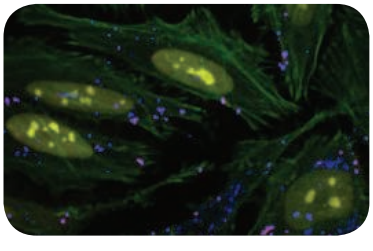

High Efficiency Delivery of Plasmid DNA and siRNA. *Trans*IT-X2™ Dynamic Delivery System was used to *simultaneously* transfect Cy™5-labeled plasmid DNA (blue) encoding nuclear YFP (yellow) and Cy™3-labeled siRNA (red) into HeLa cells. Actin cytoskeleton is stained green.

Visit www.mirusbio.com for full experimental details.

ADVANCE YOUR TRANSFECTIONS.
Request a FREE SAMPLE of
*Trans*IT-X2™ Dynamic Delivery System,
Visit www.mirusbio.com,
call 888.530.0801 (U.S. only) or +1.608.441.2852 (outside the U.S.)

www.mirusbio.com

Providing gene delivery expertise since 1995

The Human Diseasome

Albert-László Barabási,
Distinguished Professor of Physics

Meet Northeastern University professor **Albert-László Barabási.** He and his world-leading network science team are revolutionizing medicine by mapping the molecular and genetic links between diseases—the human "diseasome." It's a breakthrough that will give physicians and researchers alike a powerful new tool to forecast and treat disease.

Learn how this professor and our other faculty researchers are making the world healthier. Northeastern University: making tomorrow happen.

northeastern.edu/tomorrow

Northeastern University

Making Tomorrow Happen

Produced by the *Science*/AAAS Custom Publishing Office

Life Science Technologies
Genomics

The Digital PCR Revolution

Researchers studying rare variant biomarkers often find themselves on the lookout for faint genetic signals against an overwhelming background, sometimes as little as a single positive in 100,000 negatives or more. Such a situation cries out for polymerase chain reaction (PCR), but standard PCR won't do. These days, there's digital PCR (dPCR). By discretizing those 100,000 molecules in a large number of individual reactions, dPCR makes the rare positive surprisingly easy to find.

See the full story on page 212.

Upcoming Features

Microscopy—May 2
Big Data—June 13
Digital Lab Management—July 25

WEBINAR

The Importance of Bioinformatics in NGS

Breaking the Bottleneck in Data Interpretation

Wednesday, May 14, 2014

12 noon Eastern, 9 a.m. Pacific, 5 p.m. UK, 6 p.m. Central Europe

Unprecedented advances have been made in the speed and throughput of next generation sequencing (NGS) platforms over the last decade. This progress has imposed increasingly high demands on the bioinformatics tools necessary for analysis of the data generated, which has grown exponentially. Although hundreds of thousands of samples have been sequenced, our ability to find, associate, and implicate genetic variants and candidate disease genes far outstrips our ability to understand them. Many researchers are comfortable with NGS technology, but encounter difficulties with the bioinformatics portion of their workflow, rendering NGS a less attractive option as their primary sequencing platform. However, once clear bioinformatics procedures are established and optimized this bottleneck can be removed, resulting in smooth and routine data interpretation processes and expedited research discoveries. During this webinar, our expert speakers will discuss their bioinformatics strategies and applications in range of fields of clinical research.

During the webinar, viewers will:

- Be introduced to the bioinformatics workflow and the importance of accurate NGS data analysis and interpretation
- Learn how bioinformatics concepts are applied to detect and characterize disease-related mutations
- Hear about the use of bioinformatics workflows in a translational setting for tumor mutation detection
- Have their questions answered live by our expert panel!

Speakers

Vincent Funari, Ph.D.
Cedars-Sinai Medical Center
Los Angeles, CA

Sandra J. Canosa, M.S.
Yale University
New Haven, CT

REGISTER NOW! webinar.sciencemag.org

Webinar sponsored by

ion torrent by life technologies™

@SciMagWebinars

Brought to you by the *Science*/AAAS Custom Publishing Office

Science AAAS

AAAS 2015 ANNUAL MEETING

12–16 FEBRUARY • SAN JOSE, CA

25 April: Deadline for Symposia Proposals

Share your work and connect with the broader scientific community.
To submit a proposal, visit www.aaas.org/meetings.

Innovations, Information, and Imaging

Science and technology are being transformed by new ways to collect and use information. Progress in all fields is increasingly driven by the ability to organize, visualize, and analyze data. Advances in information and imaging technologies are generating novel applications in fields such as biochemistry, computer science, particle physics, genomics, and oceanography, and creating ways to interpret data across disciplines. This transformation makes scientific information more open, available, and accessible globally. The escalating amount of data, and advances in data analysis, are changing the ways we discover answers to scientific and societal problems. Thoughtful consideration of how information is used for societal benefit, evaluated for potential risks, and communicated beyond the scientific community will allow this revolution to reach its full potential.

AAAS

ADVANCING SCIENCE, SERVING SOCIETY

The Digital PCR Revolution

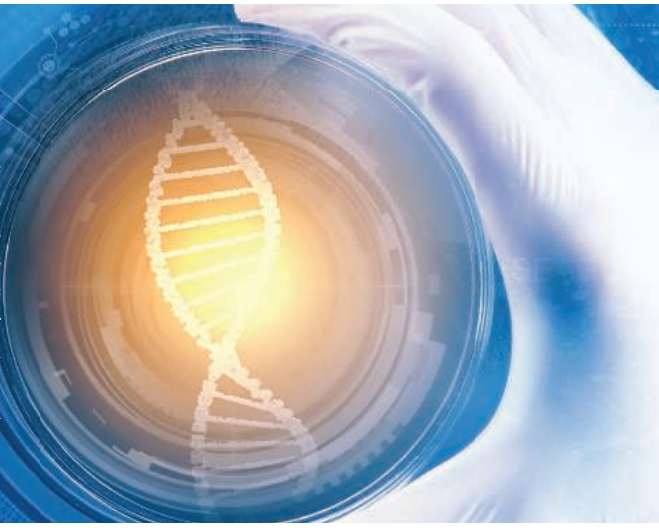

"Like finding a needle in a haystack" is an overused expression, but when it comes to some biological scavenger hunts, it fits. Researchers studying rare variant biomarkers often find themselves on the lookout for faint genetic signals against an overwhelming background, sometimes as little as a single positive in 100,000 negatives or more. Such a situation cries out for polymerase chain reaction (PCR), a technique uniquely capable of capturing the proverbial needle. But standard PCR won't do—it is a qualitative technique—and neither will quantitative real-time PCR (qPCR), which often lacks the necessary accuracy and sensitivity. These days, there's a third and increasingly popular option: digital PCR (dPCR). By discretizing those 100,000 molecules in a large number of individual reactions, dPCR makes the rare positive surprisingly easy to find. **By Jeffrey M. Perkel**

Digital PCR essentially lifts weak signals out of the noise, and researchers today are using that strategy for everything from detecting copy number variations and circulating tumor DNA to HIV viral load monitoring.

Kenneth Kinzler, co-director of the **Ludwig Center at Johns Hopkins University,** who (with colleague Bert Vogelstein) first coined the term "digital PCR," says he and Vogelstein developed the approach to better identify rare cancer mutations. "The thought that occurred to us was that the most sensitive [detection] you can get is by looking at single molecules," Kinzler explains. "When you start with single molecules, [reactions] are either 100% mutant or 100% wild type, which makes the distinction of a tumor from wild type much easier."

Of course, seeing even very rare events using just standard PCR should be possible. After all, PCR excels at plucking needles from molecular haystacks. In theory, given the right primers and cycling conditions, the reaction can copy a single piece of template DNA into millions upon millions of daughter strands, enough to clone, sequence, or detect on a gel. But because the process isn't quantitative, researchers cannot infer the DNA content of the starting sample from the number of molecules present at the end of the reaction.

qPCR addresses that problem by quantifying the reaction as it runs. By charting fluorescence intensity over time, researchers can compare, for instance, the relative expression of a given gene from sample to sample. But absolute quantification by qPCR isn't straightforward. It generally requires standard curves to convert abundance into absolute concentrations, and those concentrations can sometimes vary day to day and across labs. qPCR also struggles with detecting subtle copy-number changes—distinguishing six and seven copies, for instance—and limited sensitivity.

The resulting uncertainty can complicate, for instance, data sharing—a critical limitation when setting up multi-institutional trials, says Muneesh Tewari, associate professor at the **University of Michigan** and formerly associate member of the **Fred Hutchinson Cancer Research Center** (**FHCRC**), who uses dPCR for microRNA biomarker discovery. "Real-time PCR just doesn't have the day-to-day precision, or sometimes even the precision within the same day that we would like," he says.

dPCR circumvents these issues using a "divide-and-conquer" strategy. A mixture of molecules is discretized or compartmentalized into a large number of reaction chambers—the more the better—such that each chamber has on average either one target nucleic acid or none. Following PCR amplification of each compartment, Poisson statistics can be used to convert the count of positive signals into an absolute number.

Kinzler likens the process to Sanger sequencing. Sequencing a mixture of 100 template molecules, one of which is mutant, in a single tube would yield an electropherogram in which the dominant signal at the mutated position would be the wild-type base. "You probably wouldn't even be able to tell there was a little hump underneath [the peak] for the alternative base read, because it represents too small a percentage of the molecules." But diluting the molecules and distributing them in multiple reactions would produce 99 wild-type signals and one clear mutant —a digital, and absolutely quantitative, result.

Digital PCR essentially lifts weak signals out of the noise, and researchers today are using that strategy for everything from detecting copy number variations and circulating tumor DNA to HIV viral load monitoring and fetal aneuploidy testing. Clinical applications, in particular, seem most likely to benefit from the technology, assuming it can be made simple enough for clinical laboratory workflows.

Upcoming Features

Microscopy—May 2
Big Data—June 13
Digital Lab Management—July 25

THE ORIGINAL DIGITAL PCR

Published in 1999, Kinzler and Vogelstein's original "digital PCR" approach was a tedious, manual affair. Looking to detect and quantify K-RAS mutations in stool samples from colorectal cancer patients, the pair diluted and aliquoted genomic DNA into each well of a 384-well microtiter plate, such that the entire plate represented a single sample. They then amplified the gene region that encompassed the mutational hotspots they were looking for.

Once the reactions came to completion—dPCR generally is an endpoint PCR assay, though it doesn't have to be—they hybridized two fluorescent probes, a control that should always hybridize and a second that only binds to wild-type sequences, and read the results. Just over 100 wells had genomic DNA, of which four appeared to be mutants.

The results, Kinzler says, indicated dPCR was "a very robust, reliable, and accurate" method for rare mutation detection. But it also was labor-intensive and difficult to scale. "It was often impossible to convince a grad student to do it," he says.

In 2003, Kinzler and Vogelstein described an improved protocol, which they called "BEAMing" for its reliance on "beads, emulsion, amplification, and magnetics." In place of manual sample discretizing in a microtiter plate, BEAMing turns the individual droplets of a water-in-oil emulsion into reaction vessels. Using an emulsion PCR process that's now used widely in next generation DNA sequence library preparation, BEAMing distributes a mixture of template, primers, PCR reagents, and magnetic beads into droplets, again under conditions such that most droplets will contain either zero or one template. Following PCR, during which the amplified product is coupled to the bead via a biotin-streptavidin linkage, the emulsion is broken and the beads read by hybridization with detection oligonucleotides and flow cytometry.

Instead of manual separation on a plate, BEAMing "can do the equivalent of 100,000 wells," says Kinzler, who still uses the technology and (with Vogelstein and other colleagues) cofounded **Inostics** to commercialize it. (Inostics subsequently was acquired by Sysmex, and today Kinzler holds no equity in the company.)

Droplet-based strategies have also been commercialized by **Bio-Rad Laboratories** and **RainDance Technologies**. Instead of magnetic beads, both companies discretize (or, as RainDance President and Chief Executive Officer S. Roopom Banerjee puts it, "dropletize") the PCR mixture into either 20,000 nanoliter-sized (Bio-Rad's QX200) or 10 million picoliter-sized (RainDance RainDrop) droplets. Following PCR amplification, the reaction results are read by flowing the droplets past a fluorescence excitation source and detector, like a flow cytometer without the cells.

"Think of it as like a digital camera," says Banerjee, who says RainDance's RainDrop system was designed with single-button, "Apple-like simplicity. You have a complicated picture with lots of colors, lots of diversity. What we're doing is basically pixelizing that picture down to miniscule-sized pixels and then we literally read out every single pixel in order to say exactly what's in that biological picture." In RainDance's case, it takes four hours to read 80 million such "pixels," the output of eight parallel dPCR reactions.

POWERFUL POISSON

Because dPCR is an endpoint assay, the resulting concentration could in theory be thrown off if the target molecules didn't discretize perfectly—that is, some compartments ended up with more than one target. That's where Poisson statistics come in. According to George Karlin-Neumann, director of scientific affairs at Bio-Rad Laboratories' Digital Biology Center, Poisson statistics describe a random distribution. As long the compartments aren't saturated, users can back-calculate how many molecules they started with, even if some wells actually receive more than one molecule (an event that, in dPCR, reads as a single count). "You tell me how many compartments or how many droplets you have, [and] what fraction of those are negative. That will tell me essentially what concentration I started with that would give me that ratio of positive compartments to negative compartments," he says.

CREDIT: VASILIY KOVAL/SHUTTERSTOCK.COM

The technique clearly offers considerable advantages for a growing number of specific (and often clinical) applications.

Reginald Beer, medical diagnostics initiative leader at the **Lawrence Livermore National Laboratory**, who as a graduate student published the first report of dPCR in monodisperse (i.e., identically sized) droplets, says the advantage of the droplet-based approach lies in its scalability: It's relatively simple to increase the number of reaction vessels, which in turn increases data quality. "Poisson accuracy greatly improves as you scale or increase the number of your reactor vessels," he explains.

Published reports establish the efficacy of both Bio-Rad's and RainDance's dPCR platforms as well as the diversity of applications amenable to dPCR. RainDance's platform, for instance, has been used to detect mutant gene transcripts in cerebrospinal fluid from glioma patients and KRAS mutations in sera from colorectal cancer patients.

Jason Bielas, associate member of the FHCRC, used Bio-Rad's system to quantify tumor-infiltrating lymphocytes in ovarian cancer, while Keith Jerome, professor and head of the Virology Division in the Department of Laboratory Medicine at the **University of Washington** and associate member of the FHCRC, used it to develop a way to distinguish active HHV-6 viremia from latent, genome-integrated virus. (The former must be treated if it occurs during the course of bone marrow transplantation, but not the latter; the two are distinguished by the ratio of viral sequence copies to genome equivalents in blood, which in the case of genome integration should be 1.0.)

Bielas says his team was able to use their own method, termed QuanTILfy, to reproducibly resolve as little as one T lymphocyte in 10,000 cancer cells—enough to detect an association between T-cell tumor infiltration and patient survival. That method is considerably more quantitative, he explains, than the current standard of immunohistochemistry. "In continued>

Featured Participants

Bio-Rad Laboratories
www.bio-rad.com

Fluidigm
www.fluidigm.com

Fred Hutchinson Cancer Research Center
www.fhcrc.org

Lawrence Livermore National Laboratory
www.llnl.gov

Life Technologies
www.lifetechnologies.com

Ludwig Center at Johns Hopkins
www.ludwigcancerresearch.org/location/johns-hopkins-center

RainDance Technologies
www.raindancetech.com

Rutgers University
www.rutgers.edu

Stanford Genome Technology Center
med.stanford.edu/sgtc/

Sysmex Inostics
inostics.com

University of Washington
www.washington.edu

essence, you're counting T-cell genomes."

Hanlee Ji, senior associate director of the **Stanford Genome Technology Center**, also uses Bio-Rad, both to validate genetic aberrations from genome-sequencing studies and more recently to quality control next-gen libraries prior to sequencing. For his group, the advantage of dPCR is largely simplicity: He can get an undergrad in the lab up to speed on dPCR in weeks, whereas qPCR can take considerably longer.

"One of my tests of technology is: If I take an undergrad who has reasonably good bench skills and sit them in front of an instrument, can they generate robust results from the positive and negative controls that they're asked to do within a matter of weeks? If so, that says a lot regarding how well the system works."

DIGITAL PCR-BY-SEQUENCING

In 2011, Kinzler and Vogelstein described yet another approach to dPCR for rare allele detection, this time based on sequencing. Called Safe-Sequencing System (Safe-SeqS), the strategy entails tagging individual template molecules with unique identifiers (or barcodes), which are then amplified and read out by next generation DNA sequencing.

According to Nickolas Papadopoulos, director of translational genetics at the Ludwig Center at Johns Hopkins, professor of oncology at Johns Hopkins Medical Institutes, and coauthor of the study: Safe-SeqS enables researchers to extend the capacity of dPCR to many more loci—up to 30 or more—than BEAMing can reasonably handle.

"Massively parallel sequencing represents a particularly powerful form of dPCR in that hundreds of millions of template molecules can be analyzed one by one," explain Papadopoulos and his coauthors in their 2011 study. "It has the advantage over conventional dPCR methods in that multiple bases can be queried sequentially and easily in an automated fashion." But NGS also has an unacceptably high inherent error rate caused by mistakes in amplification, sequencing, and detection. By tagging each starting molecule with a unique identifier, Safe-SeqS enables researchers to differentiate true mutations from procedural artifacts.

In the original study, the authors assessed mutations in the *CTNNB1* gene in 100,000 normal human cells. Raw Illumina sequencing reads produced an error rate 2.1×10^{-4}. Taking into account the Safe-SeqS barcodes lowered that rate 24-fold, to 9×10^{-6}. When applied to mitochondrial DNA, Safe-SeqS dropped the observed mutation rate 15-fold.

This past year, the team extended Safe-SeqS to search for multiplexed signatures of ovarian, endometrial, and cervical cancer in the scraped cervical material that comes from routine Pap testing, a first step in developing an early detection system for gynecologic tumors. In this case, the team used the assay to assess mutations in 46 gene regions from 12 cancer-associated genes.

Papadopoulos, who discussed the method at a recent digital biology conference in San Diego, says Safe-SeqS may be particularly useful for early tumor detection from plasma. Overall, his team could detect mutations in more than 80% of tumor plasma samples. But some tumor types worked better than others. Particularly difficult, he says, were malignancies in brain. "Currently, we can detect mutations in the plasma from only 10% of the patients with these tumor types," he says.

ARRAY-BASED STRATEGIES

For Andrzej Pietrzykowski, assistant professor of animal sciences at **Rutgers University**, who studies the molecular and genetic bases of alcoholism, dPCR's precision is particularly beneficial. Many of the changes he sees are less than twofold and thus difficult to discern by qPCR. That difference is readily detected digitally, he says.

But Pietrzykowski also cites another advantage. He has identified a particular microRNA that seems to be associated with alcoholism, and can quantify that molecule using qPCR. But qPCR assays for microRNA precursors are harder to pull off, as identifying reliable controls for standard curve calibration can be problematic. "You need to … have that housekeeping gene double or triple-checked that it doesn't change due to conditions." That's a non-issue with dPCR, though, as the technique doesn't require a standard curve.

Pietrzykowski was one of five Innovation Grant recipients of **Life Technologies**' Digital PCR Applications Grant program, which in late 2013 provided him with the company's QuantStudio 3-D chip reader, chip loader, and thermo cycler. The QuantStudio 3D Digital PCR system is like a souped-up version of Kinzler's original dPCR implementation. Researchers use a tool akin to a windshield "squeegee" to discretize samples onto 20,000 wells etched into the surface of a silicon wafer. **Fluidigm**, too, uses this physical array strategy; its qdPCR 37K "integrated fluidic circuit" leverages the company's microfluidics expertise to distribute 48 samples into 770 chambers each (though a single sample can be spread over multiple sets of chambers to increase accuracy, up to 37,000).

The technique clearly offers considerable advantages for a growing number of specific (and often clinical) applications. But don't discard your real-time thermocycler just yet. For most researchers dPCR represents a complement to qPCR, not a replacement. Indeed, for many applications, says Beer, qPCR is "by far sufficient"— plus, the technology is far more mature and the assays established. "qPCR certainly still has a significant advantage from a throughput perspective," says Iain Russell, senior product manager for dPCR at Life Technologies (recently purchased by Thermo Fisher Scientific), "and to be quite honest, for a large number of applications out there it meets all the needs of the customer."

Says Pietrzykowski, "It really depends on what kind of question you're asking."

Jeffrey M. Perkel is a freelance science writer based in Pocatello, Idaho.

DOI: 10.1126/science.opms.p1400084

DESKTOP WHOLE-GENOME SEQUENCER

The NextSeq 500 System delivers the power of high throughput sequencing with the load-and-go simplicity of a desktop sequencer, effectively transforming a broad range of high throughput applications into affordable, everyday research tools. Its push-button operation delivers a one-day turnaround for a number of popular sequencing applications, including one whole human genome and up to 16 exomes, up to 20 noninvasive prenatal testing samples, up to 20 transcriptomes, up to 48 gene expression samples, and up to 96 targeted panels. With its streamlined informatics, sequencing data can be run through a range of open -ource or commercial pipelines or instantly transferred, analyzed, and stored securely in BaseSpace or the new BaseSpace OnSite for researchers needing an on-premises solution. Users also have the flexibility to switch to lower throughput sequencing as needed, and while other platforms require several pieces of specialized equipment, the NextSeq 500 System integrates cluster generation and sequencing into a single instrument.

Illumina

For info: 800-809-4566 | www.illumina.com/nextseq

POST-BISULFITE DNA LIBRARY PREPARATION

The new EpiNext Post-Bisulfite DNA Library Preparation Kit is designed for constructing DNA libraries directly from bisulfite-treated DNA for whole genome bisulfite sequencing. Bisulfite conversion is an essential process of modifying DNA so that methylated cytosine bases can be detected via sequencing. Currently used whole genome bisulfite sequencing methods need rather large amounts of DNA (great than 1 µg) as input material, as well as requiring the need to first shear DNA and ligate adapters to DNA fragments prior to bisulfite conversion. The innovative technology developed by Epigentek allows bisulfite-treated DNA to be directly used for ligation, thereby eliminating the possibility of breaking adapter-ligated fragments, which can often occur in currently used next generation bisulfite sequencing methods. The commercial kit, based on this technology, has high sensitivity and efficiency, enabling input DNA to be as low as 1 ng, and could be used for precious or limited biological samples.

Epigentek

For info: 877-374-4368 | www.epigentek.com

GENE-EDITING KITS

The new GENASSIST range of gene-editing kits and reagents enable easier, robust implementation of CRISPR and rAAV gene editing experiments. The current GENASSIST offering comprises both off-the-shelf reagents for using CRISPR editing technology and a unique kit combination of these reagents to allow customers to generate their own CRISPR-ready cell lines that constitutively express Cas9-nickase. Using such cell lines provides a quick start for customers, enabling them to make further modifications to the cell line more efficiently than if they were starting fresh each time. Horizon is also launching a new service for the design, manufacture and most importantly validation of CRISPR RNA guides, in order to maximize the likelihood that gene editing will occur as expected. The new GENASSIST kits, combined with access to rAAV, ZFN, and CRISPR technologies, give researchers an invaluable suite of tools to determine the function of endogenous gene alterations and their effect on disease and therapeutic responses.

Horizon Discovery

For info: +44-(0)-1223-655580 | www.horizondiscovery.com

DNA LIBRARY KIT

The Accel-NGS 2S DNA Library Kit for Illumina Next Generation Sequencing (NGS) systems provides linear yields from inputs ranging from 10 pg to 1 µg. Polymerase chain reaction-free libraries can be produced from as little as 100 ng. Unlike other commercially available kits, exceptional quality and evenness of coverage are obtained even at very low levels of DNA input. The product is also is ideally suited for clinical samples such as FFPE tissues and plasma. Accel-NGS 2S enables NGS laboratories to stock and use a single kit for their varied DNA library needs, ranging from high molecular weight DNA to limited quantity, damaged FFPE samples. In addition to whole genome sequencing, Accel-NGS 2S is also compatible with the leading hybridization capture products and is suitable for ChIP-Seq. Built with usability in mind, the 2S protocol is readily automatable for those with high throughput applications. The wide dynamic range of input makes pre-library quantification optional, further streamlining workflow.

Swift Biosciences

For info: 734-330-2568 | www.swiftbiosci.com

NGS LIBRARY PREP KITS

Current methods used for epigenetic analysis of DNA methylation are deficient in differentiating 5-methylcytosine from 5-hydroxymethylcytosine. The new Pico Methyl-Seq Library Prep and RRHP 5-hmC Library Prep kits are designed for NGS-based, whole-genome analysis of 5-methylcytosine and genome-wide analysis of 5-hydroxymethylcytosine in DNA, respectively. These unique products feature streamlined workflows and include all the technologies required for consistent and robust library construction. Pico Methyl-Seq is a post-bisulfite library preparation method that can accommodate DNA inputs as low as 10 pg. Alternatively, RRHP allows for strand-specific, single-base profiling of 5-hmC from DNA inputs as low as 100 ng by utilizing a bisulfite-free, enzymatic-based method. When combined, both technologies will elucidate genomic-scale methylation and hydroxymethylation profiles for a particular DNA sample from any species.

Zymo Research Corporation

For info: 888-882-9682 | www.zymoresearch.com

immunogenomics 2014

September 29 - October 1, 2014

HudsonAlpha Biotechnology Campus
Huntsville, Alabama, USA

Bringing together preeminent leaders and thinkers at the intersection of genomics and immunology

Our Keynote Speakers:

Christophe Benoiste
Professor, Department of Microbiology and Immunobiology, *Harvard Medical School*

Mary Ellen Conley
Federal Express Chair of Excellence and Professor, Department of Pediatrics, *University of Tennessee, College of Medicine, Memphis*

Mark Davis
Investigator, Howard Hughes Medical Institute; Professor, Department of Microbiology and Immunology; Director, Institute for Immunity, Transplantation, and Infections, *Stanford University School of Medicine*

Sponsored by

Platinum Sponsors

iRepertoire, Inc.

Gold Sponsors

UAB COMPREHENSIVE ARTHRITIS, MUSCULOSKELETAL, AND AUTOIMMUNITY CENTER

Silver Sponsors

GenapSys

illumina

Interested in sponsoring Immunogenomics 2014? Visit our website for more information.

Register today at

haig.aaas.org

follow @immunogenomics on twitter

presented by

HUDSONALPHA INSTITUTE FOR BIOTECHNOLOGY

Science AAAS

Get to the Bottom of Your Signal Transduction Research Faster.

Run one ELISA instead of multiple Western blots.
Optimize your experimental parameters with
ELISAs from R&D Systems.

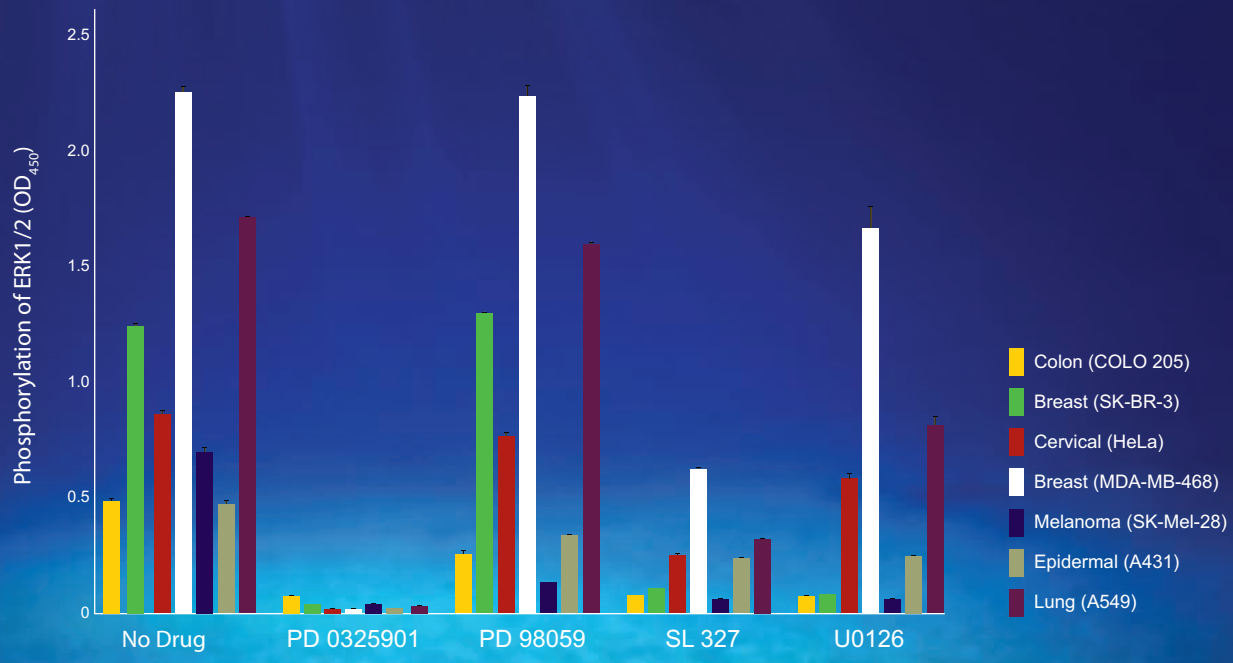

Interact with this data and learn more about our ELISA formats for intracellular targets

RnDSystems.com/Optimize

TOCRIS bioscience

R&D SYSTEMS®

BostonBiochem®

LMU LUDWIG-MAXIMILIANS-UNIVERSITÄT MÜNCHEN

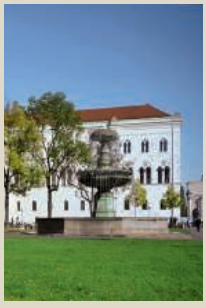

Ludwig-Maximilians-Universität (LMU) München is one of the leading research unversities in Europe, with a more than 500-year-long tradition. As part of the "LMU Academic Career Program", LMU Munich will award

10 Research Fellowships

to excellent junior academics.

The program aims to attract outstanding postdoctoral researchers from all over the world. Applications are welcome from candidates of all disciplines who have completed their doctoral studies within the last three years with outstanding results. Applicants must present an independent research project as part of their application.

The project must be supported by a professor of LMU Munich. The fellows will become members of the Young Center of the Center for Advanced Studies and be able to make use of its services.

Endowment

Research fellows will receive an attractive salary according to the German "*Tarifvertrag der Länder* (TV-L)" (typically TV-L grade E 14). Applicants may apply for an additional start-up funding up to the amount of € 25,000 as well as for material and travel expenses of up to € 10,000 per year. In the first two years after the completion of their research fellowship, the fellows may be granted up to € 5,000 for continuing cooperation with LMU Munich. The fellowships are initially tenable for two years. An extension of two years may be granted upon a positive academic evaluation.

Ludwig-Maximilians-Universität München is an equal opportunity employer committed to excellence through diversity and therefore explicitly encourages women to apply.

Closing date for applications is 1 June 2014.

The fellowships should commence between 1 October 2014 and 1 March 2015.

For all information regarding your application please consult: www.lmu.de/excellent/research-fellowships

---

Department of Health and Human Services
National Institutes of Health
Center for Human Immunology, Autoimmunity, and Inflammation
Division on Intramural Research

NIH CENTER FOR HUMAN IMMUNOLOGY

STAFF SCIENTIST/BIOINFORMATICS

The NIH Center for Human Immunology, Autoimmunity and Inflammation (CHI) is a trans-NIH Institutes initiative to study the human immune system in health and disease, using high-throughput multi-dimensional assays and integration of dense data sets with advanced computational approaches.

CHI is recruiting an individual who will have responsibilities in the broad area of computational analysis of diverse data sets from high-throughput assays, such as microarrays, highly-density flow immunocyte phenotyping, multiplex analysis of serum cytokines and proteins, and SNP genotyping. The position involves close collaboration with multiple experimentalists to answer biological questions of interest by advising on study structure and data collection procedures such as batch design to optimize data output for subsequent analysis, performing quality control of experimentally generated data, conducting relevant statistical analyses and modeling of the processed data, and developing and employing advanced bioinformatics methods to integrate the different data sets, including analysis results from CHI studies and knowledge from the literature and public databases. The Staff Scientist position is located in CHI's Bioinformatics Laboratory, and will be part of an existing group that conducts computational activities in support of CHI protocols. To facilitate efficient data retrieval and data mining, this group will build databases and software infrastructure to load, store and organize the diverse data sets, associated metadata, and analysis results from the high-throughput assays. The group also conducts advanced bioinformatics and systems biology research, such as developing novel statistical methods for the analysis and integration of high-dimensional data sets to gain biological insight. Because the computing infrastructure of CHI is by necessity very inhomogeneous, the incumbent will likely need to develop or work with custom hard- and software solutions to accomplish these various goals.

The ideal candidate will have a Ph.D. in computational biology, bioinformatics, systems biology, or relevant disciplines. Three+ years of hands-on research experience with the analysis of high-throughput data sets would be a strong plus. He/she should possess a sound knowledge of statistics and quantitative modeling and solid computer programming skills with proficiency in Matlab/R, SQL, and at least one scripting language (Perl/Python/Ruby). Proficiency in C/C++ and/or Java, as well as experience with multiple OS platforms (Windows, MAC, Linux) are pluses.

How to Apply: Applicants may be U.S. Citizens, resident aliens, or non-resident aliens holding or eligible for a valid employment visa. Applications must be accepted until the position is filled. Please submit a curriculum vitae and brief statement of how your experience relates to the needed qualifications along with 3 letters of reference to: **Neal S. Young, M.D. Director CHI c/o Christen Sandoval Building 15F2 MSC 2664 NIH Bethesda MD 20892**, or electronically to **christen.sandoval@nih.gov**.

Additional information about CHI is available online at: **http://www.nhlbi.nih.gov/resources/chi/index.htm**

CityU 30
香港城市大學
City University of Hong Kong
30th Anniversary

Worldwide Search for Talent

City University of Hong Kong is a dynamic, fast-growing university that is pursuing excellence in research and professional education. As a publicly-funded institution, the University is committed to nurturing and developing students' talents and creating applicable knowledge to support social and economic advancement.

The Department of Biomedical Sciences has recently been established by the University to develop strategic growth areas of life sciences. It aims to become one of leading centers in the Asia-Pacific region specializing in professional education and cutting-edge research in targeted areas of biomedical sciences. The Department has programs leading to MPhil and PhD degrees, and plans to offer a BSc program and a taught MSc program in biomedical sciences in the coming years. Involvement in pre-clinical teaching is being planned in connection with a proposed School of Veterinary Medicine.

Applications and nominations are invited for:

Chair Professor/Professor/ Associate Professor/Assistant Professor Department of Biomedical Sciences *[Ref. A/133/29]*

Requirements : A PhD/MD/DVM or an equivalent degree in the broadly-defined areas of biomedical sciences. Excellent academic records and English communication skills are essential. Successful candidates are expected to teach at both undergraduate and postgraduate levels, conduct original research, attract external research funding, and publish in high-impact journals. The Department currently has active research in molecular, cellular and systems study of neuroscience, cancer, or regenerative biology, and the development of novel therapeutics and nanomedicine. Candidates with strong background in these and other biomedical science-related areas, especially zoonotic infectious diseases, public health, and food safety, are welcome to apply. Preference will be given to qualified candidates whose activities can contribute to multidisciplinary and collaborative biomedical research. The Department is committed to the professional development of its faculty, enabling them to become next-generation leaders in basic and translational biomedical sciences. Priority will be given to qualified candidates who can contribute through their research, teaching, and service to the diversity and excellence of the University and its community.

Candidates for the post of Professor and above should have a distinguished academic record including significant external funding support, demonstrated leadership skills, and a strong commitment to graduate and undergraduate education. Successful candidates are expected to develop internationally competitive research programs; and assume academic and administrative leadership in the Department by assisting in faculty development, promoting collaboration in cross-disciplinary teaching and research programs within the University, and facilitating the translation of basic biomedical research to practices of health services and healthcare-related industries.

Salary and Conditions of Service
Remuneration package will be driven by market competitiveness and individual performance. Excellent fringe benefits include gratuity, leave, medical and dental schemes, and relocation assistance (where applicable). Initial appointment will be made on a fixed-term contract.

Information and Application
Further information on the posts and the University is available at http://www.cityu.edu.hk or from the Human Resources Office, City University of Hong Kong, Tat Chee Avenue, Kowloon Tong, Hong Kong [Email: hrojob@cityu.edu.hk/ Fax: (852) 2788 1154 or (852) 3442 0311]. Please send the nomination or application with a current curriculum vitae and at least 3 reference reports to Prof. Michael YANG, Faculty Search Committee, Department of Biomedical Sciences via email at bms@cityu.edu.hk. Please quote the reference number in the application. **Applications and nominations will receive full consideration until the positions are filled**, and only shortlisted applicants will be contacted and invited to visit the Department. The University's privacy policy is available on the homepage.

The University also offers a number of visiting positions through its "CityU International Transition Team" scheme for current graduate students, postdoctoral scholars, and for early-stage and established scholars, as described at http://www.cityu.edu.hk/provost/cityu_international_transition.htm.

City University of Hong Kong is an equal opportunity employer and we are committed to the principle of diversity. We encourage applications from all qualified candidates, especially those who will enhance the diversity of our staff.

Institut Pasteur

The Institut Pasteur is hiring a director and 2 senior group leaders for its new Center of Bioinformatics, Biostatistics and Integrative Biology.

Institut Pasteur is a non-profit private foundation dedicated to fundamental research in human biology and the prevention and treatment of disease, with a large focus on infectious diseases, through basic science, education, and public health activities. The Paris campus houses 146 research units belonging to 10 research departments, employing about 2,600 people. It is recognized worldwide as a leader in infectious disease research and is ranked as a top level institution for publication impact in the field of microbiology. Institut Pasteur has developed a world-class technological center, its "Technopole" composed of 10 state-of-the-art technological platforms, which closely collaborate with the researchers and cover their needs for studying modern biology from genomic to post-genomic activities, including bioinformatics, genotyping, DNA and protein sequencing, transcriptomics, proteomics, protein and antibody production, crystallography and X-ray diffraction, macromolecular interactions, collections, animal facilities and an exceptional imaging centre (Imagopole).

The Positions

The new direction of the Institut Pasteur has defined Bioinformatics/ biostatistics and integrative biology as strategic priorities. In this frame, the Pasteur Institute is seeking an outstanding scientist to direct a newly created "Centre of Bioinformatics, Biostatistics and Integrative Biology" located on the Paris campus. The goal of this Center is to federate, from a computational biology perspective, the different but highly complementary research themes that are present on the Campus: genomics of hosts and pathogens, infection biology, evolutionary and population genetics, structural biology and human health. In addition to directing the new Center, the successful candidate shall have his/her own research group, in order to pursue his/her scientific interests. To accomplish this double duty, the candidate will receive substantial financial support, both in running costs and personnel, from the Pasteur Institute. In this context, the Institut is also opening two additional senior group leader positions in these fields to increase the size of its community and its visibility.

Candidate's profile

Successful candidates will possess the following qualifications:

- PhD with a minimum of 10 years post-doctoral research experience.
- Recognized scientific leadership in bioinformatics and computational biology
- Broad experience in methodological development for the analysis of various types of data
- Consistent record of cutting-edge research as evidenced by senior author publications in top journals
- Significant experience in managing and mentoring scientists, and in designing and executing an innovative research program
- Demonstrated ability to collaborate with scientists irrespective of their computational or experimental background

The application should comprise the following (in order) in a single pdf file:

1. A brief introductory letter.
2. A Curriculum Vitae and a full publication list.
3. A description of past and present research activities (4-5 pages with 1.5 spacing).
4. The proposed research project (8-10 pages with 1.5 spacing).

Further information on the institute its facilities can be found on the web site **http://www.pasteur.fr**. Applications should be addressed to **gengeninfo@pasteur.fr** by **May 31 2014**. Short-listed candidates will be invited for interview in September 2014 and decisions will be announced by early October 2014.

Informal Inquiries can be addressed to **Didier Mazel** (Director of the **Genomes and Genetics department**).

Sun Yat-sen University, Professor or Associate Professor in Marine Sciences

South China Sea Resource Exploitation and Protection Collaborative Innovation Center (SCS-REPIC) has been recently established in Sun Yat-sen University, Guangzhou, China. SCS-REPIC invites applications for several faculty positions at Associate Professor and Full Professor levels.

All applicants must have a Ph.D. or equivalent degree, and a strong record of research accomplishments. Successful applicants are expected to establish and maintain an extramurally funded research program with emphasis in the areas of (marine geology, physical oceanography, marine ecology, marine chemistry, marine natural products, data mining with big data, marine biology).These positions include a 12-month salary, fringe benefits, competitive start-up package, and modern laboratory facilities or by negotiations.

To apply for these positions, please send your CV and a brief statement of research interests to hanmox@mail.sysu.edu.cn.

Review of applicants will begin as soon as the applications are submitted and will continue until the positions are filled. Anticipated start-date is the spring or summer of 2014.The SYSU is an equal opportunity employer and encourages persons of any races, ethnicity, ages and genders to apply.

AAAS is here – helping scientists achieve career success.

Every month, over 400,000 students and scientists visit ScienceCareers.org in search of the information, advice, and opportunities they need to take the next step in their careers.

A complete career resource, free to the public, *Science* Careers offers a suite of tools and services developed specifically for scientists. With hundreds of career development articles, webinars and downloadable booklets filled with practical advice, a community forum providing answers to career questions, and thousands of job listings in academia, government, and industry, *Science* Careers has helped countless individuals prepare themselves for successful careers.

As a AAAS member, your dues help AAAS make this service freely available to the scientific community. If you're not a member, join us. Together we can make a difference.

To learn more, visit
aaas.org/plusyou/sciencecareers

AAAS + U = Δ

泽生科技 ZENSUN

Company: Zensun (Shanghai) Sci. & Tech. Co., Ltd.

Job Title: **Vice President of R&D** (Location Shanghai)

www.zensun.com

Responsibilities:

1. Leading an innovative drug discovery research team, establish a scientific management system.
2. Organizing research projects for novel drugs.
3. Conducting basic research in molecular biology, cell biology and other aspects.

Job requirements:

1. Doctoral degree in either Molecular biology, cell biology, medicine or immunology. More than 5 years of managerial experience in the pharmaceutical or biotechnology industry.
2. Be familiar with the complete development process of biological drugs, working experience in drug development and team management is preferred.

Please submit your resume and cover letter to **xutao@zensun.com**

VCU MASSEY CANCER CENTER
Virginia Commonwealth University

SCIENTIFIC PROGRAM LEADER

Associate/Full Professor (tenure eligible)
Position Number: F35670

Hire Date: August 1, 2014
Deadline: Open until Filled

The Massey Cancer Center of Virginia Commonwealth University (VCU), an NCI-designated Cancer Center and VCU School of Medicine are recruiting a senior scientist to lead its Radiation Biology and Oncology (RBO) Scientific Program. One of five scientific programs with the Massey Cancer Center, and one of only nine programs in NCI-designated Cancer Centers in the country with an emphasis on radiation sciences, the RBO has a scientific focus in the areas of DNA repair, tumor microenvironment, and the impact of inflammation on tumor radio responsiveness and normal tissue radio sensitivity. The RBO program also is one of the only two programs in the Cancer Center with an active clinical trial component. A multidisciplinary program with sixteen members representing four different departments and two schools, membership in the RBO consists of five laboratory scientists, three medical physicists, one biostatistician and seven clinicians.

This is a tenure-track appointment at the rank of Associate Professor or Professor in the VCU School of Medicine, commensurate with the candidate's experience. The successful candidate will have a track record of sustained extramural funding, publication and recognition as a leader in his/her field of study. He/she will be expected to provide scientific direction, foster inter- and intra-programmatic collaborations leading to growth of the program, and expand the program's translational research component. He/she must have a Ph.D. and/or M.D. in a relevant scientific area. The successful candidate must have demonstrated experience working in and fostering a diverse faculty, staff, and student environment or commitment to do so as a faculty member at VCU.

Richmond is a midsized metropolitan area with close proximity to Washington, D.C., the beautiful Blue Ridge Mountains, and scenic coastal areas.

Applications shall be forwarded by email, preferably in one pdf file, to: **Jeannie Rummel, Human Resources Administrator, VCU Massey Cancer Center**; **jcrummel@vcu.edu**.

Virginia Commonwealth University is an equal opportunity/affirmative action employer. Women, minorities, and persons with disabilities are encouraged to apply.

Introducing the new
***Science* Careers Jobs app** from Science

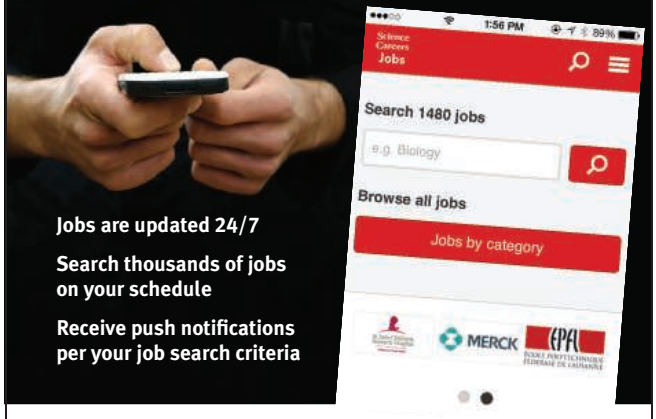

Jobs are updated 24/7

Search thousands of jobs on your schedule

Receive push notifications per your job search criteria

Get a job on the go.
Search worldwide for thousands of scientific jobs in academia, industry, and government. Keep your finger on the pulse of your field—set up an alert for the type of job you are looking for and receive push notifications when jobs are posted that meet your criteria. The application process is seamless, linking you directly to job postings from your customized push notifications.

Scan this code to download app or visit **apps.sciencemag.org** for information.

Science Careers
From the journal *Science* AAAS

ScienceCareers.org

UNIVERSITÄT BASEL

The Faculty of Science (Philosophisch-Naturwissenschaftliche Fakultät) of the University of Basel invites applications for the position of

Professor of Chemistry (open rank)

We are seeking for candidates with an internationally recognized research program and an outstanding publication record in

Organic Synthesis

While all areas of organic chemistry will be considered, upon equal qualifications, preference will be given to candidates with a focus on synthetic methodology. The selected candidate is expected to participate to teaching chemistry at all levels of the BSc, MSc and PhD programs. The University of Basel has an established program for career progression allowing promotion to associate and full professor upon successful evaluation.

The Department of Chemistry is located near the centre of Basel, a town which provides a stimulating and supportive environment for interdisciplinary research thanks to the strong presence of science institutes as well as the chemical and pharmaceutical industries. For further information see http://www.chemie.unibas.ch

The selected candidate is expected to commence the appointment in Summer 2015. Applications received by April 30, 2014 are guaranteed full consideration. The University of Basel is an equal opportunity employer and applications from female candidates are particularly encouraged. Applications, including a curriculum vitae, list of publications, an outline of current and future research plans and names of four referees should be sent by email (as pdf file) to Prof. Dr. Jörg Schibler University of Basel, Dean of the Faculty of Sciences, Klingelbergstrasse 50, 4056 Basel, dekanat-philnat@unibas.ch. For further information, please contact: Prof. Dr. Thomas Ward, Head, Department of Chemistry, E-mail: thomas.ward@unibas.ch

UNI BASEL

THE UNIVERSITY OF HONG KONG
香 港 大 學

Founded in 1911, The University of Hong Kong is committed to the highest international standards of excellence in teaching and research, and has been at the international forefront of academic scholarship for many years. The University has a comprehensive range of study programmes and research disciplines spread across 10 faculties and over 140 academic departments and institutes/centres. There are over 27,800 undergraduate and postgraduate students coming from 50 countries, and more than 2,000 members of academic and academic-related staff, many of whom are internationally renowned.

Post-doctoral Fellowships and Research Assistant Professorships

Applications are invited for a number of positions as Post-doctoral Fellow (PDF) and Research Assistant Professor (RAP), at the University of Hong Kong, on or before February 28, 2015. Appointments will be made for a period of 2 to 3 years.

PDF and RAP posts are created specifically to bring new impetus and vigour to the University's research enterprise. Positions are available from time to time to meet the strategic research needs identified by the University. Positions are available in the following Faculties/Departments/Schools/Centres:

- School of Modern Languages and Cultures
- Faculty of Education
- Computer Science
- Electrical and Electronic Engineering
- Industrial and Manufacturing Systems Engineering
- Mechanical Engineering
- Law
- Anatomy
- Biochemistry
- Centre for Cancer Research
- School of Chinese Medicine
- Research Centre of Heart, Brain, Hormone and Healthy Aging
- Research Centre of Infection and Immunology
- Centre of Influenza Research
- Medicine
- Ophthalmology
- Orthopaedics and Traumatology
- School of Biological Sciences
- Chemistry
- Earth Sciences
- Geography
- Journalism and Media Studies Centre
- Psychology
- Social Work and Social Administration
- The State Key Laboratory for Liver Research
- The State Key Laboratory of Pharmaceutical Biotechnology

Post-doctoral Fellows

PDFs are expected to devote full-time to research. Applicants should be doctoral degree holders having undertaken original research that has contributed to the body of knowledge. A highly competitive salary commensurate with qualifications and experience will be offered. Annual leave and medical benefits will also be available.

Research Assistant Professors

The main focus of an RAP's duty is research. RAPs can however be assigned some teaching duties, up to 50% of the normal teaching load. Applicants should be research active and have a proven publication record. A highly competitive salary commensurate with qualifications and experience will be offered, with a contract-end gratuity and University contribution to a retirement benefits scheme (totalling up to 15% of basic salary). Annual leave and medical benefits will also be offered.

Procedures

Prospective applicants are invited to visit our webpage at http://jobs.hku.hk/ to view the list of the Faculties/Departments/Schools/Centres and their research areas for which PDF/RAP positions are currently available. Before preparing an application, they should contact the Head of the appropriate academic unit to ascertain that their research expertise matches the research area for which a vacant PDF/RAP post is available.

Applicants must submit a completed University application form, which should clearly state **which position** they are applying for; and in which academic discipline. They should also provide further information such as details of their research experience, publications, research proposals, etc.

Application forms (341/1111) can be obtained at http://www.hku.hk/apptunit/form-ext.doc. Further particulars can be obtained at http://jobs.hku.hk/. **Closes May 9, 2014**. The University thanks applicants for their interest, but advises that only shortlisted applicants will be notified of the application result.

The University is an equal opportunity employer and is committed to a No-Smoking Policy